Topics in Medicinal Chemistry 34

Zhen Cheng *Editor*

Fluorescent Imaging in Medicinal Chemistry

Springer

34
Topics in Medicinal Chemistry

Aims and Scope

Topics in Medicinal Chemistry (TMC) covers all relevant aspects of medicinal chemistry research, e.g. pathobiochemistry of diseases, identification and validation of (emerging) drug targets, structural biology, drugability of targets, drug design approaches, chemogenomics, synthetic chemistry including combinatorial methods, bioorganic chemistry, natural compounds, high-throughput screening, pharmacological in vitro and in vivo investigations, drug-receptor interactions on the molecular level, structure-activity relationships, drug absorption, distribution, metabolism, elimination, toxicology and pharmacogenomics. Drug research requires interdisciplinary team-work at the interface between chemistry, biology and medicine. To fulfil this need, TMC is intended for researchers and experts working in academia and in the pharmaceutical industry, and also for graduates that look for a carefully selected collection of high quality review articles on their respective field of expertise.

Medicinal chemistry is both science and art. The science of medicinal chemistry offers mankind one of its best hopes for improving the quality of life. The art of medicinal chemistry continues to challenge its practitioners with the need for both intuition and experience to discover new drugs. Hence sharing the experience of drug research is uniquely beneficial to the field of medicinal chemistry.

All chapters from Topics in Medicinal Chemistry are published OnlineFirst with an individual DOI. In references, Topics in Medicinal Chemistry is abbreviated as Top Med Chem and cited as a journal.

More information about this series at http://www.springer.com/series/7355

Zhen Cheng
Editor

Fluorescent Imaging in Medicinal Chemistry

With contributions by

Y. An · A. Bi · Z. Cheng · Y. Du · T. Gao · J. Grimm · S. He · X. Jiang · J. V. Jokerst · T. Kim · X. Liu · Y. Liu · J. F. Lovell · T. F. Massoud · N. Murthy · A. Natarajan · R. Paulmurugan · M. Skubal · E. P. Stater · U. K. Sukumar · R. Tamura · C. Tang · J. Tian · D. Vernekohl · L. Xing · S. Yang · X. Yang · W. Zeng · Y. Zhang

Springer

Editor
Zhen Cheng
Stanford University
Stanford, CA, USA

ISSN 1862-2461 ISSN 1862-247X (electronic)
Topics in Medicinal Chemistry
ISBN 978-3-030-46706-7 ISBN 978-3-030-46707-4 (eBook)
https://doi.org/10.1007/978-3-030-46707-4

This Springer imprint is published by the registered company Springer Nature Switzerland AG.
The registered company address is: Gewerbestrasse 11, 6330 Cham, Switzerland

Preface

Fluorescent imaging techniques have broad and profound impact on numerous research fields including chemical biology, cancer biology, medical imaging, and pharmaceutical sciences. It provides powerful tools to reinforce medicinal chemistry research, facilitate drug discovery and development, and help diseases diagnosis and treatment. This book summarizes the most recent developments of fluorescent imaging techniques for medicinal chemistry research and biomedical applications.

In Chapter "Fluorescence Molecular Imaging of Medicinal Chemistry in Cancer", some fundamental issues of fluorescence molecular imaging including imaging probe and imaging analysis methods are described, followed by an introduction to its medical applications in drug discovery. Then organic molecules-based fluorescent imaging probes and inorganic nanoprobes are presented in Chapter "Organic Fluorescent Probes for Diagnostics and Bio-Imaging" and Chapter "Inorganic Fluorescent Nanomaterials", respectively. In Chapter "Advancements of Second Near-Infrared Biological Window Fluorophores: Mechanism, Synthesis, and Application In Vivo", fluorescent imaging at long wavelengths (1,000–17,000 nm), namely near-infrared window II imaging, is introduced. Chapter "X-Ray Excited Fluorescent Materials for Medical Application" covers a novel approach to using X-ray to illuminate materials and produce fluorescence for medical imaging applications. In Chapter "Applications of Fluorescent Protein-Based Sensors in Bioimaging", fluorescent proteins used for bioassays and their applications are reviewed. Chapter "Fluorescent Probes for Diagnostics of β-Galactosidase: From Micro to Macro" summarizes the fluorescent probes, nanomaterials, and biomolecules for the detection of an important enzyme (β-galactosidase) and their applications in health monitoring. The last chapter focuses on the current state of fluorescent imaging techniques, especially endoscopic imaging and Cerenkov luminescence imaging for the diagnosis and treatment of diseases in clinics.

Through this book, it is hoped that more people will appreciate the role of fluorescent imaging, explore this exciting field, and develop new fluorescent imaging techniques for addressing unmet medical needs.

Stanford, CA, USA Zhen Cheng

Contents

Top Med Chem (2020) 34: 1–32
DOI: 10.1007/7355_2019_86

Published online: 29 February 2020

Fluorescence Molecular Imaging of Medicinal Chemistry in Cancer

Jie Tian, Yang Du, Chu Tang, and Yu An

Contents

J. Tian (✉)
CAS Key Laboratory of Molecular Imaging, The State Key Laboratory of Management and Control for Complex Systems, Institute of Automation, Chinese Academy of Sciences, Beijing, China

Beijing Key Laboratory of Molecular Imaging, Beijing, China

University of Chinese Academy of Sciences, Beijing, China

Beijing Advanced Innovation Center for Big Data-Based Precision Medicine, Beihang University, Beijing, China

Engineering Research Center of Molecular and Neuro Imaging of Ministry of Education, School of Life Science and Technology, Xidian University, Xi'an, Shaanxi, China
e-mail: jie.tian@ia.ac.cn; tian@ieee.org; http://www.3dmed.net

Y. Du and Y. An
CAS Key Laboratory of Molecular Imaging, The State Key Laboratory of Management and Control for Complex Systems, Institute of Automation, Chinese Academy of Sciences, Beijing, China

Beijing Key Laboratory of Molecular Imaging, Beijing, China

University of Chinese Academy of Sciences, Beijing, China

C. Tang
Engineering Research Center of Molecular and Neuro Imaging of Ministry of Education, School of Life Science and Technology, Xidian University, Xi'an, Shaanxi, China

Abstract The process of new drug discovery and development is a lengthy, high-risk, and costly task. Fluorescent molecular imaging (FMI) has tremendous potential for improving the efficiency of drug screening, evaluating drug effects, accelerating the process, and markedly reducing the cost of new drug development from initial target validation and high-throughput screening identification campaigns to the final human translation phases. FMI can help evaluate the role of new candidate drugs under the influence of complex biological responses in living subjects and better understand the mechanism between drug activity and disease, which can help select candidates that seem most likely to succeed or prevent the development of drugs that seem to fail in the end. Hence, in this chapter, FMI was described for its application in drug discovery, including identification of tumor-specific markers, candidate drug screening, determination of pharmacokinetics of drugs, and preparation of prodrugs.

Keywords Cancer, Drug discovery, Fluorescent molecular imaging, Medicinal chemistry

Abbreviations

BBTD	Benzobisthiadiazole
BEM	Boundary element method
BLI	Bioluminescence imaging
BODIPY	Boron dipyrromethene
Cy	Cyanine
D-A-D	Donor-acceptor-donor scaffold
DE	Diffusion equation
FDM	Finite difference method
FEM	Finite element method
FITC	Fluorescein isothiocyanate
FMI	Fluorescence molecular imaging
FMT	Fluorescence molecular tomography
GFP	Green fluorescent protein
HDACs	Histone deacetylases
ICG	Indocyanine green
MM	Meshless method
NIR	Near-infrared
ROS	Reactive oxygen species
SBR	Signal-to-background ratio

1 Introduction

Fluorescence molecular imaging (FMI) utilizes molecular probes to label target organisms. Under certain external conditions, the molecular probe releases a fluorescent light in the visible or near-infrared spectrum using high-sensitivity detection equipment for fluorescence. The signal is collected, and the position and intensity of the fluorescent light source are displayed to obtain the physiological activity information of the organism (Fig. 1). FMI is the most intuitive imaging modality, and the fluorescent methods allow us to detect photons with familiar parallels to our eyesight, allowing spatial and temporal resolutions that are otherwise unachievable [1, 2]. Compared to the positron emission tomography (PET) imaging and magnetic resonance imaging (MRI), FMI is a noninvasive and nonionizing imaging modality with higher sensitivity and higher specificity, is safer, has a lower cost, and is easier to perform, and it offers anatomical, physiological, and even molecular information within the bodies of living subjects [3–5]. Therefore, FMI has been widely applied for tumor detection, drug development, image-guide surgery, and other biomedical fields.

From a medicinal chemistry perspective, FMI is a potent tool for probing biomolecules in their natural environment and for visualizing dynamic processes in complex biological samples, living cells, and organisms [6–9], which are well suited for highlighting molecular alterations associated with pathological disorders. Thereby, it offers means of implementing sensitive and alternative technologies for diagnostic purposes, which constitute as attractive tools for drug discovery programs from initial target validation and high-throughput screening identification campaigns to the final clinical translation phases. In this chapter, the FMI probe, imaging analysis methods, and medical application in drug discovery will be described.

2 Imaging Probe

Fluorescence probe is one of the basic elements of FMI. Fluorescence probes are usually made up of fluorophores and targeting ligands.

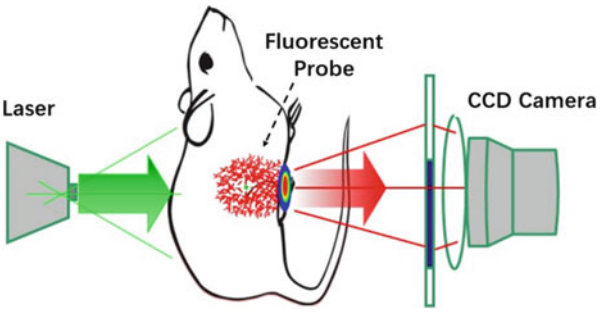

Fig. 1 The principle of fluorescence molecular imaging (FMI)

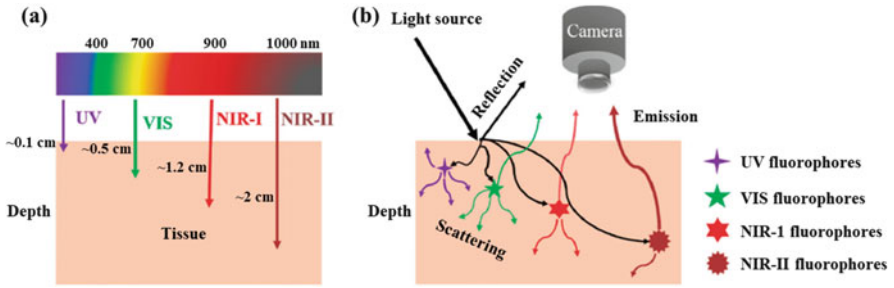

Fig. 2 Wavelengths for fluorescence molecular imaging. (**a**) Tissue penetration depth of light with different wavelengths. (**b**) Light when entering a tissue can be reflected or adsorbed by molecules within the tissue or excite fluorophores to emit light at a different wavelength. Reproduced from Ref. [11]

2.1 Fluorophores

The fluorophore can convert molecular recognition information into a fluorescence signal, which has the advantages of high sensitivity, rapid reaction time, and the ability to realize in situ detection. An ideal fluorophore has a large value of Stokes shift [difference between the absorption maximum (λ_{max}) and the emission maximum (λ_{em})] to minimize the reabsorption of emitted photons. According to the fluorophore with emission in different regions, it can be divided into three categories: visible light ($\lambda_{em} < 700$ nm), near-infrared I (NIR-I, $700 < \lambda_{em} < 1{,}000$ nm), and near-infrared II (NIR-II, $\lambda_{em} > 1{,}000$ nm) fluorophores (Fig. 2) [10, 11].

2.1.1 Visible Light Imaging Fluorophores

Visible light fluorophores mainly include fluorescein isothiocyanate (FITC), cyanine (Cy), rhodamine, BODIPY, coumarin, quinoline, etc. (Fig. 3) [12–16]. These fluorophores are fluorescent indicators with rapid detection, good reproducibility, and low sample size, which can be used to detect the changes of cations (Na^+, K^+, Mg^{2+}, Ca^{2+}, etc.), anions (phosphate radical, etc.), free radicals (reactive oxygen species H_2O_2, superoxide ion), monolinear oxygen, hydroxyl radical, sugar (glucose, chitosan, etc.), nucleic acid (DNA, RNA), and enzymes (trypsin, viral protease, no synthase) in biological systems after drug therapy [17–19]. The visible light fluorophores (400–700 nm) are used quite often in biomedical studies, but the key issues in fluorescence imaging of visible regions include autofluorescence, quenching, photobleaching, and a low depth of tissue penetration. In comparison, fluorescence imaging in NIR offers considerable advantages. However, the use of NIR fluorophores requires a special camera, as the light is not visible to the naked eye or conventional video cameras.

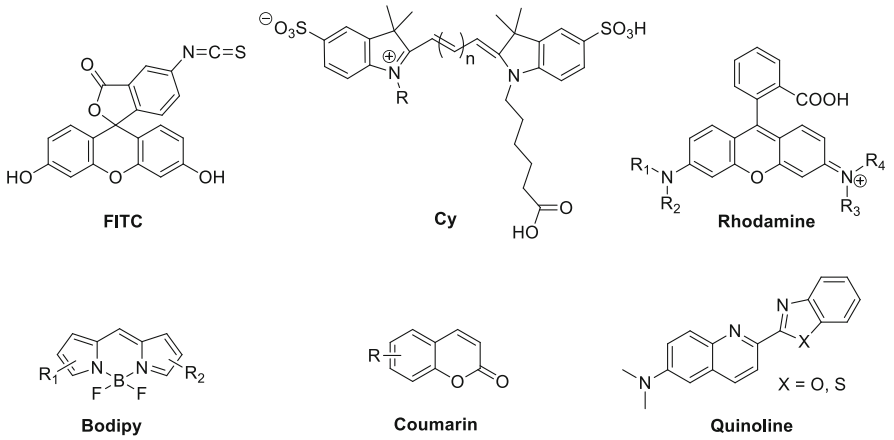

Fig. 3 Representative visible light fluorophores

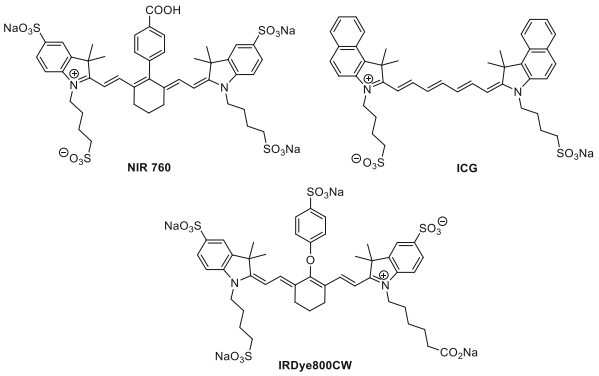

Fig. 4 Representative NIR-I fluorophores

2.1.2 NIR-I Imaging Fluorophores

Fluorophores with emission in the NIR region possess less absorption and scatter from tissues much more efficiently than fluorophores based on visible light, which is favorable for in vivo imaging with a high signal-to-background ratio (SBR). This imaging modality also inherited quick feedback, high-resolution, and noninvasive properties of optical imaging and can be utilized to visualize the real-time dynamics in living organisms [20–23]. Over the past decade, fluorescence imaging in the first NIR window (NIR-I, 700–900 nm) has been widely studied in fundamental research and preclinical/clinical applications, which is partially because of the immediate availability of a wide range of fluorophores, such as NIR-760, IRDye800CW, indocyanine green (ICG), methylene blue, and their derivatives (Fig. 4) [24–26].

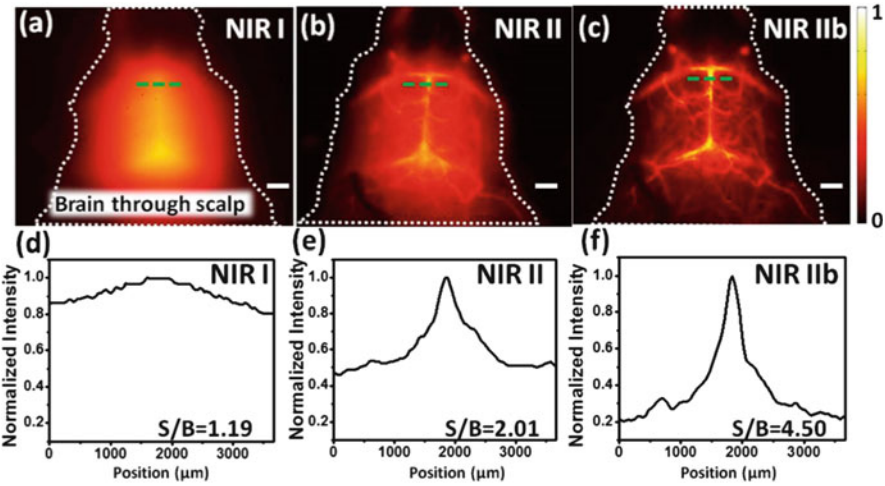

Fig. 5 Fluorescence imaging of the cerebrovasculature of mice without craniotomy in the (**a**) NIR-I, (**b**) NIR-II, and (**c**) NIR-IIb regions, with the corresponding SBR analysis shown in (**d**)–(**f**). Scale bars, 2 mm. Reproduced from Ref. [30]

2.1.3 NIR-II Imaging Fluorophores

The generation of new fluorophores and the development of fluorescent labeling technology provide specific and efficient contrast for FMI and greatly improve the detection sensitivity and specificity of in vivo imaging. Compared to NIR-I, fluorescence imaging at the second near-infrared region (NIR-II, 1,000–1,700 nm) can realize better fluorescence image quality (Fig. 5) [27]. The NIR-II biological window is broadly defined as wavelengths in range of 1,000–1,700 nm. Smaller optical sub-windows such as NIR-IIa (1,300–1,400 nm) and NIR-IIb (1,500–1,700 nm) have provided further improvements in fluorescence imaging metrics. The 1,400–1,500 nm window is typically avoided owing to the presence of an absorbance peak due to a water overtone. Significant improvements in imaging temporal and spatial resolution (~20 ms and ~25 μm) and penetration depth (up to ~3 cm), which are very difficult to achieve with NIR-I and also PET and SPECT imaging, have been fulfilled by this innovative NIR-II region on biomedical imaging, thanks to the reduced scattering, negligible tissue absorption, and minimal autofluorescence [28, 29].

However, NIR-II fluorophores also suffer from poor water solubility, low photostability, low quantum yield, and the scarcity of molecules with suitable NIR-II band gaps have further limited the applications and development of NIR-II imaging techniques. So far, a series of fluorophores with emission wavelengths longer than 1,000 nm in the NIR-II region have been designed based on the donor-acceptor-donor scaffold (D-A-D). These NIR-II fluorophores are usually composed of various spacers (thiophene), electron donor (fluorene and triphenylamine), and the central electron-accepting aromatic backbone (benzobisthiadiazole, BBTD), which can greatly expand the library of small-molecule NIR-II fluorophores (Fig. 6) [31–33]. Fortunately, a series of organic small molecules and organic and inorganic nanomaterials with precisely

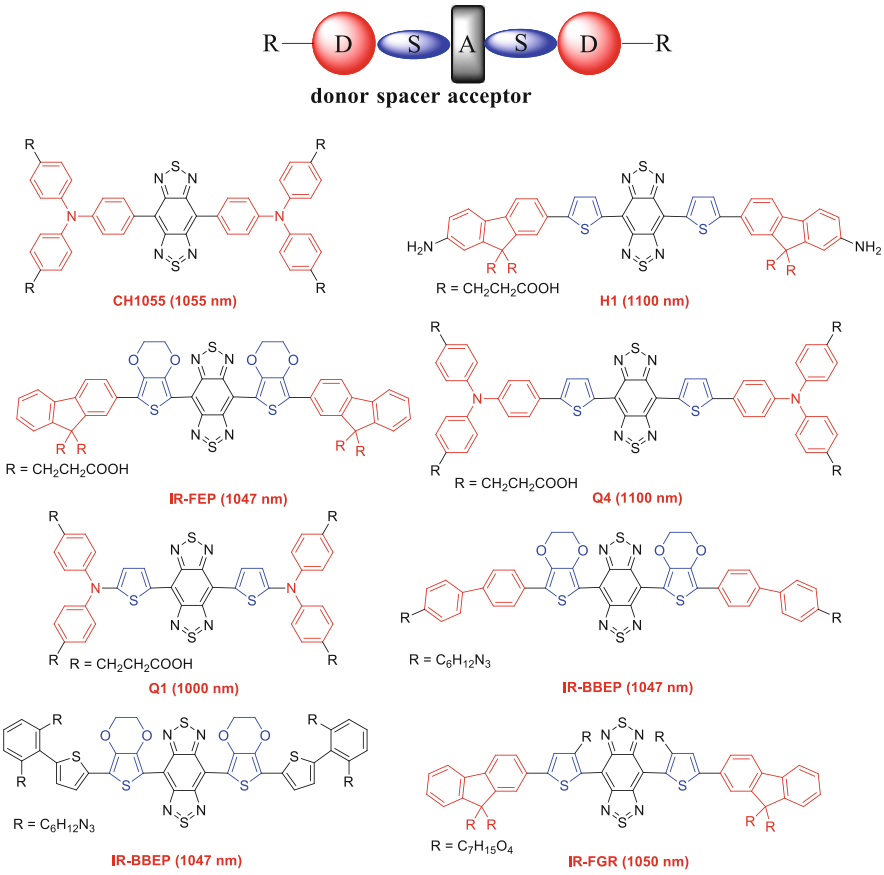

Fig. 6 Representative NIR-II fluorophores

controlled structures and intrinsic near-infrared emissions in the NIR-II window have been developed to enable the acquisition of high-definition NIR-II images at wavelengths well in excess of 1,000 nm. These NIR-I and NIR-II fluorophores can be used to develop diagnostics, biomedical imaging technologies, and drug discovery programs.

2.2 Targeted Ligand of Fluorescent Probes

In the field of medicinal chemistry, the target is the key element for the drug design and development. FMI has the advantages of high sensitivity, convenience, reliability, and suitability for large-scale detection of drug targets. Using FMI, not only the receptors, proteins, and genes that interact with drugs can be imaged, but the drug targets can also be located and evaluated for their presence in an organism. The spatial and temporal distribution of the target is evaluated quantitatively. Verification

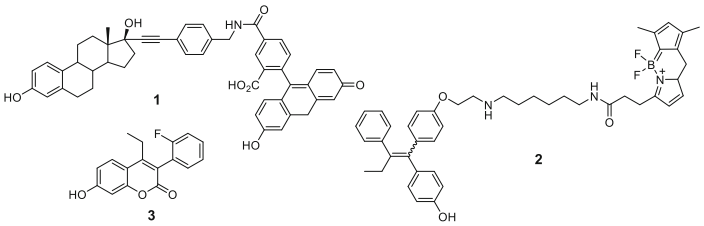

Fig. 7 Representative estrogen receptor-targeted fluorescent probes **1**–**3**

of target expression is valuable for diagnosis, as well as the selection of treatment regimen and pre-evaluation. There are often overexpressed specific receptors on the surface of tumor cells. For example, abnormal overexpression of estrogen receptor (ER) [34–36] and fructose transporter (GLUT5) [37] has been found in breast cancer; prostate-specific membrane antigen (PSMA) is overexpressed in prostate cancer [38–41]. FMI can be used to determine the expression level of related hormone receptors in tumor biopsy specimens, which can help select the best treatment plan. Using these receptors as targets to develop new, potential drugs with high specificity and affinity is the main direction of development of antitumor drugs. Currently, many active targeted fluorescence probes have been developed.

2.2.1 Estrogen Receptor-Targeted Fluorescent Probes

Estrogen receptor (ER) is a ligand-regulated transcription factor that regulates many physiological and pathological processes and also plays a predominant role in breast cancer growth. Therefore, ER is regarded as an important pharmaceutical target for the treatment of breast cancer, and the development of ER-targeted fluorescence probes has emerged as an active research field for breast cancer detection, and many of these probes have been developed (compounds **1**–**3**, Fig. 7) [34–36].

2.2.2 GLUT5 Transporter-Targeted Fluorescent Probes

Facilitated hexose transporters (Gluts) are a group of transmembrane proteins responsible for transporting sugars such as glucose or galactose across the cell membrane. Tumor cells usually overexpress the Glut transporter to meet their high levels of energy consumption needs. For example, GLUT5 is overexpressed in breast cancer cells but not in normal breast cells. Therefore, the selection of a high GLUT5-binding affinity compound as the targeting ligand is an effective strategy for the development of imaging probes for breast cancer detection (compounds **4**–**5**, Fig. 8) [37].

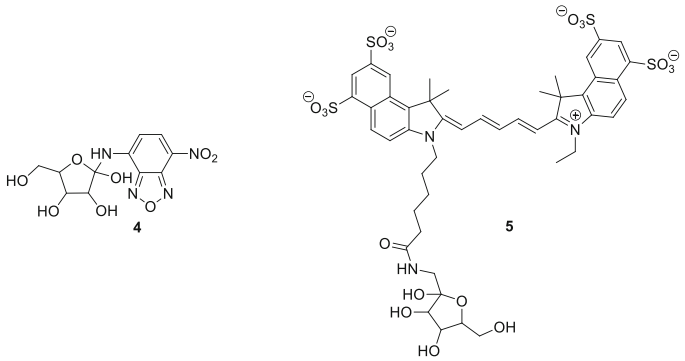

Fig. 8 Representative GLUT5 ligand **4** and targeted fluorescent probe **5**

2.2.3 Prostate-Specific Membrane Antigen (PSMA)-Targeted Fluorescence Probes

Prostate cancer is the most commonly diagnosed malignancy in men, and the integral membrane protein PSMA is becoming increasingly recognized as a viable target for prostate cancer diagnosis and treatment. Therefore, PSMA-specific antibodies, peptides, peptide derivatives, or other small molecules have been developed as targeting ligands for the development of imaging probes for prostate cancer detection (compounds **6**–**9**, Fig. 9) [38–41].

2.2.4 Folate Receptor-Targeted Fluorescent Probes

Folates are essential for the maintenance of all cells and tissue regeneration. Folates have a high affinity for their cell surface folate receptor (FR), which is primarily expressed on healthy cells where it does not readily encounter folate from the bloodstream. When the malignant transformation occurs, high levels of FR are expressed in a number of malignancies, including ovarian and endometrial cancers and myeloid leukemias. Thus, the high affinity of FR offers a potential means for tumor targeting, which has already become the main design strategy for the FR-targeted tumor imaging probes (compounds **10**–**11**, Fig. 10) [42, 43].

2.2.5 Cyclooxygenase-2 (COX-2)-Targeted Fluorescent Probes

COX-2 is a crucial biological mediator in the etiology of cancer. This enzyme is absent or present at low levels in normal cells but shows high expression levels in inflamed tissues as well as many premalignant and malignant tumors such as colorectal adenomas and adenocarcinomas. COX-2 has been used as an ideal imaging biomarker for cancer cells. Currently, many fluorescent probes have been engineered to target COX-2 for tumor detection (compounds **12**–**15**, Fig. 11) [44, 45].

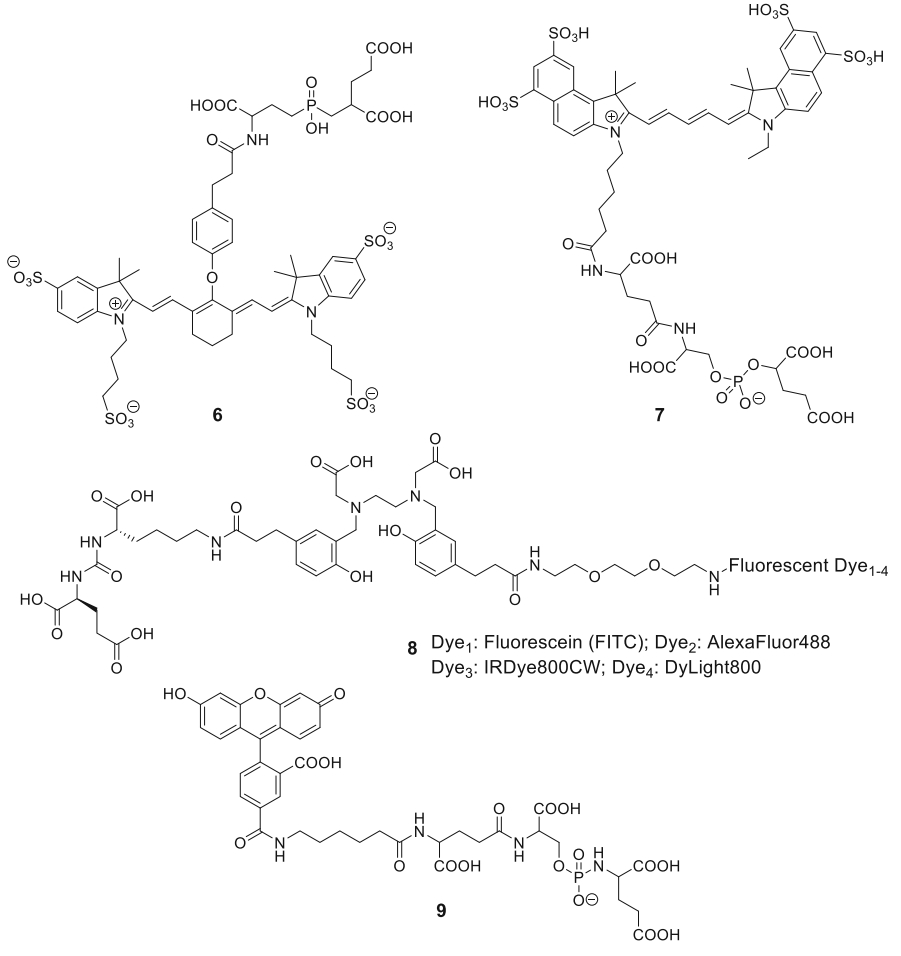

Fig. 9 Representative PSMA-targeted fluorescent probes **6–9**

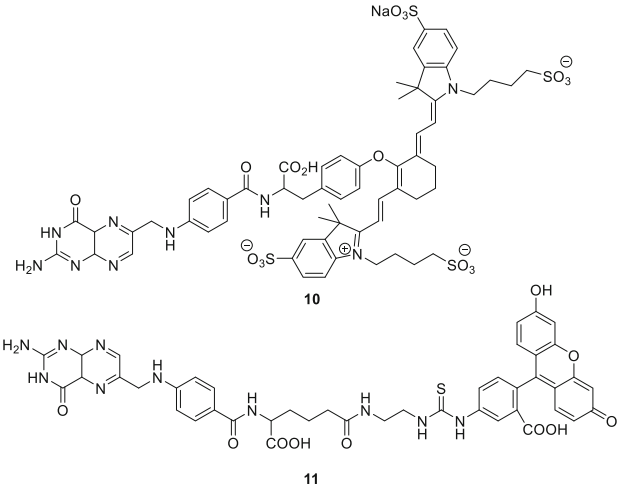

Fig. 10 Representative folate receptor-targeted fluorescent probes **10–11**

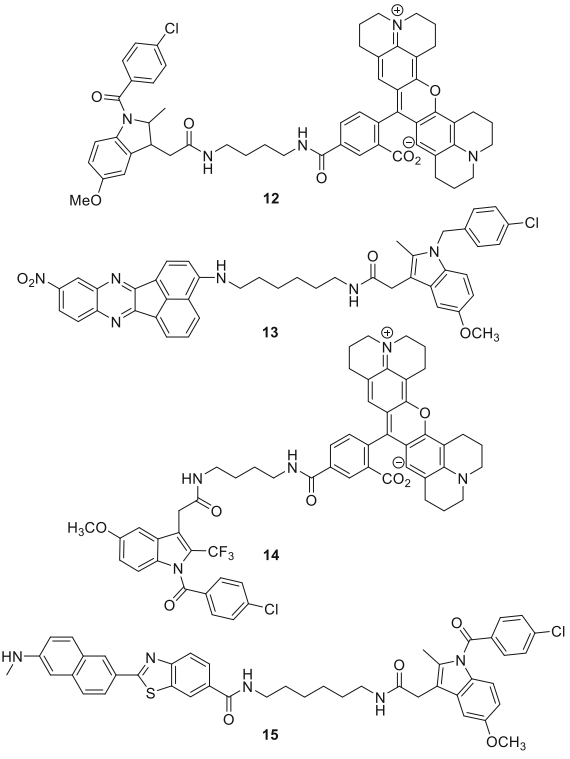

Fig. 11 Representative COX-2-targeted fluorescent probes **12–15**

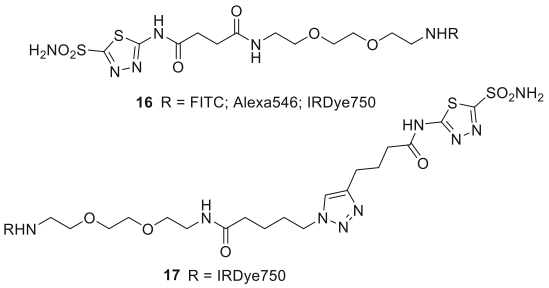

Fig. 12 Representative CAIX-targeted fluorescent probes **16–17**

2.2.6 Other Targeted Fluorescent Probes

In addition to the targeted fluorescence probes mentioned above, various other targeted fluorescence probes have also been reported, such as carbonic anhydrases IX (CAIX) probes. CAIX has been associated with tumor progression and invasion, which is usually expressed in normal tissues at certain levels, but overexpressed in many solid tumors, such as colorectal tumors. Therefore, CAIX can be used as a potential tumor target for the development of imaging probes (compounds **16–17**, Fig. 12) [46, 47].

In general, the targeted fluorescent probes were accomplished by conjugating fluorescence dye to the targeted ligand, which may have a great application prospect in the clinic for tumor diagnosis.

3 Imaging Analysis

Fluorescence molecular tomography (FMT) is a three-dimensional imaging method based on FMI, which is based on the distribution of fluorescence in biological tissues [48–53]. It was developed from two-dimensional (2D) qualitative imaging to three-dimensional (3D) quantitative research and further expanded the integration of stimulated fluorescence in the diagnosis and treatment of cancer and preclinical and clinical applications. The advent of FMT led to the three-dimensional reconstruction of FMI agent accumulation in living animals based on light recordings collected at the tissue boundary. FMT has been used to visualize and quantitate a variety of cellular and molecular events and, as opposed to planar fluorescence imaging, yields quantitative information and allows imaging at greater depth, up to several centimeters. It has developed rapidly in recent years and has become a research frontier and research hotspot for FMI technology [54–56].

When imaging spatial data needed for FMT reconstruction are obtained, then the reconstruction of the structural data and optical data based on the biological model can be carried out [57]. In general, the image reconstruction process includes two steps: solving the forward problem and solving the inverse problem. The solution of

the forward problem is used to calculate the photon propagation model of the fluorescence transmitted in the imaging space to obtain the linear relationship between the fluorescence measurement data on the surface of the tissue and the fluorescence distribution inside the bio-tissue. After the linear relationship is obtained by solving the photon transfer model, various methods are used to solve the linear model, and the distribution of fluorescence inside the imaging space is obtained, which is called the inverse problem [52].

3.1 Photon Propagation Model

The process of transmitting fluorescence from a light source to a biological body through a specific biological tissue is extremely complicated and includes various physical processes such as scattering of light, inter-tissue reflection, refraction, diffusion, and absorption. For FMT imaging, imaging is usually performed in the visible and near-infrared optical bands, and the scattering and absorption effects of this band of light inside the biological tissues are the main forms of our study. Therefore, the FMT photon propagation model can be simplified to a photon stochastic propagation model that contains only the scattering and absorption effects without considering the reflection and refraction of different tissues. Current mainstream mathematical theory to solve these problems is mainly based on Boltzmann's radiative transfer equation (RTE) [58], which is equivalent to photon propagation as transport of photon flux in a medium from particle fluctuation to energy transport and to study transport of light energy in biological tissue problems.

In three-dimensional biological tissue, the RTE solution is transformed into a six-dimensional space-time problem. There are few methods in solving mathematical and computer problems, and they are usually not able to directly close the analytical solution. Moreover, because of its unknowns, it can be solved precisely only in rare cases. Usually it cannot get a closed analytical solution. At the same time, it is extremely difficult to solve RTE directly, while the exact solution will only exist in rare cases. Therefore, it is common practice to replace itself with a simplified approximation of the radiation transfer equation [59], such as diffusion equation (DE), which is a widely used RTE-based simplified model [60–65]. It utilizes the first-order spherical harmonic function to expand important function items in the RTE equation and performs the approximate processing, which significantly reduces the computational complexity and is suitable for the visible and near-infrared bands of FMT imaging. In recent years, researchers have proposed such high-order approximations as RTE [66–71]. Compared with diffusion equations, higher-order approximation models can significantly improve FMT accuracy. The SN model [72], PN model [73], and SPN model [69] are three commonly used RTE high-order approximation models and usually give more accurate RTE solutions to the more diffusive equations. By these approximation methods, the traditional RTE equation can be transformed into several coupled higher-order partial differential equations for easy calculation and solution.

3.2 Forward Problem-Solving

The linear relationship between the measured data on the surface of the imaging area and the internal fluorescence distribution in the imaging area based on the photon propagation model is the core of the FMT forward problem. In recent years, researchers have proposed various mathematical solution methods including the analytic method, statistical method, and numerical analysis method to solve the forward problem of FMT [52]. Numerical analysis method is the main solving method currently used in optical molecular imaging reconstruction. Its computational efficiency is high and its applicability is wide. Numerical analysis methods include the finite difference method (FDM) [70], boundary element method (BEM), finite element method (FEM) [74], and meshless method (MM) [75]. FDM uses equidistant grid points and regular grids to solve the forward problem, which is more efficient than irregular grids. However, FDM has difficulty in dealing with geometrically complex imaging spaces and boundary conditions. In contrast, FEM is the mainstream solution to FMT forward problems in recent years. The main advantage of FEM is its effectiveness in dealing with complex geometric problems. In addition, the system matrices obtained by FEM are usually sparse and positive definite, which leads to a more stable solution and high computational efficiency, which is also beneficial to FMT reconstruction [76, 77]. However, the main drawback of FEM is that it is difficult to generate the FEM grid. In contrast, BEM only needs to discretize the imaging surface and the boundaries of the heterogeneous tissue within the space without the need to mesh the entire imaging space. Therefore, compared with FEM, BEM can effectively reduce the computational dimension and complexity to improve computational efficiency. However, fast and stable 3D mesh generation for complex geometry problems remains a challenging issue. In order to overcome the problem of 3D mesh generation, An et al. proposed a meshless method and applied it to solve the forward problem of FMT [78]. The method only needs to obtain nodes that are relatively independent from each other to discretize the imaging space and does not require a cumbersome gridding process.

3.3 Inverse Problem-Solving

In FMT preclinical and clinical trials, the fluorescence signal is usually only measured from the imaging surface. However, the dimension of the measurement data on the imaging space surface is usually much less than the number of internal nodes in the imaging space. Therefore, the inverse problem of FMT is ill-conditioned [55]. Moreover, because of the high scattering properties of photons in the imaging space, the inverse problem is also ill-posed, and it is difficult to find the exact solution [79–81]. At the same time, the noise generated during the experiment also affects the accuracy of the FMT reconstruction [82].

The ill-posedness of the FMT inverse problem is mainly due to the lack of information and uncertainty due to the high scattering of photons. In order to overcome the ill-posedness of reverse problems, researchers started from the light source prior information and combined it with a variety of a priori information related to the light source and photon transmission to reduce the uncertainty of the information so as to improve the accuracy of inverse problem-solving [83–89]. Researchers usually combined the prior information of the structure into the FMT reconstruction and proposed a nonhomogeneous imaging space model and a priori reconstruction method, which greatly improved the reconstruction accuracy. The structure of imaging space prior information can usually be obtained by high-resolution structural imaging modalities such as CT and MRI [90–94]. The optical parameters of various organs and tissues can be obtained by other imaging techniques such as DOT. The imaging technique that combines imaging modalities to increase imaging prior information is also known as multimodality imaging and is the focus of current medical imaging research [95].

Although researchers have put forward prior knowledge such as feasible regions, structural prior information to augment the information needed for reconstruction, the morbidity of the FMT reconstruction equation remains unresolved. Moreover, the actual FMT acquisition data usually contain a certain amount of noise, which has a great impact on the reconstruction of the pathological equation. A small signal disturbance may lead to a large reconstruction error. Therefore, researchers apply regularization techniques to FMT reconstruction to constrain the reconstruction process and reduce morbidity [96–104]. The classical regularization term is Lp-norm regularization. The Lp-norm regularization ($p = 0.5$–2) usually obtains a smoother reconstructed result of a large reconstructed area and has a good reconstruction effect for a large light source volume in an imaging space. Another available regularization method is total variation (TV) [105]. The main idea of TV norm regularization is to constrain the variation terms of the distribution of the fluorescent light sources while preserving the boundaries of the light source zones (Fig. 13).

4 Medical Application

Precision medicine has promoted the development of treatment modalities that are developed to specifically kill tumor cells but not normal cells. The traditional methods of drug discovery have many disadvantages, such as a long research period and the antitumor drug treatment effects in situ cannot be monitored in real time. Therefore, the use of new technologies such as FMI for drug discovery is urgently needed. It seems likely that FMI will meet this challenge for the evaluation of therapeutic effects. The results were more accurate and reliable than the traditional measurement of tumor size. In this chapter, the application of FMI will be described in drug discovery, including identification of therapeutic targets, candidate drug screening, pharmacokinetics of drugs, and prodrug development.

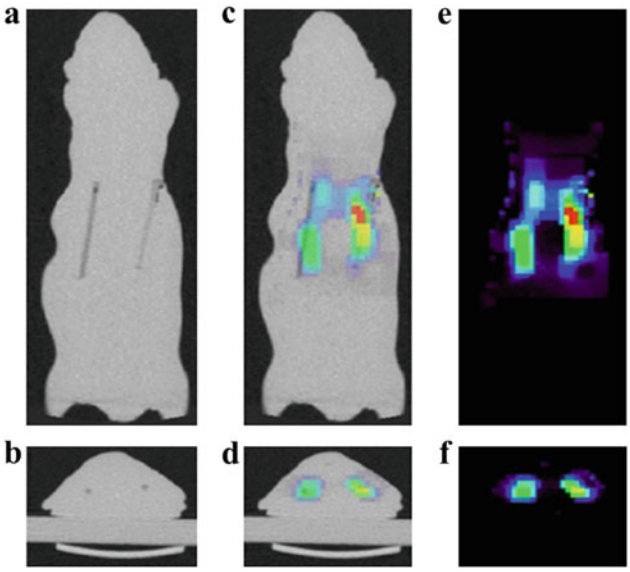

Fig. 13 (**a**) Coronal and (**b**) transverse sections of the CT image of the mouse-shaped phantom showing the two embedded fluorescent line sources. (**c**) Coronal and (**d**) transverse overlay of CT and FMT images. (**e**) Coronal and (**f**) transverse sections of the FMT imaging showing the two fluorescent line sources reconstructed using both L1 and TV penalties with regularization parameters of 10 and 1, respectively. The figure is reproduced from Ref. [105]

4.1 Identification of Therapeutic Targets

Specific therapeutic target is the key for therapy, but traditional drug chemistry methods find targets at slow speed. FMI can improve the process of target identification and identify suitable treatment regimens, hence improving patient treatment outcomes. For example, breast cancer is the most common cancer among women with different subtypes. Nearly 75% of patients demonstrate abnormally high expression of ERα. Therefore, ERα is regarded as an important pharmaceutical target for the treatment of breast cancer, and many ERα ligands have been developed into hormone agents. However, hormone therapy is ineffective for ERα(−) and triple-negative breast cancers (TNBCs). The ERα fluorescent probe P1 can be used to identify a suitable therapeutic regimen for breast cancer. As shown in Fig. 14, the fluorescence signals can be observed in the cell nucleus of the ERα-positive MCF-7 breast cancer cell, but not in MDA-MB-231 TNBC cells. Therefore, FMI is able to identify the target expression and determine treatment [45].

4.2 Candidate Drug Screening

To evaluate the therapeutic effects of antitumor drugs in vivo, a traditional medical imaging method is used to measure the tumor volume at the late stage of tumor

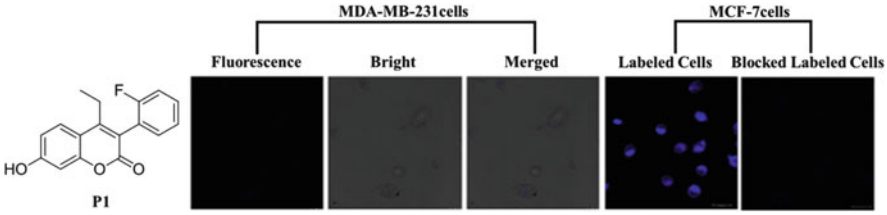

Fig. 14 Fluorescence imaging of intracellular targets in triple-negative breast cancer cells MDA-MB-231 and ER(+) MCF-7 cells. Images of cells treated with compound P1. Reproduced from Ref. [44]

growth with treatment for a period of time. However, this method can only tell the changes in tumors when they show anatomical changes; in addition, it is difficult to evaluate the effect of in situ tumor therapy by the traditional method. FMI can completely overcome the shortcomings of the traditional method and can not only monitor the changes of the tumor biomarker but also evaluate the therapeutic effect in an early and dynamic manner. For example, histone deacetylases (HDACs) are overexpressed in TNBC. The FMI of the LBH589-Cy5.5 probe has been successfully applied not only for measuring the expression and functions of HDACs in tumors but also in evaluating the therapeutic response of HDAC inhibitor SAHA treatment, as evidenced by the significantly reduced HDAC signals in SAHA-treated breast tumors (Fig. 15) [106].

4.3 Tracking the Drug Biodistribution and Metabolism

When the tumor cells were treated with drugs, it was difficult to observe the drug interaction with the corresponding targets by traditional pharmacochemical methods. The majority of drugs tested clinically exhibit off-target effects, which is easy to produce side effects. FMI is able to directly visualize the binding of the drug to the target, which can effectively improve the success rate of drug development. For example, 2-((3-(3-fluoro-4-hydroxyphenyl)-7-hydroxynaphthalen-1-yl) methylene) malononitrile (FPNM) can potently inhibit the growth of MDA-MB-231 tumors, and the relative binding affinity (RBA) value shows FPNM is an estrogen receptor β (ERβ) ligand. In order to confirm the interaction between FPNM and ERβ, FMI of FPNM is performed in MCF-7 cells. As shown in Fig. 16, ERβ is a nuclear hormone receptor, and the fluorescence derived from the complex between FPNM and ERβ was mainly detected in the cell nucleus. The data suggested that FPNM showed specifically selective affinity toward ERβ in the living MCF-7 cells. These results indicated that FPNM possesses the ability to selectively bind to the ERβ in living cells [107].

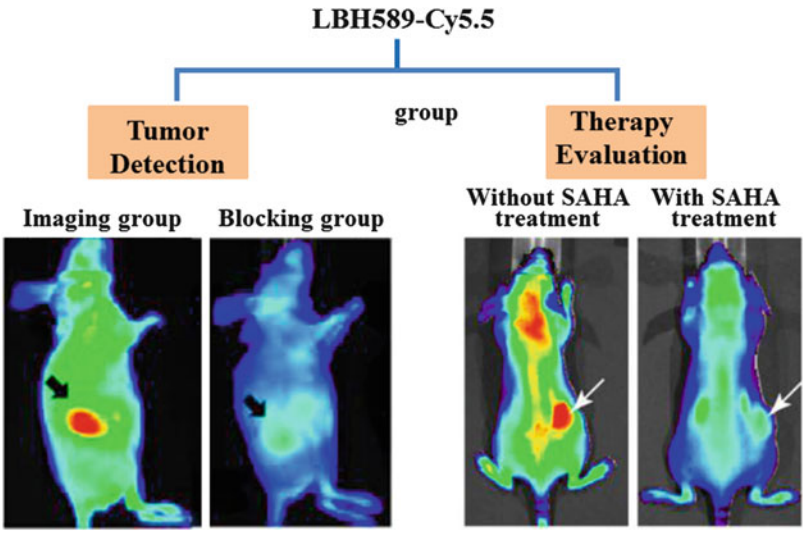

Fig. 15 Detection of tumor and evaluation of antitumor activity of drugs by FMI. Reproduced from Ref. [106]

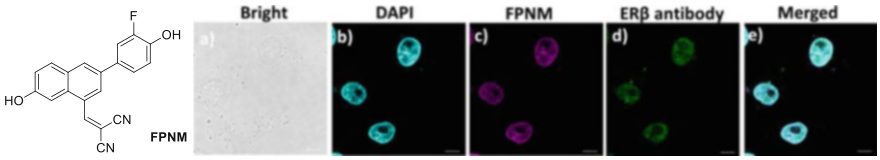

Fig. 16 Co-localization of MCF-7 cells with FPNM (10.0 μM) and ERβ antibody. (**a**) Bright field of cells. (**b**) Nuclei were stained with DAPI. Cells were stained with FPNM (**c**) and ERβ antibody (**d**). Co-localization of FPNM and ERβ antibody. Scale bar = 10 μm. Reproduced from Ref. [107]

4.4 Determination of Pharmacokinetics of Drugs

Targeting specific, small molecules as modulators of drug delivery may play a significant role in the development of therapeutics. Small molecules can alter the pharmacokinetics of therapeutic macromolecules leading to more efficient drug delivery with less systemic toxicity. McCann et al. used FMI to observe the biodistribution and excretion patterns associated with molecular probes composed of human serum albumin (HSA) conjugated to high and low numbers of various monosaccharides: Glc-α, Gal-β, Man-α, Fuc-α, and Fuc-β. First, the conjugation of IRDye800CW to HSA demonstrated nonspecific distribution throughout the body, suggesting the addition of IRDye800CW minimally changed the biodistribution of HSA. However, the conjugation with either low numbers or high numbers of sugar molecules resulted in rapid and specific changes in biodistribution. The conjugation of HSA to a low number of sugar molecules leads to slower clearance of the probe from the blood circulation compared to HSA conjugated to a high number of sugar molecules (Fig. 17) [108].

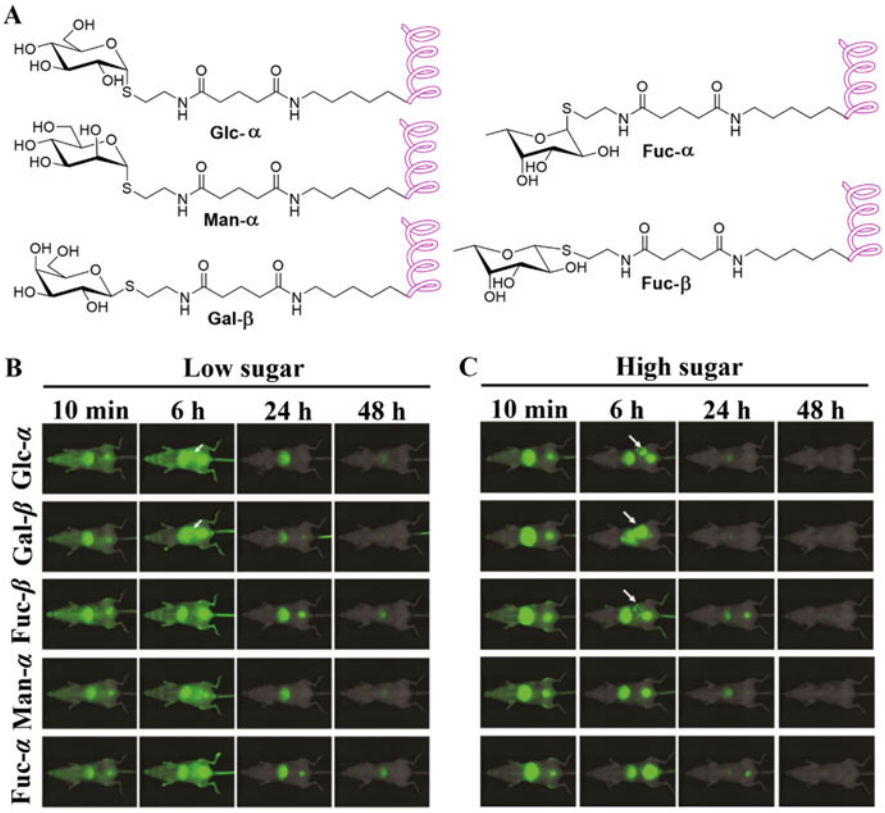

Fig. 17 Chemical structure of the linkage between sugar and albumin. (**a**) the images of HSA glycosylated with a low (**b**) and high (**c**) sugar number at different time points as 10 min, 6 h, 24 h, and 48 h post-injection. Reproduced from Ref. [108]

4.5 Fluorescence Prodrug Conjugates

Fluorescence prodrug conjugates are dual functional systems that offer both therapeutic promise and potential for concurrent diagnosis, which are able to target cancer cells selectively, provide cytotoxic chemotherapeutics, and allow facile monitoring of the location and efficacy of drugs [109, 110]. Fluorescence prodrug conjugates are of particular interest since they are stable in blood plasma, which can be activated efficiently by various cellular constituents, such as thiols, reactive oxygen species (ROS), and enzymes that are overexpressed in tumors [111, 112].

Fluorescence prodrug conjugates can realize both targeted therapeutic release and targeted FMI. Such prodrug conjugates usually contain fluorophores, cleavable linkers, and targeting ligands or chemotherapeutic agents. Fluorophores are usually naphthalimide, coumarin, BODIPY, rhodol, cyanine, etc. Cleavage linkers include hydrolysis of esters, amides, and hydrazine linkers, disulfide exchange-based

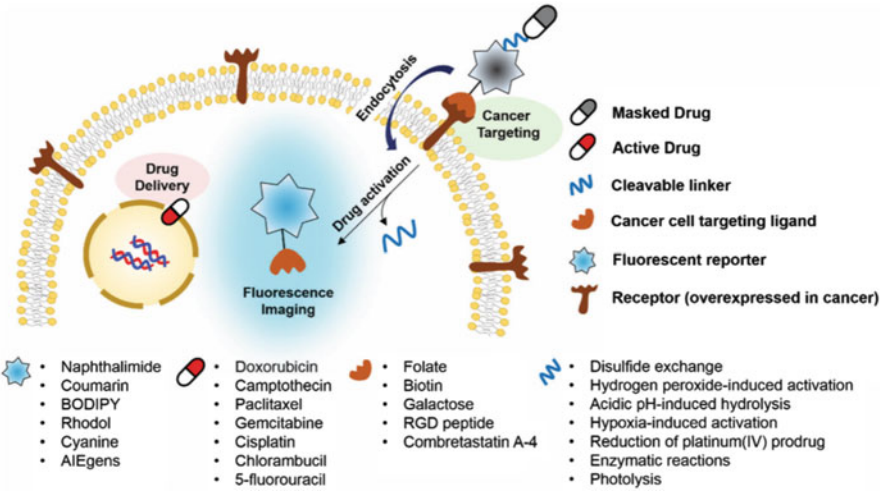

Fig. 18 Design principle for achieving fluorescent prodrug conjugates that are able to target cancer cells selectively, provide cytotoxic chemotherapeutics, and produce readily monitored imaging signals. Reproduced from Ref. [114]

scission, hypoxia-induced activation, enzymatic reactions, photolysis, and thermolysis [113]. Targeting ligands include folate, biotin, galactose, and RGD (Arg-Gly-Asp) peptide sequences. Doxorubicin, camptothecin, paclitaxel, gemcitabine, and cisplatin are commonly used chemotherapeutic agents. To date, much effort has been devoted to develop systems that undergo cleavage under physiological conditions. When the cleavable linkers serve to tether a fluorophore to a prodrug in such a way that the fluorescence signal can be controlled upon cleavage, it becomes a potential system that operates as both therapeutics and diagnostics (Fig. 18) [114].

To date, many fluorescence prodrug conjugates have been reported, including cellular thiol-activatable fluorescent prodrugs (compound **18**) [114], hydrogen peroxide-activated fluorogenic prodrugs (compounds **20**–**21**) [115, 116], acidic pH-activated fluorogenic prodrugs (compounds **22**–**23**) [117, 118], hypoxia-activated fluorogenic prodrugs (compound **24**) [119], platinum reduction-based fluorogenic prodrugs (compound **28**) [120], enzymatic cleavage-based fluorogenic prodrugs (compound **29**) [121], light-activated fluorogenic prodrugs (compounds **32**–**33**) [112, 122], etc. (Fig. 19).

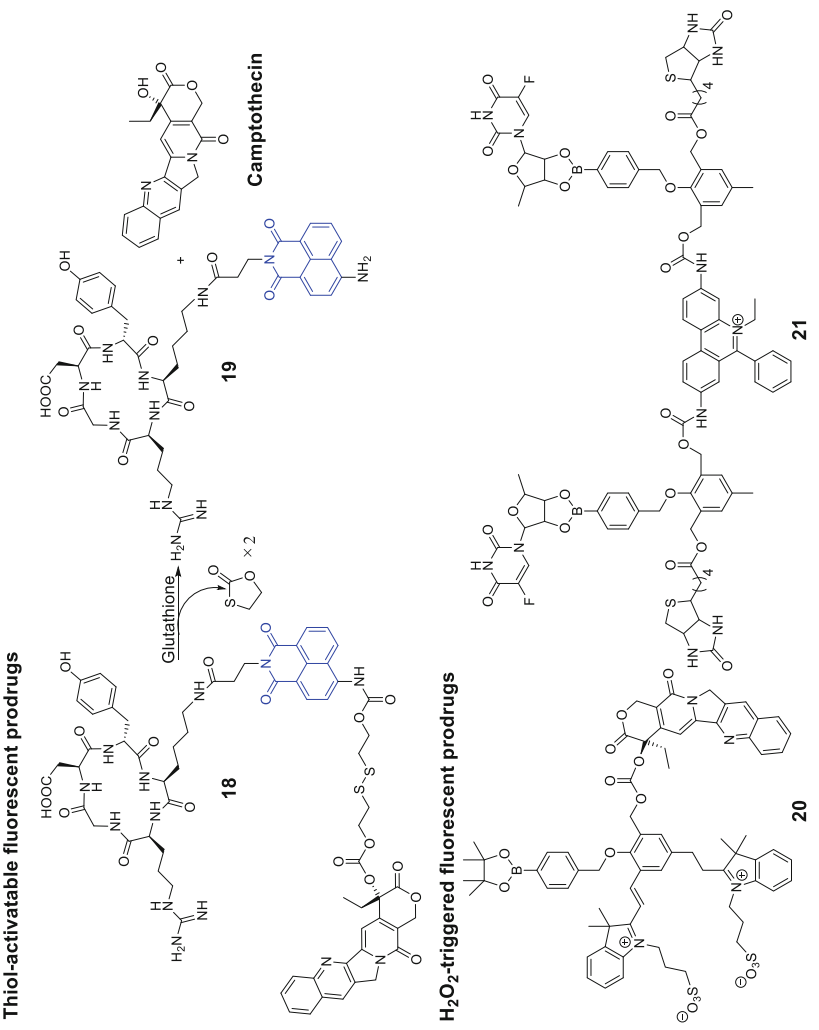

Fig. 19 Representative fluorescent prodrug conjugates

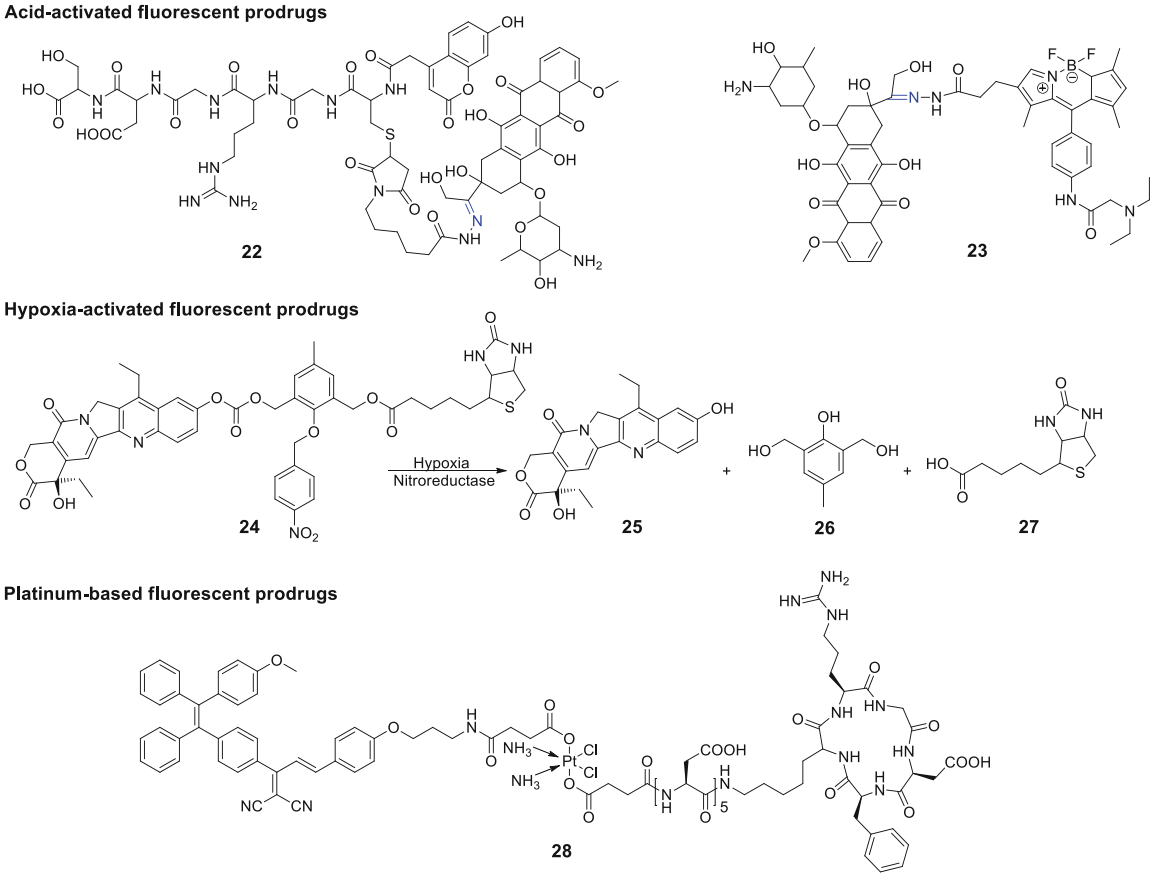

Fig. 19 (continued)

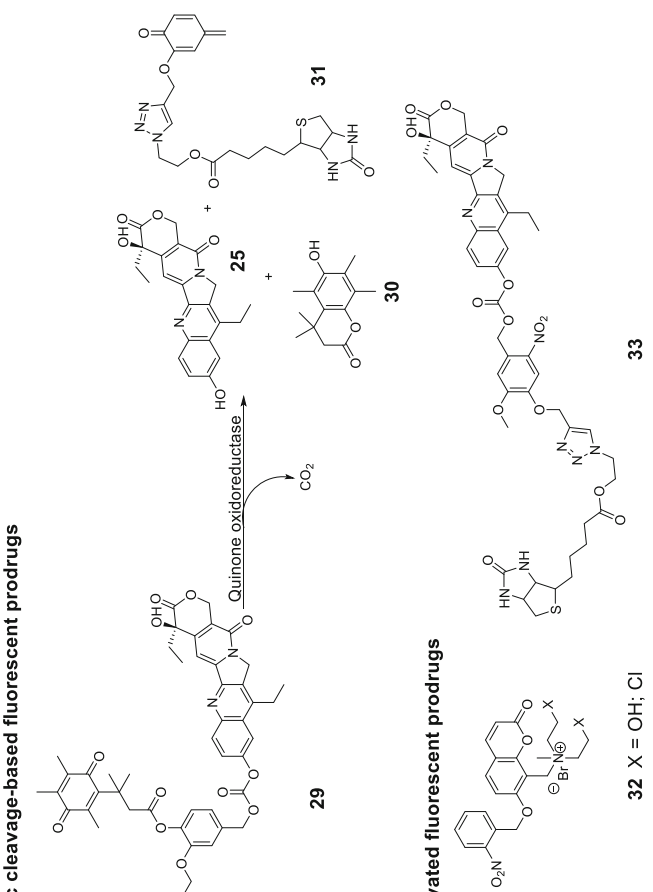

Fig. 19 (continued)

5 Future Perspectives

Currently, FMI has become a powerful and effective tool for drug development. The study of specific probes and targets depends on the development of chemistry and biology, and the FMI tracers do not interfere with the biological process by themselves. The involvement of FMI in metabolic or specific biological processes can more realistically reflect the physiological and pathological processes occurring in organisms, such as gene expression, activation of biochemical pathways, protein interaction, and tracing of cell proliferation and death. Using this noninvasive method to detect cell function can help evaluate the role of new candidate drugs under the influence of complex biological responses in animals. The development of new probes, especially NIR probes, can facilitate the clinical application of this nonradioactive imaging technology. In the last 10 years, FMI has developed rapidly for its low cost, non-ionization, and high throughput, and it plays an important role in all stages of drug development. This technique also has some shortcomings:

1. The detection depth is limited: because of the different wavelengths of the fluorophores and the influence of light absorption and scattering, optical molecular imaging equipment cannot detect cell activity at deeper depths in vivo.
2. Target selection: in order to apply FMI to monitor the efficacy of drug treatment, it is necessary to find specific targets for the diseases. Currently, specific targets of diseases representing the occurrence and development of diseases are not fully discovered.
3. Probe development: the ideal probe should have a high sensitivity and specificity for detection and should not cause an immune response and can be easily cleared by the body. However, the existing FMI probes do not fully meet the above conditions, and the development of new probes is costly.
4. Clinical trials: safety and effectiveness of the application of fluorescence probes in the clinical trials or treatments. In summary, the development of new FMI probes and their application in various stages of drug development will ultimately improve the efficiency of developing new and effective drugs, reduce the cost of research and development, and provide a wider and clinical application prospect in the field of drug development.

Acknowledgments Thanks to Dr. Yang Du, Dr. Chu Tang, and Dr. Yu An for their kind contribution to writing this chapter. This paper is supported by the National Key Research and Development Program of China under Grant Nos. 2017YFA0205200, 2016YFA0201401, 2016YFC0103702, and 2016YFC0102000; the National Natural Science Foundation of China under Grant Nos. 81871514, 81470083, 81227901, 81527805, 61231004, 81601548, and 81772011; the International Innovation Team of CAS under Grant No. 20140491524; and Beijing Municipal Science and Technology Commission No. Z161100002616022.

Compliance with Ethical Standards

Funding: This study was funded by Ministry of Science and Technology of China (grant number 2017YFA0205200, 2017YFA0700401), National Natural Science Foundations of China (grant number 81871514, 81527805), the Strategic Priority Research Program of Chinese Academy of

Sciences (grant number XDB32030200, XDB01030200), and Chinese Academy of Sciences (grant number QYZDJ-SSW-JSC005).

Ethical Approval: This chapter does not contain any studies with human participants or animals performed by any of the authors.

Conflict of Interest: The authors declare no conflict of interest.

References

1. Corrêa IR Jr (2014) Live-cell reporters for fluorescence imaging. Curr Opin Chem Biol 20:36–45
2. Dean KM, Palmer AE (2014) Advances in fluorescence labeling strategies for dynamic cellular imaging. Nat Chem Biol 10(7):512–523
3. Hu Z, Qu Y, Wang K, Zhang X, Zha J, Song T, Bao C, Liu H, Wang Z, Wang J, Liu Z, Liu H, Tian J (2015) In vivo nanoparticle-mediated radiopharmaceutical-excited fluorescence molecular imaging. Nat Commun 6:7560
4. de Jong M, Essers J, van Weerden WM (2014) Imaging preclinical tumour models: improving translational power. Nat Rev Cancer 14(7):481–493
5. Chen X, Wang F, Hyun JY, Wei T, Qiang J, Ren X, Shin I, Yoon J (2016) Recent progress in the development of fluorescent, luminescent and colorimetric probes for detection of reactive oxygen and nitrogen species. Chem Soc Rev 45(10):2976–3016
6. Chi C, Du Y, Ye J, Kou D, Qiu J, Wang J, Tian J, Chen X (2014) Intraoperative imaging-guided cancer surgery: from current fluorescence molecular imaging methods to future multi-modality imaging technology. Theranostics 4(11):1072–1084
7. Gao M, Yu F, Lv C, Choo J, Chen L (2017) Fluorescent chemical probes for accurate tumor diagnosis and targeting therapy. Chem Soc Rev 46(8):2237–2271
8. Jiao X, Li Y, Niu J, Xie X, Wang X, Tang B (2018) Small-molecule fluorescent probes for imaging and detection of reactive oxygen, nitrogen, and sulfur species in biological systems. Anal Chem 90(1):533–555
9. Liu JN, Bu W, Shi J (2017) Chemical design and synthesis of functionalized probes for imaging and treating tumor hypoxia. Chem Rev 117(9):6160–6224
10. Ding F, Zhan Y, Lu X, Sun Y (2018) Recent advances in near-infrared II fluorophores for multifunctional biomedical imaging. Chem Sci 9(19):4370–4380
11. He SQ, Song J, Qu JL, Cheng Z (2018) Crucial breakthrough of second near-infrared biological window fluorophores: design and synthesis toward multimodal imaging and theranostics. Chem Soc Rev 47(12):4258–4278
12. Lavis LD, Raines RT (2014) Bright building blocks for chemical biology. ACS Chem Biol 9 (4):855–866
13. Gonçalves MS (2009) Fluorescent labeling of biomolecules with organic probes. Chem Rev 109(1):190–212
14. Zheng Y, Ji S, Czerwinski A, Valenzuela F, Pennington M, Liu S (2014) FITC-conjugated cyclic RGD peptides as fluorescent probes for staining integrin αvβ3/αvβ5 in tumor tissues. Bioconjug Chem 25(11):1925–1941
15. Bartholomä MD, Gottumukkala V, Zhang S, Baker A, Dunning P, Fahey FH, Treves ST, Packard AB (2012) Effect of the prosthetic group on the pharmacologic properties of 18F-labeled rhodamine B, a potential myocardial perfusion agent for positron emission tomography (PET). J Med Chem 55(24):11004–11012
16. Sun T, Guan X, Zheng M, Jing X, Xie Z (2015) Mitochondria-localized fluorescent BODIPY-platinum conjugate. ACS Med Chem Lett 6(4):430–433
17. Fei XN, Gu YC (2009) Progress in modifications and applications of fluorescent dye probe. Prog Nat Sci 19(1):1–7

18. Qian X, Xu Z (2015) Fluorescence imaging of metal ions implicated in diseases. Chem Soc Rev 44(14):4487–4493
19. Fernández A, Vendrell M (2016) Smart fluorescent probes for imaging macrophageactivity. Chem Soc Rev 45(5):1182–1196
20. Li X, Gao X, Shi W, Ma H (2014) Design strategies for water-soluble small molecular chromogenic and fluorogenic probes. Chem Rev 114(1):590–659
21. Yang Z, Sharma A, Qi J, Peng X, Lee DY, Hu R, Lin D, Qu J, Kim JS (2016) Super-resolution fluorescent materials: an insight into design and bioimaging applications. Chem Soc Rev 45 (17):4651–4667
22. Yang Z, Cao J, He Y, Yang JH, Kim T, Peng X, Kim JS (2014) Macro−/micro-environment-sensitive chemosensing and biological imaging. Chem Soc Rev 43(13):4563–4601
23. Liu K, Kong X, Ma Y, Lin W (2017) Rational design of a robust fluorescent probe for the detection of endogenous carbon monoxide in living zebrafish embryos and mouse tissue. Angew Chem Int Ed Engl 56(43):13489–13492
24. Ling X, Zhang S, Shao P, Li W, Yang L, Ding Y, Xu C, Stella N, Bai M (2015) A novel near-infrared fluorescence imaging probe that preferentially binds to cannabinoid receptors CB2R over CB1R. Biomaterials 57:169–178
25. Deutscher SL (2010) Phage display in molecular imaging and diagnosis of cancer. Chem Rev 110(5):3196–3211
26. Kobayashi H, Ogawa M, Alford R, Choyke PL, Urano Y (2010) New strategies for fluorescent probe design in medical diagnostic imaging. Chem Rev 110(5):2620–2640
27. Smith AM, Mancini MC, Nie S (2009) Bioimaging: second window for in vivo imaging. Nat Nanotechnol 4(11):710–7111
28. Hong G, Diao S, Antaris AL, Dai H (2015) Carbon nanomaterials for biological imaging and nanomedicinal therapy. Chem Rev 115(19):10816–10906
29. Welsher K, Liu Z, Sherlock SP, Robinson JT, Chen Z, Daranciang D, Dai H (2009) A route to brightly fluorescent carbon nanotubes for near-infrared imaging in mice. Nat Nanotechnol 4 (11):773–780
30. Diao S, Blackburn JL, Hong G, Antaris AL, Chang J, Wu JZ, Zhang B, Cheng K, Kuo CJ, Dai H (2015) Fluorescence imaging in vivo at wavelengths beyond 1500 nm. Angew Chem Int Ed Engl 54(49):14758–14762
31. Antaris AL, Chen H, Cheng K, Sun Y, Hong G, Qu C, Diao S, Deng Z, Hu X, Zhang B, Zhang X, Yaghi OK, Alamparambil ZR, Hong X, Cheng Z, Dai HJ (2016) A small-molecule dye for NIR-II imaging. Nat Mater 15(2):235–242
32. Jiang YX, Ding BB, Xiao YL, Xing L, Hong XC, Cheng Z (2016) Novel benzo-bis(1,2,5-thiadiazole) fluorophores for in vivo NIR-II imaging of cancer. Chem Sci 7(9):6203–6207
33. Yang Q, Hu Z, Zhu S, Ma R, Ma H, Ma Z, Wan H, Zhu T, Jiang Z, Liu W, Jiao L, Sun H, Liang Y, Dai H (2018) Donor engineering for NIR-II molecular fluorophores with enhanced fluorescent performance. J Am Chem Soc 140(5):1715–1724
34. Céspedes-Guirao FJ, Ropero AB, Font-Sanchis E, Nadal Á, Fernández-Lázaro F, Sastre-Santo Á (2011) A water-soluble perylene dye functionalised with a 17β-estradiol: a new fluorescent tool for steroid hormones. Chem Commun 47(29):8307–8309
35. Rickert EL, Oriana S, Hartman-Frey C, Long X, Webb TT, Nephew KP, Weatherman RV (2010) Synthesis and characterization of fluorescent 4-hydroxytamoxifen conjugates with unique antiestrogenic properties. Bioconjug Chem 21(5):903–910
36. Yang L, Hu ZY, Luo JJ, Tang C, Zhang SL, Ning WT, Dong C, Huang J, Liu XJ, Zhou HB (2017) Dual functional small molecule fluorescent probes for image-guided estrogen receptor-specific targeting coupled potent antiproliferative potency for breast cancer therapy. Bioorg Med Chem 25(13):3531–3539
37. Levi J, Cheng Z, Gheysens O, Patel M, Chan CT, Wang Y, Namavari M, Gambhir SS (2007) Fluorescent fructose derivatives for imaging breast cancer cells. Bioconjug Chem 18 (3):628–634

38. Humblet V, Lapidus R, Williams LR, Tsukamoto T, Rojas C, Majer P, Hin B, Ohnishi S, De Grand AM, Zaheer A, Renze JT, Nakayama A, Slusher BS, Frangioni JV (2005) High-affinity near-infrared fluorescent small-molecule contrast agents for in vivo imaging of prostate-specific membrane antigen. Mol Imaging 4(4):448–462
39. Liu T, Wu LY, Kazak M, Berkman CE (2008) Cell-surface labeling and internalization by a fluorescent inhibitor of prostate-specific membrane antigen. Prostate 68(9):955–964
40. Liu T, Wu LY, Hopkins MR, Choi JK, Berkman CE (2010) A targeted low molecular weight near-infrared fluorescent probe for prostate cancer. Bioorg Med Chem Lett 20(23):7124–7126
41. Baranski AC, Schäfer M, Bauder-Wüst U, Roscher M, Schmidt J, Stenau E, Simpfendörfer T, Teber D, Maier-Hein L, Hadaschik B, Haberkorn U, Eder M, Kopka K (2018) PSMA-11-derived dual-labeled PSMA inhibitors for preoperative PET imaging and precise fluorescence-guided surgery of prostate cancer. J Nucl Med 59(4):639–645
42. Kennedy MD, Jallad KN, Thompson DH, Ben-Amotz D, Low PS (2003) Optical imaging of metastatic tumors using a folate-targeted fluorescent probe. J Biomed Opt 8(4):636–641
43. van Dam GM, Themelis G, Crane LM, Harlaar NJ, Pleijhuis RG, Kelder W, Sarantopoulos A, de Jong JS, Arts HJ, van der Zee AG, Bart J, Low PS, Ntziachristos V (2011) Intraoperative tumor-specific fluorescence imaging in ovarian cancer by folate receptor-α targeting: first in-human results. Nat Med 17(10):1315–1319
44. Uddin MJ, Crews BC, Blobaum AL, Kingsley PJ, Gorden DL, McIntyre JO, Matrisian LM, Subbaramaiah K, Dannenberg AJ, Piston DW, Marnett LJ (2010) Selective visualization of cyclooxygenase-2 in inflammation and cancer by targeted fluorescent imaging agents. Cancer Res 70(9):3618–3627
45. Zhang H, Fan J, Wang J, Dou B, Zhou F, Cao J, Qu J, Cao Z, Zhao W, Peng X (2013) Fluorescence discrimination of cancer from inflammation by molecular response to COX-2 enzymes. J Am Chem Soc 135(46):17469–17475
46. Krall N, Pretto F, Decurtins W, Bernardes GJ, Supuran CT, Neri D (2014) A small-molecule drug conjugate for the treatment of carbonic anhydrase IX expressing tumors. Angew Chem Int Ed Engl 53(16):4231–4235
47. Krall N, Pretto F, Neri D (2014) A bivalent small molecule-drug conjugate directed against carbonic anhydrase IX can elicit complete tumour regression in mice. Chem Sci 5:3640–3644
48. Chenouard N, Smal I, de Chaumont F, Maška M, Sbalzarini IF, Gong Y, Cardinale J, Carthel C, Coraluppi S, Winter M, Cohen AR, Godinez WJ, Rohr K, Kalaidzidis Y, Liang L, Duncan J, Shen H, Xu Y, Magnusson KE, Jaldén J, Blau HM, Paul-Gilloteaux P, Roudot P, Kervrann C, Waharte F, Tinevez JY, Shorte SL, Willemse J, Celler K, van Wezel GP, Dan HW, Tsai YS, Ortiz de Solórzano C, Olivo-Marin JC, Meijering E (2014) Nat Methods 11(3):281–289
49. Xie W, Deng Y, Wang K, Yang X, Luo Q (2014) Reweighted L1 regularization for restraining artifacts in FMT reconstruction images with limited measurements. Opt Lett 39 (14):4148–4151
50. Qin CH, Feng JC, Zhu SP, Ma XB, Zhong JH, Wu P, Jin ZY, Tian J (2014) Recent advances in bioluminescence tomography: methodology and system as well as application. Laser Photonics Revs 8(1):94–114
51. Wang K, Wang Q, Luo Q, Yang X (2015) Fluorescence molecular tomography in the second near-infrared window. Opt Express 23(10):12669–12679
52. Leng CC, Tian J (2015) Mathematical method in optical molecular imaging. Sci China Inf Sci 58(3):1–13
53. Zhang S, Wang K, Liu HB, Leng CC, Gao Y, Tian J (2017) Reconstruction method for in vivo bioluminescence tomography based on the split Bregman iterative and surrogate functions. Mol Imaging Biol 19(2):245–255
54. Fan-Minogue H, Cao Z, Paulmurugan R, Chan CT, Massoud TF, Felsher DW, Gambhir SS (2010) Noninvasive molecular imaging of c-Myc activation in living mice. Proc Natl Acad Sci U S A 107(36):15892–15897

55. van Dam GM, Themelis G, Crane LM, Harlaar NJ, Pleijhuis RG, Kelder W, Sarantopoulos A, de Jong JS, Arts HJ, van der Zee AG, Bart J, Low PS, Ntziachristos V (2011) Intraoperative tumor-specific fluorescence imaging in ovarian cancer by folate receptor-alpha targeting: first in-human results. Nat Med 17(10):1315–1319
56. Whitney MA, Crisp JL, Nguyen LT, Friedman B, Gross LA, Steinbach P, Tsien RY, Nguyen QT (2011) Fluorescent peptides highlight peripheral nerves during surgery in mice. Nat Biotechnol 29(4):352–356
57. Solomon B, Cornelis F (2016) Interventional molecular imaging. J Nucl Med 57(4):493–496
58. Tarvainen T, Vauhkonen M, Kolehmainen V, Kaipio JP (2005) Hybrid radiative-transfer-diffusion model for optical tomography. Appl Optics 44(6):876–886
59. Tualle JM, Tinet E (2003) Derivation of the radiative transfer equation for scattering media with a spatially varying refractive index. Opt Commun 228(1–3):33–38
60. Song X, Wang D, Chen N, Bai J, Wang H (2007) Reconstruction for free-space fluorescence tomography using a novel hybrid adaptive finite element algorithm. Opt Express 15 (26):18300–18317
61. Han D, Yang X, Liu K, Qin C, Zhang B, Ma X, Tian J (2010) Efficient reconstruction method for L1 regularization in fluorescence molecular tomography. Appl Optics 49(36):6930–6937
62. Hyde D, Miller EL, Brooks DH, Ntziachristos V (2010) Data specific spatially varying regularization for multimodal fluorescence molecular tomography. IEEE Trans Med Imaging 29(2):365–374
63. Guo X, Liu X, Wang X, Tian F, Liu F, Zhang B, Hu G, Bai J (2010) A combined fluorescence and microcomputed tomography system for small animal imaging. IEEE Trans Biomed Eng 57(12):2876–2883
64. Zhang B, Yang X, Qin C, Liu D, Zhu S, Feng J, Sun L, Liu K, Han D, Ma X, Zhang X, Zhong J, Li X, Yang X, Tian J (2010) A trust region method in adaptive finite element framework for bioluminescence tomography. Opt Express 18(7):6477–6491
65. Lin Y, Kwong TC, Bolisay L, Gulsen G (2012) Temperature-modulated fluorescence tomography based on both concentration and lifetime contrast. J Biomed Opt 17(5):056007
66. Han D, Tian J, Liu K, Feng J, Zhang B, Ma X, Qin C (2010) Sparsity-promoting tomographic fluorescence imaging with simplified spherical harmonics approximation. IEEE Trans Biomed Eng 57(10):2564–2567
67. Aydin ED, de Oliveira CR, Goddard AJ (2002) A comparison between transport and diffusion calculations using a finite element-spherical harmonics radiation transport method. Med Phys 29(9):2013–2023
68. Khan T, Thomas A (2005) Comparison of P-N or spherical harmonics approximation for scattering media with spatially varying and spatially constant refractive indices. Opt Commun 255(1–3):130–166
69. Klose AD, Larsen EW (2006) Light transport in biological tissue based on the simplified spherical harmonics equations. J Comput Phys 220(1):441–470
70. Klose AD (2010) The forward and inverse problem in tissue optics based on the radiative transfer equation: a brief review. J Quant Spectrosc Radiat Transf 111(11):1852–1853
71. Grella K, Schwab C (2011) Sparse tensor spherical harmonics approximation in radiative transfer. J Comput Phys 230(23):8452–8473
72. Duderstadt JJ, Martin WR (1979) Transport theory. Wiley, New York
73. Arridge SR, Hebden JC (1997) Optical imaging in medicine: II. Modelling and reconstruction. Phys Med Biol 42(5):841–853
74. Cong W, Wang G (2006) Boundary integral method for bioluminescence tomography. J Biomed Opt 11(2):020503
75. Qin C, Tian J, Yang X, Liu K, Yan G, Feng J, Lv Y, Xu M (2008) Galerkin-based meshless methods for photon transport in the biological tissue. Opt Express 16(25):20317–20333
76. Wright S, Schweiger M, Arridge SR (2007) Reconstruction in optical tomography using the PN approximations. Meas Sci Technol 18(18):79–86

77. Lu Y, Zhang X, Douraghy A, Stout D, Tian J, Chan TF, Chatziioannou AF (2009) Source reconstruction for spectrally-resolved bioluminescence tomography with sparse a priori information. Opt Express 17(10):8062–8080
78. An Y, Liu J, Zhang G, Jiang S, Ye J, Chi C, Tian J (2017) Compactly supported radial basis function-based meshless method for photon propagation model of fluorescence molecular tomography. IEEE Trans Med Imaging 36(2):366–373
79. Zhu W, Wang Y, Yao Y, Chang J, Graber HL, Barbour RL (1997) Iterative total least-squares image reconstruction algorithm for optical tomography by the conjugate gradient method. J Opt Soc Am A Opt Image Sci Vis 14(4):799–807
80. Paulsen KD, Jiang H (1996) Enhanced frequency-domain optical image reconstruction in tissues through total-variation minimization. Appl Optics 35(19):3447–3458
81. Yu DF, Fessler JA (1998) Edge-preserving tomographic reconstruction with nonlocal regularization. IEEE Trans Med Imaging 21(2):159–173
82. Darne C, Lu Y, Sevick-Muraca EM (2014) Small animal fluorescence and bioluminescence tomography: a review of approaches, algorithms and technology update. Phys Med Biol 59(1): R1–R64
83. Han D, Tian J, Zhu S, Feng J, Qin C, Zhang B, Yang X (2010) A fast reconstruction algorithm for fluorescence molecular tomography with sparsity regularization. Opt Express 18 (8):8630–8646
84. Zacharakis G, Kambara H, Shih H, Ripoll J, Grimm J, Saeki Y, Weissleder R, Ntziachristos V (2005) Volumetric tomography of fluorescent proteins through small animals in vivo. Proc Natl Acad Sci U S A 102(51):18252–18257
85. Ntziachristos V (2010) Going deeper than microscopy: the optical imaging frontier in biology. Nat Methods 7(8):603–614
86. Ale A, Ermolayev V, Herzog E, Cohrs C, de Angelis MH, Ntziachristos V (2012) FMT-XCT: in vivo animal studies with hybrid fluorescence molecular tomography-X-ray computed tomography. Nat Methods 9(6):615–620
87. Mohajerani P, Hipp A, Willner M, Marschner M, Trajkovic-Arsic M, Ma X, Burton NC, Klemm U, Radrich K, Ermolayev V, Tzoumas S, Siveke JT, Bech M, Pfeiffer F, Ntziachristos V (2014) FMT-PCCT: hybrid fluorescence molecular tomography-x-ray phase-contrast CT imaging of mouse models. IEEE Trans Med Imaging 33(7):1434–1446
88. Mohajerani P, Ntziachristos V (2016) An inversion scheme for hybrid fluorescence molecular tomography using a fuzzy inference system. IEEE Trans Med Imaging 35(2):381–390
89. Berninger MT, Mohajerani P, Kimm M, Masius S, Ma X, Wildgruber M, Haller B, Anton M, Imhoff AB, Ntziachristos V, Henning TD, Meier R (2017) Fluorescence molecular tomography of DiR-labeled mesenchymal stem cell implants for osteochondral defect repair in rabbit knees. Eur Radiol 27(3):1105–1113
90. Allard M, Côté D, Davidson L, Dazai J, Henkelman RM (2007) Combined magnetic resonance and bioluminescence imaging of live mice. J Biomed Opt 12(3):034018
91. Cao X, Yang J, Gao Y, Guo Y, Wu G, Shen D (2017) Dual-core steered non-rigid registration for multi-modal images via bi-directional image synthesis. Med Image Anal 41:18–31
92. Phillips EH, Di Achille P, Bersi MR, Humphrey JD, Goergen CJ (2017) Multi-modality imaging enables detailed hemodynamic simulations in dissecting aneurysms in mice. IEEE Trans Med Imaging 36(6):1297–1305
93. Chen ZY, Wang YX, Yang F, Lin Y, Zhou QL, Liao YY (2014) New researches and application progress of commonly used optical molecular imaging technology. Biomed Res Int 2014:429198
94. Zhang Y, Zhang B, Liu F, Luo J, Bai J (2014) In vivo tomographic imaging with fluorescence and MRI using tumor-targeted dual-labeled nanoparticles. Int J Nanomedicine 9:33–41
95. Wang K, Chi CW, Hu ZH, Liu MH, Hui H, Shang WT, Peng D, Zhang S, Ye JZ, Liu HX, Tian J (2015) Optical molecular imaging frontiers in oncology: the pursuit of accuracy and sensitivity. Engineering 1(3):309–323

96. An Y, Liu J, Zhang G, Ye J, Du Y, Mao Y, Chi C, Tian J (2015) A novel region reconstruction method for fluorescence molecular tomography. IEEE Trans Biomed Eng 62(7):1818–1826
97. Zhang J, Shi J, Guang H, Zuo S, Liu F, Bai J, Luo J (2016) Iterative correction scheme based on discrete cosine transform and L1 regularization for fluorescence molecular tomography with background fluorescence. IEEE Trans Biomed Eng 63(6):1107–1115
98. Pera V, Brooks DH, Niedre M (2016) Multiplexed fluorescence tomography with spectral and temporal data: demixing with intrinsic regularization. Biomed Opt Express 7(1):111–131
99. Lian L, Deng Y, Xie W, Xu G, Yang X, Zhang Z, Luo Q (2016) High-dynamic-range fluorescence molecular tomography for imaging of fluorescent targets with large concentration differences. Opt Express 24(17):19920–19933
100. Zhang G, Liu F, Liu J, Luo J, Xie Y, Bai J, Xing L (2017) Cone beam X-ray luminescence computed tomography based on bayesian method. IEEE Trans Med Imaging 36(1):225–235
101. Zhou Y, Chen M, Su H, Luo J (2017) Self-prior strategy for organ reconstruction in fluorescence molecular tomography. Biomed Opt Express 8(10):4671–4686
102. Shi J, Udayakumar TS, Wang Z, Dogan N, Pollack A, Yang Y (2017) Optical molecular imaging-guided radiation therapy part 2: integrated x-ray and fluorescence molecular tomography. Med Phys 44(9):4795–4803
103. Baikejiang R, Zhao Y, Fite BZ, Ferrara KW, Li C (2017) Anatomical image-guided fluorescence molecular tomography reconstruction using kernel method. J Biomed Opt 22(5):055001
104. He X, Wang X, Yi H, Chen Y, Zhang X, Yu J, He X (2017) Laplacian manifold regularization method for fluorescence molecular tomography. J Biomed Opt 22(4):45009
105. Dutta J, Ahn S, Li C, Cherry SR, Leahy RM (2012) Joint L1 and total variation regularization for fluorescence molecular tomography. Phys Med Biol 57(6):1459–1476
106. Meng Q, Liu Z, Li F, Ma J, Wang H, Huan Y, Li Z (2015) An HDAC-targeted imaging probe LBH589-Cy5.5 for tumor detection and therapy evaluation. Mol Pharm 12(7):2469–2476
107. Hu ZY, Yang L, Ning W, Tang C, Meng Q, Zheng J, Dong C, Zhou HB (2018) A high-affinity subtype-selective fluorescent probe for estrogen receptor β imaging in living cells. Chem Commun 54(31):3887–3890
108. McCann TE, Kosaka N, Mitsunaga M, Choyke PL, Gildersleeve JC, Kobayashi H (2010) Biodistribution and excretion of monosaccharide-albumin conjugates measured with in vivo near-infrared fluorescence imaging. Bioconjug Chem 21(10):1925–1932
109. Kumar R, Shin WS, Sunwoo K, Kim WY, Koo S, Bhuniya S, Kim JS (2015) Small conjugate-based theranostic agents: an encouraging approach for cancer therapy. Chem Soc Rev 44 (19):6670–6683
110. Lim EK, Kim T, Paik S, Haam S, Huh YM, Lee K (2015) Nanomaterials for theranostics: recent advances and future challenges. Chem Rev 115(1):327–394
111. Lee MH, Yang Z, Lim CW, Lee YH, Dongbang S, Kang C, Kim JS (2013) Disulfide-cleavage-triggered chemosensors and their biological applications. Chem Rev 113(7):5071–5109
112. Lee MH, Sharma A, Chang MJ, Lee J, Son S, Sessler JL, Kang C, Kim JS (2018) Fluorogenic reaction-based prodrug conjugates as targeted cancer theranostics. Chem Soc Rev 47(1):28–52
113. Wong PT, Choi SK (2015) Mechanisms of drug release in nanotherapeutic delivery systems. Chem Rev 115(9):3388–3432
114. Lee MH, Kim JY, Han JH, Bhuniya S, Sessler JL, Kang C, Kim JS (2012) Direct fluorescence monitoring of the delivery and cellular uptake of a cancer-targeted RGD peptide-appended naphthalimide theranostic prodrug. J Am Chem Soc 134(30):12668–12674
115. Redy-Keisar O, Ferber S, Satchi-Fainaro R, Shabat D (2015) NIR fluorogenic dye as a modular platform for prodrug assembly: real-time in vivo monitoring of drug release. ChemMedChem 10(6):999–1007
116. Kumar R, Han J, Lim HJ, Ren WX, Lim JY, Kim JH, Kim JS (2014) Mitochondrial induced and self-monitored intrinsic apoptosis by antitumor theranostic prodrug: in vivo imaging and precise cancer treatment. J Am Chem Soc 136(51):17836–17843

117. Li SY, Liu LH, Jia HZ, Qiu WX, Rong L, Cheng H, Zhang XZ (2014) A pH-responsive prodrug for real-time drug release monitoring and targeted cancer therapy. Chem Commun 50 (80):11852–11855
118. Fernandez A, Vermeren M, Humphries D, Subiros-Funosas R, Barth N, Campana L, MacKinnon A, Feng Y, Vendrell M (2017) Chemical modulation of in vivo macrophage function with subpopulation-specific fluorescent prodrug conjugates. ACS Cent Sci 3 (9):995–1005
119. Kumar R, Kim EJ, Han J, Lee H, Shin WS, Kim HM, Bhuniya S, Kim JS, Hong KS (2016) Hypoxia-directed and activated theranostic agent: imaging and treatment of solid tumor. Biomaterials 104:119–128
120. Yuan Y, Zhang CJ, Liu B (2015) A platinum prodrug conjugated with a photosensitizer with aggregation-induced emission (AIE) characteristics for drug activation monitoring and combinatorial photodynamic-chemotherapy against cisplatin resistant cancer cells. Chem Commun 51(41):8626–8629
121. Shin WS, Han J, Verwilst P, Kumar R, Kim JH, Kim JS (2016) Cancer targeted enzymatic theranostic prodrug: precise diagnosis and chemotherapy. Bioconjug Chem 27(5):1419–1426
122. Cao Y, Pan R, Xuan W, Wei Y, Liu K, Zhou J, Wang W (2015) Photo-triggered fluorescent theranostic prodrugs as DNA alkylating agents for mechlorethamine release and spatiotemporal monitoring. Org Biomol Chem 13(24):6742–6748

Top Med Chem (2020) 34: 33–54
DOI: 10.1007/7355_2019_88

Published online: 29 February 2020

Organic Fluorescent Probes for Diagnostics and Bio-Imaging

Xingyue Yang, Jonathan F. Lovell, Niren Murthy, and Yumiao Zhang

Contents

X. Yang
School of Chemical Engineering and Technology, Tianjin University, Tianjin, China

J. F. Lovell
Department of Biomedical Engineering, State University of New York at Buffalo, Buffalo, NY, USA

N. Murthy
Department of Bioengineering, University of California, Berkeley, CA, USA

Y. Zhang (✉)
School of Chemical Engineering and Technology, Tianjin University, Tianjin, China

Department of Bioengineering, University of California, Berkeley, CA, USA
e-mail: ymzhang88@tju.edu.cn

Abstract Fluorescence bio-imaging holds potential for new approaches for disease detection and diagnosis. Compared with conventional clinical contrast imaging modalities, such as X-ray and MRI, which use contrast agents that are "always on," fluorescence imaging contrast agents can readily be designed to be activatable under specific circumstances and also can be used in multiplexed imaging schemes. While a wide variety of fluorescence imaging probes have been developed, small organic fluorescence probes have the advantages of being robustly synthesized and characterized, as well as a track record for clinical translation. In this chapter, we discuss organic fluorophores and highlighted some examples of their biological applications. The aim of this chapter is to provide a literature review of the development of organic fluorescent probes for biomedical imaging and diagnosis.

Keywords Disease diagnosis, Fluorescence imaging, Fluorescence probes, Imaging modalities, Organic fluorophores

1 Introduction

Near-infrared fluorescence imaging has developed as a powerful optical imaging modality for visualization of molecular process and biological activities, which uses a low-light camera to collect fluorescence emission from fluorophores [1]. The fluorescence imaging technique is based on the fact that the transillumination of light through normal tissue is significantly different from that through an object (e.g., tumor or infected tissues). Compared to other well-developed imaging techniques such as X-ray, computed tomography (CT) [2], magnetic resonance imaging (MRI), and ultrasound [3], fluorescence imaging is advantageous because of high sensitivity, excellent resolution, and minimum photodamage to tissues [4]. Fluorescence imaging has been widely applied for real-time detection of biological species [5–8]. One challenge of imaging biology in its native physiological state using fluorescence imaging method is the autofluorescence. Scattered light generated a noise background that might even wash out the image of targets [9]. In addition, most of the traditional fluorescent probes have absorption and emission in UV-Vis range; however, interference from absorption by hemoglobin, myoglobin, and other heme proteins is significantly high, leading to light scattering and impaired tissue penetration [10]. Therefore, NIR (700–1,000 nm) light was recommended for wavelength selection for body imaging [11]. Meanwhile, in recent years, dyes in the second near-infrared region (NIR-II, 1,000–1,700 nm) have been explored with a number of merits over the NIR-I imaging modalities in terms of reduced photon scattering and improved penetration depth [12–14], as well as good sensitivity, enhanced spatial resolution, and better safety profile [15, 16]. A wide variety of NIR excitable fluorescence contrast agents have been developed for targeting and diagnosis of cancers, inflammation, and other tissue abnormalities. Representative contrast agents

of fluorescence imaging include inorganic nanoparticles, quantum dots, fluorescent protein, and organic fluorophores. While inorganic materials account for an important category of fluorescent contrast materials, the main focus of this chapter is limited to organic fluorophore developments, followed by some examples of common biological applications.

2 Representative Organic Fluorophores

Organic fluorophores are widely used as contrast agents in optical microscopy. Numerous fluorophores have been developed for fluorescence imaging. In this section, we will summarize some commonly used organic fluorophores including cyanines, 5-aminolevulinic acid (5-ALA), methylene blue (MB), difluoroboron dipyrromethene (BODIPY), rhodamine, nicotinamide adenine dinucleotide (NADH), flavin adenine dinucleotide (FAD), porphyrins, phthalocyanines (Pcs), naphthalocyanines (Ncs), etc. Their backbone chemical structures were illustrated in Fig. 1.

2.1 Cyanines

Cyanine dyes represent a large family of fluorescent compounds with the chemical structure of two aromatic or heterocyclic rings connected with a polymethine chain. Cyanines and their derivatives are a common source of organic fluorophores with excitation wavelength in the range of 600–900 nm [17]. Among them, indocyanine green (ICG) is a widely used fluorophore that has been approved by FDA for medical use. Compared to other dyes such as Cy5, ICG has longer emission wavelength so that it has deeper penetration and less autofluorescence. ICG was initially used for medical imaging because of its minimal toxicity [18]. It has also been used for cardiovascular function test, retinal angiography, and hepatic clearance, as well as for sentinel lymph node mapping, coronary arteriography during cardiac bypass surgery [19], cholangiography during hepatobiliary surgery [20–22], and blood flow measurement during aneurysm surgery [23]. Based on the characteristics of ICG, one FDA-approved intraoperative fluorescent imaging system (Novadaq Technologies, SPY system) has been developed. The whole system comprises an 806 nm laser to excite ICG and camera unit, monitor, central processing unit, and laser generator. For image acquisition, the camera was positioned about 30 cm above the place of interest. An automatic distance sensor can indicate the correct position to ensure the camera is at the right place. After injection of ICG, the laser is activated, and image acquisition is started by a single command to the computer. For example, in one study, Novadaq SPY system was used for quality assessment in off-pump coronary artery bypass grafting [21]. This is based on the fact that ICG can bind to plasma proteins and protein-ICG complex emits light

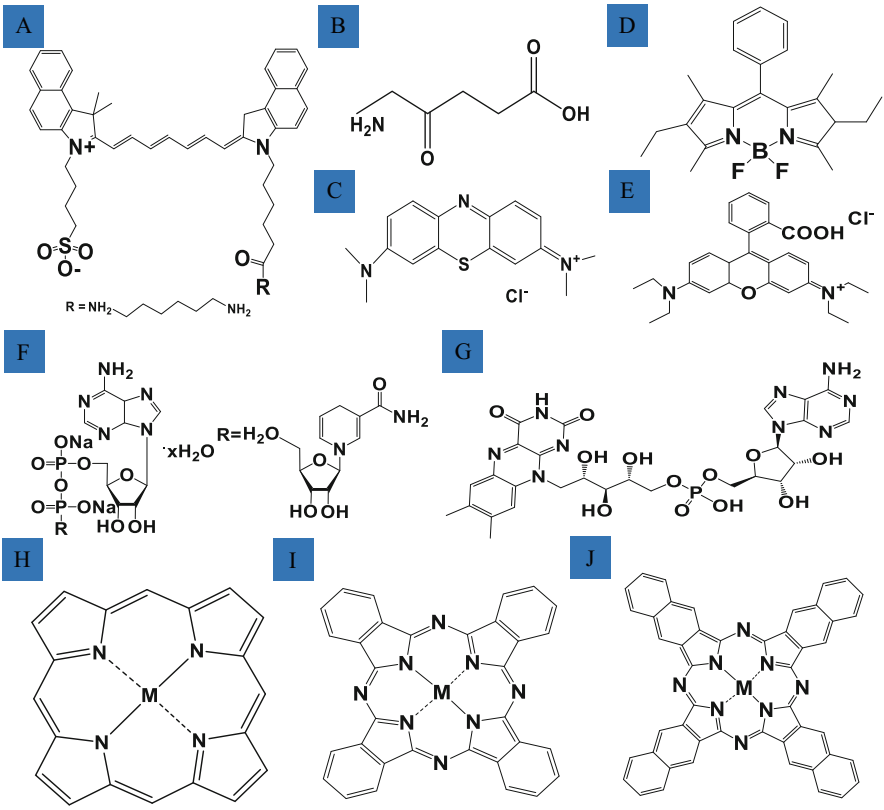

Fig. 1 Chemical structures of (**a**) indocyanine green (ICG); (**b**) 5-aminolevulinic acid (5-ALA); (**c**) methylene blue (MB); (**d**) difluoroboron dipyrromethene (BODIPY); (**e**) rhodamine B; (**f**) nicotinamide adenine dinucleotide (NADH); (**g**) flavin adenine dinucleotide (FAD); (**h**) porphyrins; (**i**) phthalocyanines (Pcs); (**j**) naphthalocyanines (Ncs) (M = 2H or metal)

at the wavelength of around 830 nm. Thirty-eight patients undergoing surgery were included and 107 grafts were analyzed. ICG-based SPY system was shown to be easy to handle with minimal adverse effects.

2.2 5-Aminolevulinic Acid (5-ALA)

5-ALA is a precursor for the heme biosynthesis. After taking up cells, 5-ALA produces a photoactive protoporphyrin IX (PpIX), which is preferentially accumulated in cancer cells [24–26]. 5-Aminolevulinic acid (5-ALA) has been used for intraoperative mapping and monitoring the efficiency of complete resection of enhancing tumor (CRET) and gross total resection (GTR). Schucht et al. have used 5-ALA-induced fluorescence as guidance during tumor resection. 20 mg/kg

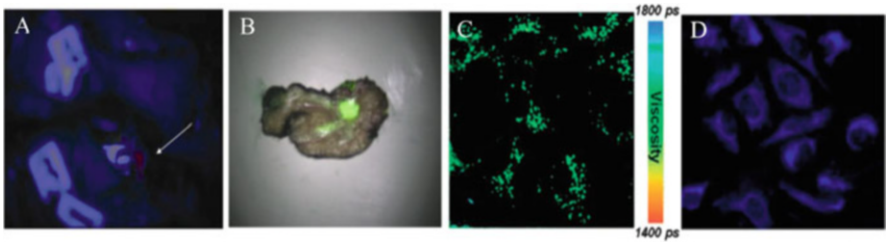

Fig. 2 Fluorescence imaging using various organic probes. (**a**) Fluorescence imaging guided by 5-ALA (white arrow indicated corticospinal tract in a right motor area) (Adapted from the Ref. [28] with permission); (**b**) a clear fluorescent spot was seen at the site of tumor with methylene blue as contrast agent (Adapted from the Ref. [29] with permission); (**c**) fluorescence lifetime image of SK-OV-3 cells with BODIPY as contrast agent (Adapted from the Ref. [35] with permission); (**d**) fluorescence images of RAW cells co-stained fluorescent imidazo[1,5-a]pyridine-rhodamine probe (Adapted from the Ref. [40] with permission)

5-ALA was administered 3 h prior to anesthesia, and resection was conducted until all fluorescence was completely removed while preserving neurological function. Consequently, high rate of CRET and GTR was achieved [27]. However, increasing resection toward the abnormality border might lead to neurological defects such as brain tissue injury or vascular injury. In addition, 5-ALA was used for imaging-guided surgery of high-grade gliomas in eloquent areas. For example, in one study, assisted by 5-ALA fluorescence and monitoring, gross total resection (GTR) $> 98\%$ and GTR $> 90\%$ were observed in 93% and 100% of cases, respectively [28] (see Fig. 2a).

2.3 Methylene Blue

Methylene blue (MB), also known as methylthioninium chloride, is commonly used as medication for the treatment of methemoglobinemia or as dyes for contrast imaging. MB is used for several clinical indications. Also, as a NIR fluorescent dye, methylene blue could be used to detect breast cancer intraoperatively. Twenty-four patients with breast cancer were investigated. The mini-FLARE imaging system was employed to provide NIR fluorescence during surgery. It was found that 20 out of 24 (83%) patients of breast tumors were detected in resected specimen by MB fluorescence imaging method and the concordance of fluorescence signal and tumor tissue was confirmed by histology [29] (see Fig. 2b). Another example is using MB for intraoperative NIR fluorescence imaging of parathyroid adenomas. 0.5 mg/kg MB was administered into 12 patients undergoing parathyroid surgery. Mini-FLARE imaging system was used. Ten out of twelve patients are identified to have parathyroid adenoma, and nine out of these patients, parathyroid adenoma could be clearly detected by NIR fluorescence using MB [30]. And this was the first study showing that low-dose MB can be used to identify parathyroid adenomas.

2.4 BODIPY

BODIPY (4,4-difluoro-4-bora-3a,4a-diaza-s-indacene, or difluoroboron dipyrromethene) has gained notoriety for its excellent photostability and chemical stability and high molar absorption coefficient and fluorescence quantum yield [31]. A wide variety of BODIPY-based fluorescent dyes have been developed, and some of them are commercially available such as ER-Tracker Green and LysoTracker Red. The photophysical properties of BODIPY are tuned by conjugation of various chemical residues on the difluoroboron dipyrromethene backbone. For example, (a) 2,6-positions are available for the electrophilic substitution reactions for the introduction of bromine or iodine [32] for further synthetic modification; (b) active methyl groups at 3,5-position are subject to chemical modification owing to their strong nucleophilic character [33]; (c) nucleophilic substitution of leaving groups is also great modification site for a thiomethyl group, for example, at the 8-position [34]; (d) a halogen atom could be used for further extension of the conjugation or the structure via palladium-catalyzed coupling reaction; (e) extension of Pi electron conjugation; and (f) modification at the boron center. Readers are referred to these comprehensive review papers that have described the synthesis and photophysical properties of BODIPY [35–37] (see Fig. 2c). BODIPY could be used for many biological applications such as indicators of pH, ion, biomolecules (e.g., peptide, thiol, saxitoxin), reactive oxygen species and reactive nitrogen species, and others (e.g., hydrolysis esters, biocatalytic reactions).

2.5 Rhodamine

Rhodamine is another fluorescent dye used for bio-imaging, and many rhodamine-based imaging systems have been developed. For example, a sugar-rhodamine fluorescent probe was designed as a specific sensor for Cu^{2+}, exhibiting fluorescent color changes by naked eye. More importantly, the probe also could detect the Cu^{2+} at 0.2 mg/L concentration, which is ten times lower than minimum Cu^{2+} value (2.0 mg/L) in drinking water recommended by WHO [38]. Another chemosensor system based on the conjugation of rhodamine with quinoline was developed for the detection of Cu^{2+} and Fe^{3+} in vivo with good selectivity and sensitivity [39]. In addition, a ratiometric fluorescent probe (RIM) based on fluorescence resonance energy transfer (FRET) was synthesized from imidazo[1,5-a] pyridine and rhodamine for the detection of HOCl. Without HOCl, the RIM displayed absorption spectra at 360 nm, whereas, in the presence of HOCl, ring-opening form of rhodamine moiety resulted in the FRET process with imidazo[1,5-a] pyridine as donor and rhodamine as acceptor, showing an additional absorption peak at 560 nm. The detection range is 0–5 μM with high selectivity and sensitivity [40] (see Fig. 2d). Another novel rhodamine derivative fluorescent probe (RDP) was synthesized through the reaction of rhodamine B derivative with di(pyridin-2-yl)methanone in

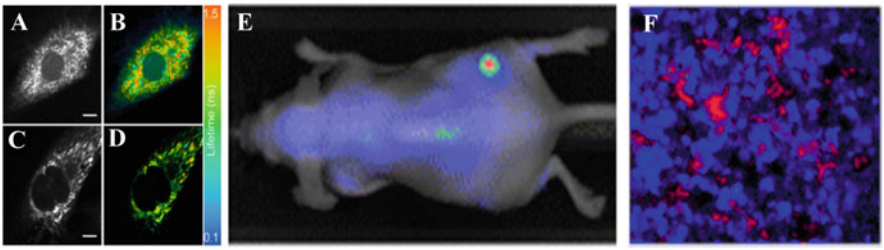

Fig. 3 Fluorescence imaging using various organic probes. Two-photon autofluorescence lifetime imaging reveals heterogeneous environment of the intracellular NADH in breast cancer (**a**, **b**) and normal cells (**c**, **d**) (Adapted from the Ref. [45] with permission); silicon naphthalocyanine (SiNc) polymeric nanoparticles could be used for imaging (**e**) and phototherapy (**f**) with good fluorescence contrast (Adapted from the Ref. [67] with permission)

ethyl alcohol. This study found that RDP exhibited nonfluorescent properties itself; however, a new fluorescence spectrum peak of RDP at 560 nm was observed in the presence of trivalent metal ions (M^{3+}) (where $M^{3+} = Fe^{3+}$, Al^{3+}, and Cr^{3+}), with the color change from colorless to pink, resulting from the ring-opened RDP-M^{3+} complex [41].

2.6 NADH and FAD as Endogenous Fluorophores

Various endogenous chromophores existing in cells and tissues play important role in metabolic activities and cell functions. Common endogenous fluorophores include retinol, tryptophan, elastin, collagen, and porphyrins [42]. Among them, nicotinamide adenine dinucleotide (NADH) and flavin adenine dinucleotide (FAD) are most extensively investigated. For example, using the intracellular NADH as contrast agent, breast cancer cells are easily differentiated from normal cells under two-photon autofluorescence lifetime imaging system [43–46] (see Fig. 3a–d). The redox states of endogenous fluorophores NADH and FAD can be measured as a direct indicator of oxygen amount in the cells. The reduced form (NADH) acts ubiquitously as electron carrier that plays significant role in both oxidative metabolism and glycolysis, and it is naturally fluorescent, whereas the oxidized form (NAD^+) is fluorescently quenched [47]. Another pair of redox markers is FAD/FADH that exhibits the opposite effect. Yaseen et al. used two-photon fluorescence lifetime microcopy of NADH for imaging of cerebral energy metabolism [48]. They found that using NADH as fluorescence probe, four different components responded to anoxia and indicated different enzymatic formulations [48]. In addition, to monitor the conformational and functional states of NADH, fluorescence lifetime imaging microscopy (FLIM) has been developed that is based on the measurement of the time fluorescent molecules stayed in their excited states. One important feature of FLIM is that the lifetime of a chromophore keeps

unchanged, which is advantageous for quantification of ion concentrations and biological environment [49–55].

2.7 *Porphyrins, Phthalocyanines (Pcs), and Naphthalocyanines (Ncs) and Their Nanosystems*

Most porphyrins, Pcs, and Ncs are hydrophobic. To improve their solubility, polymeric nanoparticles, liposomes, and chemical modification are employed. Liposomes have proven biocompatibility, whereas polymeric nanoparticles are readily available for a range of chemical modifications. Porphyrins can emit fluorescence in the NIR range that can be used for in vivo imaging. The first use of porphyrin fluorescence for tumor detection can date back to as early as 1924 [56]. Auler and Banzer found that hematoporphyrins can be preferentially accumulated in tumors and lymph nodes. Following studies also found that porphyrins show great affinity for neoplastic tissue [57]. Porphyrin fluorescence imaging could be used to assess the success or failure of photodynamic therapy [58, 59] or imaging-guided surgical tumor resection [60]. Another important fluorescence imaging example is that compared with hematoporphyrins, tetratraphenylporphinesulfonate (TPPS) that was found to better localize in tumor [61]. Porphyrin and phospholipid conjugates were also synthesized that can form self-assembled organic nanoparticles (termed porphysome) [62]. Porphysomes exhibit liposome-like structure with high loading capacity, high absorption of NIR light, and excellent biocompatibility. Owing to the presence of porphyrin, porphysomes enabled the visualization of lymph nodes by photoacoustic imaging, and also the fluorescence could be restored upon dissociations, enabling low-background fluorescence imaging. In addition, various porphyrin-PEG conjugates were also made for fluorescence imaging application [63, 64]. Compared to porphyrins, Pcs and Ncs typically show higher extinction coefficient and longer absorption wavelengths because of additional aromatic rings fused to pyrrolic subunits. In addition, Pcs also show promise in photodynamic therapy for cancers [65]. Zinc phthalocyanine (ZnPc) was encapsulated in liposomes by solvent exchange method for fluorescence imaging of tumor. After introducing into blood intravenously, ZnPc liposomes was taken up by lipoprotein and then accumulated in the tumor; after 120 min, the fluorescence in the tumor and blood reached a plateau [66]. Recently, silicon naphthalocyanine (SiNc) polymeric nanoparticles have been synthesized for fluorescence imaging and photodynamic therapy [67] (see Fig. 3e, f). SiNc was loaded in poly(ethylene glycol)-poly (ε-caprolactone) (PEG-PCL) copolymers. It was demonstrated that Nc polymeric nanoparticles have good photostability. Silicon 2,3-naphthalocyanine bis (trihexylsilyloxide) (NIR775) was co-loaded with 2,3-bis(4-(phenyl(4-(1,2,2-triphenylvinyl)phenylamino)phenyl)fumaronitrile (TPETPAFN) into DSPE-PEG2000. Taking advantage of FRET between NIR775 and TPETPAFN, the fluorescence of the nanoparticles was enhanced by 47-fold compared to excitation

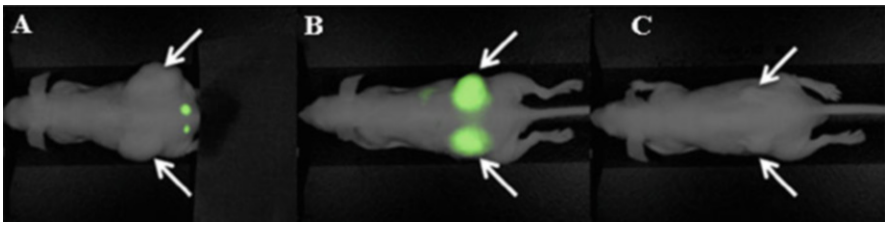

Fig. 4 Fluorescence imaging of antibody-IRDye conjugates. Mice were imaged at different time points to determine optimal imaging time after administration of Claudin-1-IRDye800CW (**a**) 24 h, (**b**) 48 h, and (**c**) 72 h. Arrows point to tumors on the bilateral flanks (Adapted from the Ref. [71] with permission)

of NIR775 alone. This nanoplatform also showed photostability and low cytotoxicity.

2.8 Antibody Conjugates

Antibody-IR dye conjugates or antibody conjugated nanoparticles are playing an important role in the medicine field [68, 69]. Monoclonal antibodies have been conjugated to a wide variety of nanoplatforms such as micelles, liposomes, nanoparticles, and many others [70]. Among them, indocyanine green (ICG) was widely used for molecular imaging via effective perfusion into tissues, which provides a great pathway for fluorescence imaging-guided surgical operations. And antibody IR dye probes could specifically target the diseased tissue clearly. Claudins, which are important proteins acting as epithelial barrier in colon cells, are overexpressed for the development of colon cancer; therefore, conjugation of claudin antibody with IR800CW had great potential in clinical practice. As shown in Fig. 4, in one colon tumor study, tumor margin in mice administered with Claudin-1-IRDye800CW could be clearly visualized after 48 h and 72 h without significant background signal. More importantly, visualization of local metastases could be achieved with anti-claudin antibody conjugating with IR800CW as contrast agent, and no noticeable side effects or toxicity on organs were observed [71]. CEA (carcinoembryonic antigen) is another representative target example, and its overexpression was found in 90% colorectal cancer cells and could be the specific target for colorectal cancer diagnosis and treatment in intraoperation. Photosensitizer phthalocyanine dye IR700 was found to be cytotoxic once exposed to NIR light irradiation, and a study on treatment of pancreatic cancer revealed that the conjugation of phthalocyanine dye IR700 with anti-CEA antibody could effectively target pancreatic tumor cells and kill most of the tumor cells upon NIR light activation [72, 73]. Fluorescent dye-antibody conjugates also show great promise in clinical performance. For example, SGM-101, the CEA antibody, has been used in clinical detection of colorectal cancer without significant adverse events related to antibody

fluorescent probes; and in a study based on 26 patients, 98% sensitivity and 84% accuracy in the expansion cohort were achieved [74]. Other antibody-NIR dye conjugates such as IRDye 800CW or Alexa Fluor 680 also show good clinical performance [75]. Therefore, NIR antibody combination is a powerful tool in diagnosis of tumor cells and metastases with high specificity and availability, providing useful information for decision-making during clinical surgery.

3 Biological Applications

3.1 Imaging-Guided Surgery

Fluorescence molecular imaging has been developed as an emerging tool for imaging-guided surgery. For precise intraoperative positioning, a fluorescent fluorophore coupled with an imaging system will be used to help surgeons to differentiate normal tissues and malignant tissues. Imaging-guided surgeries have been used for better treatment for liver metastases [76], cervical cancer [77, 78], melanoma [79, 80], ovarian cancer [81], and vulvar cancer [77]. After injection of fluorescent contrast agents, imaging guiding system indirectly activates fluorescent contrast agents with NIR light, followed by image registration processing, providing video-rate images. The imaging contrast agents and surgical navigation systems are two most important components of fluorescence molecular imaging technology. With respect to contrast agents, indocyanine green is a commonly used FDA-approved dye. It has been used in sentinel lymph node mapping [82] and hepatic micrometastases detection [83]. In addition, 5-aminolevulinic acid (5-ALA) was also orally administered to better detect patients with glioma [84]; Alexa-647 was also used to assess tumor margins and better detect head and neck squamous cell carcinoma [85]. Also, in order to selectively detect tumor, fluorescent contrast agents were also conjugated with targeting moieties such as sugars, peptides, or antibodies [86]. As of surgical navigation systems, there are several surgical navigation systems existing for clinical studies including SPY, Artemis, Photodynamic Eye, Fluobeam, SurgOptix, FLARE, and GXMI Navigator. SPY system has been utilized to monitor skin perfusion using ICG as contrast agent during nipple-sparing mastectomies [87]. FLARE™ imaging systems were created that use three cameras and collect signals from two NIR channels. FLARE™ imaging systems are mostly used for intraoperative SLN mapping and cancer surgeries [88, 89]; Artemis™ can collect both color images and the fluorescent overlay, providing a powerful tool for nerve surgery. For more detailed surgical navigation systems, readers are referred to these comprehensive review papers [90, 91]. For example, compared with the white-light reflectance imaging, the image of main nerve trunk and small branches in muscle planes was better visualized under fluorescent imaging with organic probes injected (see Fig. 5).

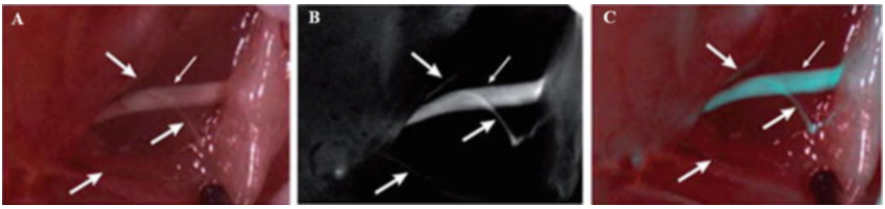

Fig. 5 White-light reflectance image and the fluorescence image of sciatic nerve branching within muscle planes. (**a**) A white-light reflectance image of a sciatic nerve branching within muscle planes. The main trunk of the nerve was clearly imaged (thin white arrow), but the smaller branches were difficult to distinguish from surrounding tissue (thick white arrows); (**b**) a fluorescence image clearly showing both the main nerve trunk and small branches using fluorescent contrast agent; (**c**) an overlay of fluorescence and white-light reflectance images (Adapted from the Ref. [87] with permission)

3.2 Thiol Detection

Bio-thiols such as cysteine (Cys), homocysteine (Hcy), and glutathione (GSH) as necessary reactive sulfur species play an indispensable role in cellular activity [92–94]. For example, GSH can regulate the cellular redox activities, signal transduction, and gene expression [95], whereas Cys and Hcy are the precursors of hydrogen sulfide. Many diseases including cancers can be possibly caused by the abnormally high levels of intracellular Cys [96]. Elevated amount of homocysteine might give rise to Alzheimer's disease or inflammatory bowel diseases. Therefore, accurate detection of intracellular thiols is intriguing for disease diagnosis. A fluorescein-based fluorescent probe was synthesized by conjugation of 2-cyclopentenone to fluorescein-monoaldehyde in the presence of imidazole in THF for the detection of various thiol-containing analytes including Cys, Hcy, GSH, Gly, Phe, Ser, Glu, Lys, Arg, His, Ala, Gln, Met, Tyr, and cysteine. This probe itself is nonfluorescent, but after addition of Cys, Hcy, and GSH, stronger fluorescence intensity and greater UV-Vis spectral changes occurred because of the formation of thioether. The probe itself is nonfluorescent without GSH, but after addition of GSH under neutral and basic conditions, a new emission peak was observed, and the fluorescence intensity was increased by 61-fold. This probe was also applied to monitor thiols in cells and independent tissues and organs of zebra fish. Strong fluorescence was observed from murine P19 embryonic carcinoma cells and 3-day-old zebra fish after incubation with 20 μM of the probe [97] (see Fig. 6a). Another example is 4-aminonaphthalimide dimer connected by a disulfide linker that can detect thiol quantitatively. Once thiol triggers the cleavage of the disulfide group, 4-aminonaphthalimide is released, and its fluorescence can be restored showing jade green color seen by naked eyes. This probe was also applied successfully for the thiol imaging in living HeLa cells without pH interference [98]. Also, two-photon fluorescent probe could be used to detect the thiols in mitochondria in live cells and living tissues at 90–190 μm depth. Compared to one-photon microscopy, two-photon microscopy can provide deeper

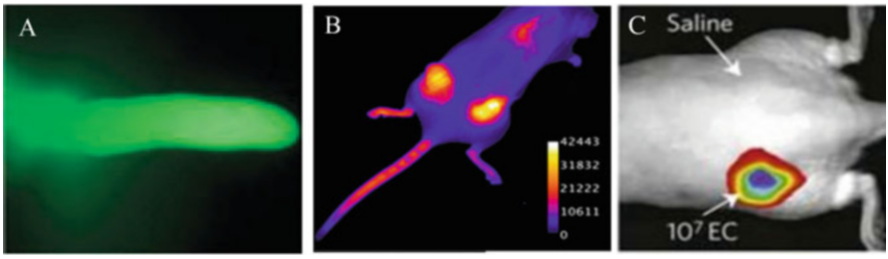

Fig. 6 Images of fluorescent imaging with organic probes. (**a**) Images of zebra fish eyes treated with fluorescent probe (Adapted from the Ref. [97] with permission); (**b**) images were acquired 48 h after injection of 200 nmol of organic fluorescent probe-chiral porphyrazine (pz), H_2[pz(trans-A_2B_2)], by tail-vein intravenous injection in mice bearing MDA-231 human breast xenograft tumors (Adapted from the Ref. [115] with permission); (**c**) fluorescence image of a rat showing that MDP-2 can image 107 *E. coli* CFUs in vivo (Adapted from the Ref. [123] with permission)

penetration depth and prolonged observation time. 6-(benzo[d]thiazol-2′-yl)-2-(N, N-dimethylamino)naphthalene (BTDAN) with disulfide group was developed as reporter and triphenylphosphonium salt as mitochondrial targeting site. This thiol reporter system provided selectivity and low cytotoxicity without the pH interference [99].

3.3 pH Imaging

pH measurement is important because various diseases such as cancer, immune dysfunction, and cystic fibrosis are associated with acid/base homeostasis [100–102]. Small molecules [103–107] and nanoparticles [108–110] have been employed for the ratiometric determination of pH. For example, a nanoplatform was designed by coupling of a pH-sensitive dye, cyanine HCyC-646, or a pH-insensitive dye, Cy 7, to the bacteriophage for the pH ratiometric imaging. The emission from bacteriophage probe conjugated with HCyC-646 varies with the change of pH, whereas the signal of probe with Cy 7 remained the same. In addition, intracellular ratiometric pH map in RAW cells was obtained by fluorescence imaging of bacteriophage probe with HCyC-646 [111]. Also, a pH-sensitive dendritic nanoprobe using pentaerythritol as the core was developed, demonstrating that nanoprobes incubated at pH 4.5 presented six times higher fluorescence than that incubated at pH 7. Fluorescent lifetime and intensity of nanoprobes for NIR fluorescent dyes could be activated in acidic environment owing to acid-sensitive linkage formed between fluorescent dye and dendritic scaffold. The fluorescence intensity and lifetime can provide both physiological and molecular information. This nanosystem with pH-sensitive linkages can be used to noninvasively detect and analyze acidic tissues with high sensitivity and specificity [112]. Another example is a NIR fluorescence

probe composed of 4′-(aminomethylphenyl)-2,2′:6′,2″-terpyridine (Tpy) and tricarbocyanine (Cy) that could detect the minor pH fluctuation in the range of 6.7–7.9 in vivo. Furthermore, real-time imaging of pH was obtained in living HepG2 and HL-7702 cells. The probe did not exhibit autofluorescence and can provide fluorescence contrast with high sensitivity, excellent photostability, and remarkable cell membrane permeability [113].

3.4 Cancer Imaging

The typical distribution of phospholipid can be disrupted when cells are at the stage of apoptosis. Therefore, targeting phosphatidylserine on the membrane surface would be useful to evaluate the treatment efficacy. Porphyrin-ytterbium complex was designed as a marker to distinguish tumor cells from normal cells because the fluorescence of porphyrin ytterbium complex can strongly bind to phosphatidylserine for tumor cell targeting [114]. Another example for cancer cell imaging is a porphyrin derivative, a chiral porphyrazine that exhibits remarkable accumulation of tumor cell in vivo, especially in breast tumor cells. It showed that the high selectivity of chiral porphyrazine for tumor cell in vivo is a critical factor in the cancer therapy [115] (see Fig. 6b). Optimized analogues of chiral porphyrazine with enhanced photophysical properties were synthesized for applications in cancer imaging [116]. BODIPY polymer with emission wavelength in NIR range conjugated with cancer-homing peptide residues could be employed for fluorescence imaging of cancer cells, and compared with original polymer, the conjugate has higher water solubility, more excellent photostability, better biocompatibility, and specific interaction to breast tumor cells [117]. Another recent study showed that 2,4,6-trisubstituted pyridine-based fluorescent probe that is pH-dependent displayed selectivity, photostability, and reversibility so that the HeLa cancer cells could be distinguished from other cells in a pH range of 2.2–7.0 [118].

3.5 Bacterial Imaging

Bacterial imaging is an emerging technology that can be used in a wide variety of fields such as food science and biomedicines. Compared to mammalian membranes, bacterial ones have some unique characterizations that can act as targets for antimicrobial drug candidate such as peptidoglycan cell wall on bacteria and yeast [119] or O-antigen unit of lipopolysaccharide on the outer membrane of gram-negative bacteria [120] or anionic phospholipids (e.g., phosphatidylglycerol) [121]. Fluorescence and radiolabeling are two contrast methods for bacterial imaging. For example, zinc dipicolylamine (Zn-DPA) complexes (probe 1) were made to selectively target the surface of bacterial cells because they have high affinity for bilayer membrane with anionic phospholipids. Bis(Zn-DPA), probe 2, was also synthesized.

Probes 1 and 2 can effectively target gram-negative and gram-positive bacteria. These compounds also preferentially stain bacteria compared to mammalian cells [122]. In addition, detection of small numbers of bacteria would be beneficial for early detection of inflammation. To achieve that, maltodextrin-based imaging probes (MDPs) were designed for bacterial infection imaging in vivo, including *E. coli*, *P. aeruginosa*, *S. aureus*, and *B. subtilis* detection [123] (see Fig. 6c). MDP could be selectively internalized to bacterial MDPs made by conjugating a fluorescent dye to maltohexaose so that the bacteria can be selectively internalized through maltodextrin transport pathway. This represents the first targeting strategy that can deliver an imaging probe as low as millimolar to bacteria. Another type of MDP could accurately image bacterial infections in rat injected with *E. coli* with excellent fluorescent intensity compared to uninfected controls.

4 Prospective and Conclusions

Fluorescence imaging has emerged as a powerful tool for diagnosis and treatment with high sensitivity, good biocompatibility, and noninvasiveness [124–126]. Conventional imaging modalities such as CT, MRI, and radionuclide imaging involve using contrast agents that are "always on" [127]. In these cases, the "always on" probes are not able to well distinguish the target tissues/cells and their proximity, leading to considerable background [128]. One unique feature of fluorescence imaging is that probes can be designed to be activatable in response to certain biological environments such as enzymatic digestion or acidification. In addition, compared to inorganic fluorescence probes, organic fluorescent probes have many advantages such as larger molar extinction coefficient in the deep NIR regions, relatively higher quantum yields, better photostability, and great biocompatibility (e.g., in zwitterionic structures and nanoformulation forms) [129, 130]. The molecular interactions such as hydrophobic and electrostatic interactions and hydrogen bonding between organic fluorescent dyes and biological species can lead to better sensitivity, selectivity, and bio-imaging capacity for diagnostics [131]. While inorganic fluorescence probes have unique properties, potential lack of body clearance and toxicity of inorganic probes may be a limiting safety concern. For example, Cd and Pb metals show high toxicity profile, and Ag- and Hg-based materials need more careful assessment [132]. On the other hand, there are also challenges and corresponding strategies for fluorescence imaging development. For example, due to the light scattering and attenuation, fluorescence might suffer from limited depth penetration, and also it is difficult to provide quantitative and tomographic information. Therefore, numerous multimodal imaging modalities were developed to complement each other. However, no imaging contrast for fused imaging has been approved by the FDA yet probably because it is still questionable whether a single probe for multimodalities is better than a mixture of two [133].

Further efforts will be made to improve imaging methods and probe development in the aspects of imaging techniques and instrument, contrast agents, and synthetic methodology. For example, multimodal imaging modalities fused with fluorescence imaging have attracted attention in order to achieve enhanced imaging depth and more accurate and comprehensive diagnosis [62, 134, 135]. Imaging-guided surgery and personalized medicine continue to be the hot research areas to solve some unmet medical needs. Meanwhile, fluorescence probes with longer wavelength are desired and advantageous for bio-imaging owing to the minimum photodamage and deeper tissue penetration [10, 136]. To conclude, in this chapter we have briefly discussed some representative fluorescent dyes including ICG, NADH/FAD, porphyrin, phthalocyanine, naphthalocyanine, BODIPY, and rhodamine, followed by some of their applications. With ongoing research efforts, fluorescence imaging using organic fluorophores has potential to make significant contributions for diagnosis and bio-imaging.

Acknowledgments We thank the Tianjin University Start-up Funding and the Chinese One-thousand Young Talent Funding.

Compliance with Ethical Standards

Funding: This chapter was made possible by Tianjin University Start-up Funding.

Conflict of Interest: The authors declare no conflict of interest.

Ethical Approval: This chapter does not contain any studies with human participants or animals performed by any of the authors.

References

1. Rao J, Dragulescu-Andrasi A, Yao H (2007) Fluorescence imaging in vivo: recent advances. Curr Opin Biotechnol 18:17–25
2. Gopalakrishnan V et al (2019) Use of CT imaging to quantify progression and response to treatment in lymphangioleiomyomatosis. Chest 155:962–971
3. Jeon SK et al (2019) Prospective evaluation of hepatic steatosis using ultrasound attenuation imaging in patients with chronic liver disease with magnetic resonance imaging proton density fat fraction as the reference standard. Ultrasound Med Biol 45:1407–1416
4. Bu L, Shen B, Cheng Z (2014) Fluorescent imaging of cancerous tissues for targeted surgery. Adv Drug Deliv Rev 76:21–38
5. Kobayashi H, Ogawa M, Alford R, Choyke PL, Urano Y (2010) New strategies for fluorescent probe design in medical diagnostic imaging. Chem Rev 110:2620–2640
6. Ponnuvel K, Kumar M, Padmini V (2016) A new quinoline-based chemosensor for Zn2+ ions and their application in living cell imaging. Sens Actuators B Chem 227:242–247
7. Callan JF, de Silva AP, Magri DC (2005) Luminescent sensors and switches in the early 21st century. Tetrahedron 61:8551–8588
8. Wang Z et al (2019) A novel isolongifolanone based fluorescent probe with super selectivity and sensitivity for hypochlorite and its application in bio-imaging. Anal Chim Acta 1051:169–178
9. Alfano RR, Demos SG, Gayen SK (1997) Advances in optical imaging of biomedical mediaa. Ann N Y Acad Sci 820:248–271

10. Yuan L, Lin W, Zheng K, He L, Huang W (2012) Far-red to near infrared analyte-responsive fluorescent probes based on organic fluorophore platforms for fluorescence imaging. Chem Soc Rev 42:622–661
11. Frangioni JV (2003) In vivo near-infrared fluorescence imaging. Curr Opin Chem Biol 7:626–634
12. Ding F, Zhan Y, Lu X, Sun Y (2018) Recent advances in near-infrared II fluorophores for multifunctional biomedical imaging. Chem Sci 9:4370–4380
13. Wang X et al (2019) LuPO4:Nd3+ nanophosphors for dual-mode deep tissue NIR-II luminescence/CT imaging. JOL 209:420–426
14. Cao Z et al (2018) Semiconducting polymer-based nanoparticles with strong absorbance in NIR-II window for in vivo photothermal therapy and photoacoustic imaging. Biomaterials 155:103–111
15. Li X et al (2019) 808 nm laser-triggered NIR-II emissive rare-earth nanoprobes for small tumor detection and blood vessel imaging. Mater Sci Eng C 100:260–268
16. Xue Z, Zeng S, Hao J (2018) Non-invasive through-skull brain vascular imaging and small tumor diagnosis based on NIR-II emissive lanthanide nanoprobes beyond 1500 nm. Biomaterials 171:153–163
17. Gonçalves MST (2008) Fluorescent labeling of biomolecules with organic probes. Chem Rev 109:190–212
18. McCorquodale EM, Colyer CL (2001) Indocyanine green as a noncovalent, pseudofluorogenic label for protein determination by capillary electrophoresis. Electrophoresis 22:2403–2408
19. Rubens FD, Ruel M, Fremes SE (2002) A new and simplified method for coronary and graft imaging during CABG. Heart Surg Forum 5:141–144
20. Mitsuhashi N et al (2008) Usefulness of intraoperative fluorescence imaging to evaluate local anatomy in hepatobiliary surgery. J Hepatobiliary Pancreat Surg 15:508–514
21. Ishizawa T et al (2009) Intraoperative fluorescent cholangiography using indocyanine green: a biliary road map for safe surgery. J Am Coll Surg 208:e1–e4
22. Ishizawa T et al (2010) Fluorescent cholangiography illuminating the biliary tree during laparoscopic cholecystectomy. Br J Surg 97:1369–1377
23. Raabe A et al (2005) Prospective evaluation of surgical microscope – integrated intraoperative near-infrared indocyanine green videoangiography during aneurysm surgery. J Neurosurg 103:982–989
24. Stummer W et al (2000) Fluorescence-guided resection of glioblastoma multiforme utilizing 5-ALA-induced porphyrins: a prospective study in 52 consecutive patients. J Neurosurg 93:1003–1013
25. Peng Q et al (1997) 5-Aminolevulinic acid-based photodynamic therapy. Cancer 79:2282–2308
26. Stummer W et al (2006) Fluorescence-guided surgery with 5-aminolevulinic acid for resection of malignant glioma: a randomised controlled multicentre phase III trial. Lancet Oncol 7:392–401
27. Schucht P et al (2012) Gross total resection rates in contemporary glioblastoma surgery: results of an institutional protocol combining 5-aminolevulinic acid intraoperative fluorescence imaging and brain mapping. Neurosurgery 71:927–936
28. Puppa AD et al (2013) 5-aminolevulinic acid (5-ALA) fluorescence guided surgery of high-grade gliomas in eloquent areas assisted by functional mapping. Our experience and review of the literature. Acta Neurochir 155:965–972
29. Tummers QRJG et al (2014) Real-time intraoperative detection of breast cancer using near-infrared fluorescence imaging and methylene blue. Eur J Surg Oncol 40:850–858
30. van der Vorst JR et al (2014) Intraoperative near-infrared fluorescence imaging of parathyroid adenomas with use of low-dose methylene blue. Head neck-J. Sci. Spec. Head Neck 36:853–858
31. Kolemen S, Akkaya EU (2018) Reaction-based BODIPY probes for selective bio-imaging. Coord Chem Rev 354:121–134

32. Rurack K, Kollmannsberger M, Daub J (2001) A highly efficient sensor molecule emitting in the near infrared (NIR): 3,5-distyryl-8-(p-dimethylaminophenyl)difluoroboradiaza-s-indacene. New J Chem 25:289–292
33. Saki N, Dinc T, Akkaya EU (2006) Excimer emission and energy transfer in cofacial boradiazaindacene (BODIPY) dimers built on a xanthene scaffold. Tetrahedron 62:2721–2725
34. Goud TV, Tutar A, Biellmann J-F (2006) Synthesis of 8-heteroatom-substituted 4,4-difluoro-4-bora-3a,4a-diaza-s-indacene dyes (BODIPY). Tetrahedron 62:5084–5091
35. Benniston AC, Copley G (2009) Lighting the way ahead with boron dipyrromethene (Bodipy) dyes. Phys Chem Chem Phys 11:4124–4131
36. Loudet A, Burgess K (2007) BODIPY dyes and their derivatives: syntheses and spectroscopic properties. Chem Rev 107:4891–4932
37. Ulrich G, Ziessel R, Harriman A (2008) The chemistry of fluorescent bodipy dyes: versatility unsurpassed. Angew Chem Int Ed 47:1184–1201
38. Ma X, Tan Z, Wei G, Wei D, Du Y (2012) Solvent controlled sugar-rhodamine fluorescence sensor for Cu(2+) detection. Analyst 137:1436–1439
39. Senthil Murugan A, Vidhyalakshmi N, Ramesh U, Annaraj J (2018) In vivo bio-imaging studies of highly selective, sensitive rhodamine based fluorescent chemosensor for the detection of Cu2+/Fe3+ ions. Sens Actuators B Chem. 274:22–29
40. Shen S-L, Zhang X-F, Ge Y-Q, Zhu Y, Cao X-Q (2018) A novel ratiometric fluorescent probe for the detection of HOCl based on FRET strategy. Sens Actuators B Chem 254:736–741
41. Kilic H, Bozkurt E (2018) A rhodamine-based novel turn on trivalent ions sensor. J Photochem Photobiol A Chem 363:23–30
42. Palero JA, De Bruijn HS, Sterenborg H, Gerritsen HC (2006) In vivo nonlinear spectral imaging in mouse skin. Opt Express 14:4395–4402
43. Skala MC et al (2007) In vivo multiphoton microscopy of NADH and FAD redox states, fluorescence lifetimes, and cellular morphology in precancerous epithelia. Proc Natl Acad Sci U S A 104:19494–19499
44. Schweitzer D et al (2007) Towards metabolic mapping of the human retina. Microsc Res Tech 70:410–419
45. Yu Q, Heikal AA (2009) Two-photon autofluorescence dynamics imaging reveals sensitivity of intracellular NADH concentration and conformation to cell physiology at the single-cell level. J Photochem Photobiol B Biol 95:46–57
46. Ghukasyan VV, Kao F-J (2009) Monitoring cellular metabolism with fluorescence lifetime of reduced Nicotinamide adenine dinucleotide. J Phys Chem C 113:11532–11540
47. Huang S, Heikal AA, Webb WW (2002) Two-photon fluorescence spectroscopy and microscopy of NAD(P)H and flavoprotein. Biophys J 82:2811–2825
48. Yaseen MA et al (2013) In vivo imaging of cerebral energy metabolism with two-photon fluorescence lifetime microscopy of NADH. Biomed Opt Express 4:307–321
49. Wang H-P et al (2007) Fluorescence lifetime image of a single halobacterium. Chem Phys Lett 442:441–444
50. Nakabayashi T, Wang H-P, Kinjo M, Ohta N (2008) Application of fluorescence lifetime imaging of enhanced green fluorescent protein to intracellular pH measurements. Photochem Photobiol Sci 7:668–670
51. Ogikubo S et al (2011) Intracellular pH sensing using autofluorescence lifetime microscopy. J Phys Chem B 115:10385–10390
52. Nakabayashi T et al (2008) Stress-induced environmental changes in a single cell as revealed by fluorescence lifetime imaging. Photochem Photobiol Sci 7:671–674
53. Ito T et al (2009) Fluorescence lifetime images of green fluorescent protein in HeLa cells during TNF-α induced apoptosis. Photochem Photobiol Sci 8:763–767
54. Awasthi K, Nakabayashi T, Ohta N (2012) Application of nanosecond pulsed electric fields into HeLa cells expressing enhanced green fluorescent protein and fluorescence lifetime microscopy. J Phys Chem B 116:11159–11165

55. Wallrabe H, Periasamy A (2005) Imaging protein molecules using FRET and FLIM microscopy. Curr Opin Biotechnol 16:19–27
56. Ackroyd R, Kelty C, Brown N, Reed M (2001) The history of photodetection and photodynamic therapy. Photochem Photobiol 74:656–669
57. Auler H, Banzer G (1942) Untersuchungen über die Rolle der Porphyrine bei geschwulstkranken Menschen und Tieren. Z Krebsforsch 53:65–68
58. Josefsen LB, Boyle RW (2008) Photodynamic therapy and the development of metal-based photosensitisers. Met Based Drugs 2008:276109
59. Wilson BC, Patterson MS (2008) The physics, biophysics and technology of photodynamic therapy. Phys Med Biol 53:R61–R109
60. Blake E, Allen J, Curnow A (2011) An in vitro comparison of the effects of the iron-chelating agents, CP94 and dexrazoxane, on protoporphyrin IX accumulation for photodynamic therapy and/or fluorescence guided resection. Photochem Photobiol 87:1419–1426
61. Winkelman J (1962) The distribution of tetraphenylporphinesulfonate in the tumor-bearing rat. Cancer Res 22:589–596
62. Lovell JF et al (2011) Porphysome nanovesicles generated by porphyrin bilayers for use as multimodal biophotonic contrast agents. Nat Mater 10:324–332
63. Huang H et al (2017) Implantable tin porphyrin-PEG hydrogels with pH-responsive fluorescence. Biomacromolecules 18:562–567
64. Huang H et al (2014) Pd-porphyrin-cross-linked implantable hydrogels with oxygen-responsive phosphorescence. Adv Healthc Mater 3:891–896
65. Wong RCH, Lo P-C, Ng DKP (2019) Stimuli responsive phthalocyanine-based fluorescent probes and photosensitizers. Coord Chem Rev 379:30–46
66. van Leengoed HL et al (1994) In vivo fluorescence and photodynamic activity of zinc phthalocyanine administered in liposomes. Br J Cancer 69:840–845
67. Taratula O et al (2015) Naphthalocyanine-based biodegradable polymeric nanoparticles for image-guided combinatorial phototherapy. Chem Mater 27:6155–6165
68. Gasser M, Waaga-Gasser AM (2016) Therapeutic antibodies in cancer therapy. Adv Exp Med Biol 917:95–120
69. Fay F, Scott CJ (2011) Antibody-targeted nanoparticles for cancer therapy. Immunotherapy 3:381–394
70. Alibakhshi A et al (2017) Targeted cancer therapy through antibody fragments-decorated nanomedicines. J Control Release 268:323–334
71. Hollandsworth HM et al (2019) Anti-Claudin-1 conjugated to a near-infrared Fluorophore targets colon cancer in PDOX mouse models. J Surg Res 242:145–150
72. Maawy AA et al (2015) Near infra-red photoimmunotherapy with anti-CEA-IR700 results in extensive tumor lysis and a significant decrease in tumor burden in orthotopic mouse models of pancreatic cancer. PLoS One 10:e0121989
73. Hiroshima Y et al (2015) Photoimmunotherapy inhibits tumor recurrence after surgical resection on a pancreatic cancer patient-derived orthotopic xenograft (PDOX) nude mouse model. Ann Surg Oncol 22(Suppl 3):S1469–S1474
74. Boogerd LSF et al (2018) Safety and effectiveness of SGM-101, a fluorescent antibody targeting carcinoembryonic antigen, for intraoperative detection of colorectal cancer: a dose-escalation pilot study. Lancet Gastroenterol Hepatol 3:181–191
75. Kijanka M et al (2013) Rapid optical imaging of human breast tumour xenografts using anti-HER2 VHHs site-directly conjugated to IRDye 800CW for image-guided surgery. Eur J Nucl Med Mol Imaging 40:1718–1729
76. van der Vorst JR et al (2013) Near-infrared fluorescence-guided resection of colorectal liver metastases. Cancer 119:3411–3418
77. van der Vorst JR et al (2011) Optimization of near-infrared fluorescent sentinel lymph node mapping in cervical cancer patients. Int J Gynecol Cancer 21:1472–1478
78. Crane LMA et al (2011) Intraoperative multispectral fluorescence imaging for the detection of the sentinel lymph node in cervical cancer: a novel concept. Mol Imaging Biol 13:1043–1049

79. Fujiwara M, Mizukami T, Suzuki A, Fukamizu H (2009) Sentinel lymph node detection in skin cancer patients using real-time fluorescence navigation with indocyanine green: preliminary experience. J Plast Reconstr Aesthet Surg 62:E373–E378
80. van der Vorst JR et al (2013) Dose optimization for near-infrared fluorescence sentinel lymph node mapping in patients with melanoma. Br J Dermatol 168:93–98
81. van Dam GM et al (2011) Intraoperative tumor-specific fluorescence imaging in ovarian cancer by folate receptor-alpha targeting: first in-human results. Nat Med 17:1315–U202
82. Tsujino Y, Mizumoto K, Matsuzaka Y, Niihara H, Morita E (2009) Fluorescence navigation with indocyanine green for detecting sentinel nodes in extramammary Paget's disease and squamous cell carcinoma. J Dermatol 36:90–94
83. Yokoyama N et al (2012) Real-time detection of hepatic micrometastases from pancreatic cancer by intraoperative fluorescence imaging preliminary results of a prospective study. Cancer 118:2813–2819
84. Suzuki T et al (2013) Cadherin 13 overexpression as an important factor related to the absence of tumor fluorescence in 5-aminolevulinic acid-guided resection of glioma laboratory investigation. J Neurosurg 119:1331–1339
85. Loja MN et al (2013) Optical molecular imaging detects changes in extracellular pH with the development of head and neck cancer. Int J Cancer 132:1613–1623
86. Sevick-Muraca EM (2012) Translation of near-infrared fluorescence imaging technologies: emerging clinical applications. Annu Rev Med 63:217–231
87. Wapnir I et al (2014) Intraoperative imaging of nipple perfusion patterns and ischemic complications in nipple-sparing mastectomies. Ann Surg Oncol 21:100–106
88. Vahrmeijer AL, Hutteman M, van der Vorst JR, van de Velde CJH, Frangioni JV (2013) Image-guided cancer surgery using near-infrared fluorescence. Nat Rev Clin Oncol 10:507–518
89. van der Vorst JR et al (2012) 46. Near-infrared fluorescence sentinel lymph node mapping of the oral cavity in head and neck cancer patients. Eur J Surg Oncol 38:745
90. Chi C et al (2014) Intraoperative imaging-guided Cancer surgery: from current fluorescence molecular imaging methods to future multi-modality imaging technology. Theranostics 4:1072–1084
91. Nguyen QT, Tsien RY (2013) Fluorescence-guided surgery with live molecular navigation – a new cutting edge. Nat Rev Cancer 13:653–662
92. He L, Yang X, Xu K, Kong X, Lin W (2017) A multi-signal fluorescent probe for simultaneously distinguishing and sequentially sensing cysteine/homocysteine, glutathione, and hydrogen sulfide in living cells. Chem Sci 8:6257–6265
93. Zhang L et al (2016) A highly selective and sensitive near-infrared fluorescent probe for imaging of hydrogen sulphide in living cells and mice. Sci Rep 6:18868
94. Xie X, Yin C, Yue Y, Chao J, Huo F (2018) Fluorescent probe detect distinguishly sulfite/hydrogen sulfide and thiol via two emission channels in vivo. Sens Actuators B Chem 277:647–653
95. Yin J et al (2016) Correction to 'cyanine-based fluorescent probe for highly selective detection of glutathione in cell cultures and live mouse tissues'. J Am Chem Soc 138:7442
96. Zhang X et al (2019) Mitochondria-targeting near-infrared ratiometric fluorescent probe for selective imaging of cysteine in orthotopic lung cancer mice. Sens Actuators B Chem 282:69–77
97. Chen X, Ko S-K, Kim MJ, Shin I, Yoon J (2010) A thiol-specific fluorescent probe and its application for bioimaging. Chem Commun 46:2751–2753
98. Zhu B et al (2010) A colorimetric and ratiometric fluorescent probe for thiols and its bioimaging applications. Chem Commun 46:5710–5712
99. Lim CS et al (2011) Ratiometric detection of mitochondrial thiols with a two-photon fluorescent probe. J Am Chem Soc 133:11132–11135
100. Kellum JA, Song M, Li J (2004) Science review: extracellular acidosis and the immune response: clinical and physiologic implications. Crit Care 8:331

101. Coakley RD et al (2003) Abnormal surface liquid pH regulation by cultured cystic fibrosis bronchial epithelium. Proc Natl Acad Sci 100:16083–16088
102. Gillies RJ, Schomack PA, Secomb TW, Raghunand N (1999) Causes and effects of heterogeneous perfusion in tumors. Neoplasia 1:197–207
103. Overly CC, Lee K-D, Berthiaume E, Hollenbeck PJ (1995) Quantitative measurement of intraorganelle pH in the endosomal-lysosomal pathway in neurons by using ratiometric imaging with pyranine. Proc Natl Acad Sci 92:3156–3160
104. Martin GR, Jain RK (1993) Fluorescence ratio imaging measurement of pH gradients: calibration and application in normal and tumor tissues. Microvasc Res 46:216–230
105. Bassnett S, Reinisch L, Beebe DC (1990) Intracellular pH measurement using single excitation-dual emission fluorescence ratios. Am J Physiol 258:C171–C178
106. Murphy RF, Powers S, Cantor CR (1984) Endosome pH measured in single cells by dual fluorescence flow cytometry: rapid acidification of insulin to pH 6. J Cell Biol 98:1757–1762
107. Thomas JA, Buchsbaum RN, Zimniak A, Racker E (1979) Intracellular pH measurements in Ehrlich ascites tumor cells utilizing spectroscopic probes generated in situ. Biochemistry 18:2210–2218
108. Kim S, Pudavar HE, Prasad PN (2006) Dye-concentrated organically modified silica nanoparticles as a ratiometric fluorescent pH probe by one-and two-photon excitation. Chem Commun 19:2071–2073
109. McNamara KP et al (2001) Synthesis, characterization, and application of fluorescence sensing lipobeads for intracellular pH measurements. Anal Chem 73:3240–3246
110. Ji J, Rosenzweig N, Griffin C, Rosenzweig Z (2000) Synthesis and application of submicrometer fluorescence sensing particles for lysosomal pH measurements in murine macrophages. Anal Chem 72:3497–3503
111. Marshall MV et al (2010) Near-infrared fluorescence imaging in humans with indocyanine green: a review and update. Open Surg Oncol J 2:12–25
112. Almutairi A, Guillaudeu SJ, Berezin MY, Achilefu S, Fréchet JMJ (2008) Biodegradable pH-sensing dendritic Nanoprobes for near-infrared fluorescence lifetime and intensity imaging. J Am Chem Soc 130:444–445
113. Tang B et al (2009) A near-infrared neutral pH fluorescent probe for monitoring minor pH changes: imaging in living HepG2 and HL-7702 cells. J Am Chem Soc 131:3016–3023
114. Zhang T et al (2013) Porphyrin-based ytterbium complexes targeting anionic phospholipid membranes as selective biomarkers for cancer cell imaging. Chem Commun 49:7252–7254
115. Trivedi ER et al (2010) Chiral porphyrazine near-IR optical imaging agent exhibiting preferential tumor accumulation. Proc Natl Acad Sci 107:1284–1288
116. Trivedi ER et al (2010) Synthesis of heteroatom substituted naphthoporphyrazine derivatives with near-infrared absorption and emission. J Org Chem 75:1799–1802
117. Zhu S et al (2013) Highly water-soluble, near-infrared emissive BODIPY polymeric dye bearing RGD peptide residues for cancer imaging. Anal Chim Acta 758:138–144
118. Ma J et al (2018) A small molecular pH-dependent fluorescent probe for cancer cell imaging in living cell. Talanta 182:464–469
119. Cooper MA, Williams DH (1999) Binding of glycopeptide antibiotics to a model of a vancomycin-resistant bacterium. Chem Biol 6:891–899
120. Kotra LP, Amro NA, Liu GY, Mobashery S (2000) Visualizing bacteria at high resolution. ASM News 66:675–681
121. Fernandez-Lopez S et al (2001) Antibacterial agents based on the cyclic D,L-alpha-peptide architecture. Nature 412:452–455
122. Leevy WM et al (2006) Optical imaging of bacterial infection in living mice using a fluorescent near-infrared molecular probe. J Am Chem Soc 128:16476–16477
123. Ning X et al (2011) Maltodextrin-based imaging probes detect bacteria in vivo with high sensitivity and specificity. Nat Mater 10:602–607

124. Wang L, Xia Q, Liu R, Qu J (2018) A red fluorescent probe for ribonucleic acid (RNA) detection, cancer cell tracing and tumor growth monitoring. Sens Actuators B Chem 273:935–943
125. Cal PMSD et al (2016) Site-selective installation of BASHY fluorescent dyes to Annexin V for targeted detection of apoptotic cells. Chem Commun 53:368–371
126. Georgiev NI, Krasteva PV, Bojinov VB (2019) A ratiometric 4-amido-1,8-naphthalimide fluorescent probe based on excimer-monomer emission for determination of pH and water content in organic solvents. JOL 212:271–278
127. Weissleder R, Pittet MJ (2008) Imaging in the era of molecular oncology. Nature 452:580–589
128. Kobayashi H, Choyke PL (2011) Target-cancer-cell-specific activatable fluorescence imaging probes: rational design and in vivo applications. Acc Chem Res 44:83–90
129. Wang L, Zhuo S, Tang H, Cao D (2018) A near-infrared turn on fluorescent probe for cysteine based on organic nanoparticles. Sens Actuators B Chem 277:437–444
130. Martinić I, Eliseeva SV, Petoud S (2017) Near-infrared emitting probes for biological imaging: organic fluorophores, quantum dots, fluorescent proteins, lanthanide(III) complexes and nanomaterials. JOL 189:19–43
131. Kim D, Ryu HG, Ahn KH (2014) Recent development of two-photon fluorescent probes for bioimaging. Org Biomol Chem 12:4550–4566
132. Chinnathambi S, Shirahata N (2019) Recent advances on fluorescent biomarkers of near-infrared quantum dots for in vitro and in vivo imaging. Sci Technol Adv Mater 20:337–355
133. Zhao J et al (2018) Recent developments in multimodality fluorescence imaging probes. Acta Pharm Sin B 8:320–338
134. Rieffel J et al (2015) Hexamodal imaging with porphyrin-phospholipid-coated upconversion nanoparticles. Adv Mater 27:1785–1790
135. Zhang Y et al (2016) Surfactant-stripped frozen pheophytin micelles for multimodal gut imaging. Adv Mater 28:8524–8530
136. Zhou Y et al (2016) A phosphorus phthalocyanine formulation with intense absorbance at 1000 nm for deep optical imaging. Theranostics 6:688–697

Top Med Chem (2020) 34: 55–80
DOI: 10.1007/7355_2019_85

Published online: 28 January 2020

Inorganic Fluorescent Nanomaterials

Taeho Kim and Jesse V. Jokerst

Contents

Abstract Optical imaging is a noninvasive imaging technology to visualize the specific biological processes by detecting the emissive photons under external energy excitation. In particular, inorganic nanomaterials have attracted great attention as exogenous fluorescent probes for optical imaging due to their superiority in imaging sensitivity, systemic circulation, target specificity, and versatility in chemical design for theranostic purposes. This book chapter comprehensively summarizes the recent advances in inorganic fluorescent nanomaterials, including quantum dots, upconversion, metal nanoclusters, and carbon-based and silicon-based nanomaterials. It will be reviewed in detail the fluorescence mechanism of the

T. Kim (✉)
Department of NanoEngineering, University of California San Diego, La Jolla, CA, USA

Department of Biomedical Engineering, Michigan State University, East Lansing, MI, USA

Institute for Quantitative Health Science and Engineering, Michigan State University, East Lansing, MI, USA
e-mail: kimtae47@msu.edu

J. V. Jokerst (✉)
Department of NanoEngineering, University of California San Diego, La Jolla, CA, USA

Materials Science Program, University of California San Diego, La Jolla, CA, USA

Department of Radiology, University of California San Diego, La Jolla, CA, USA
e-mail: jjokerst@ucsd.edu

nanomaterials based on their optical excitations, the current utility in high-resolution (preclinical) in vivo imaging, and the underlying issues for future clinical translations.

Keywords Fluorescence, In vivo, Molecular imaging, Nanomaterials, Optical imaging, Quantum dots

1 Overview

Most clinical optical imaging agents are organic fluorescent dyes (e.g., cyanine, rhodamine, oxazine dyes). However, these suffer from several drawbacks such as photo-bleaching and short blood circulation, which limit their repeated use for long-term imaging of cellular and molecular processes in living systems. In the last two decades, many efforts have been devoted to developing inorganic (metal-containing) nanoparticles as targetable optical probes with superior photostability. In this chapter, we will discuss several types of inorganic nanoparticles that use fluorescence. We will also introduce some recent studies to validate their interesting features as contrast agents in preclinical in vivo imaging. Finally, we will address the potential issues for each type of fluorescent nanomaterials to attain better sensitivity and lower toxicity for potential clinical translations.

2 Quantum Dots

Quantum dots (QDs; semiconductor nanoparticles) are composed of II–VI, III–V, and IV–VI group elements of the periodic table and are representative inorganic fluorescent nanomaterials (CdSe, CdS, CdTe, ZnS, InP, InAs, etc.). Their fluorescence is induced from the quantum confinement effect, which occurs when the QD radius is smaller than the exciton Bohr radius (5.3 nm) of the original material [1].

QDs have many photo-physical advantages. QDs display narrower emission bands than the traditional organic fluorophores. QDs have high photostability that preclude the fast quenching of emissive light after repeated, high-intensity light excitations. Therefore, these highly bright and photostable QDs offer fluorescence imaging of live cells and in vivo animal imaging for long time periods [2]. QDs have multiplexed imaging for simultaneous detection of multiple distinctive biological species due to their unique size-dependent light emission [3]. This is because QDs follow the quantum behaviors of a particle in a box (the smaller the box is, the larger is the separation between energy levels); for example, while the larger CdSe QDs (5–6 nm) emit red light (relatively long wavelength), smaller CdSe QDs (2–3 nm) have blue-shifted (short) emission (higher photon energies)

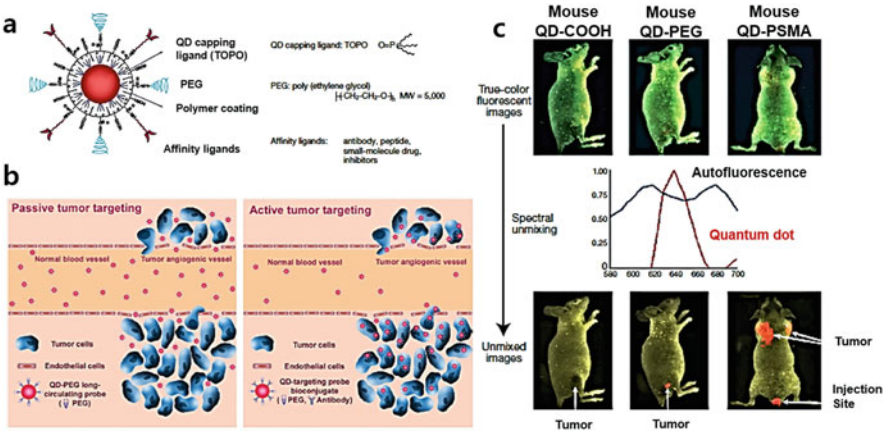

Fig. 1 Schematic illustration of QD probes for in vivo cancer targeting and imaging. (**a**) Multilayered structure of QDs, consisting of the capping ligand trioctylphosphine oxide (TOPO), encapsulating polymer layer, tumor-targeting ligand (e.g., peptides, antibodies, or small molecules), and polyethylene glycol (PEG). (**b**) Tumor targeting by enhanced permeation and retention (EPR) of QD probes via leaky tumor vasculatures (passive tumor targeting; left) or high affinity binding of QD-antibody conjugates to tumor antigens (active tumor targeting; right). (**c**) In vivo fluorescence images using QD probes with three different surface coatings with carboxylic acid groups (QD-COOH; left), PEG groups (QD-PEG; middle), and PSMA antibody conjugates (QD-PSMA; right). For all three QDs, a color image (top), two fluorescence spectra from QD and animal skin (middle), and a wavelength-resolved spectral image (bottom) were obtained from the live mouse bearing C4-2 human prostate tumors (0.5–1.0 cm in diameter) after systemic intravenous administrations of each QD. Adapted from Gao et al. [5] with permission

[4]. Remarkably, both of these systems can still utilize the same ~400 nm excitation.

Consequently, by capitalizing on the striking optical features of QDs (e.g., stale and sharp emission, spectral nature of emitted photons), Nie and coworkers reported the first study of QDs for targeting and spectral optical imaging in animal models [5]. In this study, ZnS-capped CdSe QDs were synthesized and subsequently conjugated with targeting ligands for tumor antigen recognition and polyethylene glycol (PEG) molecules for improved blood circulation (Fig. 1a). Here, the experimental groups included three different QDs with carboxylic acid groups (QD-COOH), PEG groups (QD-PEG), and prostate-specific membrane antigen (QD-PSMA). Next, each QD was intravenously injected into mice bearing human C4-2 prostate cancer xenografts (0.5–1.0 cm in diameter), and the in vivo fluorescence imaging was performed with wavelength-resolved spectral imaging. The fluorescence spectrum of the QD and the animal skin is shown in Fig. 1c. The autofluorescence spanned a broad range of wavelengths (580–700 nm), but the as-prepared QDs had a characteristic sharp emission band near 640 nm.

The authors also found that the surface-modified QD probes can be accumulated at tumors either by the enhanced permeability and retention (EPR) via leaky tumor vasculatures (passive targeting) [6, 7] or by antibody binding to cancer-specific cell

surface biomarkers (active targeting) (Fig. 1b) [8]. Figure 1c (bottom) shows no tumor signals detected with QD-COOH (no specific targeting), and the only weak signals were observed for QD-PEG (passive targeting); however, very intense signals were detected for QD-PSMA (active targeting). These results indicate the active tumor targeting is more efficient than passive targeting [5].

Since this groundbreaking work, there have been studies to show the surface-modified QDs with a variety of biological targeting moieties (e.g., small molecule [9], peptide [10, 11], aptamer [12]) allowed successful identification with high resolutions for tumor cells in vivo. Further recent studies for QDs for optical imaging have been particularly focused on improving the imaging sensitivity with use of near-infrared (NIR)-emitting QDs or decreasing the toxicity by using Cd-free QDs.

QDs that emit in the near-infrared (NIR) region (700–900 nm) can minimize the problems of endogenous fluorescence of tissues (autofluorescence) and increase tissue penetration, which is particularly suitable for in vivo animal imaging [14, 15]. In a pioneering study, Bawendi and coworkers first reported core/shell (CdTe/CdSe) QDs with fluorescence emission at 840–860 nm while preserving the absorption cross section (Fig. 2a, b) [13]. These NIR-emitting QDs were then rendered soluble and stable in serum by polydentate phosphine coating and used for to identify cancer cells in lymph nodes during surgery (sentinel lymph node mapping). As shown in Fig. 2c, when these QDs (10 pmol) were intradermally injected to the mouse, they entered the lymphatics and migrated within minutes to an axillary sentinel lymph node (SLN) that could be detected using intraoperative NIR fluorescence imaging system. Furthermore, even in a large animals (pigs), the authors found NIR fluorescence from intradermally injected ODs (400 pmol) was sensitive enough for imaging SLN 1 cm deep in real time and ensuring complete resection of the SLN under optical image guidance (Fig. 2d) [13].

Second near-infrared (NIR-II) window is nearly biologically transparent due to its much less optical scattering from endogenous molecules (e.g., hemoglobin, melanin, lipids), and thus NIR-II imaging can afford deeper anatomical penetration at high spatial resolution, compared to NIR-I imaging [17]. Hence, in 2010, the Dai group has developed single-walled carbon nanotubes (SWCNTs) as sensitive NIR-II fluorescent probes for whole-body imaging as well as real-time intravital small vessel imaging. Here, SWCNTs were emitted in the NIR-II region (1,000–1,400 nm) upon excitation by a 785 nm laser, with large Stokes shift up to ~400 nm (Fig. 3a) and thus allowed for high spatial (~30 mm) and temporal (<200 ms per frame) resolution for small-vessel imaging at 1–3 mm deep in the hind limb (Fig. 3b) [16]. Also, these NIR-II-emitting SWCNTs have permitted the high through-skull fluorescence imaging of mouse cerebral vasculature to a depth of >2 mm in mouse brain with sub-10-μm resolution [18]. However, the optical cross section of SWCNT is a bit limited, and thus Ag_2S QDs have been developed with 5.6 times higher photoluminescence quantum yield than SWCNT for emission in the NIR-II region. These probes also have negligible cytotoxicity [19] and the potential for deep tissue imaging (with theoretical penetration depth of 5 cm) [20]. Ag_2S QDs can be used to study angiogenesis mediated by a tiny tumor (2–3 mm in diameter) [21]. More recently, Bawendi and coworkers introduced InAs-based, core/shell QDs

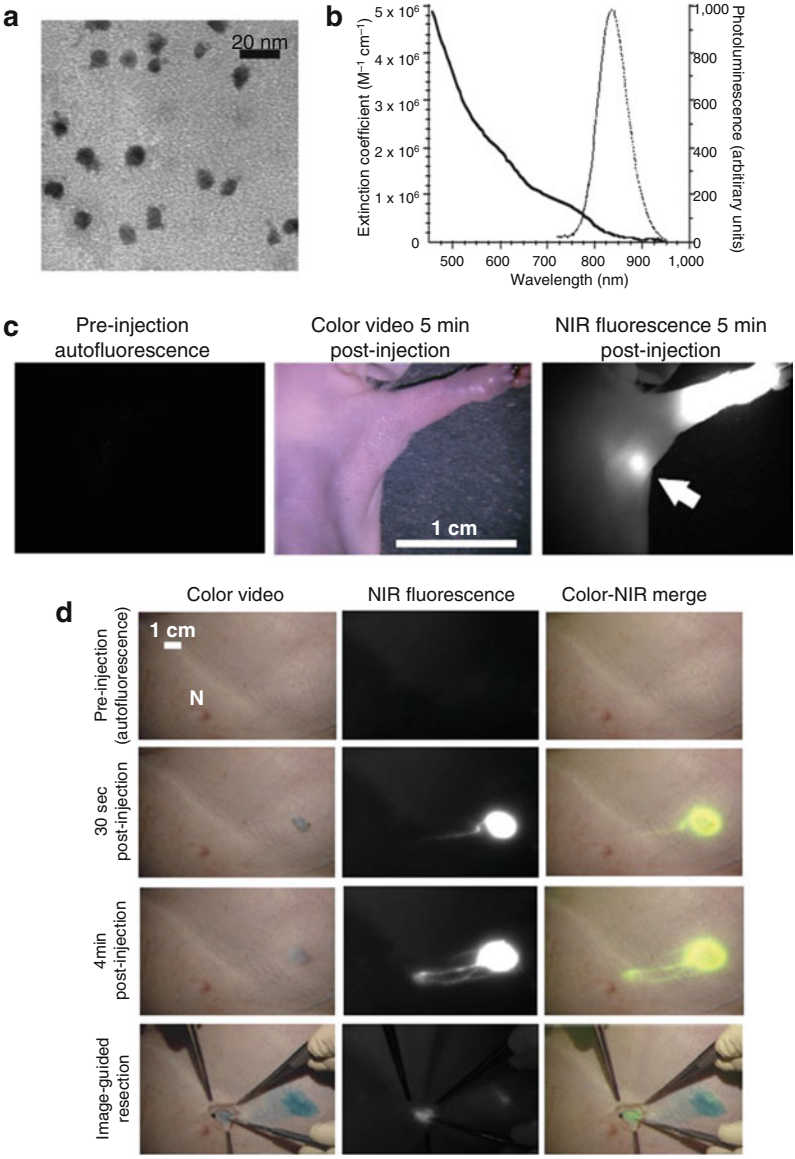

Fig. 2 NIR-emitting QDs for sentinel lymph node (SLN) mapping in the mouse and pigs. (**a**) TEM image of NIR QDs. (**b**) Molar extinction coefficient (solid curve) and photoluminescence intensity (dashed curve) of NIR QDs. (**c**) Images of mouse intradermally injected with NIR QDs (10 pmol) to the left paw; preinjection (autofluorescence), 5 min postinjection color video image, 5 min postinjection NIR fluorescence image. The putative axillary sentinel lymph node (SLN) is indicated by a white arrow. (**d**) Images of the surgical procedures in the pig intradermally injected with NIR QDs (400 pmol) at different time points; preinjection (autofluorescence), 30 s postinjection, 4 min postinjection, and during image-guided resection. Adapted from Kim et al. [13] with permission

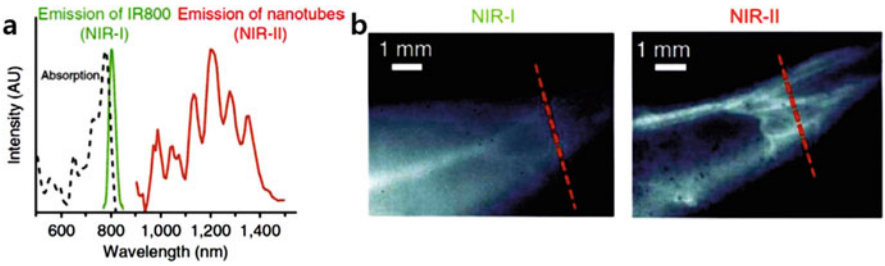

Fig. 3 In vivo mouse imaging in the NIR-II region. (**a**) The absorption spectrum of SWCNT-IRDye-800 conjugates (black dashed line), the emission spectrum of IRDye-800 dye (NIR-I) (green line), and SWCNTs (NIR-II) (red line). (**b**) NIR-I and NIR-II fluorescence images of a mouse injected with the SWCNT-IRDye-800 conjugates. This led to clearer vasculature imaging in the NIR-II region. Adapted from Hong et al. [16] with permission

(e.g., InAs/CdSe or InAs/CdSe/ZnSe) leading to a dramatically higher quantum yield (10 times to Ag_2Se QDs) and size-tunable emission in NIR-II region. In this study, they demonstrated that these QDs functionalized via three distinct surface coatings (e.g., triglyceride-rich lipoproteins, phospholipid micelles, PEG2000 PE) can allow for functional imaging to measure metabolic rates of lipoproteins in several organs and heartbeat/breathing rates as well as to quantify the blood flow of mouse brain vasculature [22].

Despite all of these photo-physical advantages of QDs, a substantial challenge for conventional Cd-containing QDs is their inherent cytotoxicity [23]. For example, CdSe QDs were found to induce cell death due to the liberated free Cd^{2+} from the CdSe lattice. Therefore, many studies have been performed to develop Cd-free QDs (e.g., InP, InAs, Ag) with comparable or even better performance than existing Cd-containing QDs [24]. Surface passivation via an additional inorganic shell (e.g., ZnS capping of CdSe QDs) is another way of reducing the oxidation-mediated cytotoxicity of Cd-QDs; here, PL improvement also appears owing to the effective passivation of surface non-radiative recombination of excitons [25]. Nevertheless, besides the aforementioned composition controls, toxicity issues can be circumvented by size control of QDs to make them renally clearable. In a pioneering study using QDs as a model inorganic nanoparticle, Frangioni and coworkers proposed the design considerations to reduce metal-induced toxicity [26]. In this study, it was revealed that nanoparticles of hydrodynamic diameter <5.5 nm could be efficiently excreted in urine via systemic intravenously injections.

3 Anti-Stokes Shift Luminescent Nanoparticles

Anti-Stokes shift luminescence is a special optical process of converting (low energy) long wavelength of light to (higher-energy) short-wavelength radiation, which can permit the deeper tissue penetration with minimal photo-bleaching

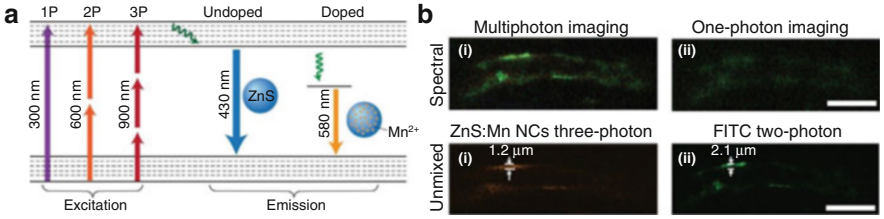

Fig. 4 Multiphoton fluorescence imaging with manganese-doped ZnS QDs (ZnS:Mn QDs). (**a**) A Jablonski diagram comparing one-, two-, and three-photon fluorescence of QDs. While the normal fluorescence emission from ZnS QDs is near 430 nm, ZnS:Mn QDs redshifts the emission to 580 nm reducing tissue absorbance and scattering of emitted light. Adapted from Zagorovsky et al. [28] with permission. (**b**) Comparison between a multiphoton micrograph (i) and a one-photon confocal laser-scanning micrograph (ii), which were acquired from spectral fluorescence of the tumor vasculature targeted by ZnS:Mn QDs-RGD-FITC conjugates (top). Comparison between three-photon luminescence of ZnS:Mn QDs (i) and two-photon luminescence of FITC (ii), which were acquired from spectral unmixing of the tumor vasculature targeted by ZnS:Mn QDs-RGD-FITC conjugates (bottom). Adapted from Yu et al. [29] with permission

[27]. Among the various anti-Stokes optical processes, both multiphoton absorption and upconversion mechanisms have been given much attention in recent years.

Transition metal-doped semiconductor nanoparticles can exhibit high multiphoton light absorption. In particular, three-photon imaging can effectively reduce the out-of-focus excitation and background autofluorescence; thus, in a recent study by Hyeon and coworkers, manganese-doped ZnS QDs (ZnS:Mn QDs) were developed to exhibit a large three-photon cross section ($1.3\ (\pm 0.5) \times 10^{-79}$ $cm^6\ s^2\ photon^{-2}$) [29]. Interestingly, in this study, manganese doping redshifted the emission wavelength of ZnS QDs from 430 to 580 nm to attain more efficient light path through tissue (Fig. 4a). Therefore, upon NIR excitation with a deep-penetrating 920 nm laser, three-photon optical imaging with ZnS:Mn QDs exhibited better resolution compared to two-photon imaging with fluorescein isothiocyanate (FITC) (Fig. 4b). This also allowed highly resolved imaging of tumor vasculatures with an experimental penetration depth of ~3 mm [29]. These QDs also have a large two-photon absorption cross section under irradiation of NIR-II light (1,050–1,310 nm) and improved the penetration depth and imaging quality [30].

Lanthanide ion-doped nanoparticles are a new generation of luminescent probes to achieve photon upconversion. Typical upconversion nanoparticles (UCNPs) consist of Yb^{3+} ion as a sensitizer and Er^{3+} ion as an emitter to generate the visible green emission upon excitation at 980 nm [33, 34]. Similar to ZnS:Mn QDs, NIR light absorbing, UCNPs can allow the imaging of deeper tissue penetration than conventional QDs (Fig. 5a) [31]. In addition, UCNPs can be used for multicolor multiplexed imaging [32] because they can exhibit tunable emission (blue, green, to red) by varying the lanthanide dopant ions (Fig. 5b) [35, 36]. The UCNPs offer sequential photon absorption via real intermediate, long-lived, electronic states of dopant ions, while the metal-doped semiconductors have multiphoton absorption based on virtual intermediate states [37, 38]. Consequently, UCNPs do not need

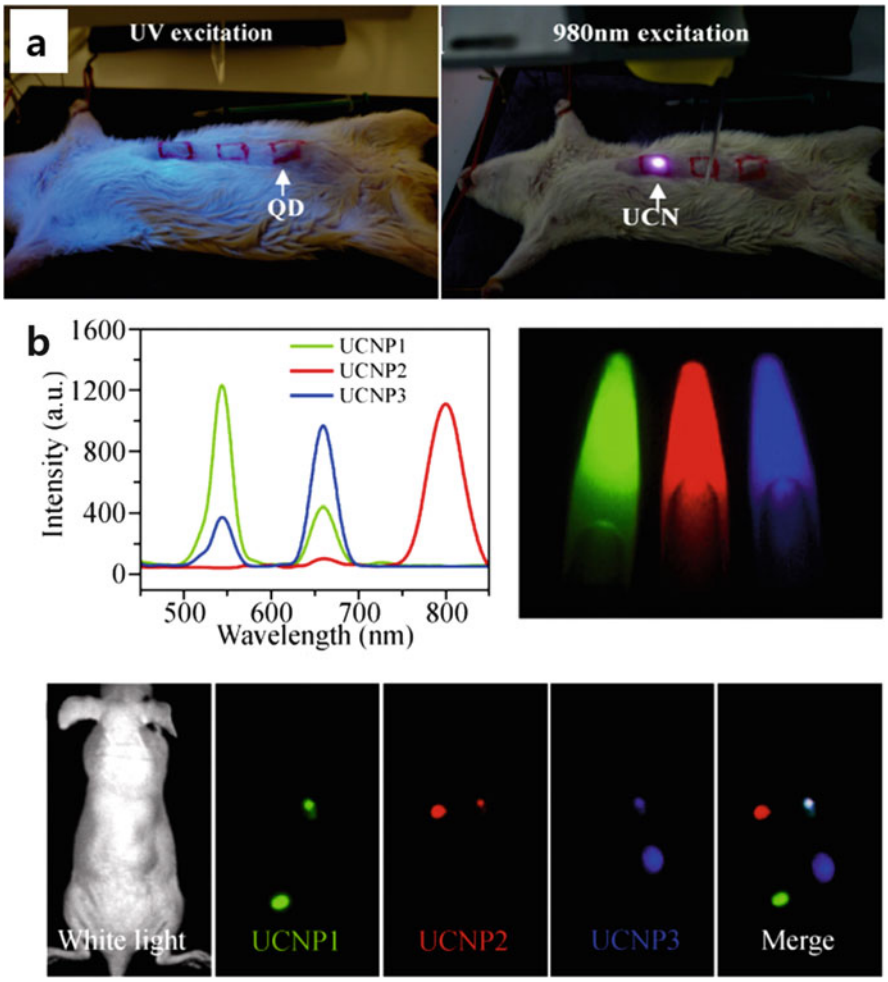

Fig. 5 (**a**) In vivo imaging of rat subcutaneously injected to abdominal skin with green-emitting QDs (CdTe) under UV excitation (left) and green-emitting UCNPs of PEI/$NaYF_4$:Yb,Er under NIR excitation (right). Adapted from Chatterjee et al. [31] with permission. (**b**) Multicolor imaging of a mouse using NIR-to-blue UCNPs of $NaY_{0.78}Yb_{0.2}Tm_{0.02}F_4$, NIR-to-green UCNPs of $NaY_{0.78}Yb_{0.2}Er_{0.02}F_4$, and NIR-to-red UCNPs of $NaY_{0.78}Yb_{0.3}Er_{0.01}F_4$: three colors of UCNPs were clearly differentiated after spectral unmixing. Adapted from Cheng et al. with permission [32]

expensive high-power, femtosecond pulsed laser [39] and can be excited by continuous-wave (CW) diode lasers operating at low power (1 W cm^{-2}) [40] – this can facilitate fast imaging using a wide-field microscopy. In summary, NIR light-absorbing, real-time imaging UCNPs offer broad applications as real-time, long-term tracker for cell imaging [41] as well as sensitive contrast agent with high-contrast resolutions for whole-body optical imaging [42].

However, one limitation for the conventional Yb^{3+}-doped UCNPs [42] is the heating effect that is generated by water molecules under 980 nm laser excitation. Therefore, in recent years, considerable effort has been made to control the excitation wavelength because this is where water has lower absorption. In one study, Andersson-Engels and coworkers utilized $NaYbF_4$:Tm;Er and $NaYbF_4$:Tm;Ho nanoparticles under 915 nm excitation [43]. Nd^{3+} was introduced to the conventional Yb^{3+}-doped UCNPs as a new sensitizer to be excited at 800 nm [44]. These nanoparticles showed a larger absorption cross section and deeper image penetration depth than those with 980 nm excitation. It is also very desirable to construct UCNPs with both excitation and emission in the NIR range (NIR_{in}-NIR_{out} UCNPs) to further improve the imaging contrast. Therefore, Prasad and coworkers reported core/shell (α-$NaYbF_4$:Tm^{3+})/CaF_2 nanoparticles with excitation at ~980 nm and PL emission at 800 nm. In this study, the authors found that these nanoparticles allowed tenfold higher signal-to-background ratio (SBR) than previously reported UCNPs for in vivo imaging enabling deep-penetration imaging through 3.2 cm pork tissue [45].

4 Carbon Dots, Porous Silicon Nanoparticles, and Au Nanoclusters

Quantum-sized carbon- and silicon-based optical imaging probes have recently been developed as benign alternatives to conventional semiconductor QDs. Although these nanomaterials lack a classical bandgap structures of QDs, they can achieve fluorescence emission from the surface passivation-created defects (surface energy traps [46]). Here, surface passivation stabilize the surface defects and facilitate more effective radiative recombination of surface-confined excitons [47, 48].

In a pioneering study, Sun et al. [49] prepared 5 nm carbon dots (C-Dots) via laser ablation of graphite powder and cement. The surface of the C-Dots was then effectively passivated with organic moieties (diamine-terminated oligomeric PEG; PEG1500N) resulting in strong photoluminescence with no blinking as well as tunable emissions from visible to NIR under the argon ion laser excitation (458 nm) [49]. They also found that these C-Dots capped with poly-(propionylethylenimine-co-ethylenimine) (PEI-EI) were two-photon active with pulsed laser excitation in the NIR region (800 nm). The two-photon absorption cross sections of the C-Dots were comparable with the best-performing semiconductor QDs. Next, upon incubation to the human breast cancer cells, the authors demonstrated the potential of C-Dots for cell imaging with two-photon luminescence microscopy [50]. Indeed, recent studies have included the careful selection of carbon source as well as surface modifier for C-dots with enhanced photoluminescence [51] resulting in C-Dots with a quantum yield 2–2.5-fold that of CdSe/ZnS QDs [52, 53]. In particular, C-dots can offer significant advantages in terms of potential translatability and applicability because they exhibit very low toxicity and great availability in scale-up production through various inexpensive renewable resources [54–56].

Quantum-sized, porous silicon nanoparticles prepared by electrochemical etching of silicon wafer have subsequent luminescence arising in the 600–1,000 nm range from a combination of a quantum confinement effect and surface defect localized at the Si-SiO_2 interface [59]. Porous silicon has become one of the most powerful nanomaterials for optical in vivo imaging with respect to its adaptability, biodegradability, and capability for background-free imaging. Porous silicon nanoparticles are highly adaptable to load large volumes of various drugs (e.g., small molecules, nucleic acid, protein drugs) or additional imaging agents (e.g., Gd complex, magnetic particles) within their size-tunable pores [60]. Porous silicon nanoparticles can biodegrade into benign orthosilicic acid ($Si(OH)_4$; the element silicon itself is an endogenous substance (Fig. 6a) followed by excretion as urine [57]. The intravenously administered porous silicon nanoparticles were completely degraded in 4 weeks without any measurable in vivo toxicity over 1–12 months (Fig. 6b, c). In addition, porous silicon nanoparticles enable autofluorescence-free and time-gated fluorescence (TGF) imaging of tissue in vivo because they can provide the unusual long emission lifetime (5–13 ms) compared to nanosecond lifetimes of typical fluorescent organic molecules or QDs [58]. Thus, in time-gated fluorescence (TGF) imaging (images are captured at a delayed time after excitation), the signal could be effectively eliminated from the shorter-lived emission signals.

Figure 6d shows a nude mouse injected subcutaneously with PEGylated luminescent porous silicon nanoparticles (PEG-LPSiNPs). Here, the TGF imaging revealed intensive signals in the PEG-LPSiNP injection (T1) with negligible signals from the Cy3.5 injection (T2) or from the background tissue autofluorescence (T3). The fluorescent signals appeared in all three spots under the continuous-wave (CW) imaging (steady-state conditions; no time gating). Therefore, as an alternative to cytotoxic QDs, there has been much progress in the use of porous silicon nanoparticles for multimodal bio-imaging [61] and targeted therapy [62]. However, considerable future research still remains to overcome the limitations of luminescent porous silicon nanoparticles such as low quantum yield and difficulty in size-controlled mass production.

Gold nanoparticles (10–100 nm in size) are an efficient light scattering and absorbing center known to generate visible luminescence and heat upon excitation at λ_{SPR} based on its surface resonant oscillation of electrons [63]. In contrast, gold nanoclusters (AuNCs) consisting of several tens of atoms (<2 nm in size) have molecular-like, discrete electronic states due to the spatial confinement of free electrons [64]. Therefore, gold nanoclusters can feature all unique optical properties that semiconductor QDs have. In the past decade, there have been many investigations of synthetic methods for fine control of the number of gold atoms in a cluster.

Generally, gold nanoclusters (AuNCs) are synthesized by the chemical reduction of gold precursors in the presence of strong stabilizer. Owing to a strong affinity of thiols to the Au surface, thiol-containing small molecules (e.g., glutathione [66, 67], dodecanethiol [68]) have been extensively used as a stabilizing template for gold clusters [69]. As a simple, green synthetic route, macromolecules (e.g., protein [70], DNA [71], dendrimer [64]) have also been also employed as a surface template to direct the formation of Au clusters with a substantial quantum yield (e.g., bovine

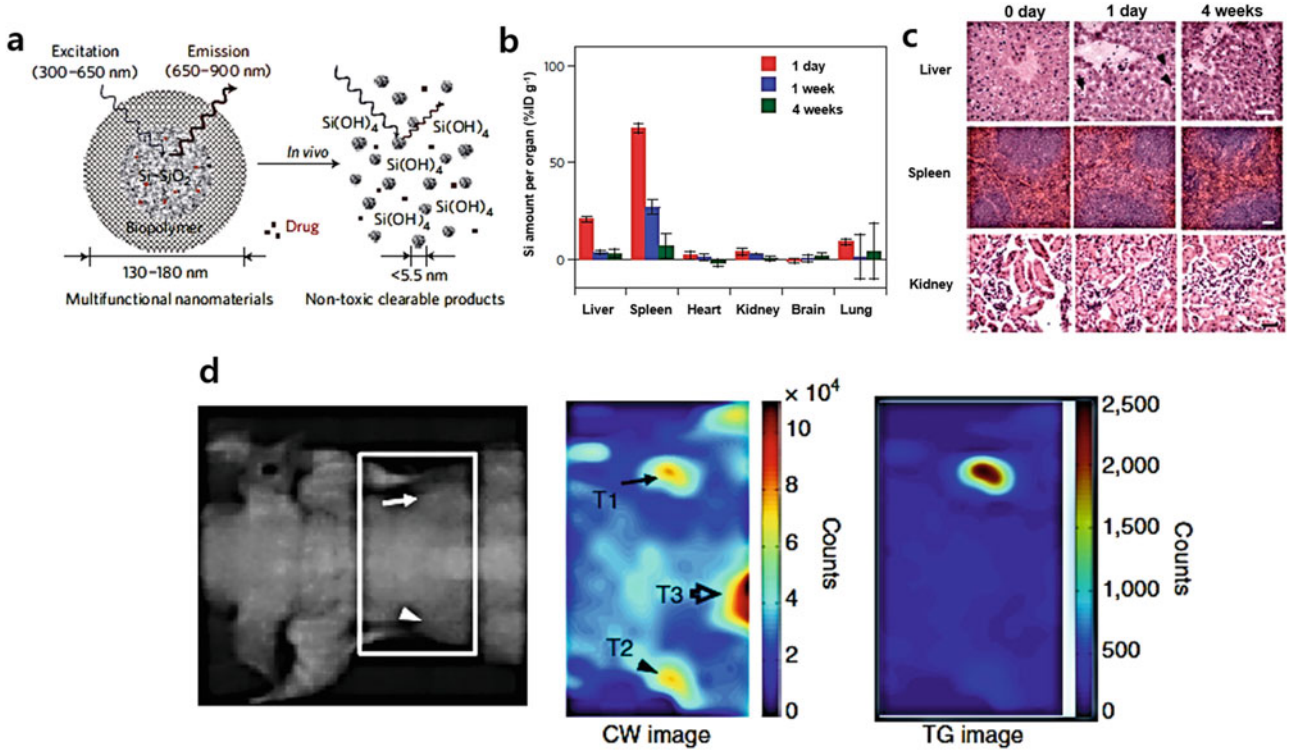

Fig. 6 (**a**) Schematic illustrations describing the structure and in vivo biodegradation process of luminescent porous silicon nanoparticles (LPSiNPs). (**b**) Biodistribution and biodegradation of LPSiNPs for 1 month in the mouse with intravenously injection of LPSiNPs (20 mg/kg). (**c**) Histopathological analysis of the tissue sections from the organs (kidneys, liver, and spleen) in the mouse with LPSiNPs. Adapted from Park et al. [57] with permission. (**d**) Continuous-wave (CW) and time-gated fluorescence (TGF) imaging of LPSiNPs from the mouse with subcutaneous injection of LPSiNPs; PEG-LPSiNP injection (T1), Cy3.5 injection (T2), and background tissue autofluorescence (T3). Adapted from Gu et al. [58] with permission

serum albumin (BSA)-protected Au_{25}: ~6% QY). In particular, Jin and coworkers reported that surface ligands with many electron-rich atoms (e.g., N, O) or groups (e.g., –COOH, NH_2) can promote the fluorescence of gold clusters either by charge transfer through the Au-S bonds or by direct donation of delocalized electrons to the metal core [72].

Besides the aforementioned route ("Au atoms to Au clusters"), there is alternative route to prepare gold nanoclusters by etching the surface atoms of gold nanoparticles by appropriate ligands. For example, gold nanoclusters capped with dihydrolipoic acid (AuNC@DHLA) with a quantum yield of around 1–3% were synthesized. Upon etching and ligand exchanging with DHLA, the original gold nanoparticles stabilized with didodecyldimethylammonium bromide (AuNP@DDAB) (~5.6 nm) becoming smaller. These water-soluble gold clusters (<2 nm) have red photoluminescence under UV excitation (Fig. 7) [65]. As for the etchant, hyperbranched polymers were also applied to induce the gold nanoclusters with a quantum yield of 10–20% [73].

The photoluminescence quantum yield of gold clusters is still lower than the organic fluorophore or QDs. However, they are ultra-small and exceptionally biocompatible nanoparticles with reduced photo-blinking behavior. Therefore, in a recent study by Hung-I Yeh and coworkers, gold nanoclusters have been exploited as a fluorescent biomarker for live cell tracking in vivo using hind-limb ischemic mice. Here, the Au clusters showed nonspecific incorporation into living endothelial progenitor cells (EPC) with no acute cytotoxicity. Thus, after intramuscular injection of Au-labelled human EPC, the cells preserved angiogenic potentials and exhibited detectable fluorescent signals for up to 21 days [74].

In another example to demonstrate utility in the early diagnosis for cancers, mice with MDA-MB-45 and HeLa tumor xenografts were treated with ultra-small NIR-emitting Au nanoclusters (BSA-capped gold cluster). These clusters accumulated in the tumors and showed tumor-to-background signals of ~15 for 6 h postinjection [75]. Most importantly, gold nanocluster can also have good clearance after administration through the kidneys due to its renal cutoff size (<5.5 nm) (this is below the kidney filtration threshold (7–8 nm). Zheng et al. recently demonstrated renal-clearable, NIR-emitting, gold nanoclusters (zwitterionic thiolated gold clusters) enabling the real-time fluorescence visualization of kidney clearance kinetics with a 50-fold increase of contrast to conventional organic dyes. This is a useful and sensitive tool for early staging of kidney dysfunctions [76].

5 Nano-diamond and Persistent Luminescent Nanoparticles

Nano-diamonds (ND) mainly consist of sp^3 carbon and are optically transparent, biologically inert, and chemically modifiable. When these materials are irradiated by high-energy ion beam, followed by thermal annealing, they can be immobilized with a high concentration of point defects (e.g., nitrogen-vacancy (NV^-) complexes) in the sp^3 carbon lattice (Fig. 8a) [77]. These point defects can form a photoluminescent

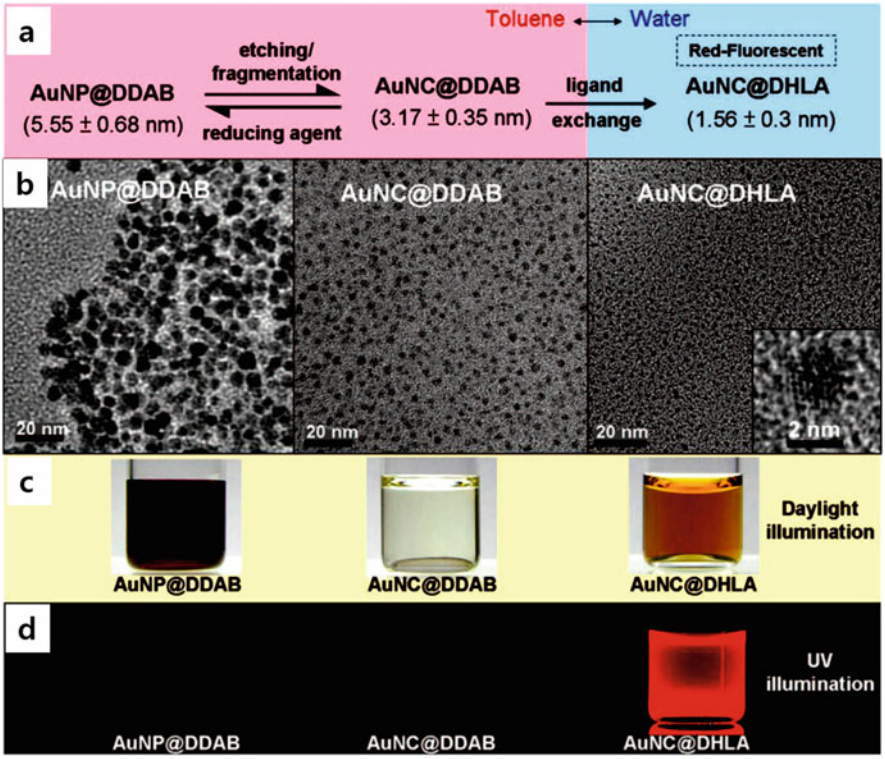

Fig. 7 Strategy to synthesize water-soluble fluorescent Au nanoclusters (AuNC) via ligand-assisted etching of gold nanoparticles (AuNP). (**a**, **b**) Gold nanoparticles stabilized with didodecyldimethylammonium bromide (AuNP@DDAB) (5.6 nm) are etched by the addition of Au precursors ($HAuCl_4$ or $AuCl_3$) to smaller nanoclusters (AuNC@DDAB) (3.2 nm). They become water-soluble upon ligand exchange with dihydrolipoic acid (DHLA). (**c**, **d**) Only the AuNC@DHLA solution (<2 nm) shows the red photoluminescence under UV excitation. Adapted from Lin et al. [65] with permission

center to produce a broad light absorption at 550 nm and emission at 700 nm. There are many unique optical properties that are not shown in conventional florescence dyes. This fluorescent nanoparticle is exceptionally photostable with no photo-bleaching under continuous high intensity of light excitation [78, 79]. The fluorescence lifetime is much longer (five- to sevenfold) than that of biological tissue, which can facilitate background, autofluorescence-free imaging (Fig. 8b) [80]. Therefore, nano-diamonds have been extensively exploited as cellular biomarkers for long-term in vitro and in vivo imaging applications [81].

Nano-diamonds can be used with super-resolution microscopy to track single molecules or image subcellular structures on the nanometer scale. In a pioneering study, stimulated emission depletion (STED) microscopy was used to overcome the diffraction limit of light: Chang et al. showed that single fluorescent nano-diamond (30 nm BSA coated nano-diamonds) can be distinguished in cells with a sub-diffraction spatial resolution of approximately 40 nm [83]. Typical confocal

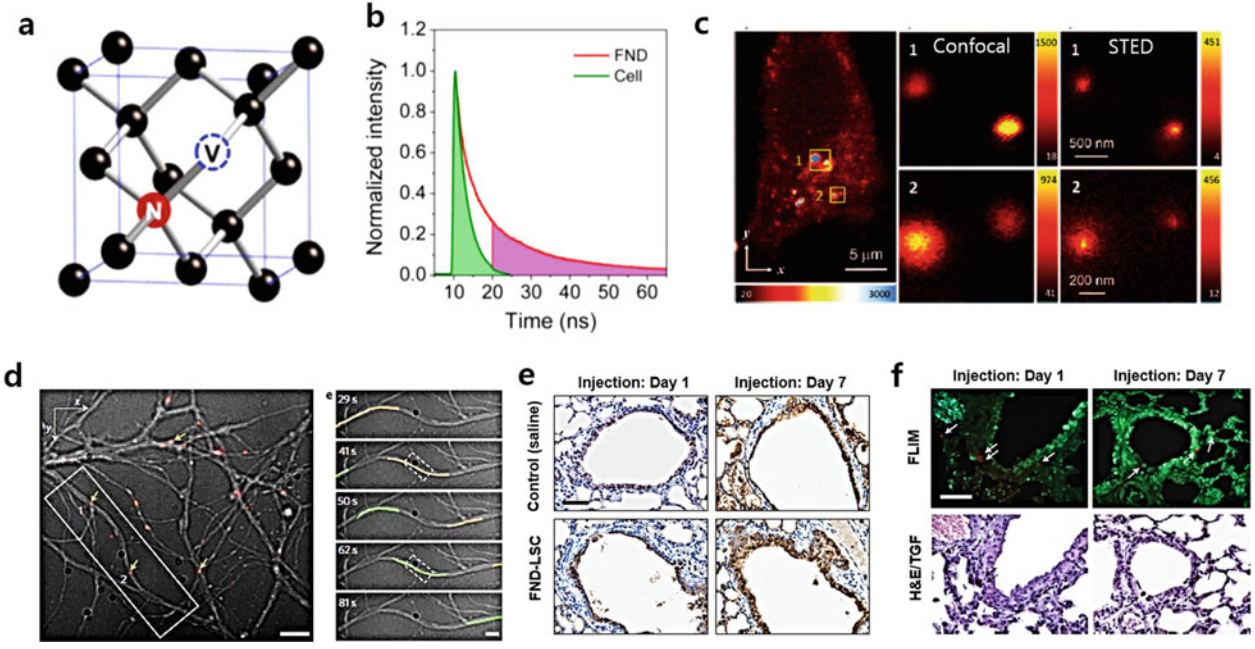

Fig. 8 (**a**) Structure of fluorescent nano-diamond (ND). (**b**) Comparison between the fluorescence lifetimes of NDs in water (red) and endogenous fluorophores in cells (green). The background-free detection can be facilitated by time-gated imaging at 10 ns. Adapted from Hsiao et al. [82] with permission. (**c**) Confocal and STED imaging of HeLa cells labelled with BSA-conjugated NDs by electroporation. Adapted from Tzeng et al. [83] with permission. (**d**) Intraneuronal transport monitoring by ND tracking assay. Bright-field (BF) images of the neuronal branches were merged with the fluorescence (FL) channel images, showing the movement of NDs within dendrites (yellow arrows). More specifically, the two ND-containing endosomes moved toward the cell soma (labelled 1 and 2 on left images). The movement of two NDs was also determined by particle tracking (1 in yellow; 2 in green) with a persistence of 10 s at different time points (right images). Adapted from Haziza et al. [84] with permission. (**e**, **f**) ND-labelled lung stem cells (LSCs) in lung-injured mice. (**e**) Immunostaining analysis indicated that the bronchiolar epithelium of the mice injected with ND-labelled LSCs was observed with repopulation of $CCSP^{+}$ cells (brown) at day 7. These materials had a higher regenerative capacity with rapid restoration of lung epithelium. (**f**) Representative fluorescence lifetime imaging microscopy (FLIM; top) and TGF/H&E staining images (bottom) from the same lung tissue sections show that ND-labelled LSCs (white and black arrows, respectively) were located to the terminal bronchioles of the lungs. Adapted from Wu et al. [85] with permission

microscopy cannot resolve whether the particles are internalized or well-dispersed/aggregated due to the diffraction-limited image resolutions; however, STED microscopy images successfully identified the individual nano-diamond in the cytoplasm (Fig. 8c). This not only identifies the cellular process, but the nano-diamonds (ND) can also provide further information on cellular function in disease diagnostics.

For example, a ND-based tracking assay was recently developed to observe intraneuronal transport abnormalities with a spatial resolution of 12 nm and a temporal resolution of 50 ms. [84] Figure 8d shows that when NDs were internalized to primary hippocampal neuron cells, they could be tracked in real time using pseudo-total internal reflection fluorescence video microscopy (pseudo-TIRF). Here, the overlay images (BF and FL) can display the precise localization of ND overall trajectories and movement throughout the microtubules. Therefore, using the primary hippocampal neurons treated with amyloid-β_{1-42} peptide, the authors successfully found the decreased transport velocities of ND – this indicates abnormal intraneuronal transport in Alzheimer's disease.

In addition, exceptionally biocompatible and photostable, fluorescent nano-diamonds (NDs) can allow the monitoring of the long-term fate of stem cells in vivo. In a recent study, Wu et al. delivered ND-labelled lung stem cells (LSCs) by intravenous injection and observed their engraftment and regenerative capabilities with single-cell resolution through time-gated fluorescence (TGF) imaging and immunostaining [85]. Here, the authors first demonstrated that fluorescent nano-diamond labelling did not impair the lung stem cells' self-renewal and differentiation into type I and type II pneumocytes. Since the regenerative capacity of LSCs could be activated after tissue injury, using naphthalene-injured mice, they found that the transplanted LSCs migrated and integrated into bronchiolar epithelium of the murine lungs to successfully regenerate the damaged epithelial linings (Fig. 8e, f). However, this still required a sufficiently large number of photoluminescent nitrogen-vacancy (NV) centers to increase the optical cross sections for fluorescent nano-diamonds. Unfortunately, the use of nano-diamonds is still limited in multiplexed imaging.

Persistent luminescent nanoparticles store energy by pre-charging with UV excitations and gradually releasing the photon energies. The emission is steady for several hours or days with no additional input of energies. Therefore, there is no need for external continuous excitation – this approach can lead to sensitive imaging without background autofluorescence [86]. Scherman and coworkers prepared silicate crystals doped with Eu^{2+}, Dy^{3+}, and Mn^{2+} ions via a sol-gel process followed by successive high temperature calcination. These nanoparticles possess energy traps where the excited lights can be non-radiatively captured to induce persistent luminescence. They found that these particles can successfully emit light at 700 nm with a long-lasting luminescence for more than 1 h upon excitation ex vivo by UV light (6 W UV lamp, <5 min). The authors have also shown that when such particles were pre-excited and implanted to BALB/c mice, the sensitive fluorescent signals could be easily detected in real time using a photon counting system [87]. However, these probes could only be excited ex vivo by UV lights, which prevent long-term imaging in vivo.

One possible strategy is to develop a new class of nanoparticles whose persistent luminescence can be renewable in vivo through living tissues. In 2014, Scherman and coworkers synthesized 80 nm Cr^{3+}-doped zinc gallium oxide (ZGO) nanoparticles and observed whether the persistent luminescence can be activated in situ whenever required with no time limit [88]. The particles have several excitation peaks with one within the tissue transparency window (rectangle with hatching) (Fig. 9a) resulting in a NIR = persistent luminescence by a low-powered, orange/red light-emitting diode (LED) illumination (Fig. 9b). Simple illumination through living tissues with visible light was sufficient to activate persistent luminescence of ZGO-OH nanoparticles – intense signals were shown from the reticuloendothelial system (RES) organs (e.g., liver) within the deep tissues (Fig. 9c). As for the applications, the authors assessed the ability of as-prepared nanoparticles for in vivo imaging for vasculature imaging, tumor detection, and longitudinal cell tracking in a mouse model. With additional surface coating (amino, carboxy, or PEG), these nanoparticles become very colloidal stable and long circulating after intravenous injections; therefore, they successfully showed these persistent luminescent nanoparticles could be used to image the tumors via passive targeting (PEG coating) (Fig. 9d). Furthermore, the amino-coated probes could label macrophage cells for visualization in vivo (Fig. 9e). Additionally, the pathway of nanoparticles could be detected in the gastrointestinal tract after oral administration.

6 Dye-Doped Inorganic Nanoparticles (Calcium Phosphate, Silica)

Biologically resorbable and optically transparent inorganic materials (e.g., calcium phosphate, silica) can encapsulate dyes into their well-defined, large-surfaced, nanoporous structures and are an effective way of enhancing the photostability of organic fluorophores. These dye-doped nanoparticles can minimize their fluorescence quenching or enzymatic degradation. However, to achieve high sensitivity and specificity of the fluorescence signals, it is critically important to select appropriate dye molecules and increase the loading capacity with no change in particle size and morphology.

Calcium phosphate is found in endogenous biominerals including bone and teeth. It can easily form colloidally stable nanoparticles by reverse microemulsion synthesis [90]. In the first such study, Adir et al. successfully synthesized and investigated the potentials of NIR-emitting calcium phosphate nanoparticles (CPNPs) by entrapping indocyanine green (ICG) [91]. In this study, they prepared the well-dispersed, ICG dye-doped CPNP (ICG-CPNP) (Fig. 10a), and found that the photostability is 500% longer relative to the free dye (Fig. 10b). PEGylated ICG dye-doped CPNPs exhibited much longer blood circulation than free ICG (free ICG in physiological environments experience the rapid aggregation and clearance from the body) and passively accumulated to xenografted breast

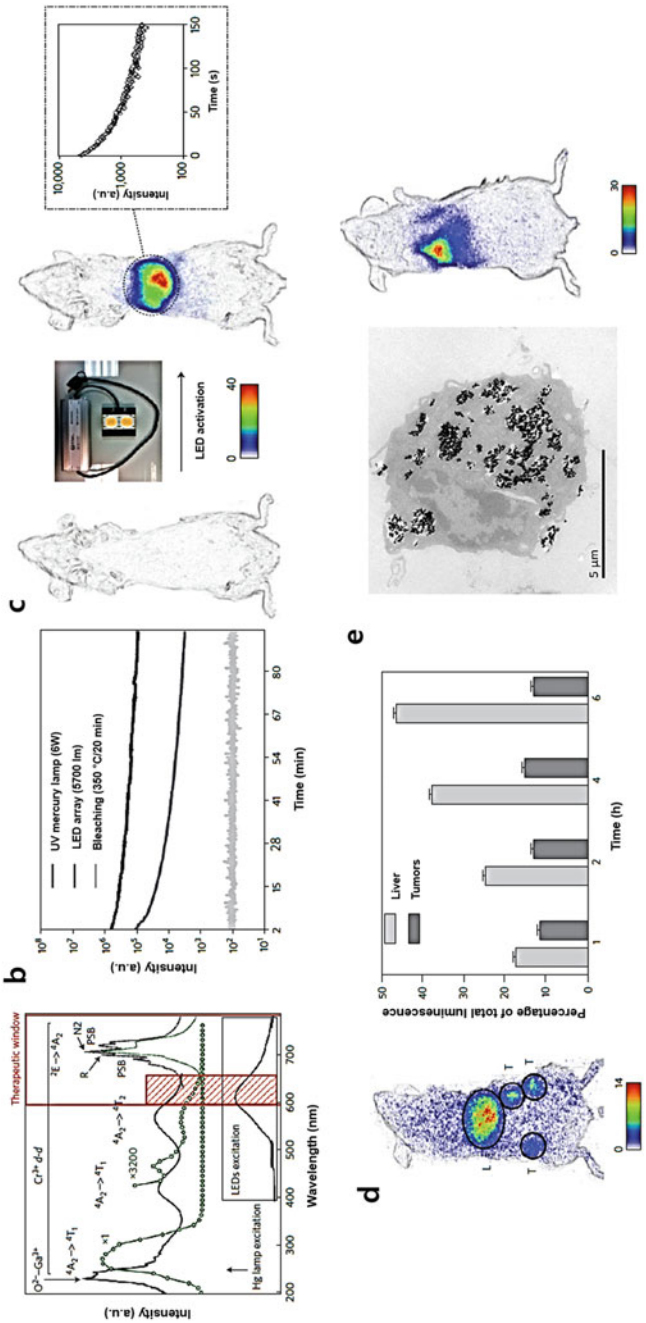

Fig. 9 (**a**) PL excitation (black line) and emission (red line) spectra of Cr^{3+}-doped zinc gallium oxide (ZGO). (**b**) Persistent luminescence decay curves from Cr^{3+}-doped ZGO obtained at 2 min excitations either by UV light or LED array source. (**c**) The detection of persistent luminescence nanoparticles after in vivo activation. Here, the animals intravenously injected with ZGO-OH were irradiated with an orange/red LED source for 2 min, and images were acquired for 3 min with the photon counting system. The inset shows a persistent luminescence decay curve from the liver. (**d**) The biodistribution of persistent luminescence nanoparticles in a tumor-bearing mouse. Images were acquired 4 h after the injection of ZGO-PEG nanoparticles following visible activation of persistent luminescence with orange/red LED illuminations, which clearly showed the enhanced tumor uptakes as well as the accumulation kinetics. (**e**) ZGO-NH_2 persistent luminescence NPs used for labelling of RAW cells in vitro (left images) and cells tracking in vivo (right images). Adapted from Maldiney et al. [88] with permission

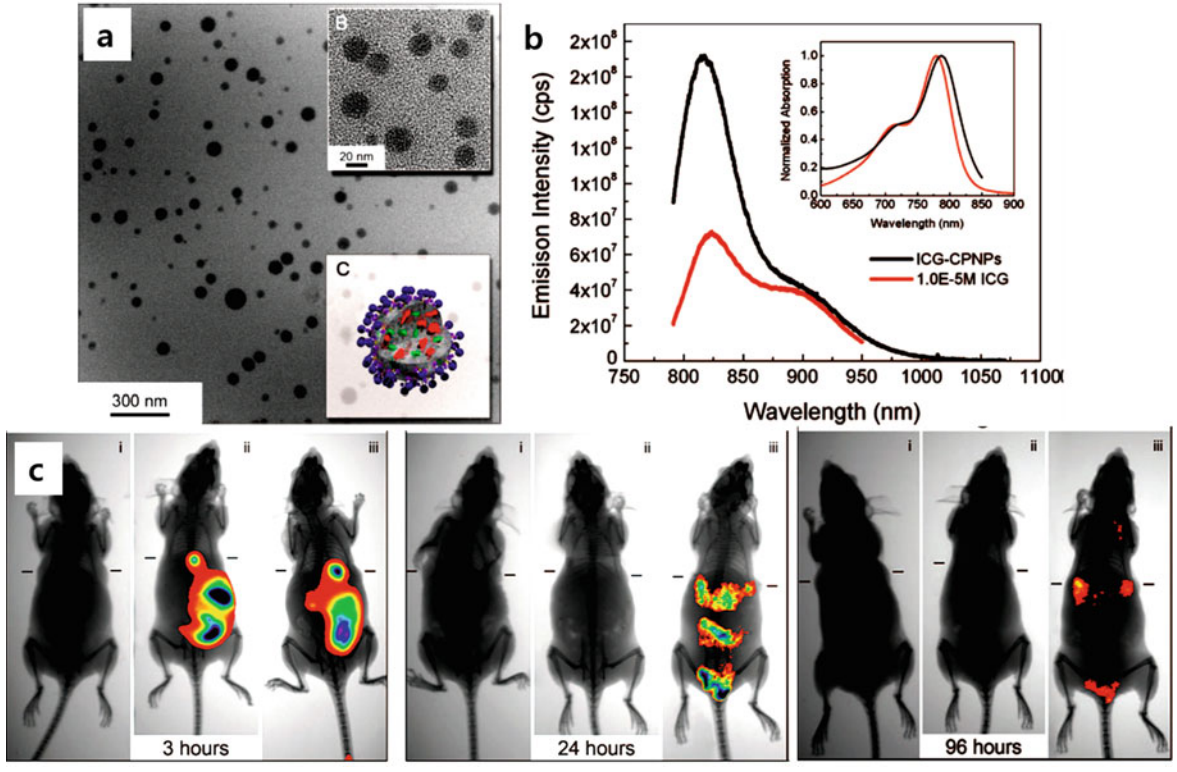

Fig. 10 (**a**) TEM images and schematics of ICG dye-encapsulating calcium phosphate nanoparticles (ICG-CPNP). (**b**) Fluorescence emission spectra of free ICG (red) and ICG-CPNPs (black). The inset displays the absorption spectra. (**c**) NIR images (Ex. 755 nm, Em. 830 nm) acquired at various time points (3, 24, and 96 h) to track the fluorescence signals from the carboxylate-terminated CPNPs without ICG (i), free ICG (ii), and PEGylated ICG-CPNPs (iii). Nanoparticles were systematically delivered via tail vein injections to nude mice bearing human breast adenocarcinoma tumors. No fluorescence signal was detected from the free ICG (ii) at 24 h postinjection, while the PEG-ICG-CPNP sample (iii) exhibited significant fluorescent signal even after 96 h postinjection. Adapted from Altinoglu et al. [89] with permission

adenocarcinoma – the fluorescence signals lasted >96 h post-systemic injection (Fig. 10c) [89]. In the next study, they further modified these nanoparticles with active targeting moieties of human holotransferrin, anti-CD71 antibody, and short gastrin peptides. They validated the systemic in vivo targeting to breast and pancreatic cancer lesions, respectively [92].

Elemental silicon itself is an endogenous substance, and it has been used extensively to fabricate (porous) silica nanostructures with a well-defined size and morphology via simple sol-gel synthesis [61]. Fluorescent dye molecules can be physically entrapped into the porous nano-channels of silica matrix [93]. The fluorescence remained unquenched up to very high concentrations of dye molecules. In 2011, Igor Sokolov and coworkers described small silica particles (ranging from 20 to 50 nm) with a high dye loading capacity (0.8–9.3 mg rhodamin6G (R6G dye) per g particles) using several organotriethoxysilanes (MTMS, ETES, or PTES) for the co-precursors of silica. They found the relative brightness from the fluorescent dye-doped silica particles has 30–770 times a QY that is higher than non-dimerized R6G dye molecules and 1.5–39 times of CdSe/ZnS QDs [94]. Importantly, some fluorescent silica nanoparticles (e.g., Cornell dots; core-shell type of dye-rich core surrounded by denser silica network [95]) have exceptional biocompatibility and were approved for the first human clinical trials for cancer diagnosis [96]. These 6–7-nm-sized Cornell dots (containing the dye, Cy5) attached with cyclic arginine-glycine-aspartic acid (cRGDY) peptides that target integrin $\alpha_v\beta_3$ and ^{124}I radiotracer for positron emission tomography (PET) imaging have been administered to five patients with metastatic melanoma [97]. Their favorable PK/biodistribution profiles and safety assessment showed the potential for clinical translation of these cancer-targeted, renally excreted inorganic nanoparticles. In addition to the visible light dyes (R6G, Cy5, FITC), NIR-emitting ICG dyes have also been encapsulated to the nanostructures of dense silica [98], mesoporous silica [99, 100], and porous silicon [101] and successfully utilized as for NIR optical imaging as well as for photoacoustic imaging in recent years.

7 Conclusion

Innovative nanotechnology has enabled the development of several new inorganic fluorescent nanomaterials to realize sensitive, high-resolution, optical imaging. QDs have been extensively investigated to overcome the limitations of organic fluorescent dyes with its superior photo-physical properties such as size-tunable photoluminescence, narrow emission, and low photo-bleaching. Chemical modifications with additional organic layers (e.g., PEG, targeting ligands) on QD surfaces can improve the blood circulation and diffusion of QD for sentinel lymph node (SLN) mapping, vasculature imaging, or more complex targeted imaging of tumor cells in vivo. Subsequently, further research has focused more on NIR-emitting QDs (NIR-I or NIR-II) (e.g., core/shell CdSe/CdTe QDs, Ag_2S QDs) to improve the imaging sensitivity of the conventional, visible luminescent QDs.

Based on the anti-Stokes shift luminescence mechanism and NIR light absorption, transition metal-doped semiconductor nanoparticles and lanthanide ion-doped nanoparticles (upconversion nanoparticles) offer high-resolution whole-body imaging with deep tissue penetrations (up to several ~cm). Interestingly, persistent luminescent nanoparticles were found to be excited (either by ex vivo or in situ) with no input energy during in vivo imaging resulting in minimal tissue autofluorescence. Nano-diamonds can also facilitate background-free imaging by time gating due to the longer emission lifetime than that of biological tissue. Additionally, some optically transparent inorganic nanomaterials (e.g., calcium phosphate, silica) have been used as a host matrix to encapsulate organic fluorophores to improve their physiological stability for longer in vivo imaging despite the fact they do not possess the intrinsic luminescence.

However, despite all of these considerable advances in inorganic fluorescent nanomaterials, there are still several challenging issues that need to be resolved. The unique optical properties of inorganic nanomaterials are generally dependent on their size, shape, and compositions, and thus large-scale synthesis is needed to maintain the uniformity of the nanoparticles between batches. In addition, due to the metal-induced toxicity, the potential safety issues of inorganic nanoparticles should be addressed for further clinical trials. An effective strategy is to make nanomaterials biodegradable into nontoxic byproducts (e.g., porous silicon nanoparticles) or nanomaterials that are solely composed of benign elements (e.g., silicon, silver, gold, calcium phosphate, carbon analogue) to exert less systemic toxicities. Renal clearance through urine can minimize the exposure of body to nanomaterials; likewise Au nanoclusters (<2 nm) or QDs with renal cutoff size (<5.5 nm) were found to be easily filtered by the kidneys. However, these changes can lead to trade-offs for the intended applications, and it is critical to tailor nanomaterials to balance between safety concerns, scale-up synthesis, and sensitivity/resolution that needs to fulfill the specific medical goal.

Compliance with Ethical Standards

Funding: This work was supported by the NIH R00 117048 and HL 137187.

Conflict of Interest: The authors declare that they have no conflicts of interest.

Ethical approval: This chapter does not contain any studies with human participants or animals performed by any of the authors.

References

1. Alivisatos AP (1996) Semiconductor clusters, nanocrystals, and quantum dots. Science 271:933–937
2. Jaiswal JK, Mattoussi H, Mauro JM, Simon SM (2003) Long-term multiple color imaging of live cells using quantum dot bioconjugates. Nat Biotechnol 21:47–51
3. Bruchez M, Moronne M, Gin P, Weiss S, Alivisatos AP (1998) Semiconductor nanocrystals as fluorescent biological labels. Science 281:2013–2016

4. Smith AM, Dave S, Nie SM, True L, Gao XH (2006) Multicolor quantum dots for molecular diagnostics of cancer. Expert Rev Mol Diagn 6:231–244
5. Gao X, Cui Y, Levenson RM, Chung LW, Nie S (2004) In vivo cancer targeting and imaging with semiconductor quantum dots. Nat Biotechnol 22:969–976
6. Maeda H, Wu J, Sawa T, Matsumura Y, Hori K (2000) Tumor vascular permeability and the EPR effect in macromolecular therapeutics: a review. J Control Release 65:271–284
7. Iyer AK, Khaled G, Fang J, Maeda H (2006) Exploiting the enhanced permeability and retention effect for tumor targeting. Drug Discov Today 11:812–818
8. Ruoslahti E, Bhatia SN, Sailor MJ (2010) Targeting of drugs and nanoparticles to tumors. J Cell Biol 188:759–768
9. Duman FD, Erkisa M, Khodadust R, Ari F, Ulukaya E, Acar HY (2017) Folic acid-conjugated cationic Ag2S quantum dots for optical imaging and selective doxorubicin delivery to HeLa cells. Nanomedicine 12:2319–2333
10. Gao J, Chen K, Luong R, Bouley DM, Mao H, Qiao T, Gambhir SS, Cheng Z (2012) A novel clinically translatable fluorescent nanoparticle for targeted molecular imaging of tumors in living subjects. Nano Lett 12:281–286
11. Cai WB, Shin DW, Chen K, Gheysens O, Cao QZ, Wang SX, Gambhir SS, Chen XY (2006) Peptide-labeled near-infrared quantum dots for imaging tumor vasculature in living subjects. Nano Lett 6:669–676
12. Jokerst JV, Raamanathan A, Christodoulides N, Floriano PN, Pollard AA, Simmons GW, Wong J, Gage C, Furmaga WB, Redding SW, McDevitt JT (2009) Nano-bio-chips for high performance multiplexed protein detection: determinations of cancer biomarkers in serum and saliva using quantum dot bioconjugate labels. Biosens Bioelectron 24:3622–3629
13. Kim S, Lim YT, Soltesz EG, De Grand AM, Lee J, Nakayama A, Parker JA, Mihaljevic T, Laurence RG, Dor DM, Cohn LH, Bawendi MG, Frangioni JV (2004) Near-infrared fluorescent type II quantum dots for sentinel lymph node mapping. Nat Biotechnol 22:93–97
14. Hilderbrand SA, Weissleder R (2010) Near-infrared fluorescence: application to in vivo molecular imaging. Curr Opin Chem Biol 14:71–79
15. Hong GS, Antaris AL, Dai HJ (2017) Near-infrared fluorophores for biomedical imaging. Nat Biomed Eng 1
16. Hong G, Lee JC, Robinson JT, Raaz U, Xie L, Huang NF, Cooke JP, Dai H (2012) Multifunctional in vivo vascular imaging using near-infrared II fluorescence. Nat Med 18:1841–1846
17. Smith AM, Mancini MC, Nie SM (2009) BIOIMAGING second window for in vivo imaging. Nat Nanotechnol 4:710–711
18. Hong GS, Diao S, Chang JL, Antaris AL, Chen CX, Zhang B, Zhao S, Atochin DN, Huang PL, Andreasson KI, Kuo CJ, Dai HJ (2014) Through-skull fluorescence imaging of the brain in a new near-infrared window. Nat Photonics 8:723–730
19. Zhang Y, Hong GS, Zhang YJ, Chen GC, Li F, Dai HJ, Wang QB (2012) Ag2S quantum dot: a bright and biocompatible fluorescent nanoprobe in the second near-infrared window. ACS Nano 6:3695–3702
20. Won N, Jeong S, Kim K, Kwag J, Park J, Kim SG, Kim S (2012) Imaging depths of near-infrared quantum dots in first and second optical windows. Mol Imaging 11:338–352
21. Li CY, Zhang YJ, Wang M, Zhang Y, Chen GC, Li L, Wu DM, Wang QB (2014) In vivo real-time visualization of tissue blood flow and angiogenesis using Ag2S quantum dots in the NIR-II window. Biomaterials 35:393–400
22. Bruns OT, Bischof TS, Harris DK, Franke D, Shi Y, Riedemann L, Bartelt A, Jaworski FB, Carr JA, Rowlands CJ, Wilson MWB, Chen O, Wei H, Hwang GW, Montana DM, Coropceanu I, Achorn OB, Kloepper J, Heeren J, So PTC, Fukumura D, Jensen KF, Jain RK, Bawendi MG (2017) Next-generation in vivo optical imaging with short-wave infrared quantum dots. Nat Biomed Eng 1
23. Derfus AM, Chan WCW, Bhatia SN (2004) Probing the cytotoxicity of semiconductor quantum dots. Nano Lett 4:11–18

24. Xu G, Zeng S, Zhang B, Swihart MT, Yong KT, Prasad PN (2016) New generation cadmium-free quantum dots for biophotonics and nanomedicine. Chem Rev 116:12234–12327
25. Dabbousi BO, RodriguezViejo J, Mikulec FV, Heine JR, Mattoussi H, Ober R, Jensen KF, Bawendi MG (1997) (CdSe)ZnS core-shell quantum dots: synthesis and characterization of a size series of highly luminescent nanocrystallites. J Phys Chem B 101:9463–9475
26. Choi HS, Liu W, Misra P, Tanaka E, Zimmer JP, Ipe BI, Bawendi MG, Frangioni JV (2007) Renal clearance of quantum dots. Nat Biotechnol 25:1165–1170
27. Zhu XJ, Su QQ, Feng W, Li FY (2017) Anti-stokes shift luminescent materials for bio-applications. Chem Soc Rev 46:1025–1039
28. Zagorovsky K, Chan WCW (2013) BIOIMAGING illuminating the deep. Nat Mater 12:285–287
29. Yu JH, Kwon SH, Petrasek Z, Park OK, Jun SW, Shin K, Choi M, Park YI, Park K, Na HB, Lee N, Lee DW, Kim JH, Schwille P, Hyeon T (2013) High-resolution three-photon biomedical imaging using doped ZnS nanocrystals. Nat Mater 12:359–366
30. Subha R, Nalla V, Yu JH, Jun SW, Shin K, Hyeon T, Vijayan C, Ji W (2013) Efficient photoluminescence of Mn2+-doped ZnS quantum dots excited by two-photon absorption in near-infrared window II. J Phys Chem C 117:20905–20911
31. Chatteriee DK, Rufalhah AJ, Zhang Y (2008) Upconversion fluorescence imaging of cells and small animals using lanthanide doped nanocrystals. Biomaterials 29:937–943
32. Cheng L, Yang K, Zhang S, Shao M, Lee S, Liu Z (2010) Highly-sensitive multiplexed in vivo imaging using pegylated upconversion nanoparticles. Nano Res 3:722–732
33. Chen G, Qiu H, Prasad PN, Chen X (2014) Upconversion nanoparticles: design, nanochemistry, and applications in theranostics. Chem Rev 114:5161–5214
34. Park YI, Lee KT, Suh YD, Hyeon T (2015) Upconverting nanoparticles: a versatile platform for wide-field two-photon microscopy and multi-modal in vivo imaging. Chem Soc Rev 44:1302–1317
35. Wang F, Han Y, Lim CS, Lu YH, Wang J, Xu J, Chen HY, Zhang C, Hong MH, Liu XG (2010) Simultaneous phase and size control of upconversion nanocrystals through lanthanide doping. Nature 463:1061–1065
36. Wang F, Liu XG (2008) Upconversion multicolor fine-tuning: visible to near-infrared emission from lanthanide-doped NaYF4 nanoparticles. J Am Chem Soc 130:5642–5643
37. Auzel F (2004) Upconversion and anti-stokes processes with f and d ions in solids. Chem Rev 104:139–173
38. Wang F, Deng RR, Wang J, Wang QX, Han Y, Zhu HM, Chen XY, Liu XG (2011) Tuning upconversion through energy migration in core-shell nanoparticles. Nat Mater 10:968–973
39. Meshulach D, Silberberg Y (1998) Coherent quantum control of two-photon transitions by a femtosecond laser pulse. Nature 396:239–242
40. Liu Q, Feng W, Yang T, Yi T, Li F (2013) Upconversion luminescence imaging of cells and small animals. Nat Protoc 8:2033–2044
41. Nam SH, Bae YM, Park YI, Kim JH, Kim HM, Choi JS, Lee KT, Hyeon T, Suh YD (2011) Long-term real-time tracking of lanthanide ion doped upconverting nanoparticles in living cells. Angew Chem-Int Edit 50:6093–6097
42. Liu Q, Sun Y, Yang T, Feng W, Li C, Li F (2011) Sub-10 nm hexagonal lanthanide-doped NaLuF4 upconversion nanocrystals for sensitive bioimaging in vivo. J Am Chem Soc 133:17122–17125
43. Zhan QQ, Qian J, Liang HJ, Somesfalean G, Wang D, He SL, Zhang ZG, Andersson-Engels S (2011) Using 915 nm laser excited Tm3+/Er3+/Ho3+-doped NaYbF4 upconversion nanoparticles for in vitro and deeper in vivo bioimaging without overheating irradiation. ACS Nano 5:3744–3757
44. Wang YF, Liu GY, Sun LD, Xiao JW, Zhou JC, Yan CH (2013) Nd3+-sensitized upconversion nanophosphors: efficient in vivo bioimaging probes with minimized heating effect. ACS Nano 7:7200–7206

45. Chen GY, Shen J, Ohulchanskyy TY, Patel NJ, Kutikov A, Li ZP, Song J, Pandey RK, Agren H, Prasad PN, Han G (2012) Alpha-NaYbF4:Tm(3+)/CaF2 core/shell nanoparticles with efficient near-infrared to near-infrared upconversion for high-contrast deep tissue bioimaging. ACS Nano 6:8280–8287
46. Wang L, Zhu SJ, Wang HY, Qu SN, Zhang YL, Zhang JH, Chen QD, Xu HL, Han W, Yang B, Sun HB (2014) Common origin of green luminescence in carbon nanodots and graphene quantum dots. ACS Nano 8:2541–2547
47. Zhu SJ, Song YB, Zhao XH, Shao JR, Zhang JH, Yang B (2015) The photoluminescence mechanism in carbon dots (graphene quantum dots, carbon nanodots, and polymer dots): current state and future perspective. Nano Res 8:355–381
48. Lim SY, Shen W, Gao ZQ (2015) Carbon quantum dots and their applications. Chem Soc Rev 44:362–381
49. Sun YP, Zhou B, Lin Y, Wang W, Fernando KAS, Pathak P, Meziani MJ, Harruff BA, Wang X, Wang HF, Luo PJG, Yang H, Kose ME, Chen BL, Veca LM, Xie SY (2006) Quantum-sized carbon dots for bright and colorful photoluminescence. J Am Chem Soc 128:7756–7757
50. Cao L, Wang X, Meziani MJ, Lu FS, Wang HF, Luo PJG, Lin Y, Harruff BA, Veca LM, Murray D, Xie SY, Sun YP (2007) Carbon dots for multiphoton bioimaging. J Am Chem Soc 129:11318–11319
51. Baker SN, Baker GA (2010) Luminescent carbon nanodots: emergent nanolights. Angew Chem-Int Edit 49:6726–6744
52. Wang X, Cao L, Yang ST, Lu FS, Meziani MJ, Tian LL, Sun KW, Bloodgood MA, Sun YP (2010) Bandgap-like strong fluorescence in functionalized carbon nanoparticles. Angew Chem-Int Edit 49:5310–5314
53. Cao L, Yang ST, Wang X, Luo PJG, Liu JH, Sahu S, Liu YM, Sun YP (2012) Competitive performance of carbon "quantum" dots in optical bioimaging. Theranostics 2:295–301
54. Liu S, Tian JQ, Wang L, Zhang YW, Qin XY, Luo YL, Asiri AM, Al-Youbi AO, Sun XP (2012) Hydrothermal treatment of grass: a low-cost, green route to nitrogen-doped, carbon-rich, photoluminescent polymer nanodots as an effective fluorescent sensing platform for label-free detection of cu(II) ions. Adv Mater 24:2037–2041
55. Zhang J, Yuan Y, Liang GL, Yu SH (2015) Scale-up synthesis of fragrant nitrogen-doped carbon dots from bee pollens for bioimaging and catalysis. Adv Sci 2(4):1500002
56. Pal T, Mohiyuddin S, Packirisamy G (2018) Facile and green synthesis of multicolor fluorescence carbon dots from curcumin: in vitro and in vivo bioimaging and other applications. ACS Omega 3:831–843
57. Park JH, Gu L, von Maltzahn G, Ruoslahti E, Bhatia SN, Sailor MJ (2009) Biodegradable luminescent porous silicon nanoparticles for in vivo applications. Nat Mater 8:331–336
58. Gu L, Hall DJ, Qin Z, Anglin E, Joo J, Mooney DJ, Howell SB, Sailor MJ (2013) In vivo time-gated fluorescence imaging with biodegradable luminescent porous silicon nanoparticles. Nat Commun 4:2326
59. Cullis AG, Canham LT, Calcott PDJ (1997) The structural and luminescence properties of porous silicon. J Appl Phys 82:909–965
60. Tasciotti E, Liu X, Bhavane R, Plant K, Leonard AD, Price BK, Cheng MM-C, Decuzzi P, Tour JM, Robertson F, Ferrari M (2008) Mesoporous silicon particles as a multistage delivery system for imaging and therapeutic applications. Nat Nanotechnol 3:151
61. Karaman DS, Sarparanta MP, Rosenholm JM, Airaksinen AJ (2018) Multimodality imaging of silica and silicon materials in vivo. Adv Mater 30:e1703651
62. Li W, Liu Z, Fontana F, Ding Y, Liu D, Hirvonen JT, Santos HA (2018) Tailoring porous silicon for biomedical applications: from drug delivery to cancer immunotherapy. Adv Mater 30:e1703740
63. Eustis S, El-Sayed MA (2006) Why gold nanoparticles are more precious than pretty gold: noble metal surface plasmon resonance and its enhancement of the radiative and nonradiative properties of nanocrystals of different shapes. Chem Soc Rev 35:209–217

64. Zheng J, Zhang CW, Dickson RM (2004) Highly fluorescent, water-soluble, size-tunable gold quantum dots. Phys Rev Lett 93(7):077402
65. Lin CAJ, Yang TY, Lee CH, Huang SH, Sperling RA, Zanella M, Li JK, Shen JL, Wang HH, Yeh HI, Parak WJ, Chang WH (2009) Synthesis, characterization, and bioconjugation of fluorescent gold nanoclusters toward biological labeling applications. ACS Nano 3:395–401
66. Negishi Y, Takasugi Y, Sato S, Yao H, Kimura K, Tsukuda T (2004) Magic-numbered Au-n clusters protected by glutathione monolayers (n=18, 21, 25, 28, 32, 39): isolation and spectroscopic characterization. J Am Chem Soc 126:6518–6519
67. Negishi Y, Nobusada K, Tsukuda T (2005) Glutathione-protected gold clusters revisited: bridging the gap between gold(I)-thiolate complexes and thiolate-protected gold nanocrystals. J Am Chem Soc 127:5261–5270
68. Wang GL, Huang T, Murray RW, Menard L, Nuzzo RG (2005) Near-IR luminescence of monolayer-protected metal clusters. J Am Chem Soc 127:812–813
69. Palmal S, Basiruddin SK, Maity AR, Ray SC, Jana NR (2013) Thiol-directed synthesis of highly fluorescent gold clusters and their conversion into stable imaging nanoprobes. Chem-Eur J 19:943–949
70. Xie JP, Zheng YG, Ying JY (2009) Protein-directed synthesis of highly fluorescent gold nanoclusters. J Am Chem Soc 131:888–889
71. Vosch T, Antoku Y, Hsiang JC, Richards CI, Gonzalez JI, Dickson RM (2007) Strongly emissive individual DNA-encapsulated Ag nanoclusters as single-molecule fluorophores. Proc Natl Acad Sci U S A 104:12616–12621
72. Wu Z, Jin R (2010) On the ligand's role in the fluorescence of gold nanoclusters. Nano Lett 10:2568–2573
73. Duan HW, Nie SM (2007) Etching colloidal gold nanocrystals with hyperbranched and multivalent polymers: a new route to fluorescent and water-soluble atomic clusters. J Am Chem Soc 129:2412–2413
74. Wang HH, Lin CAJ, Lee CH, Lin YC, Tseng YM, Hsieh CL, Chen CH, Tsai CH, Hsieh CT, Shen JL, Chan WH, Chang WH, Yeh HI (2011) Fluorescent gold nanoclusters as a biocompatible marker for in vitro and in vivo tracking of endothelial cells. ACS Nano 5:4337–4344
75. Wu X, He X, Wang K, Xie C, Zhou B, Qing Z (2010) Ultrasmall near-infrared gold nanoclusters for tumor fluorescence imaging in vivo. Nanoscale 2:2244–2249
76. Yu MX, Zhou JC, Du BJ, Ning XH, Authement C, Gandee L, Kapur P, Hsieh JT, Zheng J (2016) Noninvasive staging of kidney dysfunction enabled by renal-clearable luminescent gold nanoparticles. Angew Chem-Int Edit 55:2787–2791
77. Mochalin VN, Shenderova O, Ho D, Gogotsi Y (2012) The properties and applications of nanodiamonds. Nat Nanotechnol 7:11–23
78. Gruber A, Drabenstedt A, Tietz C, Fleury L, Wrachtrup J, vonBorczyskowski C (1997) Scanning confocal optical microscopy and magnetic resonance on single defect centers. Science 276:2012–2014
79. Yu SJ, Kang MW, Chang HC, Chen KM, Yu YC (2005) Bright fluorescent nanodiamonds: no photobleaching and low cytotoxicity. J Am Chem Soc 127:17604–17605
80. Tisler J, Balasubramanian G, Naydenov B, Kolesov R, Grotz B, Reuter R, Boudou JP, Curmi PA, Sennour M, Thorel A, Borsch M, Aulenbacher K, Erdmann R, Hemmer PR, Jelezko F, Wrachtrup J (2009) Fluorescence and spin properties of defects in single digit nanodiamonds. ACS Nano 3:1959–1965
81. Fu CC, Lee HY, Chen K, Lim TS, Wu HY, Lin PK, Wei PK, Tsao PH, Chang HC, Fann W (2007) Characterization and application of single fluorescent nanodiamonds as cellular biomarkers. Proc Natl Acad Sci U S A 104:727–732
82. Hsiao WW, Hui YY, Tsai PC, Chang HC (2016) Fluorescent nanodiamond: a versatile tool for long-term cell tracking, super-resolution imaging, and nanoscale temperature sensing. Acc Chem Res 49:400–407

83. Tzeng YK, Faklaris O, Chang BM, Kuo Y, Hsu JH, Chang HC (2011) Superresolution imaging of albumin-conjugated fluorescent nanodiamonds in cells by stimulated emission depletion. Angew Chem-Int Edit 50:2262–2265
84. Haziza S, Mohan N, Loe-Mie Y, Lepagnol-Bestel AM, Massou S, Adam MP, Le XL, Viard J, Plancon C, Daudin R, Koebel P, Dorard E, Rose C, Hsieh FJ, Wu CC, Potier B, Herault Y, Sala C, Corvin A, Allinquant B, Chang HC, Treussart F, Simonneau M (2017) Fluorescent nanodiamond tracking reveals intraneuronal transport abnormalities induced by brain-disease-related genetic risk factors. Nat Nanotechnol 12:322–328
85. Wu TJ, Tzeng YK, Chang WW, Cheng CA, Kuo Y, Chien CH, Chang HC, Yu J (2013) Tracking the engraftment and regenerative capabilities of transplanted lung stem cells using fluorescent nanodiamonds. Nat Nanotechnol 8:682–689
86. Lecuyer T, Teston E, Ramirez-Garcia G, Maldiney T, Viana B, Seguin J, Mignet N, Scherman D, Richard C (2016) Chemically engineered persistent luminescence nanoprobes for bioimaging. Theranostics 6:2488–2524
87. le Masne de Chermont Q, Chaneac C, Seguin J, Pelle F, Maitrejean S, Jolivet JP, Gourier D, Bessodes M, Scherman D (2007) Nanoprobes with near-infrared persistent luminescence for in vivo imaging. Proc Natl Acad Sci U S A 104:9266–9271
88. Maldiney T, Bessiere A, Seguin J, Teston E, Sharma SK, Viana B, Bos AJJ, Dorenbos P, Bessodes M, Gourier D, Scherman D, Richard C (2014) The in vivo activation of persistent nanophosphors for optical imaging of vascularization, tumours and grafted cells. Nat Mater 13:418–426
89. Altinoglu EI, Russin TJ, Kaiser JM, Barth BM, Eklund PC, Kester M, Adair JH (2008) Near-infrared emitting fluorophore-doped calcium phosphate nanoparticles for in vivo imaging of human breast cancer. ACS Nano 2:2075–2084
90. Tabakovic A, Kester M, Adair JH (2012) Calcium phosphate-based composite nanoparticles in bioimaging and therapeutic delivery applications. Wiley Interdiscip Rev-Nanomed Nanobiotechnol 4:96–112
91. Frangioni JV (2003) In vivo near-infrared fluorescence imaging. Curr Opin Chem Biol 7:626–634
92. Barth BM, Sharma R, Altinoglu EI, Morgan TT, Shanmugavelandy SS, Kaiser JM, McGovern C, Matters GL, Smith JP, Kester M, Adair JH (2010) Bioconjugation of calcium phosphosilicate composite nanoparticles for selective targeting of human breast and pancreatic cancers in vivo. ACS Nano 4:1279–1287
93. Tarn D, Ashley CE, Xue M, Carnes EC, Zink JI, Brinker CJ (2013) Mesoporous silica nanoparticle nanocarriers: biofunctionality and biocompatibility. Acc Chem Res 46:792–801
94. Cho EB, Volkov DO, Sokolov I (2011) Ultrabright fluorescent silica mesoporous silica nanoparticles: control of particle size and dye loading. Adv Funct Mater 21:3129–3135
95. Ow H, Larson DR, Srivastava M, Baird BA, Webb WW, Wiesner U (2005) Bright and stable core-shell fluorescent silica nanoparticles. Nano Lett 5:113–117
96. Benezra M, Penate-Medina O, Zanzonico PB, Schaer D, Ow H, Burns A, DeStanchina E, Longo V, Herz E, Iyer S, Wolchok J, Larson SM, Wiesner U, Bradbury MS (2011) Multimodal silica nanoparticles are effective cancer-targeted probes in a model of human melanoma. J Clin Invest 121:2768–2780
97. Phillips E, Penate-Medina O, Zanzonico PB, Carvajal RD, Mohan P, Ye YP, Humm J, Gonen M, Kalaigian H, Schoder H, Strauss HW, Larson SM, Wiesner U, Bradbury MS (2014) Clinical translation of an ultrasmall inorganic optical-PET imaging nanoparticle probe. Sci Transl Med 6:260ra149
98. Sharma P, Bengtsson NE, Walter GA, Sohn HB, Zhou GY, Iwakuma N, Zeng HD, Grobmyer SR, Scott EW, Moudgil BM (2012) Gadolinium-doped silica nanoparticles encapsulating indocyanine green for near infrared and magnetic resonance imaging. Small 8:2856–2868

99. Lee CH, Cheng SH, Wang YJ, Chen YC, Chen NT, Souris J, Chen CT, Mou CY, Yang CS, Lo LW (2009) Near-infrared mesoporous silica nanoparticles for optical imaging: characterization and in vivo biodistribution. Adv Funct Mater 19:215–222
100. Ferrauto G, Carniato F, Di Gregorio E, Tei L, Botta M, Aime S (2017) Large photoacoustic effect enhancement for ICG confined inside MCM-41 mesoporous silica nanoparticles. Nanoscale 9:99–103
101. Kang J, Kim D, Wang J, Han Y, Zuidema JM, Hariri A, Park JH, Jokerst JV, Sailor MJ (2018) Enhanced performance of a molecular photoacoustic imaging agent by encapsulation in mesoporous silicon nanoparticles. Adv Mater 30(27):e1800512

Top Med Chem (2020) 34: 81–124
DOI: 10.1007/7355_2019_89

Published online: 29 February 2020

Advancements of Second Near-Infrared Biological Window Fluorophores: Mechanism, Synthesis, and Application In Vivo

Shuqing He and Zhen Cheng

Contents

S. He
Academy for Advanced Interdisciplinary Studies and Department of Biomedical Engineering, Southern University of Science and Technology (SUSTech), Shenzhen, China

Molecular Imaging Program at Stanford (MIPS), Bio-X Program, and Department of Radiology, Canary Center at Stanford for Cancer Early Detection, Stanford University, Stanford, CA, USA

Z. Cheng (✉)
Molecular Imaging Program at Stanford (MIPS), Bio-X Program, and Department of Radiology, Canary Center at Stanford for Cancer Early Detection, Stanford University, Stanford, CA, USA
e-mail: zcheng@stanford.edu

Abstract In vivo fluorescence imaging in second near-infrared biological window (NIR-II) is an emerging imaging technique in both fundamental research and clinical application. NIR-II fluorescence affords high-resolution images with increasing penetration depths due to the reduced scattering, minimal absorption, and negligible autofluorescence. In this chapter, we review the recent 10-year progress made on NIR-II fluorescence imaging in 1,000–1,700 nm NIR-II windows by summarizing an increasingly advanced NIR-II fluorophores including organic dyes and inorganic nanoparticles, with tunable emission wavelengths. The NIR-II fluorescence emission mechanism and the strategy for synthesis of high quantum yield with more biocompatible and higher photostability NIR-II fluorophores will be highlighted. In addition, we provide our perspective on the current development and bright future direction of NIR-II fluorophores development in frontier fields.

Keywords Quantum dots, Rare-earth-doped nanoparticles, Second near-infrared window, Single-walled carbon nanotubes, Small-molecule dye

1 Introduction

Noninvasive imaging is being used for many preclinical or clinical purposes from disease diagnosis to the visualization drug targeting [1–3]. Fluorescence imaging is a fast-growing noninvasive imaging technique that has been well-established for identification and diagnosis of lesion in real time at a relatively higher signal-to-noise ratio and relatively higher spatial and temporal resolution [4, 5]. In vivo fluorescence imaging requires an excitation light source, an emission light detector to generate a visual representation of the imaged object on the basis of the spatio-temporal distribution of fluorescent probes. It is well-known that scattering, autofluorescence, and penetration depth are the major factors that cause attenuation of fluorescence signal proportional to the depth of biological tissue. Briefly, with the increasing propagation distance, photons will be attenuated by the effects of scattering and absorption, resulting in a reduction in image quality. Absorption of light in tissue media can occur by biomolecules, such as collagen and elastin, lipids, hemoglobin, or water in tissue media, while scattering can be caused by cells or intracellular matrix. Water greatly affects image quality and penetration depth due to strong absorption peaks from vibrational modes at ∼900 nm, ∼1,200 nm, and ∼1,400 nm. In the visible window (400–700 nm) and the first near-infrared (NIR) window (NIR-I, 700–900 nm), image quality is reduced due to strong absorption peaks from lipids and from hemoglobin and deoxyhemoglobin and is blurred due to the molecular process of Rayleigh–Mie scattering (Fig. 1a). Compared with visible imaging and the NIR-I imaging, the second NIR biological window (NIR-II, 1,000–1,700 nm) provides considerable advantages due to the reduced photon scattering, lower absorption, and minimal autofluorescence (Fig. 1b–d) [6]. Generally, the sub-windows such as the NIR-IIa (1,300–1,400 nm) and the NIR-IIb

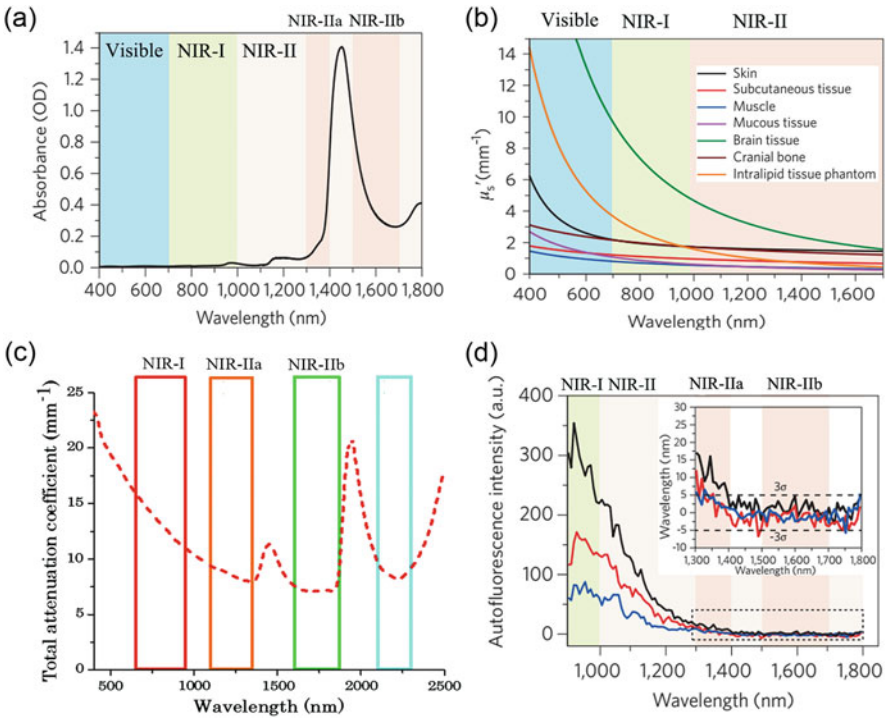

Fig. 1 Motivation for NIR-II imaging: (**a**) The absorption spectrum of water from visible to near-infrared region. (**b**) Reduced scattering coefficients of different biological tissues in the 400–1,700 nm region. (**c**) The spectrum of the total attenuation coefficient. (**d**) The autofluorescence spectra of ex vivo mouse liver (black), spleen (red), and heart tissue (blue) under 808 nm excitation light. (**a**, **b**, **d**) Reprinted (adapted) with permission from Ref. [6], Copyright 2017, Nature Publishing Group. (**c**) Reprinted (adapted) with permission from Ref. [7] Copyright 2014, SPIE

(1,500–1,700 nm) are defined in NIR-II biological window. The 1,400–1,500 nm window is typically avoided because of the strong water absorption in this range (Fig. 1a, c). In the past 10 years, a series of NIR-II fluorophores, including organic dyes, such as small-molecule dyes (SMDs) [8–13], small-molecule dye complexes (SMDCs) [14, 15], and small-molecule dyes based organic nanoparticles (SMDNPs) [16–18], and inorganic nanomaterials, such as quantum dots (QDs) [19–22], rare-earth-doped nanoparticles (RENPs) [23–26], and single-walled carbon nanotubes (SWCNTs) [27–33], have been developed with precisely controlled structures and reliable near-infrared emission in NIR-II window.

NIR-II provides relatively high spatiotemporal resolution imaging in deep tissue and can be used to visualize many dynamic processes in real time, such as cancer metastasis, cell trafficking, cellular events in immune reactions, etc. On the other hand, some of NIR-II fluorophores are multifunctional with more than one clinical purpose. Multimodal imaging and theragnosis and the integration of diagnosis and therapy represent challenging fields where the multifunctionality of NIR-II fluorophores are highly needed and remarkably applied. As a newly rising but

quickly growing optical imaging technique, NIR-II imaging demonstrates high promise to diagnose diseases, monitor disease development, and guide surgery and so on.

In this chapter, firstly we will briefly introduce the mechanism of NIR-II fluorescence emission. Secondly, we will summarize the synthesis method, including the chemical methods for synthesis donor–acceptor (D–A) structures and the luminescence characteristics, size, morphology, and surface characteristics of bright-emission NIR-II fluorophores. Thirdly, the use of emerging NIR-II fluorophores applications in single NIR-II imaging, multimodal imaging, and theragnosis will be highlighted. The future perspective and new challenges of NIR-II fluorophores are discussed in the final section of this chapter.

2 Organic Dyes

Organic dyes have been used to detect and visualize structures and processes in biological samples. Today, many of the favored NIR-II organic dyes have a fluorescent component that can be detected with extraordinary sensitivity and selectivity. To date, several types of organic NIR-II fluorophores with excellent emission performance are synthesized, such as SMDs, SMDCs, and SMDNPs. SMD NIR-II fluorophore is first reported in 2015, named CH1055 [8]. Most of the SMDs are hydrophobic and need to be encapsulated into surfactant (e.g., PEG, liposome) or conjugated with protein to form NIR-II SMD complexes or SMD nanoparticles, named as SMDCs and SMDNPs, respectively. They have different degrees of brightness in the NIR-II emission and rapid excretion, and they can be manufactured under current good manufacturing practice (cGMP) condition. Because of these advantage factors, they are highly attractive and promising NIR-II fluorophores for future clinical applications.

2.1 Mechanism of NIR-II Emission

Briefly, fluorescence occurs when an orbital electron of a molecule, or atom, relaxes to its ground state after emitting a photon from an excited singlet state. The fluorescence process can be summarized as follows: first, excitation of a fluorophore through the absorption of light energy; second, a transient excited lifetime with some loss of energy; and third, return of the fluorophore to its ground state, accompanied by the emission of light. Generally, due to the energy loss during the transient excited lifetime, the light emitted is always of a longer wavelength than the light energy absorbed. Taking the SMD CH1055 as an example, it is composed of conjugated aromatic units, with a donor–acceptor–donor (D–A–D) structure and a benzobisthiadiazole core. The energy gap can be reduced through π-spacers by attaching of strong electron donors. The spatial configuration of strong electron-

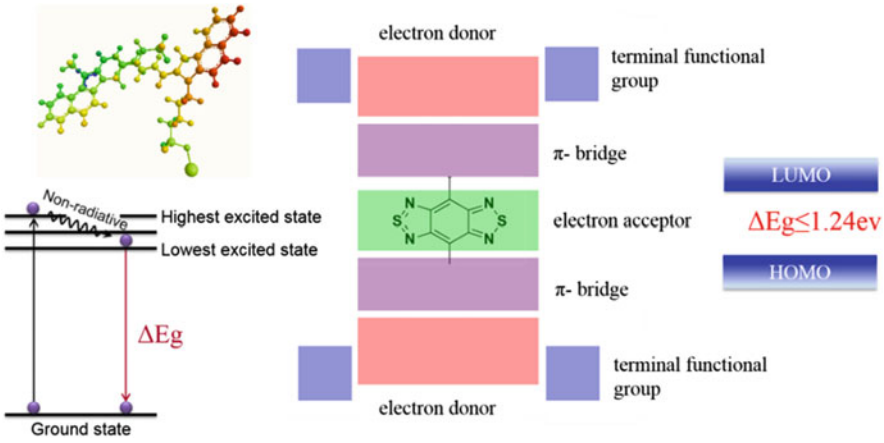

Fig. 2 The general photophysical pathways for NIR-II organic dyes in solution and the general mechanism of NIR-II fluorescence emission

donating groups flanking a central electron acceptor shrinks the energy gap separating the hybridized highest occupied molecular orbital (HOMO)/lowest unoccupied molecular orbital (LUMO) levels and shifts the fluorescence emission into the NIR-II window ($\lambda \geq 1{,}000$ nm or $\Delta E \leq 1.24$ eV) under the laser excitation as shown in Fig. 2.

2.2 Synthesis Strategy

The representative SMDs NIR-II dye, CH1055 is synthesized with high yield from the structure 4,4′-(phenylazanediyl)dibenzaldehyde and benzobisthiadiazole core. Several classic reactions are used to assemble the core structure of the target included a Suzuki cross-coupling reaction, iron reduction and N-thionylaniline induced ring closure. To achieve an aqueous soluble compound, four carboxylic acid groups are introduced into a donor–acceptor–donor (D–A–D) type. In addition, to allow facile conjugation to targeting ligands, a protection/deprotection sequence are induced. To further increase solubility, the carboxylic acid groups of CH1055 are PEGylated through EDC/NHS chemistry. To enhance the quantum yield of CH1055, the carboxylic acid groups are replaced by sulfonic acid group, named CH-4T. After supramolecular assemblies with plasma proteins, the fluorescence intensity is increased by 50-fold. Heating is also a significant strategy to improve the quantum yields. By heating the CH-4T in the FBS, the quantum yield is improved two times up to 11% [10]. Other method, such as high-efficiency click chemistry to specific molecular antibodies provide a new way to form molecular-specific SMDs NIR-II probes [14]. Moreover, SMDs based NIR-II fluorophores are rare up to date, thiophene moiety can facilitate an intramolecular charge transfer, resulting in a

further bathochromic shift. So, the donor structure thiophene expand the SMDs NIR-II fluorophores category (e.g. Q1, Q2, Q3 and Q4) [11]. These synthesis strategies open a quick route for translation of NIR-II imaging technique into clinical applications.

2.3 Application In Vivo

As a Food and Drug Administration (FDA)-approved dye, the indocyanine green (ICG) has been widely used in NIR-I window for a long period time. Recent study exhibits unprecedented imaging opportunities of ICG in NIR-II window with higher resolution than that in NIR-I window, including contact-free monitoring of vital signs, generation of microvasculature blood flow maps, real-time metabolic imaging, and molecularly targeted imaging. For example, in 2017, small-molecule dye ICG for the first time was reported with the enhanced the NIR-II fluorescent brightness (tail up to 1,150 nm) via assemblies with FBS [9, 10]. Moreover, Starosolski et al. demonstrate that ICG display a significant enhanced NIR-II (1,000–1,250 nm) emission in plasma and low polar solvents such as ethanol. In vivo imaging results have demonstrated that the signal-to-noise ratio values of ICG in the NIR-II window are two times than that of in the NIR-I window [34]. So, ICG has a very good prospect to image in clinical in NIR-II window and get the approval from FDA in the near future. CH1055-PEG has an emission peak at 1,055 nm and with a tail extending emission into the NIR-IIa region (1,300–1,400 nm). Compared with ICG for NIR-I imaging, not only it enables detection of tumors in the brain at depths up to 4 mm with a noninvasive through-skull technique [8] but offers higher resolution in diagnosis sentinel lymph nodes (SLN) for surgical resection in real time. Tumor-specific-targeting NIR-II fluorescent probe can also be obtained by conjugating CH1055 with an anti-epidermal growth factor receptor (EGFR) affibody molecule. The affibody-conjugated CH1055 allows accurate image-guided tumor removal surgery due to the specifically targeting xenograft human squamous cell carcinoma tumors. Importantly, pharmacokinetic studies of CH1055-PEG demonstrate rapid urinary 90% excretion via the kidneys in 24 h. Moreover, NIR-II window molecular imaging gives a fivefold higher tumor-to-normal tissue ratio than that in the NIR-I window, as shown in Fig. 3.

In another novel work, Feng et al. conjugate CH1055 to follicle-stimulating hormone (FSH) to specifically image ovaries in live mice [15]. They are also able to detect specific FSH receptor in bones. According to the expression of FSH receptors, it could resolve earlier controversies in osteoclasts (see Fig. 4a–c). By replacing the carboxylic acid groups of CH1055 with more negatively charged sulfonic acid groups and using supramolecular assemblies with serum proteins, Antaris et al. synthesize a water-soluble SMDC NIR-II dye in FBS (CH-4T-FBS). This novel NIR-II complex fluorophores show a 110-fold fluorescence enhancement and a fast video-rate imaging at a 50 frames per second and benefit a lot in NIR-II window for imaging deep anatomical features (Fig. 4d–f) [10].

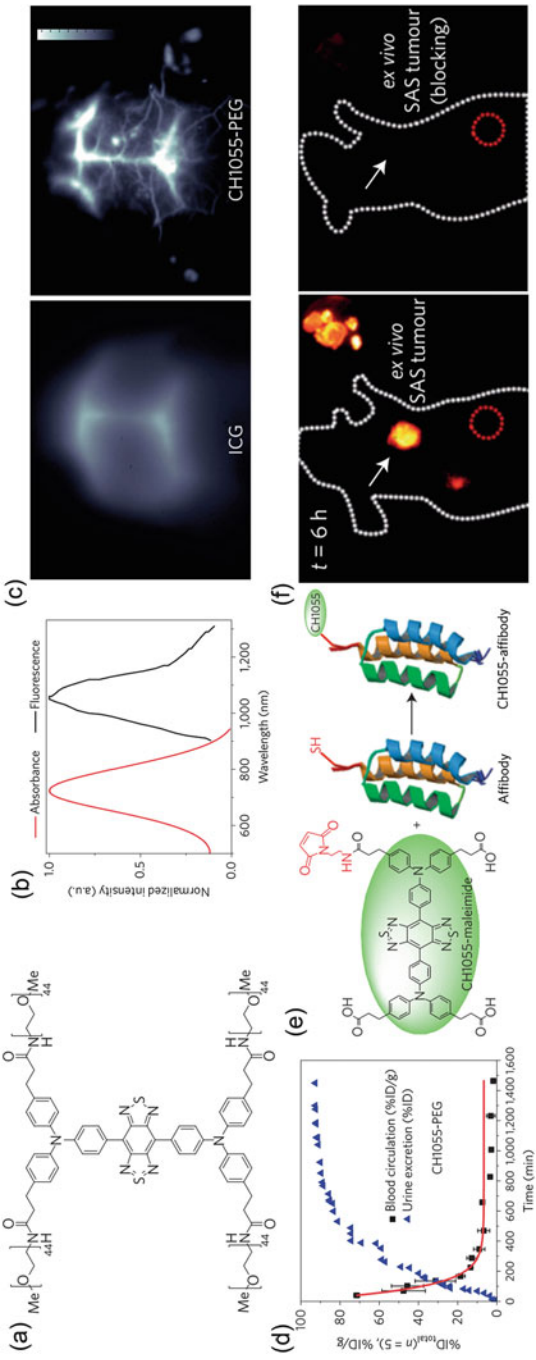

Fig. 3 NIR-II fluorophores CH1055 and imaging in vivo. (**a**) Chemical structure of CH1055-PEG. (**b**) The absorbance and fluorescent emission of CH1055-PEG (808 nm excitation). (**c**) Brain vasculature imaging through the scalp and skull in mice using either ICG and CH1055-PEG. (**d**) PEGylated CH1055 shows 90% renal clearance in the first 24 h post-injection. (**e**) A simplified reaction schematic illustrating the synthesis of the CH1055-affibody. (**f**) NIR-II fluorescent images 6 h post-injection of CH1055 conjugated to an anti-EGFR affibody as well as of a blocking dose to demonstrate molecular selectivity. (**a–f**) Reprinted (adapted) with permission from Ref. [8], Copyright 2015, Nature Publishing Group

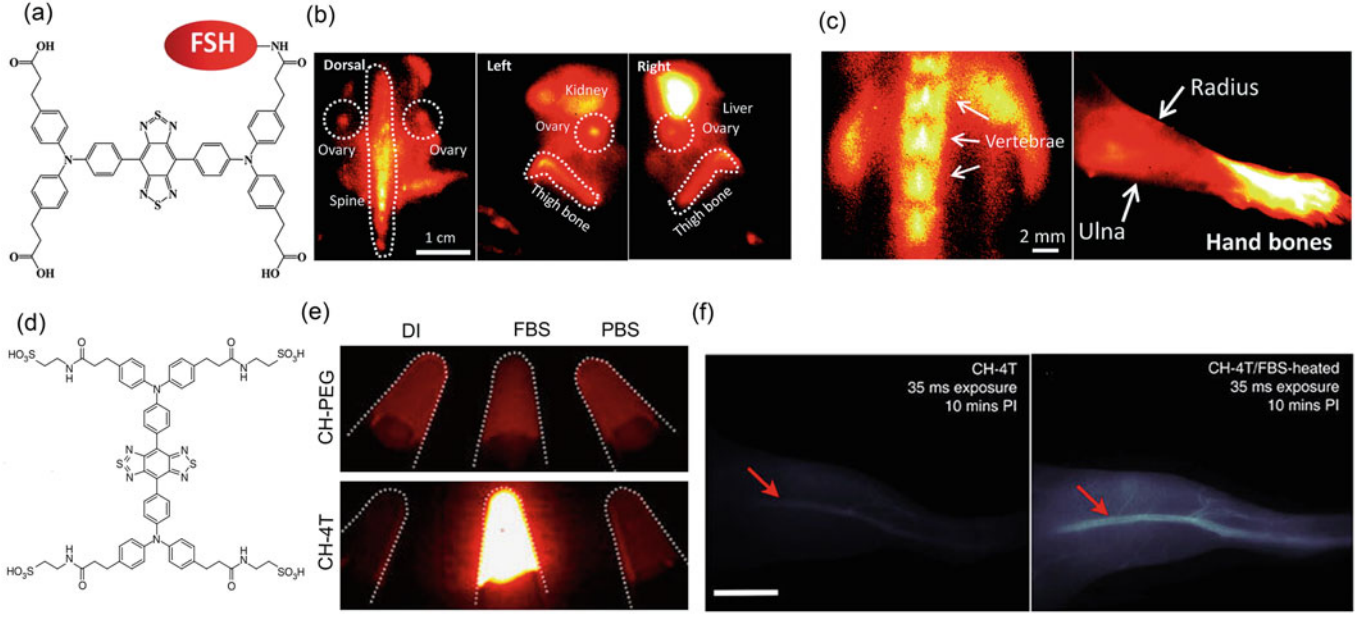

Fig. 4 SMDCs NIR-II fluorophores and imaging in vivo. (**a**) Conjugation of the FSH to the NIR-II CH1055 fluorophore. (**b**) NIR-II imaging of bones using FSH-CH in adult female and male mice. (**c**) High magnification of the vertebrae and thighbone of a female, together with the radius, ulna, and hand bones. (**d**) Chemical structure of CH-4T. (**e**) NIR-II fluorescent images of CH-PEG and CH-4T in deionized water, fetal bovine serum (FBS) and PBS at 808 nm excitation. (**f**) NIR-II fluorescent images of mouse hindlimb vasculature 10 min post-injection of free CH-4T and CH-4T heated at 70°C for 10 min in FBS. Scale bar: 10 mm. (**a**–**c**) Reprinted (adapted) with permission from Ref. [15], Copyright 2017, The Royal Society of Chemistry. (**d**–**f**) Reprinted (adapted) with permission from Ref. [10], Copyright 2017, Nature Publishing Group

Recently, SXH and SDH NIR-II SMDPs are synthesized for integrin αVβ3-targeted glioma imaging, which not only enable to delineate tumors from surrounding normal tissue but in image-guided surgery [17]. CQS1000 is a multifunctional NIR-II probe by encapsulating CH1055 into phospholipid vesicles (Fig. 5a–c) [16]. CQS1000 can visualize and monitor many physiological and pathological conditions of circulatory systems in noninvasive and dynamical, including drainage and routing lymphatic, tumor angiogenesis and vascular diseases. In sentinel lymph node mapping, CQS1000 offers particular promise in guidance surgery. In addition, by distinguishing the blood supply and lymphatic drainage, this new NIR-II fluorophore allowed precise resection of tumors, which may lead to better survival and reduced relapse rates. Using click chemistry, a novel water-soluble NIR-II SMDC, IR-FGP, is synthesized recently by Zhu et al. [14] IR-FGP not only obtains a bright NIR-II emission by tuning a D–A–D architecture systematically but also offers many targeting channels. In addition, this IR-FGP NIR-II SMDC nanoprobe allows 3D tomographic imaging in deep tissue and reduces the autofluorescence (Fig. 5d–f). Moreover, this facilitated 3D imaging brain tissue sections demonstrate multicolor molecular imaging across both the NIR-I and NIR-II windows (800–1,700 nm).

Nanoprecipitation method has been used to synthesize donor–acceptor chromophore-based nanoparticle (DAP) by encapsulating the NIR-II chromophore CH1000 molecules within amphiphilic phospholipids [35]. To enhance tumor-targeting efficiency, the EGFR affibody is conjugated with DAP successfully. This affibody–DAP organic nanoprobe demonstrates capability to selectively target EGFR-positive tumors in an FTC-133 subcutaneous mouse model with enormous enhanced PAI and NIR-II fluorescence contrast in both in vitro and in vivo (Fig. 6a–e). In a novel PET/NIR-II dual-modal imaging platform, ^{68}Ga-SCH2 is developed using base-catalyzed, highly efficient, and selective assembly method recently [13]. This small-molecule-based PET/NIR-II probe can be successfully used for αVβ3-targeted tumor imaging. The excellent NIR-II and PET dual-modal imaging properties such as high signal to background ratio and specificity lead to tumor-free resection in the small animal models. These inspiring results show high potential for tumor surgery and translational clinical.

Very recently, a small-molecule NIR-II fluorophore FD-1080 with both excitation and emission in the NIR-II region has been successfully synthesized for in vivo imaging. In this novel structure, a heptamethine structure is designed to shift the absorption and emission into NIR-II region. Sulphonic and cyclohexene groups are introduced to enhance its water solubility and stability. The quantum yield of FD-1080 can be increased from 0.31 to 5.94% after combining with FBS. Significantly, 1,064 nm NIR-II excitation was demonstrated with the high tissue penetration depth and superior imaging resolution compared to previously reported NIR excitation from 650 to 980 nm. FD-1080 not only is capable of realizing noninvasive high-resolution deep-tissue hindlimb vasculature and brain vessel bioimaging but also quantifies the respiratory rate based on the dynamic imaging of respiratory craniocaudal motion of the liver for the awake and anaesthetized mouse [36] (Fig. 7).

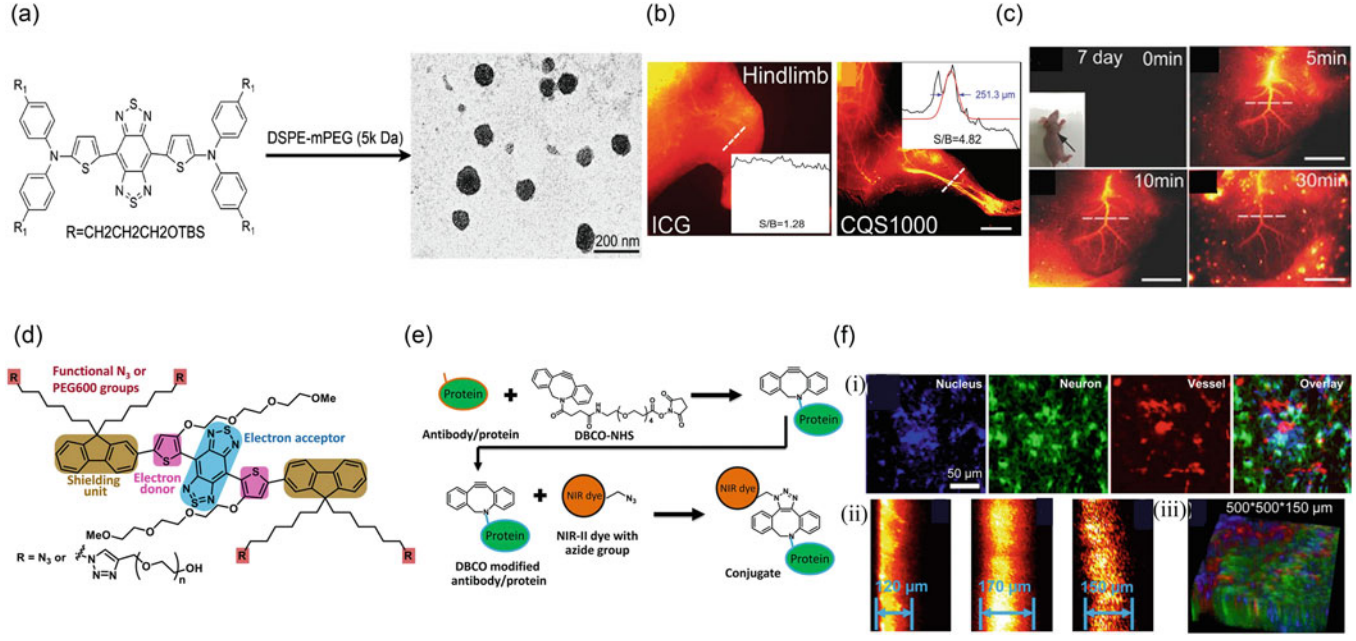

Fig. 5 SMNPs NIR-II fluorophores and imaging in vivo. (**a**) Schematic illustration of the CQS1000 NIR-II fluorophore and TEM imaging of the NIR-II particles. (**b**) Fluorescence images of the vasculature of hindlimb in mice using ICG (NIR-I) and CQS1000 (NIR-II), showing the NIR-II images with the higher SBR. (**c**) In vivo dynamic assessment of angiogenesis development of tumor. (**d**) Chemical structure of IR-FGP with D–A–D architecture containing two PEG chains and two azide groups for biocompatibility and bioconjugation. (**e**) Scheme of the conjugation route between IR-FGP and proteins by click chemistry. (**f**) Multicolor 2D/3D staining in NIR-II windows (800–1,700 nm): (i) Magnified multicolor brain tissue staining with higher resolution; (ii) confocal scanning from cross sections of brain tissue; (iii) three-color 3D rendering of nucleus, neuron, and vessel channels obtained with NIR-I/II confocal microscopy. (**a**–**c**) Reprinted (adapted) with permission from Ref. [16], Copyright 2017, Wiley-VCH Verlag GmbH & Co. KGaA. (**d**–**f**) Reprinted (adapted) with permission from Ref. [14], Copyright 2017, National Academy of Sciences

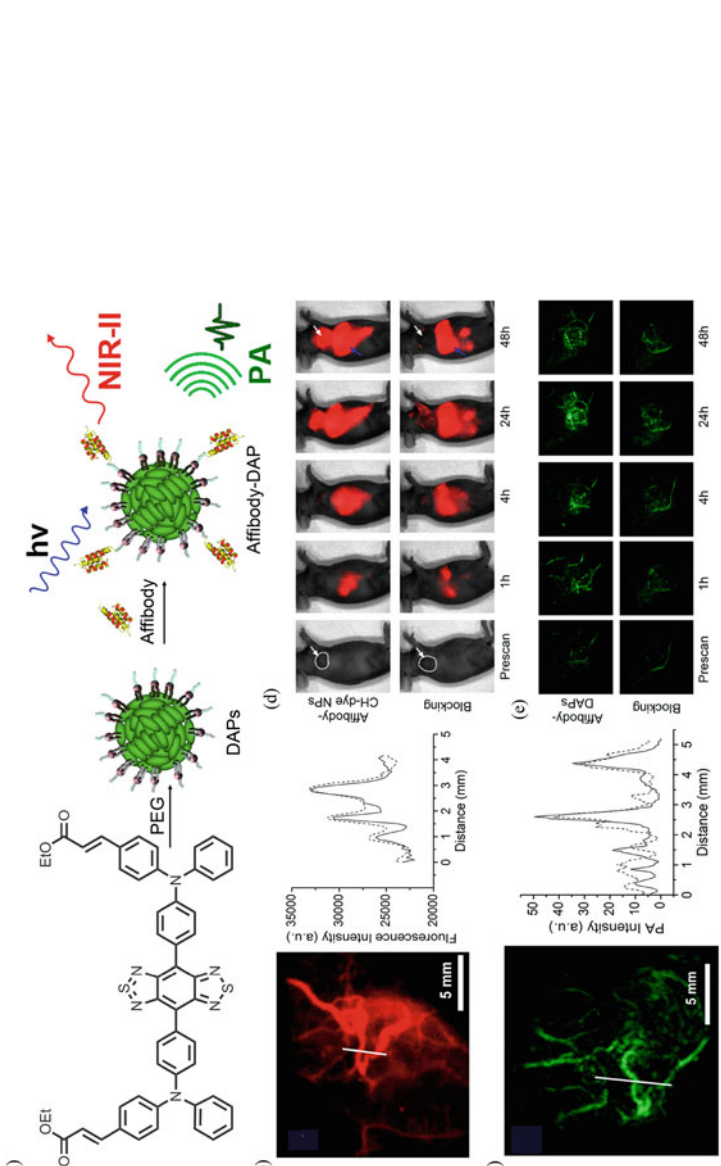

Fig. 6 NIR-II fluorophores DAP based dual-modal NIR-II and PA imaging in vivo. (**a**) Schematic illustration of preparation of affibody–DAPs and the dual-modal PA imaging and NIR-II imaging. (**b**) Fluorescence image of the FTC-133 thyroid tumor in the NIR-II and the cross-sectional fluorescence intensity profiles along a white line across FTC-133 tumor. (**c**) 3D volume rendering of photoacoustic images of the thyroid tumor in a mouse before and after the injection of DAPs. Scale bar = 5 mm. The cross-sectional PA intensity profiles along a white line across FTC-133 tumor. (**d**) NIR-II fluorescence images of EGFT-positive FTC-133 tumor-bearing mice were obtained in the NIR-II window. (**e**) Coronal views of 3D volume rendering of photoacoustic images of FTC-133 tumors were acquired immediately after fluorescence imaging at the pre-determined time intervals. (**a**–**e**) Reprinted (adapted) with permission from Ref. [35] Copyright 2017, American Chemical Society

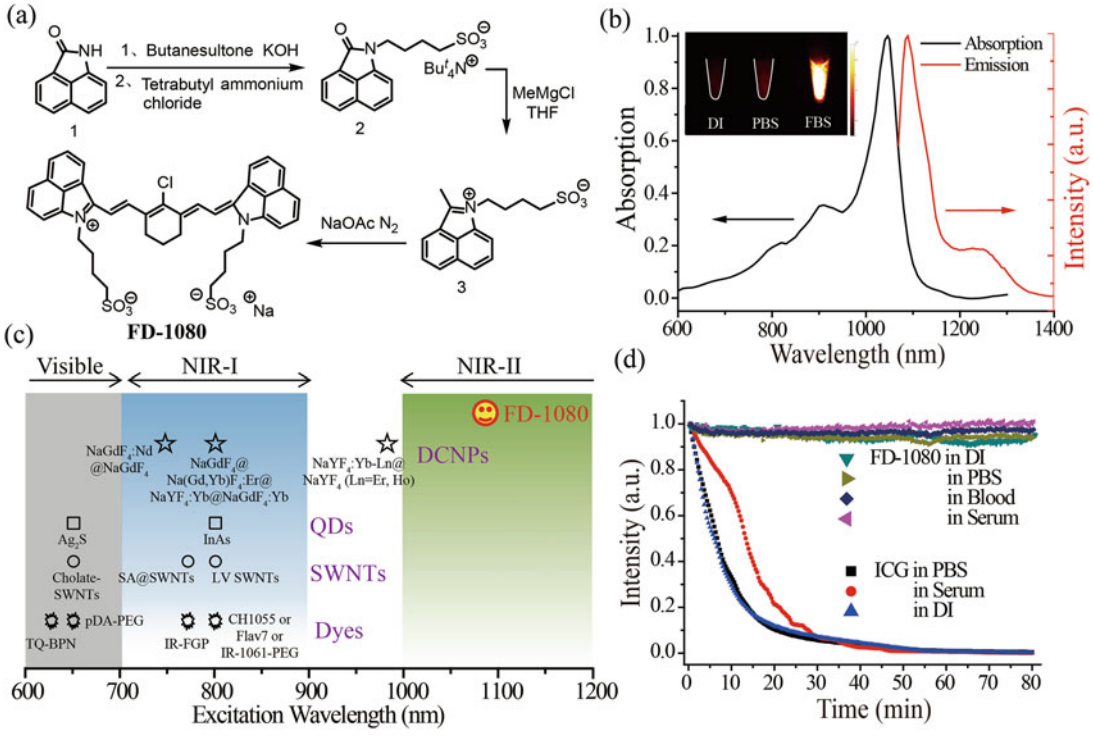

Fig. 7 NIR-II fluorophores FD-1080: (**a**) Synthetic route of FD-1080. (**b**) The absorbance and fluorescent emission spectra of FD-1080 dye with an absorbance peak at about 1,046 nm and an emission peak at about 1,080 nm. The fluorescent emission spectrum was obtained under 1,064 nm laser excitation. Inset: An NIR-II fluorescence image of FD-1080 (50 mm) in deionized water, FBS, and PBS (1,100 nm long-pass filter) under excitation of 1,064 nm. (**c**) Reported NIR-II agents with varied excitation wavelengths. (**d**) Photostability of FD-1080 and ICG complexes in a variety of biological media under continuous 1,064 nm and 808 nm exposure for about 80 min at a power density of 0.33 Wcm^{-2}, respectively. (**a**–**d**) Reprinted (adapted) with permission from Ref. [36] Copyright 2018, Wiley-VCH Verlag GmbH & Co. KGaA

Recently, it is attracted to design polymers to synthesize lower bandgap energy probes in the NIR-II regions by D–A alternating copolymerization method. For example, Hong et al. have reported a method for synthesizing polymer nanoparticles (pDA) emitting in the NIR-II region peak at 1,050 nm with a quantum yield of up to 1.7%, which is much higher than SWCNTs (~0.4%) used previously [37]. In bio-application field, this novel NIR-II fluorophore enables the imaging of dynamic changes in blood flow at a frame rate of over 25 frames per second, which extends the limits of temporal resolution to a previously unattainable level. However, one drawback of this NIR-II probe is the low photostability that photodegradation upon excitation at 808 nm for 1 h results in a decline in NIR-II fluorescence intensity of up to 20%. In another novel research work, a highly photostable polymer nanoparticle, namely, PDFT1032, was reported by Dr. Cheng [38]. PDFT1032 was synthesized from the highly planar electron acceptor diketopyrrolopyrrole (DPP), which is able to couple with many electron donors easily, and the bandgap can be tuned to obtain the expected NIR-II emission. PDFT1032 demonstrates excellent performance in NIR-II image-guided tumor surgery and embolization therapy at the high spatial resolution (mm range) and high temporal resolution (425 frames per second).

3 RENPs

Rare-earth (RE) elements are the lanthanides (from La to Lu) together with Sc and Y. Rare-earth-doped nanoparticles composed of RE ions embedded within an inorganic crystalline host matrix have attracted considerable attention owing to their unique optical properties that are controlled mostly through f–f electronic transitions [39–44]. Their distinctive optical properties featuring large Stokes and anti-Stokes shifts, narrow and multi-peak emission profiles, and long lifetime and excellent photostability have enabled RENPs to be promising alternatives to conventional organic fluorophores and quantum dots, and widely used in imaging and therapy, as shown in Fig. 8.

3.1 Mechanism of NIR-II Emission

The theories of electronic properties and transitions of RE ions were mostly established by Judd and Wybourne in 1962–1965 [45, 46]. Owing to their similar electron configurations, trivalent RE ions have similar physical and chemical properties. The $4f^n$ electronic states of RE ions are separated by spin–orbit coupling and electronic repulsion to produce a myriad of complex energy levels that allow for an immense possibility of intra-configurational transitions as shown in Fig. 9 [47]. The luminescence of RE ions stems mostly from the specific electronic transitions between the ladder-like energy levels within the 4f orbitals. These f–f transitions are shielded by 5s and 5p electrons and thus produce well-defined atomic-like

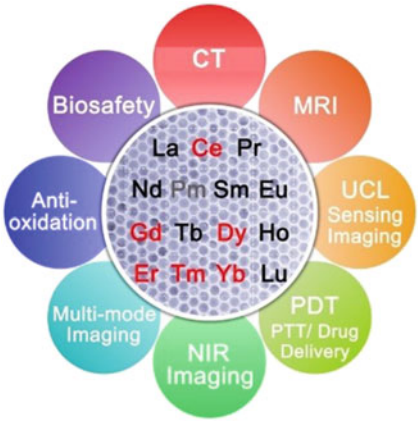

Fig. 8 Schematic illustration of the RE application in imaging and therapy (Reprinted (adapted) with permission from Ref. [40], Copyright 2015, American Chemical Society)

emission spectra which are hardly influenced by the physicochemical properties of the host materials. This unique shielding effect imparts a weak electron–phonon coupling and, thus, narrow-band emission resulting from electronic transitions.

Generally, direct excitation of RE ions is a relatively inefficient process due to the forbidden character of the 4f transitions. The doping technique that involves the introduction of a low concentration of ions (i.e., dopants) into an inorganic crystalline lattice (i.e., host) to obtain doped materials is widely employed to prepare luminescent materials with intense emission. The RE dopants usually act as localized optically active centers that emit at a specific wavelength when excited. These dopants are further divided into sensitizers and activators in the case of sensitized luminescence, where one dopant ion emits radiation from its high energetic state that results from the energy transfer from another dopant ion, as shown in Fig. 10. The dopant ion that gives out emission is described as an activator, while the ion that donates energy to the activator is called the sensitizer. The absorption cross sections of most RE activator ions are relatively low, resulting in low pump efficiency. Thus, a sensitizer ion that exhibits a high absorption cross section is usually used as an energy donor to the activator ion to enhance pump efficiency.

The mechanisms that govern the NIR-II emission originating from energy transfer within the 4f orbitals are broadly divided into two categories based on the involved photon energy and the net number of photons, as shown in Fig. 11: (1) down-conversion (DC) also known as quantum cutting and (2) down-shifting (DS). The DC process refers to a process that involves generation of two or more low-energy photons by splitting one absorbed high-energy photon. The DS process describes a single photon process in which one incident higher-energy photon is converted into one lower-energy photon.

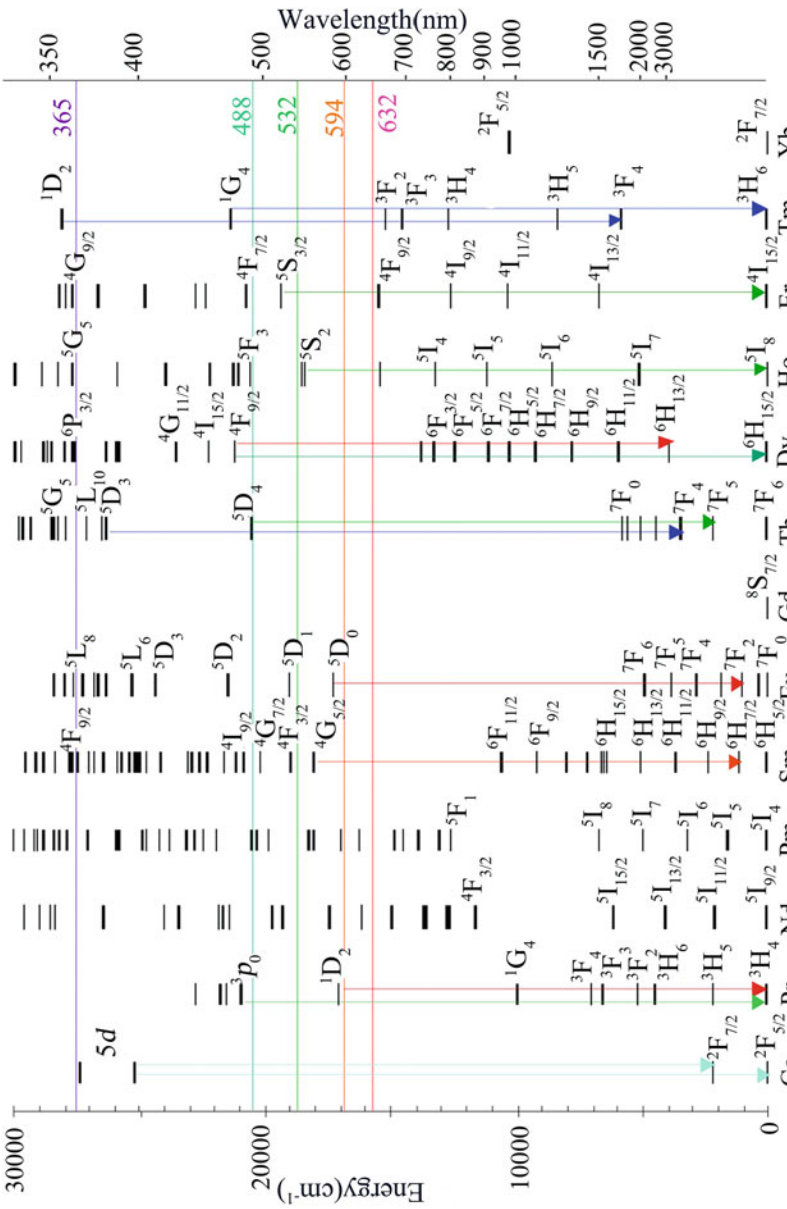

Fig. 9 Energy level diagram of trivalent RE ions with emission transitions (Reprinted (adapted) with permission from Ref. [47], Copyright 2003, National Academy of Sciences)

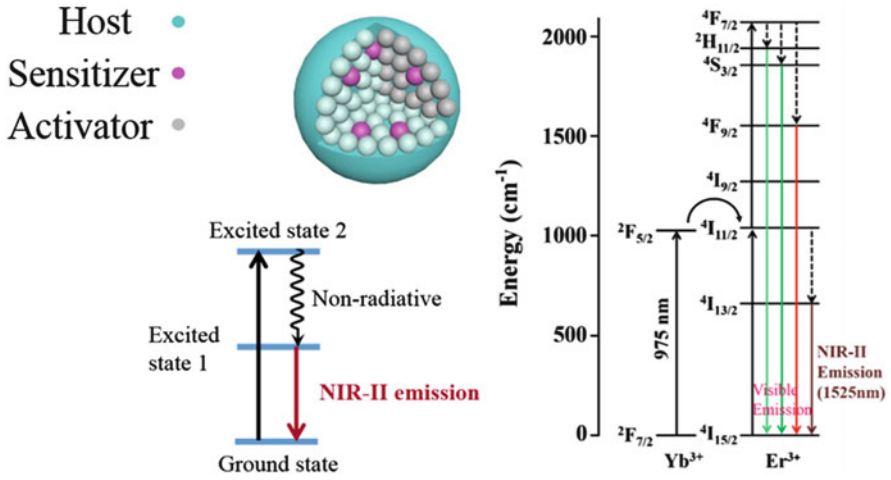

Fig. 10 The general photophysical pathways for NIR-II RENPs in solution and the general mechanism of NIR-II fluorescence emission, taking the sensitizer/activator Yb/Er doped in NaYF4 host as an example

3.2 Synthesis Strategy

Thermal decomposition and solvo(hydro)thermal methods are two methods to synthesize RENPs with controlled physical characteristics and heterostructures by adjusting the role of precursor and solvent chemistries [48–50]. The comparison of thermal decomposition and the solvo(hydro)thermal method is shown in Table 1. Generally, a higher yield of the product is obtained using the solvothermal method, while a narrower size distribution of particles in nanosize (typically sub-20 nm) at a lower yield is obtained using the thermal decomposition method.

Briefly, the thermal decomposition method involves (1) dissolution of organometallic precursors for corresponding fluorides or oxides in high-boiling point organic solvents; (2) removal of residual moisture, oxygen, and other small-molecule impurities in the solution under an inert atmosphere (e.g., N2, Ar); and (3) rapid decomposition of organometallic precursors at a specific elevated temperature leading to rapid nucleation followed by growth (see Fig. 12). Generally, the organic precursors are rare-earth-based organic salts (e.g., trifluoroacetates, oleates). Octadecene (ODE), oleic acid (OA), and oleylamine (OM) are commonly used as high-boiling point solvents. Rapid decomposition of organometallic precursors at the specific temperature allows for the burst of crystal nucleation, which essentially decouples the nucleation from the growth phase. By decoupling nucleation from growth, highly monodispersed nanocrystals are obtained. Further growth of the crystals is limited since most of the precursors are consumed. However, through the Ostwald ripening phenomenon, the small crystals may dissolve and redeposit onto larger crystals resulting in a larger average particle size and a broader size distribution. The crystal nucleation and growth processes are further adjusted using

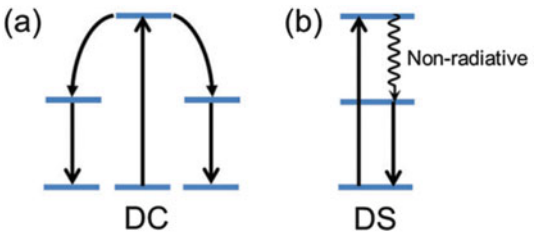

Fig. 11 Schematics of typical NIR-II emission of energy conversion processes for RENP materials: (**a**) down-conversion (DC) and (**b**) down-shifting (DS)

Table 1 Comparison of synthesis parameters and properties of products for both thermal decomposition and solvo(hydro)thermal methods

Category	Thermal decomposition	Solvo(hydro)thermal
Temperature	250–330°C	100–220°C
Time	2 h	48 h
Yield	Up to 1 g	Up to 10 g
Size	Narrow	Broad
Morphology	Sphere, rod, polyhedron	Sphere, rod, polyhedron, spindle
Solubility	Hydrophobic	Hydrophilic/hydrophobic

other processing parameters, such as precursor concentration, solvent composition, heating rate, and reaction time. This approach has been extended as a common route to yield a multitude of high-quality, monodispersed RENPs based on a myriad of hosts including $NaYF_4$, $NaGdF_4$, CaF_2, etc.

Hydrothermal or solvothermal synthesis is a versatile synthesis technique that involves reacting precursors in aqueous or nonaqueous solvent media, respectively, at elevated temperatures (25°C or greater) and pressures (1 atm or greater) to crystallize materials over a broad range of particle sizes directly from solution in a single process step [51–58]. Specialized reaction vessels known as autoclaves are usually required for the solvothermal reaction, in which a high pressure and temperature environment are generated. Generally, highly crystalline phases are prepared at much lower temperatures with higher yields than thermal decomposition method for the synthesis of RENPs. Besides selecting suitable precursors, solvents, reaction conditions (e.g., duration, temperature, pressure), the phase purity, particle size, and morphology of RENPS are tailored with the addition of surfactants.

3.3 Application In Vivo

Highly monodisperse RENPs are typically formed in high-boiling organic solvents. The poor aqueous solubility of surfactant on the surface of the nanoparticles prevents subsequent functionalization for biomedical applications. Surface modification is thus crucial for improving the dispersion of RENPs in water. For example, by encapsulating RENPs with FDA-approved albumin, Naczynski et al. successfully

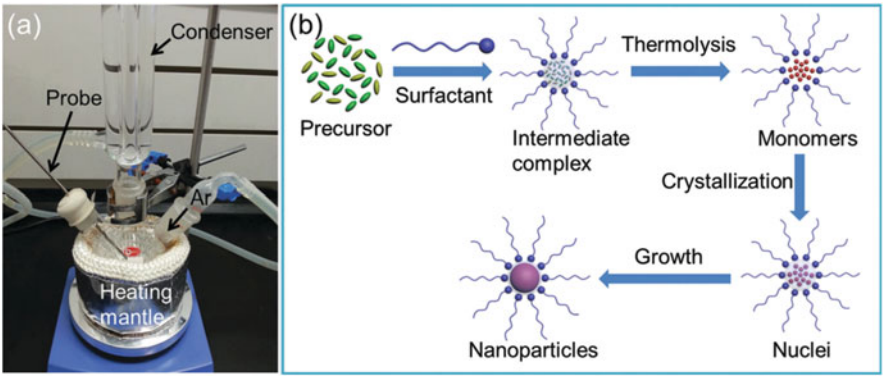

Fig. 12 (**a**) Photograph of the experimental setup for the preparation of RENPs using the thermal decomposition synthesis method. (**b**) Schematic illustration of the formation mechanism of RENPs using the thermal decomposition synthesis method (Reprinted (adapted) with permission from Ref. [39], Copyright 2016, Royal Society of Chemistry)

demonstrate real time, multispectral in vivo NIR-II imaging, which offers anatomical resolution using a library of tunable and biocompatible RENPs (Fig. 13a–d) [23]. This work introduces a new generation of versatile NIR-II nanoprobes that facilitate disease monitoring using minimally invasive NIR-II imaging.

Another novel example reported that DSPE-mPEG-modified rare-earth-doped nanoparticles (RENPs@DSPE-mPEG) show inherent affinity to bone without linking any targeting ligands and, thus, provide an alternative noninvasive and nonradiation strategy for skeletal system mapping and bone disease diagnoses [59]. Besides bone imaging, RENPs@DSPE-mPEG show an imaging application in blood vessels and lymph nodes. Importantly, RENPs@DSPE-mPEG can be internalized by circulating white blood cells. This finding may open a window to increase efficient nanoparticle delivery in the fields such as immunotherapy and improve the diagnostic and therapeutic efficacy of cancer-targeted nanoparticles in clinical applications.

Early tumor detection is crucial for cancer successful treatment. Specific targeting moieties are key factors for surface functionalization of RENPs. For example, targeting NIR-II fluorophores have been prepared by encapsulating RENPs with AMD3100, a hydrophobic small-molecule antagonist of the chemokine receptor CXCR4. These targeting RENPs preferentially localize to receptor-positive tumors in mice, allowing detection of CXCR4-positive tumors four times smaller than receptor-negative tumors (Fig. 13e, f) [25]. These targeted NIR-II fluorophores enable imaging of microlesions in the lungs at a depth of ~1 cm and are able to simultaneously identify the phenotype of the tumor population. This study is significant to functionalize NIR-II RENPs to detect sub-tissue microlesions at an early stage. In another interesting research, RENPs have also been excited by X-ray instead of laser to produce emission light for NIR-II imaging, highlighting their

potential use to obtain both anatomic and molecular information through CT and NIR-II imaging, as shown in Fig. 14 [60].

By now, it is still a great challenge to identify early metastases in cancer diagnostics and therapy. Here, Moghe et al. show that intravenously injected albumin-encapsulated NIR-II RENPs can detect targeted metastatic lesions in vivo, allowing for the longitudinal tracking of multi-organ metastases. In a murine model of human breast cancer, the NIR-II nanoprobes enabled whole-body detection of adrenal gland microlesions and bone lesions that were not available via contrast-enhanced MRI as early up to 5 weeks post-inoculation, respectively (see Fig. 15) [61]. Noninvasive monitoring of gastrointestinal drug release in vivo is another

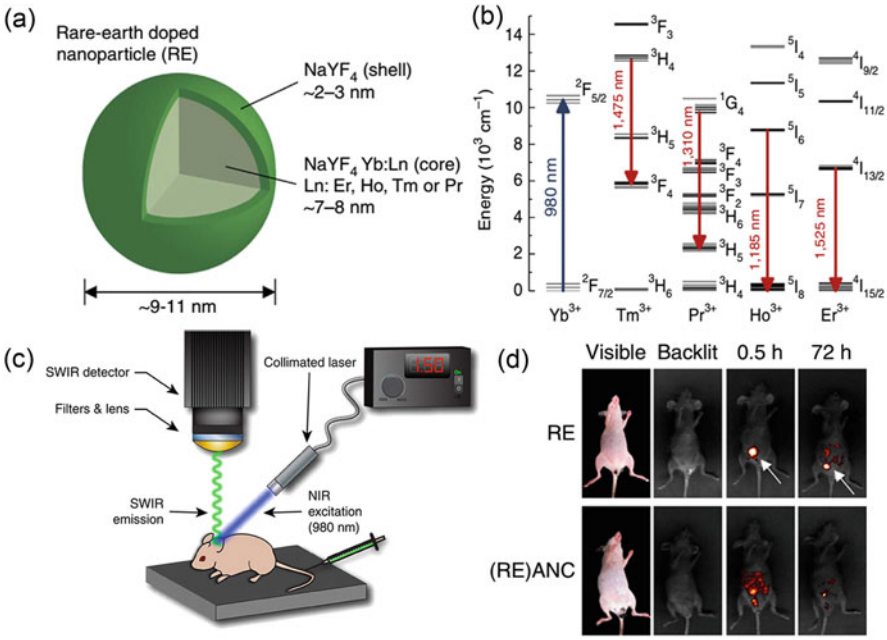

Fig. 13 RENP NIR-II fluorophores and imaging in vivo. (**a**) Rare-earth nanoprobes consist of a $NaYF_4$: Yb:Ln-doped core (Ln: Er, Ho, Tm or Pr) surrounded by an undoped shell of $NaYF_4$. (**b**) Probes consisting of a $NaYF_4$ host doped with Yb, Ho, Pr, Tm, and Er enable emissions at 1,185, 1,310, 1,475, and 1,525 nm, respectively. The emissions of Ho-, Pr-, Tm-, and Er-doped samples are attributed to the $^5I_6 \rightarrow {}^5I_8$, $^1G_4 \rightarrow {}^3H_5$, $^3H_4 \rightarrow {}^3F_4$, and $^4I_{13/2} \rightarrow {}^4I_{15/2}$ transitions, respectively. (**c**) Schematic of the portable NIR-IIb imaging prototype. (**d**) NIR-IIb imaging of REs and (RE) ANCs in a transgenic orthotopic murine melanoma model over 72 h. (**e**) AMD3100 was adsorbed onto the surface of fully formed ReANCs to generate AMD3100-functionalized ReANCs or fReANCs. Athymic nude mice were inoculated with human breast cancer cells through the tail vein. Animals were treated with either ReANCs or fReANCs and NIR-IIB imaging performed to determine nanoprobe–tumor localization. (**f**) Longitudinal tracking of internal lesions with NIR-IIB imaging. Mean and minimum volume of tumors detectable via NIR-IIB imaging was calculated to determine the smallest tumors capable of resolution using the InGaAs camera. (**a**–**d**) Reprinted (adapted) with permission from Ref. [23], Copyright 2013, Nature Publishing Group. (**e**, **f**) Reprinted (adapted) with permission from Ref. [25], Copyright 2015, Wiley-VCH Verlag GmbH & Co. KGaA

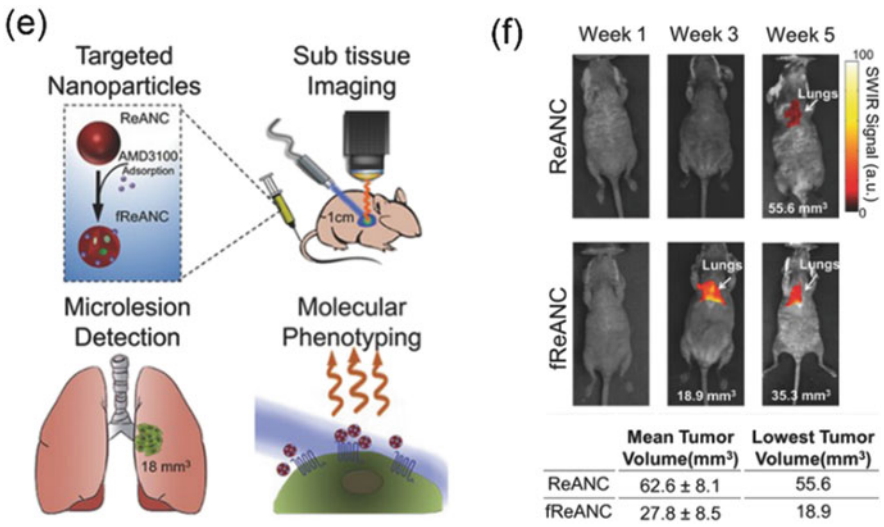

Fig. 13 (continued)

challenge because of the limited spatial resolution and long scanning time of existing bioimaging modalities. Zhang et al. report a novel microcarrier that can retain drugs and withstand the harsh conditions of gastrointestinal tract. Significantly, they can track the microcarrier fate and semiquantitatively monitor the content of drug released in vivo in real time by measuring the fluorescence signals in the second near-infrared window of RENPs with an absorption competition-induced emission bioimaging system. The microcarriers show a prolonged residence time of up to 72 h in the gastrointestinal tract, releasing up to 62% of their content [62].

Current NIR-II fluorophore-related in vivo biodetections are only focused on direct disease lesion or organ bioimaging; it's still a big challenge to realize the NIR-II real-time dynamic biosensing. Very recently, a new type of Er^{3+}-sensitized upconversion nanoparticles with both excitation (1,530 nm) and emission (1,180 nm) located in NIR-II window for in vivo biosensing is developed [63]. Significantly, the microneedle patch sensor for in vivo inflammation dynamic detection is developed based on the ratiometric fluorescence by combining the effective NIR-II upconversion emission and H_2O_2 sensing organic probes under the Fenton catalysis of Fe^{2+}. Due to the large anti-Stokes shifting, low autofluorescence, and tissue scattering of the NIR-II upconversion luminescence, the inflammation can be dynamically evaluated in vivo in real time at high resolution (200 × 200 μm).

RENPs are also attracted to fluorophores utilized for multimodal imaging. For example, Cheng et al. have reported a strategy to enhance the PAI intensity of upconverted nanoparticles (UCNPs) by functionalized with photoswitchable azobenzene-containing poly (acrylic acid) (UCNPs@PAA-Azo) to yield a PAI signal that is up to six times higher than that of UCNPs without a decay in NIR-II emission [64]. Using this nanoprobe, NIR-II imaging provides real-time means for the precise resection of the lymph node (LN) during surgery, where PA imaging

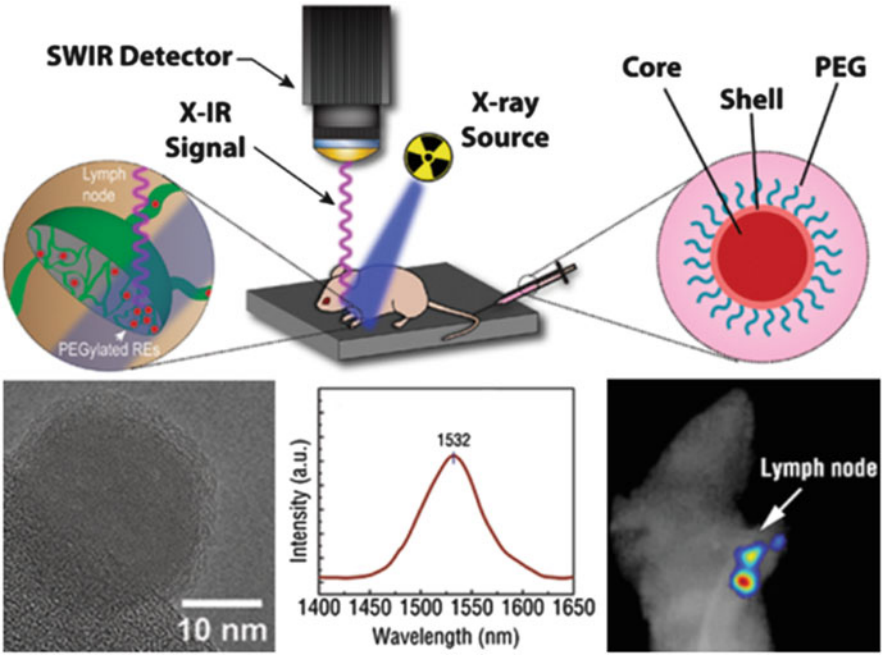

Fig. 14 Distinct focal luminescence is visualized away from the injection site near the animal's axillary and brachial lymph nodes. After dissection, X-IR signal could be traced to the local lymph nodes draining from the injection site (Reprinted (adapted) with permission from Ref. [60], Copyright 2015, American Chemical Society)

allows for quicker (up to 30 min) detection of LNs than that through NIR-II imaging. Combining the advantages of dual NIR-II and PA modalities allows us to achieve complementary information and improve the accuracy of disease diagnosis.

Although RENPs have been widely used in bioimaging for diagnostics, the optical efficiency of these RENPs is, however, quite low (<0.5%), and there is ample scope for this to be improved to maximize the full potential benefits of RENP-based bioimaging. For example, hybrid organic–inorganic nanocrystals incorporating the contrast agent ICG demonstrate a large Stokes shift (>200 nm) with multiple narrow band emissions in the NIR-II range. The ICG not only enhances the NIR-II brightness by ∼fourfold but also produces a broad excitation band at 700–860 nm [26].

4 QDs

The semiconductor nanocrystals, quantum dots (QDs), exhibit unique size-dependent optical and electronic properties originating from quantum size effect [65–70]. QDs have proven to be powerful tools for bioimaging and bioanalysis

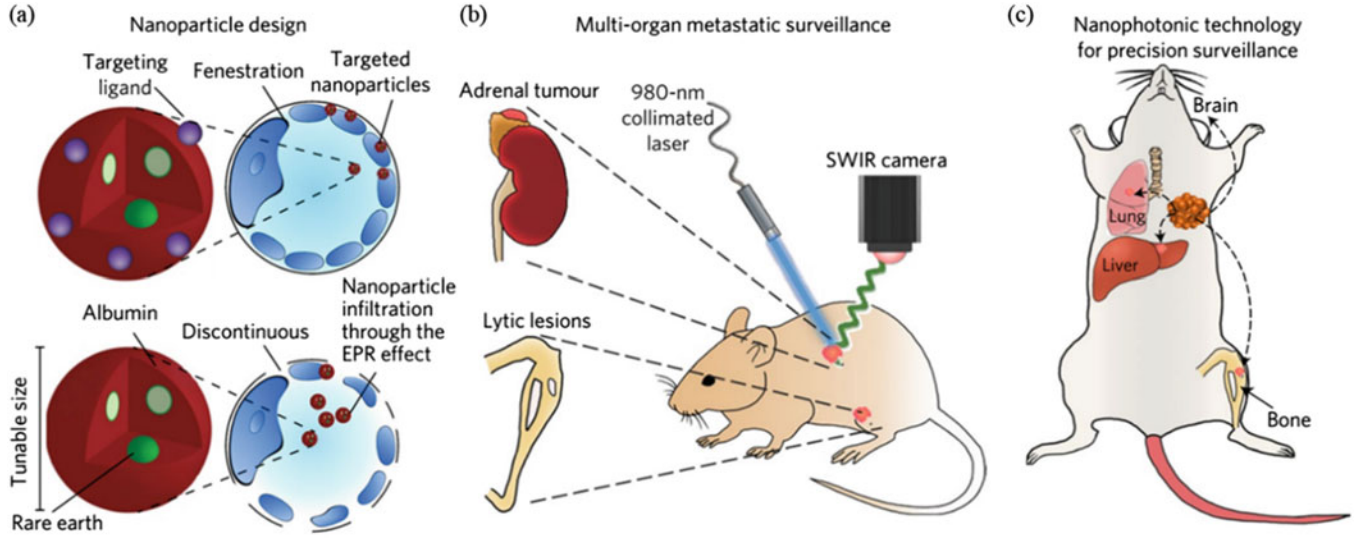

Fig. 15 Design and workflow of photonic nanotechnology for cancer metastasis detection and profiling. (**a**) Distinct nanoparticles were designed with rare-earth-doped cores for different tissue microenvironments to enable whole-body screening based on deeper tissue-emanating shortwave infrared emissions. (**b**) When administered in vivo to biomimetic breast cancer models, these nanoparticles are targeted to reach multi-organ metastatic sites across different pharmacologic barriers. (**c**) Metastatic lesions (in the long bones or adrenal glands) can be detected earlier than with conventional methods (bioluminescence, MRI, CT), and molecular changes in cancer cell signatures can be obtained, forming the basis for future metastatic-site-specific, personalized cancer therapies. (**a**–**c**) Reprinted (adapted) with permission from Ref. [61], Copyright 2017, Nature Publishing Group

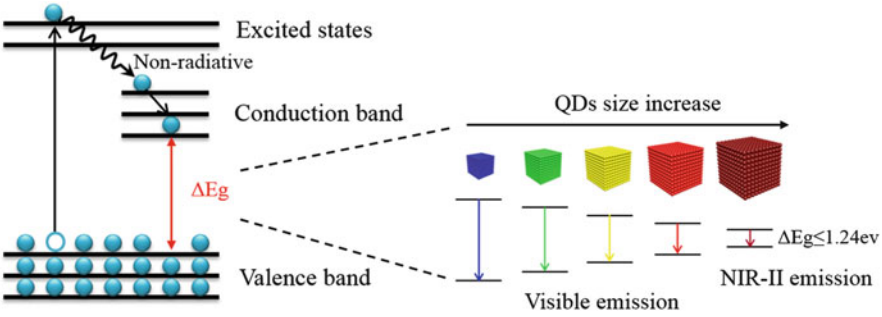

Fig. 16 The photophysical pathways for QD NIR-II fluorophores in solution and the mechanism of NIR-II fluorescence emission

because of their high photostability, broad absorption range, large extinction coefficient, and narrow, tunable emission wavelengths. In addition, among the NIR-II emitting probes reported until now, QDs show the highest NIR-II fluorescence quantum yields (up to 15.5%) [19].

4.1 Mechanism of NIR-II Emission

The emission wavelengths could be rationally tuned by changing the QDs' sizes and compositions. Since the excitons are confined in all three spatial dimensions, the electrons of QDs are quantized to certain energies, similar to those of organic dyes. As the confinement energy depends on the quantum dots size, both absorption onset and fluorescence emission can be tuned by changing the size of the QDs during synthesis process. Based on the quantum confinement effect arising from their small dimensions, the bandgap of QDs can be easily tuned (see Fig. 16). Fluorescence occurs when an excited electron relaxes to the ground state, so the excitation and emission of QDs can be easily modulated by changing the diameters, composites, or structures, resulting in broad absorption spectra with narrow, symmetric, and tunable emission spectra spanning the NIR-II region. Compared to organic dyes, QDs are characterized by large Stokes shifts, which allow overlap of the excitation and the emission spectra to be effectively avoided.

4.2 Synthesis Strategy

The QDs are typically composed of elements from groups ii–vi or iii–v [71]. Currently, key factors concerning the design and synthesis of QDs available for bioimaging include larger absorbance at a wavelength >400 nm with emission at >1,000 nm; high QYs; water solubility or easy functionalization; good colloidal

stability and photostability; relatively small size; and absence of toxic metallic elements. So far, the methods for the preparation of NIR-II QDs can be mainly divided into two major strategies: the organometallic route and aqueous synthesis approaches [72–75]. Different reaction conditions, such as temperature, hot injection time, precursor reagents, and exchange ligands, have been utilized to prepare NIR-II QDs with diverse components. As QDs synthesized in the organic phase usually have very poor water solubility and biocompatibility, the synthesis of QDs in aqueous solution has become an alternative option, which also has the advantages of convenience, easy control, reproducibility, low cost, and large-scale preparation. Because of the poor crystal quality with nonuniform particle size, broad spectra, and low QYs of the resulting QDs, this method still requires improvement. Great efforts have been made toward water solubilization and biofunctionalization of chemically synthesized QDs. The employment of biological systems as the reaction platforms has three distinctive features: (1) intrinsic generation of metal-reducing and metal-binding agents with the capability of reducing metal ions, (2) easy modulation of the platform by means of genetic engineering for the expression of specific biomolecules to regulate the QD growth and fluorescence emission, and (3) moderate reaction conditions without the involvement of high-temperature and rigorous deoxygenation. In general, the biocompatible QDs may be prepared through three different approaches: (1) using living organisms ranging from prokaryotes to eukaryotes as the bioreactors, (2) using of either artificial cellular structures or functional biomolecules as the templates, and (3) surface modification of QDs. Among them, the biosynthesis approach provides a green route to prepare biocompatible QDs without the involvement of harsh reaction conditions or toxic chemicals.

4.3 Application In Vivo

In quantum dots in types III–V, InAs and InGa are the two typical ones possessing outstanding optical properties as well as significantly lower intrinsic toxicity compared to other NIR QDs containing elements such as mercury or lead. So, they have played an important role in biomedical and bioanalytical application. For example, Bawendi has reported a class of high-quality NIR-II-emissive indium-arsenide-based quantum dots that are readily modifiable for various functional imaging applications and that exhibit narrow and size-tunable emission and a dramatically higher emission quantum yield than previously described NIR-II probes (Fig. 17) [71]. To demonstrate the unprecedented combination of deep penetration, high spatial resolution, multicolor imaging, and fast acquisition speed afforded by the NIR-II quantum dots, they quantified, in mice, the metabolic turnover rates of lipoproteins in several organs simultaneously and in real time, as well as heartbeat and breathing rates in awake and unrestrained animals, and generated detailed three-dimensional quantitative flow maps of the mouse brain vasculature.

Ag_2S is a promising NIR-II fluorescent QD in the preclinical research because of its nontoxic heavy metal and high uptake in tumors (Fig. 18e) [19]. In surgical

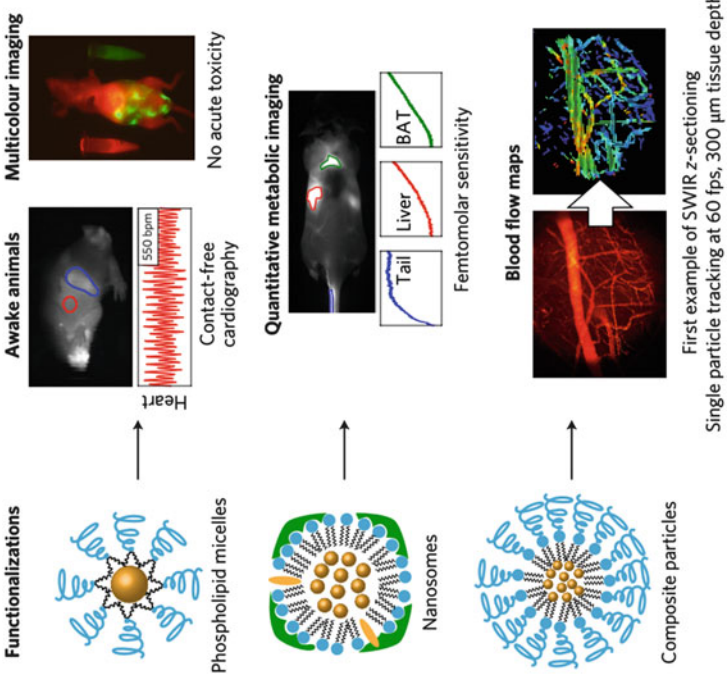

Fig. 17 A schematic overview of the synthesis of core–shell and core–shell–shell NIR-II quantum dots and the subsequent functionalization for next-generation imaging applications is shown. InAs QDs were synthesized via a continuous injection approach, which allows for improved nanocrystal growth over a long time at high reaction temperatures. Subsequently, InAs core QDs were overcoated with various shell materials to allow for a further red-shift and fine-tuning of the emission. The class of synthesized core–shell and core–shell–shell QDs were then functionalized via three distinct surface coatings that tailor the physiological properties for specific SWIR imaging applications. *bpm* beats min^{-1}. Reprinted (adapted) with permission from Ref. [71], Copyright 2017, Nature Publishing Group

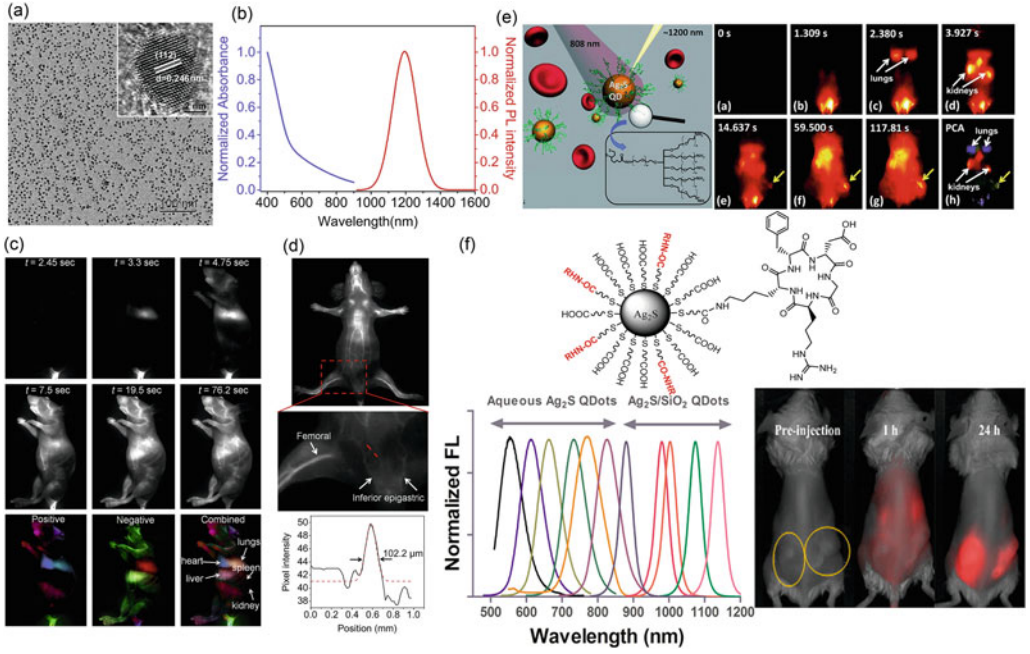

Fig. 18 Advancement of QDs NIR-II fluorophores and imaging in vivo. (**a**) TEM and HR-TEM image of monodispersed PEGylated Ag_2S QDs. (**b**) Absorbance and photoluminescence spectra of PEGylated Ag_2S QDs. (**c**) Time-course NIR-II fluorescence images of blood flow in the nude mouse after injection of PEGylated Ag_2S QDs (1 mg/mL, 200 mL) and dynamic contrast-enhanced images with PEGylated Ag_2S QDs based on PCA analysis. (**d**) Intravital NIR-II fluorescence image of the nude mouse in supine position. The PL signal from the Ag_2S QDs is easily distinguishable from the endogenous autofluorescence without any image processing. (**e**) Scheme showing the 6PEG-Ag_2S QDs that emit at 1,200 nm upon excitation at 808 nm, and the time course of NIR-II fluorescence as well as dynamic contrast-enhanced image based on PCA. (**f**) Schematic of the conjugation of cRGDfK-Ag_2S QDs and the temporal evolution of the optical properties of Ag_2S QDs and Ag_2S@SiO_2. In vivo fluorescence imaging of cRGDfK-Ag_2S in tumor bearing mouse at 1 h and 24 h points after intravenous administration, showing the excellent targeting tumor in NIR-II window. (**a**–**d**) Reprinted (adapted) with permission from Ref. [20], Copyright 2014, Elsevier B.V. (**e**) Reprinted (adapted) with permission from Ref. [19], Copyright 2012, Wiley-VCH Verlag GmbH & Co. KGaA, Weinheim. (**f**) Reprinted (adapted) with permission from Ref. [22], Copyright 2012, American Chemical Society

treatment, assessment of blood supply in tissues and screening of anti-angiogenic drugs provide new blood vessels formation, both around and within tumors. In addition, Ag_2S QD-based NIR-II imaging shows excellent clarity and penetration depth for visualizing lymphatic vessels and lymph nodes during sentinel lymph node resection than the FDA-approved, clinical standard contrast agent, ICG-based NIR-I imaging (Fig. 18a–d) [20]. Ag_2S QDs are also able to track and visualize mesenchymal stem cell (MSC) populations during intricate biological processes [21]. It provides a promising method to monitor the MSCs transplantation and acquires the important information about cell dynamics and interactions with the host central nervous system. Furthermore, Ag_2S QDs offer a chance for enhancing both early disease diagnosis sensitivity and identification of lesions by targeting functional molecules. For example, pentapeptide can bind to αVβ3 integrin receptor on tumor cells. The pentapeptide conjugated Ag2S QDs show a significant enhancement in sensitivity in NIR-II imaging specific tumor sites (Fig. 18f) [22].

In multimodal imaging field, QDs show a great potential application in preclinical research. Recently, Li et al. have reported a Gd–Ag2S nanoprobe that combines deep-tissue penetration capability of MRI with high spatiotemporal resolution of NIR-II fluorescence imaging (Fig. 19a–c) [76]. The localization of the brain tumor can be clearly delineated preoperatively using MRI signal generated from Gd component in the nanoprobe, and then precise resection of the tumor can be guided by intraoperative NIR-II fluorescence imaging produced by Ag_2S.

Photoacoustic imaging (PAI) is an emerging optical imaging modality in which absorbed photon energy is converted into acoustic waves that are detected using ultrasound. PAI provides higher spatial resolution and better contrast than conventional optical imaging techniques, because ultrasound scattering in tissues is lower by 2–3 orders of magnitude than optical scattering. A new PAI/NIR-II nanoprobe, ICG@PEG-Ag_2S, has recently been prepared recently [77]. This nanoprobe showed relatively long blood retention up to 7 h and was selectively accumulated in the region of atherosclerotic plaque due to the lipophilicity of the C18 chain to the atherosclerosis microenvironment, and thus the atherosclerosis was monitored real time by high contrast-enhanced PAI of ICG. Combining the high signal-to-noise ratio (SNR) and high spatial resolution fluorescence imaging of Ag_2S QDs in the NIR-II, the feasibility of this new nanoprobe for atherosclerosis targeting is achieved. Such a simple, multifunctional nanoprobe for targeting and PAI of atherosclerosis will have a great potential for future clinical applications. Ag_2S QDs are not only used for NR-II fluorescence imaging but also in therapy. For example, hollow nanocage multifunctional Ag_2S nanodots are synthesized by precisely controlled crystal growth in the presence of human serum albumin [78]. Ag_2S nanodots exhibit size-dependent temperature elevations and have high photothermal conversion efficiencies of 33.7–35.0%, which are comparable with those of most other photothermal nanoparticles, such as Au nanorods (up to 22.8%) and ICG-loaded micelles (up to 25.2%). In drug delivery, Ag_2S QDs also demonstrate perfect drug release under NIR-II excitation. For example, a smart Ag_2S QDs nanoplatform (DOX@PEG-Ag_2S) has been obtained by loading the anticancer drug into polyethylene glycol functionalization Ag_2S QDs (PEG-Ag_2S QDs). The Ag_2S QDs had up

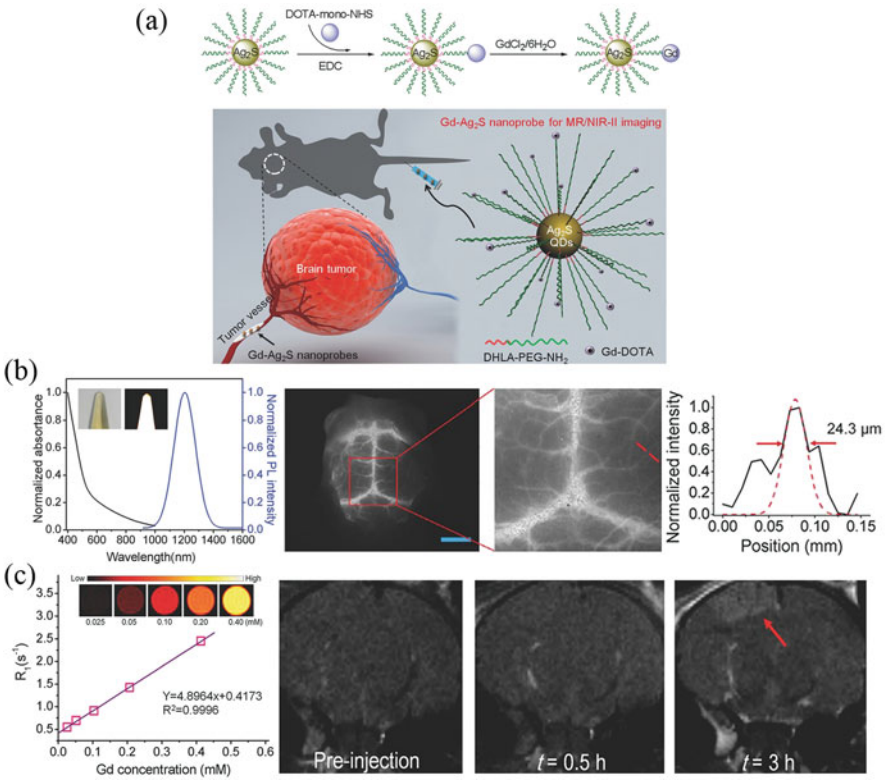

Fig. 19 (**a**) Schematic illustration of the procedure for preparing Gd–Ag_2S nanoprobe and the diagram of brain tumour targeting of Gd–Ag_2S nanoprobe. (**b**) Absorption and emission spectra of Gd–Ag_2S nanoprobe. (**c**) Intravital NIR-II fluorescence image of the brain vessels in the nude mouse (left). Amplified fluorescent image of vasculature in the nude mouse (middle). A cross-sectional intensity profile measured along the red-dashed line in (middle) with its peak fitted to Gaussian functions (right). Scale bar represents 3 mm. Relaxation rate R1, the inset shows a T1 map of a MR imaging phantom containing Gd-Ag_2S nanoprobe with different concentrations. In vivo progressive T1-weighted MR images of the U87MG brain tumour at different time points from transverse view and immunohistochemical staining of vessels in brain tissues and tumour tissues with anti-VEGF antibody. Red arrows indicate the tumour. (**a–c**) Reprinted (adapted) with permission from Ref. [76], Copyright 2015, Wiley-VCH Verlag GmbH & Co. KGaA

to 93 wt.% drug loading capability, long half circulation time in blood, and more than 8.9% ID/g passive tumor-targeting efficiency in living mice [79]. Another NIR-II QDs have also been actively pursued in NIR-II imaging. By controlling core size, it is possible to prepare PbS/CdS core-shell ligand-coated QDs with a high quantum yield of 17% and extremely bright NIR-II (1,100–1,300 nm) emission. These NIR-II QD probes increase the signal-to-noise ratio tenfold when imaging blood vasculature in mouse brain and lymphatic vasculature in mouse hindlimb [80].

5 SWCNTs

Single-walled carbon nanotube (SWCNTs) can be pictured as a single graphene sheet rolled up seamlessly into a nanocylinder with its diameter ranging from less than 1 nm to a few nanometers. SWCNTs have unique intrinsic physical and chemical properties such as Raman scattering cross sections and UV/visible/NIR absorption [27, 29, 81]. SWCNTs have shown potential for biological and medical applications because of their intrinsic ability to load both targeting ligands and chemotherapy drugs, in vitro and in vivo. Because of van Hove transitions across bandgaps, semiconducting SWCNTs demonstrate intrinsic fluorescence in the NIR-II window, which are ideal as biological probes because of the inherently low autofluorescence and large Stokes shift between the excitation and emission bands, which allows excitation in the biological transparency window near 800 nm while further reducing the background effects of autofluorescence and scattering.

5.1 Mechanism of NIR-II Emission

Due to the quantum confinement along the transverse direction of a single carbon nanotube, which can be considered as a quasi-one-dimensional nanomaterial, SWCNTs feature very sharp maxima of electronic density of states (DOS) called van Hove singularities in their energy band diagrams. The energies of van Hove maxima of SWCNTs in a band diagram are mainly dependent on the diameter of the nanotube and the chiral angle at which the specific nanotube is rolled up from a single graphene sheet with 2D honeycomb structure (Fig. 20a) [82]. The band diagram of a semiconducting SWCNT shown in Fig. 20b show great detail to fully understand the NIR-II photoluminescence process, which can be described in three consecutive steps:

First, an SWCNT absorbs a photon with the photon energy matching the bandgap of the E_{22} transition, which is the difference in energy between the second valence band V_2 and the second conduction band C_2. The absorption of this excitation photon leads to the excitation of an electron, leaving a hole behind. The excited electron and the remaining hole form a bound pair called an exciton that is held by the exciton binding energy.

Second, the electron and the hole undergo rapid nonradiative relaxations to the lowest level in both valence and conduction bands.

Lastly, the bound pair of electron and hole travel together along the length of the nanotube through diffusion until they recombine radiatively to give off a fluorescence photon with its energy corresponding to the bandgap across E_{11} minus the exciton energy.

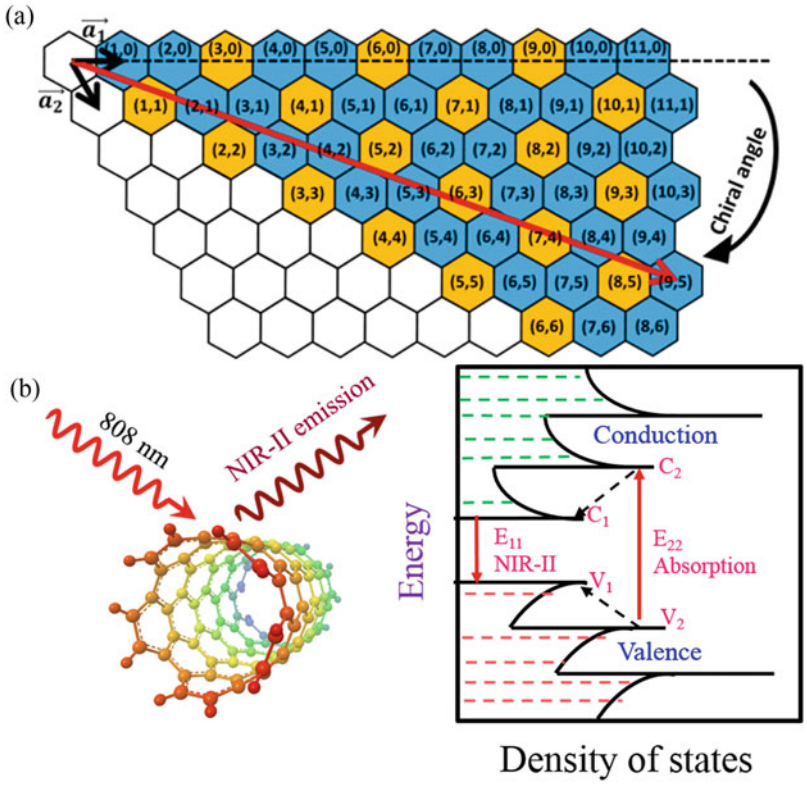

Fig. 20 The photophysical pathways for SWCNTs NIR-II fluorophores in solution and the mechanism of NIR-II fluorescence emission. (**a**) Honeycomb structure of graphene showing different roll-up vectors (red arrow) result in different (*n*, *m*) indices or chiralities (numbers labeled in each hexagon). (**b**) Band diagram of a semiconducting SWCNT. NIR-II emission wavelength of in a bandgap is mainly dependent on the diameter of the nanotube and the chiral angle. (**a**) Reprinted (adapted) with permission from Ref. [82], Copyright 2015, American Chemical Society. (**b**) Reprinted (adapted) with permission from Ref. [4], Copyright 2018, The Royal Society of Chemistry

5.2 Synthesis Strategy

Photoluminescence wavelengths of SWCNTs depend on the diameter of SWCNTs, which lie on the synthetic routes such as the ranges of 900–1,400 nm for high-pressure CO (HP co) decomposed SWCNTs (Fig. 21a), 1,500–1,700 nm for laser ablation SWCNTs (Fig. 21b), and 1,600–1,900 nm for arc discharge SWCNTs (Fig. 21c) [82].

Briefly, the arc discharge method was firstly used in synthesis of SWCNTs by Sumio Iijima in 1991 [83]. In this process, two graphite rods are placed in an enclosure that is filled with inert gas at low pressure (between 50 and 700 mbar).

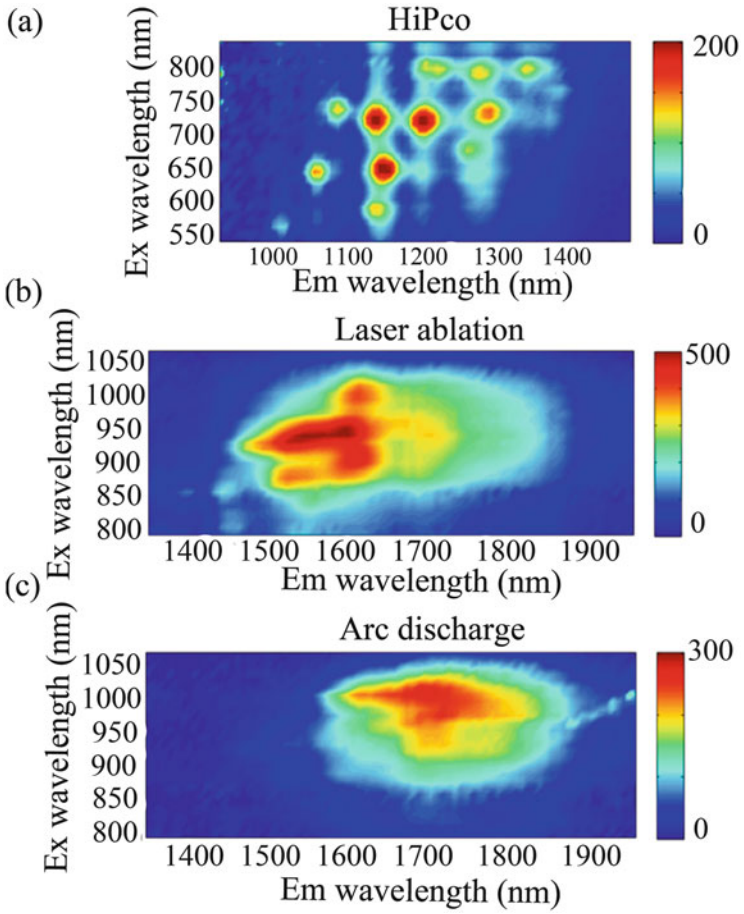

Fig. 21 Photoluminescence-versus-excitation plots of HiPco (**a**), laser ablation (**b**), and arc discharge (**c**) SWCNTs, with progressively increasing diameter distribution. (**a**–**c**) Reprinted (adapted) with permission from Ref. [82], Copyright 2015, American Chemical Society

The carbon rods act as electrodes which are kept at different potentials. The anode is moved close to the cathode until an arc appears, and the electrodes are kept at the distance of 1 mm for the whole duration of the process that takes about 1 min. After the de-pressure and cooling of the chamber, the nanotubes can be collected. The synthesis product yield is up to 60%. In 1995 Richard E. Smalley and his group used laser ablation method to grow high-quality SWCNTs [84]. During the process, intense laser pulses ablate a carbon target is heated to 1,200°C. Inert gas flow in the chamber will carry the grown nanotubes to the copper collector. After cooling of the chamber, the nanotubes and the by-products, like fullerenes and amorphous carbon overcoating on the sidewalls of nanotubes, can be collected. In 1999 Richard

E. Smalley and his co-workers developed high-pressure carbon monoxide method called HiPco for the synthesis of carbon nanotubes [85]. In this process, carbon monoxide acts as a feedstock, and iron carbon monoxide $Fe(CO)_5$ acts as a catalyst. With the HiPco method, the thinnest SWCNTs with high quality, few structural defects, and high intrinsic selectivity are obtained.

5.3 Application In Vivo

Generally, SWCNTs require surface functionalization with water-soluble polymers or proteins that allow them to be nontoxic [27, 28]. In 2009, NIR-II probes were prepared by coating SWCNTs with phospholipid–polyethylene glycol. This indicates the beginning of the use of SWCNTs for NIR-II imaging (Fig. 22a, b) [27]. Since then, SWCNTs have been extensively used for tumor-specific imaging and mouse organ registration (Fig. 22c–f) [28] with higher spatial resolution than that afforded by in vivo microCT (Fig. 22g–h) [29, 31]. In mouse cerebral vasculature NIR-II imaging, SWCNTs have shown the great promising with high spatial ($<$10 μm) and temporal ($<$200 ms per frame) resolution, at a depth of $>$2 mm (Fig. 22k) [30]. This is a truly noninvasive procedure at molecular level for real-time dynamic cerebrovascular imaging. By laser vaporization method, SWCNTs with smaller bandgaps and larger average diameters (up to 1.24 nm) were recently synthesized. At a depth of up to 3 mm in mouse hindlimb, SWCNTs allow in vivo vascular NIR-II imaging with high spatial resolution up to 4 mm. Single-vessel-resolved blood flow speed mapping for multiple hindlimb arterial vessels has also been obtained simultaneously by video-rate fluorescence NIR-II imaging (Fig. 22i, j) [32]. Moreover, in the range up to 1,700 nm, this probe may provide high-performance in vivo NIR-IIb imaging.

By creating targeted bright NIR-II emission SWCNTs, the sensitivity can be improved for early detection. For example, a multifunctional M13 phage has been assembled with SWCNTs via π–π interactions for use as a ligand for targeted NIR-II imaging of tumors. Targeting M13-SWCNTs improves the uptake up to fourfold in prostate-specific membrane antigen-positive prostate tumors compared to nontargeted SWCNTs. In addition, it can identify sub-mm tumors that are not easily identified by either visible or NIR-I fluorophore [86]. Other suitable targeting strategies, such as analyte-specific receptors, have been developed for detecting changes in NO level in response to wound-induced tissue inflammation (Fig. 22l) [33]. In one study, SWCNTs have great promising application in NIR-II imaging guidance for cancer resection [86]. In this research, many sub-millimeter tumor nodules are discovered in NIR-II image-guided system compared with non-image-guided system. In addition, NIR-II imaging observes low tissue autofluorescence, which enhances target-to-background ratios and allows detection of small tumor nodules in confined anatomic regions. However, SWCNTs have a broad absorbance overlap in the NIR-II region, which may cause NIR-II loss. Then, how to increase the quantum yields will be a major focus for SWCNTs application in vivo.

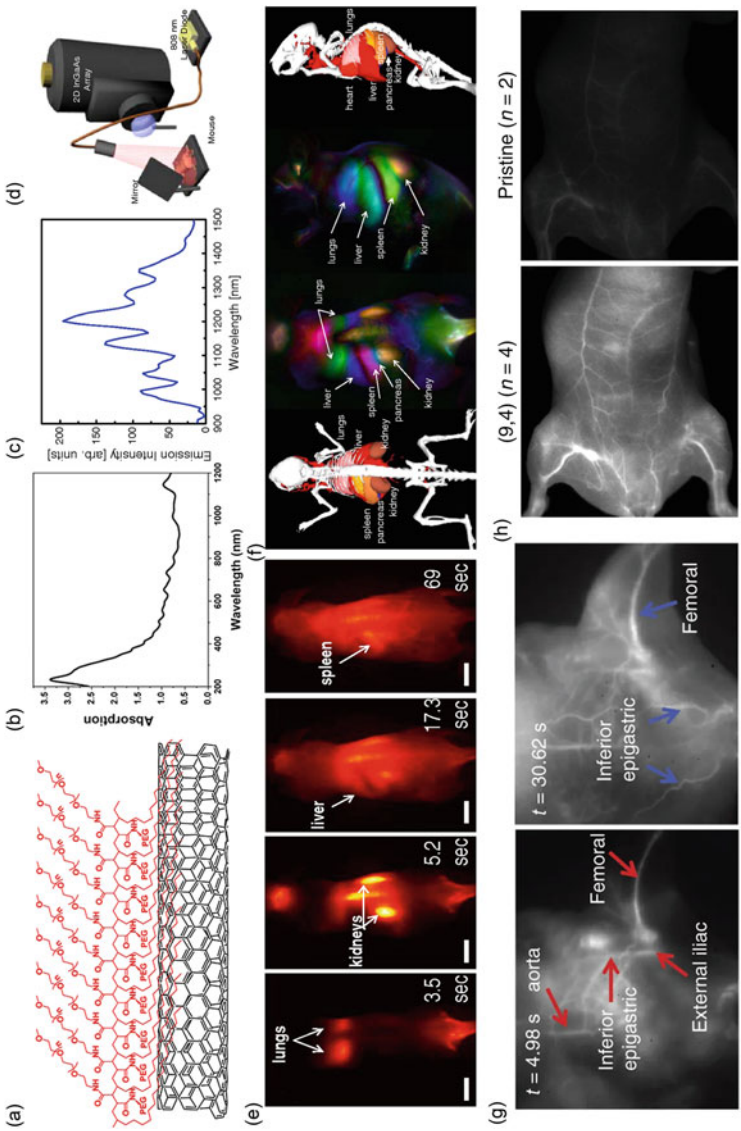

Fig. 22 Progress of NIR-II fluorophores SWCNTs and imaging in vivo. (**a**) Schematic of the water-soluble SWCNTs conjugated with C_{18}-PMH-mPEG (90 kDa). (**b**) UV-Vis-NIR absorption spectrum of the SWCNTs. (**c**) Fluorescence spectrum of biocompatible SWCNTs excited at 808 nm, showing several emission peaks spanning the NIR-II region. (**d**) Schematic of NIR-II imaging setup. NIR fluorescence (1,100–1,700 nm) is filtered and imaged onto a 2D InGaAs array. (**e**) Video-rate imaging of SWCNTs in a live mouse. Frames from video imaging of mice injected with SWCNTs. (**f**) Dynamic contrast-enhanced imaging with SWCNTs through PCA. (**g**) Time course NIR-II fluorescence images showing blood flow labelled by SWCNTs fluorescent tags. (**h**) High-efficiency

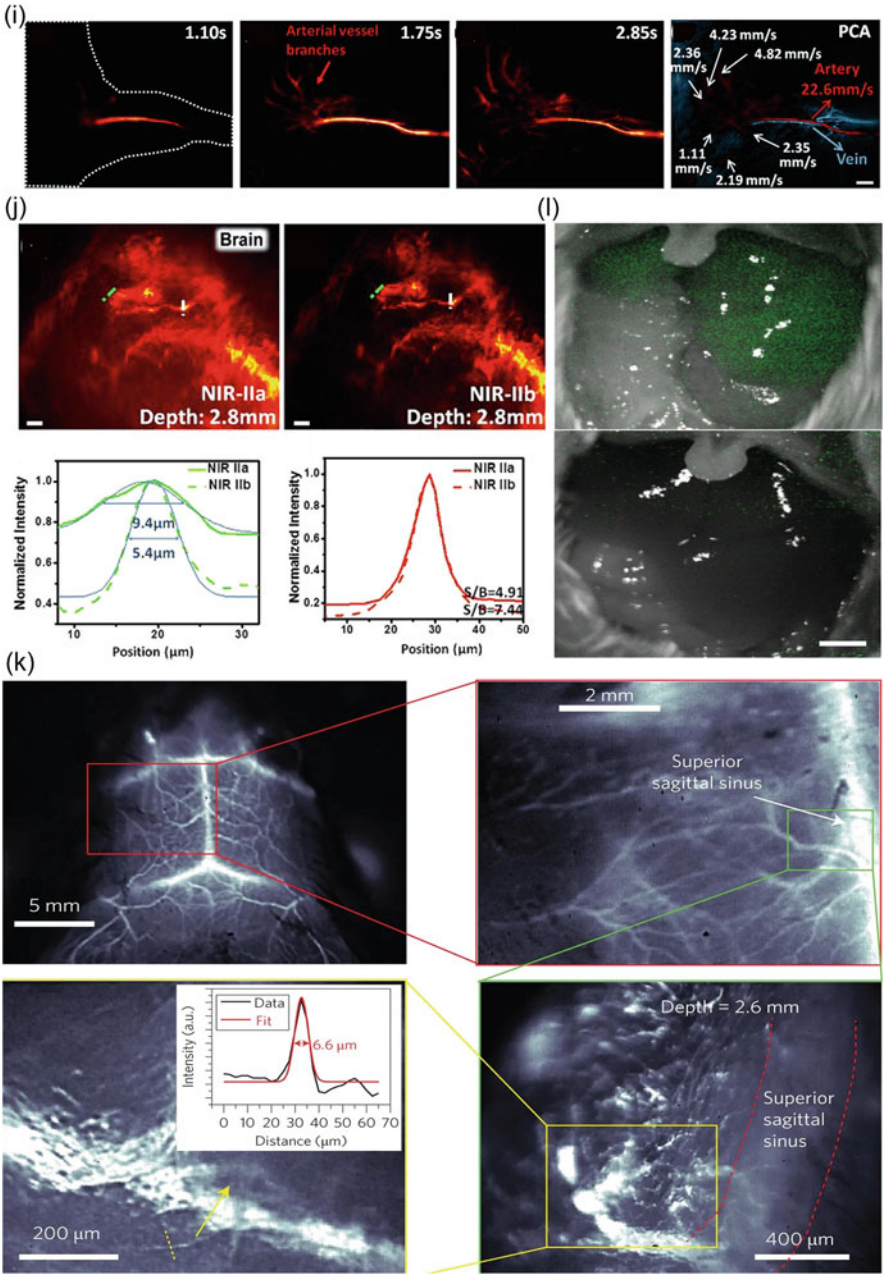

Fig. 22 (continued) bioimaging using single-chirality (9,4) SWCNTs. (**i**) Video rate NIR-IIb fluorescence imaging of mouse hindlimb vessels ($n = 3$) and dynamic contrast-based vessel-type differentiation. PCA overlaid image showing the differentiation of arterial (red) and venous (blue) vessels (scale bar: 2 μm). (**j**) High-magnification vessel imaging of the brain of mice in the NIR-IIa

6 Perspective

Organic dyes and inorganic particles in NIR-II range emission have been designed and synthesized. To expand and accelerate the applications of NIR-II imaging from experimental animal models to clinical translatability and applicability, in particular, for the understanding of design and synthesis mechanism and pathways in living organisms, several key points should be noted.

1. NIR-II imaging clinical translation: Preclinical research is the first step on the way to translate NIR-II imaging techniques into clinic. Conventional NIR-I dye ICG has been demonstrated to be capable for NIR-II imaging, which makes quick clinical translation of NIR-II imaging highly feasible. However, the photostability, NIR-II efficiency, in vivo pharmacokinetics, as well as the targeting specificity should be optimized before the clinical application. In addition, how to via chemical functionalize the ICG structure leading to emission peak red shift into NIR-II region will be great significance. Moreover, bioconjugation ICG to targeting ligands will be the highly useful visualization of specific structures during cancer screening or image-guided surgery.
2. Design and synthesis of new NIR-II fluorophores: High quantum yield, physiochemical stability, photostability, and non-biotoxicity are the first several important criteria to be considered for designing new generation of NIR-II fluorophores. In addition, the direct synthesis of NIR-II fluorophores with targeting group rather than post-synthetic surface targeting modifications is more effective in improving therapeutic efficacy. Synthesis of biodegradable NIR-II fluorophores should be encouraged. The biological use of these NIR-II fluorophores was only recently reported, and further improvements are required, including their synthesis process according to the FDA's current GMP regulations.
3. Multimodal imaging: The NIR-II penetration depth is still limited in 10 mm. Combining with other imaging mobility is an alternative method to achieve higher-resolution images. Considering PET can be used in preoperative imaging,

Fig. 22 (continued) and NIR-IIb windows. Scale bars: 40 μm. (**k**) Noninvasive, high-resolution NIR-IIa fluorescence imaging of mouse brain vasculature from low magnification to high magnification of cerebral vascular image taken at the depth of 2.6 mm. (**l**) Bright-field/NIR-II fluorescence (green) overlaid images showing a healthy mouse liver (top) and a mouse liver with inflammation (bottom), with clear quenching of the NIR-II fluorescence due to inflammation. (**a**, **b**) Reprinted (adapted) with permission from Ref. [27], Copyright 2012, American Chemical Society. (**c**–**f**) Reprinted (adapted) with permission from Ref. [28], Copyright 2011, National Academy of Sciences. (**g**) Reprinted (adapted) with permission from Ref. [29], Copyright 2012, Nature Publishing Group. (**h**) Reprinted (adapted) with permission from Ref. [31], Copyright 2016, Nature Publishing Group. (**i**, **j**) Reprinted (adapted) with permission from Ref. [32], Copyright 2015, Wiley-VCH Verlag GmbH & Co. KGaA. (**k**) Reprinted (adapted) with permission from Ref. [30], Copyright 2014, Nature Publishing Group. (**l**) Reprinted (adapted) with permission from Ref. [33], Copyright 2013, Nature Publishing Group

and NIR-II can be used in intraoperative real-time imaging in high-resolution PET/NIR-II imaging and will likely bring high impact to the patient imaging and image-guided therapy. It would be important to test the advantages of PET/NIR-II dual-modal probes in clinic. PAI has the both excellent advantages of optical and ultrasonic imaging due to the high spatial resolution and low scattering of acoustics. It provides a novel way to link different imaging systems at deeper penetration depth. It is expected that PAI/NIR-II dual-modal imaging will make rapid progress, because many dyes can serve as reporters for both PAI and optical imaging. By now, NIR-II-based three-modal imaging systems (e.g., NIR-II/MRI/PET or NIR-II/PET/PAI) are still unknown on how to design, but such multi-modal imaging systems hold great promise for acquiring complementary information. For example, with an NIR-II/MRI/PET trimodal imaging system, the high sensitivity and unlimited penetration depth of PET could be used for whole-body screening and then reduce the volume of tissue that needs to be scanned. MRI involves no radiation, and high-resolution images could be obtained. NIR-II imaging would provide real-time imaging and molecular and functional information on diseases. It is noted that the integration of several imaging modalities into one system is a great challenge due to the different hardware and the imaging mechanisms.

4. NIR-II-based guide therapy: Compared with the visible imaging, one of the most advantages of NIR-II imaging is that the photon scattering and autofluorescence background are very low. So, in my opinion, intraoperative NIR-II image-guided surgery will be the most likely to be the clinical application. In addition, it will be helpful to integrate other clinic imaging modalities, such as PET or MRI, which will obtain more information beyond the single NIR-II imaging.
5. 3D NIR-II imaging: Because of the relative deeper NIR-II penetration depth, the NIR-II photons may significantly achieve 3D volumetric tissue imaging. For example, the current brain neurology is mainly relying on optical microscopy and electron microscopy (EM) of thin tissue slices, which brings in additional difficulties and extra heavy work in the 3D reconstruction. Combined with tissue-clearing techniques, NIR-II fluorescence imaging may potentially afford volumetric brain imaging to achieve close-to-EM resolution on the whole organ or even whole body in deep volumetric scanning depth without tissue slicing.
6. NIR-II imaging system: The ability to maximize the full benefits of any NIR-II imaging is highly reliant on the thorough understanding of the requirements of each imaging system and the physical characteristics of the complementary fluorophores probes. The NIR-II imaging system can be described as acquisition of NIR-II emission signals from fluorophores probes using an image capturing system. Besides selecting suitable filters based on the fluorophores' optical characteristics (excitation/emission wavelengths and brightness), the hardware platforms (scan rate, lenses, collimators, working distance, exposure duration), and software algorithms for signal processing and image acquisition are designed to reduce undesired thermal noise often associated with NIR-II imaging and to enhance the signal-to-noise ratio. It would therefore be critical to adopt a systems–level approach to plan research efforts where the requirements of the

imaging setup that is determined by the imaging system design are considered from the start, so as to design the fluorophores probes to effectively improve detection sensitivity. For example, one of the most important hardware, the more advanced NIR-II camera with higher sensitivity and broader spectral ranges beyond the current NIR window should be developed. Besides the conventional InGaAs material widely used for NIR-II fluorescence imaging, other photosensitive semiconductor materials such as indium antimonide (InSb) and mercury cadmium telluride (HgCdTe) may provide new capabilities to NIR-II fluorescence imaging.

In summary, the future direction of NIR-II fluorophores will be mainly focused on the following properties, including biocompatible, high fluorescence quantum yield, high photostability, tunable excitation and emission wavelengths, feasible functionalization, and easy clearance. In addition, we envisage the bright future of NIR-II fluorescence imaging potential frontier applications in brain science, stem cells, genetic science and sensing in vivo, and so on.

7 Conclusions

NIR-II imaging has several advantages over NIR-I imaging and other current medical imaging modalities. Owing to the reduced photon scattering and low autofluorescence background at longer wavelengths, high imaging resolution and depth can be achieved by NIR-II imaging. NIR-II fluorophores from small organic molecules to organic and inorganic nanoparticles have been successfully developed, and their wide-ranging biomedical applications such as imaging, therapy, and guidance for intraoperative surgery have been discussed. This chapter also provides a summary overview of experimental strategies to tailor the luminescence characteristics, as well as control the physical and surface characteristics of the NIR-II probes. Optical (e.g., bright emissions with tunable excitation/emission) and biomedical (e.g., biocompatibility and targeting) characteristics of the NIR-II probes must be considered during the design and synthesis phase. To date, many probes with NIR-II emissions and large Stokes shifts have been established. The great advancement of NIR-II fluorophores has shown high impact not only on fundamental research but on preclinical application. However, their widespread utilization to diagnose diseased lesions has been largely limited due to the demanding challenges of effective in vivo targeting in a complex microenvironment. The complexity of the in vivo microenvironment (e.g., changing pH, enzymatic degradation) often results in unintended degradation of either the chemically conjugated targeting ligands or organic surface coatings and off-target localization of the probes due to charge-dependent non-specific attachment to various sites. Furthermore, the binding effectiveness of the targeting moieties could be affected during chemical conjugation leading to ineffectual localization and disease identification. The second concern is that the low QYs of the NIR-II emission are largely limited by the low absorption

cross section of the probes. To date, many efforts have been devoted to enhancing the QYs, but not very satisfactory. Third, elimination time of NIR-II probes last for weeks to months, and for large-sized nanoparticles, the excretion takes a longer time, varying from months to years. It has been suggested that small-sized NIR-II probes excreted by the renal route performed faster excretion. Therefore, further work is required in developing suitable strategies to effectively expand the existing NIR-II fluorescence imaging applications in vasculature visualization, disease identification, and diagnostics.

Acknowledgments This work was partially supported by the fund from the Department of Radiology, Stanford University.

Compliance with Ethical Standards

Funding: This work was partially supported by the fund from the Department of Radiology, Stanford University; the Office of Science (BER), US Department of Energy (DE-SC0008397) and the Shenzhen Basic Research Project (JCYJ20170817094201000).

Conflict of Interest: The authors declare that they have no conflict of interest.

Ethical Approval: This chapter does not contain any studies with human. All institutional and national guidelines for the care and use of laboratory animals were followed.

References

1. Kunjachan S, Ehling J, Storm G, Kiessling F, Lammers T (2015) Noninvasive imaging of nanomedicines and nanotheranostics: principles, progress, and prospects. Chem Rev 115 (19):10907–10937
2. Smith BR, Gambhir SS (2017) Nanomaterials for in vivo imaging. Chem Rev 117(3):901–986
3. Wang X, Pang Y, Ku G, Xie X, Stoica G, Wang LV (2003) Noninvasive laser-induced photoacoustic tomography for structural and functional in vivo imaging of the brain. Nat Biotechnol 21(7):803–806
4. He S, Song J, Qu J, Cheng Z (2018) Crucial breakthrough of second near-infrared biological window fluorophores: design and synthesis toward multimodal imaging and theranostics. Chem Soc Rev 47(12):4258–4278
5. Chernov KG, Redchuk TA, Omelina ES, Verkhusha VV (2017) Near-infrared fluorescent proteins, biosensors, and optogenetic tools engineered from phytochromes. Chem Rev 117 (9):6423–6446
6. Hong G, Antaris AL, Dai H (2017) Near-infrared fluorophores for biomedical imaging. Nat Biomed Eng 1:0010
7. Sordillo LA, Pu Y, Pratavieira S, Budansky Y, Alfano RR (2014) Deep optical imaging of tissue using the second and third near-infrared spectral windows. J Biomed Opt 19(5):056004
8. Antaris AL, Chen H, Cheng K, Sun Y, Hong G, Qu C, Diao S, Deng Z, Hu X, Zhang B et al (2015) A small-molecule dye for NIR-II imaging. Nat Mater 15(2):235–242
9. Carr JA, Franke D, Caram JR, Perkinson CF, Saif M, Askoxylakis V, Datta M, Fukumura D, Jain RK, Bawendi MG et al (2018) Shortwave infrared fluorescence imaging with the clinically approved near-infrared dye indocyanine green. Proc Natl Acad Sci 115(17):4465–4470

10. Antaris AL, Chen H, Diao S, Ma Z, Zhang Z, Zhu S, Wang J, Lozano AX, Fan Q, Chew L et al (2017) A high quantum yield molecule-protein complex fluorophore for near-infrared II imaging. Nat Commun 8:15269
11. Sun Y, Qu C, Chen H, He M, Tang C, Shou K, Hong S, Yang M, Jiang Y, Ding B et al (2016) Novel benzo-bis(1,2,5-thiadiazole) fluorophores for in vivo NIR-II imaging of cancer. Chem Sci 7(9):6203–6207
12. Zhang X-D, Wang H, Antaris AL, Li L, Diao S, Ma R, Nguyen A, Hong G, Ma Z, Wang J et al (2016) Traumatic brain injury imaging in the second near-infrared window with a molecular fluorophore. Adv Mater 28(32):6872–6879
13. Sun Y, Zeng X, Xiao Y, Liu C, Zhu H, Zhou H, Chen Z, Xu F, Wang J, Zhu M et al (2018) Novel dual-function near-infrared II fluorescence and PET probe for tumor delineation and image-guided surgery. Chem Sci 9(8):2092–2097
14. Zhu S, Yang Q, Antaris AL, Yue J, Ma Z, Wang H, Huang W, Wan H, Wang J, Diao S et al (2017) Molecular imaging of biological systems with a clickable dye in the broad 800- to 1,700-nm near-infrared window. Proc Natl Acad Sci 114(5):962–967
15. Feng Y, Zhu S, Antaris AL, Chen H, Xiao Y, Lu X, Jiang L, Diao S, Yu K, Wang Y et al (2017) Live imaging of follicle stimulating hormone receptors in gonads and bones using near infrared II fluorophore. Chem Sci 8(5):3703–3711
16. Shou K, Qu C, Sun Y, Chen H, Chen S, Zhang L, Xu H, Hong X, Yu A, Cheng Z (2017) Multifunctional biomedical imaging in physiological and pathological conditions using a NIR-II probe. Adv Funct Mater 27(23):1700995
17. Sun Y, Ding M, Zeng X, Xiao Y, Wu H, Zhou H, Ding B, Qu C, Hou W, Er-bu AGA et al (2017) Novel bright-emission small-molecule NIR-II fluorophores for in vivo tumor imaging and image-guided surgery. Chem Sci 8(5):3489–3493
18. Tao Z, Hong G, Shinji C, Chen C, Diao S, Antaris AL, Zhang B, Zou Y, Dai H (2013) Biological imaging using nanoparticles of small organic molecules with fluorescence emission at wavelengths longer than 1000 nm. Angew Chem Int Ed 52(49):13002–13006
19. Hong G, Robinson JT, Zhang Y, Diao S, Antaris AL, Wang Q, Dai H (2012) In vivo fluorescence imaging with Ag2S quantum dots in the second near-infrared region. Angew Chem 124(39):9956–9959
20. Li C, Zhang Y, Wang M, Zhang Y, Chen G, Li L, Wu D, Wang Q (2014) In vivo real-time visualization of tissue blood flow and angiogenesis using Ag2S quantum dots in the NIR-II window. Biomaterials 35(1):393–400
21. Chen G, Tian F, Zhang Y, Zhang Y, Li C, Wang Q (2014) Tracking of transplanted human mesenchymal stem cells in living mice using near-infrared Ag2S quantum dots. Adv Funct Mater 24(17):2481–2488
22. Tang R, Xue J, Xu B, Shen D, Sudlow GP, Achilefu S (2015) Tunable ultrasmall visible-to-extended near-infrared emitting silver sulfide quantum dots for integrin-targeted cancer imaging. ACS Nano 9(1):220–230
23. Naczynski DJ, Tan MC, Zevon M, Wall B, Kohl J, Kulesa A, Chen S, Roth CM, Riman RE, Moghe PV (2013) Rare-earth-doped biological composites as in vivo shortwave infrared reporters. Nat Commun 4:1–10
24. Kamimura M, Kanayama N, Tokuzen K, Soga K, Nagasaki Y (2011) Near-infrared (1550 nm) in vivo bioimaging based on rare-earth doped ceramic nanophosphors modified with PEG-b-poly(4-vinylbenzylphosphonate). Nanoscale 3(9):3705–3713
25. Zevon M, Ganapathy V, Kantamneni H, Mingozzi M, Kim P, Adler D, Sheng Y, Tan MC, Pierce M, Riman RE et al (2015) CXCR-4 targeted, short wave infrared (SWIR) emitting nanoprobes for enhanced deep tissue imaging and micrometastatic cancer lesion detection. Small 11(47):6347–6357
26. Shao W, Chen G, Kuzmin A, Kutscher HL, Pliss A, Ohulchanskyy TY, Prasad PN (2016) Tunable narrow band emissions from dye-sensitized core/shell/shell nanocrystals in the second near-infrared biological window. J Am Chem Soc 138(50):16192–16195

27. Robinson JT, Hong G, Liang Y, Zhang B, Yaghi OK, Dai H (2012) In vivo fluorescence imaging in the second near-infrared window with long circulating carbon nanotubes capable of ultrahigh tumor uptake. J Am Chem Soc 134(25):10664–10669
28. Welsher K, Sherlock SP, Dai H (2011) Deep-tissue anatomical imaging of mice using carbon nanotube fluorophores in the second near-infrared window. Proc Natl Acad Sci 108 (22):8943–8948
29. Hong G, Lee JC, Robinson JT, Raaz U, Xie L, Huang NF, Cooke JP, Dai H (2012) Multifunctional in vivo vascular imaging using near-infrared II fluorescence. Nat Med 18 (12):1841–1846
30. Hong G, Diao S, Chang J, Antaris AL, Chen C, Zhang B, Zhao S, Atochin DN, Huang PL, Andreasson KI et al (2014) Through-skull fluorescence imaging of the brain in a new near-infrared window. Nat Photonics 8(9):723–730
31. Yomogida Y, Tanaka T, Zhang M, Yudasaka M, Wei X, Kataura H (2016) Industrial-scale separation of high-purity single-chirality single-wall carbon nanotubes for biological imaging. Nat Commun 7:12056
32. Diao S, Blackburn JL, Hong G, Antaris AL, Chang J, Wu JZ, Zhang B, Cheng K, Kuo CJ, Dai H (2015) Fluorescence imaging in vivo at wavelengths beyond 1500 nm. Angew Chem Int Ed 54(49):14758–14762
33. Iverson NM, Barone PW, Shandell M, Trudel LJ, Sen S, Sen F, Ivanov V, Atolia E, Farias E, McNicholas TP et al (2013) In vivo biosensing via tissue-localizable near-infrared-fluorescent single-walled carbon nanotubes. Nat Nanotechnol 8:873–880
34. Starosolski Z, Bhavane R, Ghaghada KB, Vasudevan SA, Kaay A, Annapragada A (2017) Indocyanine green fluorescence in second near-infrared (NIR-II) window. PLoS One 12(11): e0187563
35. Cheng K, Chen H, Jenkins CH, Zhang G, Zhao W, Zhang Z, Han F, Fung J, Yang M, Jiang Y et al (2017) Synthesis, characterization and biomedical applications of a targeted dual-modal near infrared-II fluorescence and photoacoustic imaging nanoprobe. ACS Nano 11 (12):12276–12291
36. Benhao L, Lingfei L, Mengyao Z, Zuhai L, Fan Z (2018) An efficient 1064 nm NIR-II excitation fluorescent molecular dye for deep-tissue high-resolution dynamic bioimaging. Angew Chem Int Ed 57(25):7483–7487
37. Hong G, Zou Y, Antaris AL, Diao S, Wu D, Cheng K, Zhang X, Chen C, Liu B, He Y et al (2014) Ultrafast fluorescence imaging in vivo with conjugated polymer fluorophores in the second near-infrared window. Nat Commun 5:4206
38. Shou K, Tang Y, Chen H, Chen S, Zhang L, Zhang A, Fan Q, Yu A, Cheng Z (2018) Diketopyrrolopyrrole-based semiconducting polymer nano-particles for in vivo second near-infrared window imaging and image-guided tumor surgery. Chem Sci 9:3105–3110
39. Zhao X, He S, Tan MC (2016) Design of infrared-emitting rare earth doped nanoparticles and nanostructured composites. J Mater Chem C 4(36):8349–8372
40. Dong H, Du S-R, Zheng X-Y, Lyu G-M, Sun L-D, Li L-D, Zhang P-Z, Zhang C, Yan C-H (2015) Lanthanide nanoparticles: from design toward bioimaging and therapy. Chem Rev 115 (19):10725–10815
41. Wang F, Liu X (2014) Multicolor tuning of lanthanide-doped nanoparticles by single wavelength excitation. Acc Chem Res 47(4):1378–1385
42. Chen X, Peng D, Ju Q, Wang F (2015) Photon upconversion in core-shell nanoparticles. Chem Soc Rev 44(6):1318–1330
43. Huang X, Han S, Huang W, Liu X (2013) Enhancing solar cell efficiency: the search for luminescent materials as spectral converters. Chem Soc Rev 42(1):173–201
44. Zhou B, Shi B, Jin D, Liu X (2015) Controlling upconversion nanocrystals for emerging applications. Nat Nanotechnol 10(11):924–936
45. Judd B (1962) Optical absorption intensities of rare-earth ions. Phys Rev 127(3):750
46. Judd B (1963) Configuration interaction in rare earth ions. Proc Phys Soc 82(6):874

47. Dejneka MJ, Streltsov A, Pal S, Frutos AG, Powell CL, Yost K, Yuen PK, Müller U, Lahiri J (2003) Rare earth-doped glass microbarcodes. Proc Natl Acad Sci 100(2):389
48. Gai S, Li C, Yang P, Lin J (2014) Recent progress in rare earth micro/nanocrystals: soft chemical synthesis, luminescent properties, and biomedical applications. Chem Rev 114 (4):2343–2389
49. Ye X, Collins JE, Kang Y, Chen J, Chen DTN, Yodh AG, Murray CB (2010) Morphologically controlled synthesis of colloidal upconversion nanophosphors and their shape-directed self-assembly. Proc Natl Acad Sci 107(52):22430–22435
50. Naccache R, Yu Q, Capobianco JA (2015) The fluoride host: nucleation, growth, and upconversion of lanthanide-doped nanoparticles. Adv Opt Mater 3(4):482–509
51. Abel KA, Boyer J-C, Veggel FCJM (2009) Hard proof of the NaYF4/NaGdF4 nanocrystal core/shell structure. J Am Chem Soc 131(41):14644–14645
52. Li Z, Zhang Y (2006) Monodisperse silica-coated polyvinylpyrrolidone/NaYF4 nanocrystals with multicolor upconversion fluorescence emission. Angew Chem 118(46):7896–7899
53. Tu D, Liu L, Ju Q, Liu Y, Zhu H, Li R, Chen X (2011) Time-resolved fret biosensor based on amine-functionalized lanthanide-doped NaYF4 nanocrystals. Angew Chem Int Ed 50 (28):6306–6310
54. Meng F, Liu S, Wang Y, Tao C, Xu P, Guo W, Shen L, Zhang X, Ruan S (2012) Open-circuit voltage enhancement of inverted polymer bulk heterojunction solar cells by doping NaYF4 nanoparticles/PVP composites. J Mater Chem 22(42):22382–22386
55. Chatteriee DK, Rufalhah AJ, Zhang Y (2008) Upconversion fluorescence imaging of cells and small animals using lanthanide doped nanocrystals. Biomaterials 29(7):937–943
56. Lim ME, Lee Y-l, Zhang Y, Chu JJH (2012) Photodynamic inactivation of viruses using upconversion nanoparticles. Biomaterials 33(6):1912–1920
57. Sheng Y, Liao L-D, Thakor N, Tan MC (2014) Rare-earth doped particles as dual-modality contrast agent for minimally-invasive luminescence and dual-wavelength photoacoustic imaging. Sci Rep 4:6562
58. Li C, Yang J, Yang P, Lian H, Lin J (2008) Hydrothermal synthesis of lanthanide fluorides LnF3 (Ln = La to Lu) nano-/microcrystals with multiform structures and morphologies. Chem Mater 20(13):4317–4326
59. He S, Chen S, Li D, Wu Y, Zhang X, Liu J, Song J, Liu L, Qu J, Cheng Z (2019) High affinity to skeleton rare earth doped nanoparticles for near-infrared II imaging. Nano Lett 19 (5):2985–2992
60. Naczynski DJ, Sun C, Türkcan S, Jenkins C, Koh AL, Ikeda D, Pratx G, Xing L (2015) X-ray-induced shortwave infrared biomedical imaging using rare-earth nanoprobes. Nano Lett 15 (1):96–102
61. Kantamneni H, Zevon M, Donzanti MJ, Zhao X, Sheng Y, Barkund SR, McCabe LH, Banach-Petrosky W, Higgins LM, Ganesan S et al (2017) Surveillance nanotechnology for multi-organ cancer metastases. Nat Biomed Eng 1(12):993–1003
62. Wang R, Zhou L, Wang W, Li X, Zhang F (2017) In vivo gastrointestinal drug-release monitoring through second near-infrared window fluorescent bioimaging with orally delivered microcarriers. Nat Commun 8:14702
63. Fan Z, Lu L, Shangfeng W, Baozhou Z, Peng P, Yong F, Xiaomin L (2018) Er3+ sensitized 1530 nm to 1180 nm second near-infrared window upconversion nanocrystals for in vivo biosensing. Angew Chem Int Ed 57(25):7518–7522
64. He S, Song J, Liu J, Liu L, Qu J, Cheng Z (2019) Enhancing photoacoustic intensity of upconversion nanoparticles by photoswitchable azobenzene-containing polymers for dual NIR-II and photoacoustic imaging in vivo. Adv Opt Mater 0(0):1900045
65. Pichaandi J, van Veggel FCJM (2014) Near-infrared emitting quantum dots: recent progress on their synthesis and characterization. Coord Chem Rev 263–264:138–150
66. Deutsch Z, Neeman L, Oron D (2013) Luminescence upconversion in colloidal double quantum dots. Nat Nanotechnol 8(9):649–653

67. Dong B, Li C, Chen G, Zhang Y, Zhang Y, Deng M, Wang Q (2013) Facile synthesis of highly photoluminescent Ag2Se quantum dots as a new fluorescent probe in the second near-infrared window for in vivo imaging. Chem Mater 25(12):2503–2509
68. Zhou J, Yang Y, Zhang C-y (2015) Toward biocompatible semiconductor quantum dots: from biosynthesis and bioconjugation to biomedical application. Chem Rev 115(21):11669–11717
69. Chen J, Kong Y, Wang W, Fang H, Wo Y, Zhou D, Wu Z, Li Y, Chen S (2016) Direct water-phase synthesis of lead sulfide quantum dots encapsulated by [small beta]-lactoglobulin for in vivo second near infrared window imaging with reduced toxicity. Chem Commun 52 (21):4025–4028
70. Zhao D-H, Yang J, Xia R-X, Yao M-H, Jin R-M, Zhao Y-D, Liu B (2018) High quantum yield Ag2S quantum dot@polypeptide-engineered hybrid nanogels for targeted second near-infrared fluorescence/photoacoustic imaging and photothermal therapy. Chem Commun 54(5):527–530
71. Bruns OT, Bischof TS, Harris DK, Franke D, Shi Y, Riedemann L, Bartelt A, Jaworski FB, Carr JA, Rowlands CJ et al (2017) Next-generation in vivo optical imaging with short-wave infrared quantum dots. Nat Biomed Eng 1:0056
72. Cassette E, Pons T, Bouet C, Helle M, Bezdetnaya L, Marchal F, Dubertret B (2010) Synthesis and characterization of near-infrared Cu−In−Se/ZnS core/shell quantum dots for in vivo imaging. Chem Mater 22(22):6117–6124
73. Hu D, Zhang P, Gong P, Lian S, Lu Y, Gao D, Cai L (2011) A fast synthesis of near-infrared emitting CdTe/CdSe quantum dots with small hydrodynamic diameter for in vivo imaging probes. Nanoscale 3(11):4724–4732
74. Nirmal G, Anupam G, Shantimoy K, Siddaramappa BM, Robin J, Lourdu XP, Thalappil P, Kumar PS (2012) Protein-directed synthesis of NIR-emitting, tunable HgS quantum dots and their applications in metal-ion sensing. Small 8(20):3175–3184
75. Chen L, Han H (2014) Recent advances in the use of near-infrared quantum dots as optical probes for bioanalytical, imaging and solar cell application. Microchim Acta 181 (13):1485–1495
76. Li C, Cao L, Zhang Y, Yi P, Wang M, Tan B, Deng Z, Wu D, Wang Q (2015) Preoperative detection and intraoperative visualization of brain tumors for more precise surgery: a new dual-modality MRI and NIR nanoprobe. Small 11(35):4517–4525
77. Wu C, Zhang Y, Li Z, Li C, Wang Q (2016) A novel photoacoustic nanoprobe of ICG@PEG-Ag2S for atherosclerosis targeting and imaging in vivo. Nanoscale 8(25):12531–12539
78. Yang T, Tang Y, Liu L, Lv X, Wang Q, Ke H, Deng Y, Yang H, Yang X, Liu G et al (2017) Size-dependent Ag2S nanodots for second near-infrared fluorescence/photoacoustics imaging and simultaneous photothermal therapy. ACS Nano 11(2):1848–1857
79. Hu F, Li C, Zhang Y, Wang M, Wu D, Wang Q (2015) Real-time in vivo visualization of tumor therapy by a near-infrared-II Ag2S quantum dot-based theranostic nanoplatform. Nano Res 8 (5):1637–1647
80. Tsukasaki Y, Morimatsu M, Nishimura G, Sakata T, Yasuda H, Komatsuzaki A, Watanabe TM, Jin T (2014) Synthesis and optical properties of emission-tunable PbS/CdS core-shell quantum dots for in vivo fluorescence imaging in the second near-infrared window. RSC Adv 4 (77):41164–41171
81. Yi H, Ghosh D, Ham M-H, Qi J, Barone PW, Strano MS, Belcher AM (2012) M13 phage-functionalized single-walled carbon nanotubes as nanoprobes for second near-infrared window fluorescence imaging of targeted tumors. Nano Lett 12(3):1176–1183
82. Hong G, Diao S, Antaris AL, Dai H (2015) Carbon nanomaterials for biological imaging and nanomedicinal therapy. Chem Rev 115(19):10816–10906
83. Iijima S (1991) Helical microtubules of graphitic carbon. Nature 354:56
84. Guo T, Nikolaev P, Thess A, Colbert DT, Smalley RE (1995) Catalytic growth of single-walled manotubes by laser vaporization. Chem Phys Lett 243(1):49–54
85. Nikolaev P, Bronikowski MJ, Bradley RK, Rohmund F, Colbert DT, Smith KA, Smalley RE (1999) Gas-phase catalytic growth of single-walled carbon nanotubes from carbon monoxide. Chem Phys Lett 313(1):91–97

86. Ghosh D, Bagley AF, Na YJ, Birrer MJ, Bhatia SN, Belcher AM (2014) Deep, noninvasive imaging and surgical guidance of submillimeter tumors using targeted M13-stabilized single-walled carbon nanotubes. Proc Natl Acad Sci 111(38):13948–13953

Top Med Chem (2020) 34: 125–148
DOI: 10.1007/7355_2019_91

Published online: 28 January 2020

X-Ray Excited Fluorescent Materials for Medical Application

Don Vernekohl and Lei Xing

Contents

Abstract X-ray fluorescence (XF) and X-ray luminescence (XL) are X-ray stimulated processes which can be exploited for medical imaging. In recent years, the computed tomography (XFCT and XLCT) imaging of these processes has attracted much attention especially in the field of radiation therapy. These imaging modalities have potentials to offer additional functional information from the patient during exposure to X-rays for position alignment before the radiation treatment. More recently, these new techniques have been further studied in Monte Carlo simulations and benchtop experiments to characterize and optimize different imaging

D. Vernekohl (✉) and L. Xing
Department of Radiation Oncology, Stanford University, School of Medicine, Stanford, CA, USA
e-mail: lei@stanford.edu

configurations. This chapter summarizes recent instrumentational developments in X-ray excited imaging; discusses their attributes, advantages, and drawbacks; and describes specifications and applications of various contrast agents for XF- and XLCT. The feasibility of the modalities for future clinical applications will be also highlighted.

Keywords High atomic number contrast agents, Medical imaging, Molecular imaging, X-ray fluorescence, X-ray luminescence

1 Introduction

X-ray excitation is a promising mode for the field of medical imaging. The deep-penetrating X-rays can produce signals of functional information of an imaged object with high resolution and sensitivity. The nature of the generated signals is of different origins. While we focus in this chapter on fluorescent high energetic X-rays (XFCT) and optical and near-infrared (NIR) photons (XLCT), other types of signals, e.g., X-ray acoustic [1], can also be exploited for imaging.

In laboratories, XF is generally used to identify small amounts of chemical species without affecting the sample. Each element is characterized by spectral lines that are a unique signature. In XF, fluorescent X-rays emitted by the elements in the probe are either directly measured by an energy-discriminating solid-state detector (energy-resolving XF) or separated by wavelength by diffraction in a crystal (wavelength-dispersive XF). XF is non-destructive, highly sensitive (1–10 ppm), and used to measure many chemical species simultaneously and quantitatively. It is capable of determining subtle amounts of elements in biological tissues such as tumor specimen [2] or lead in bone [3] with monochromatic synchrotron radiation. The ability to perform XF imaging studies in vivo, during conventional X-ray CT, will aid tremendously in characterizing active biological processes. Preliminary work [4–6] has shown that XF can be performed in a tomographic manner using a CT-like scanning geometry with a conventional poly-energetic X-ray source.

The molecular contrast in XFCT comes from high atomic number (high-Z) elements which are present either exogenously or endogenously. The conceptual design of an XFCT imaging system consists of an X-ray source and an energy-dispersive X-ray detection system. In the physical process of fluorescence, the exciting X-ray interacts with an inner shell electron (K or L) of the probe which results in a vacancy that is subsequently filled by an electron from an outer shell as shown in Fig. 1. The difference in energy between the two states is emitted as a characteristic X-ray (aka fluorescent X-ray). The detection of these photons and subsequent image reconstruction will allow the determination of the spatial distribution of molecular probes.

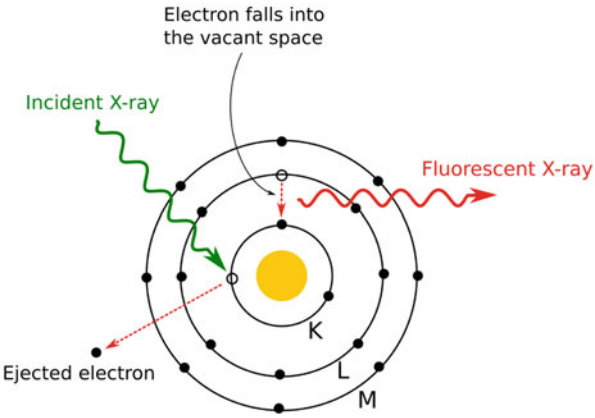

Fig. 1 Principle of X-ray fluorescence (Reprint with permission [7])

The contrast in XLCT imaging relies on the excitation of nanophosphors. These nanophosphors usually consist of a nanoparticle made from a high atomic number element, and the particle is bounded to phosphor groups which cause the emission of optical or near-infrared (NIR) photons. The emission of these photons is stimulated by a high-energy electron ejected during a Compton or photoelectric interaction of the exciting X-ray with the high atomic number element. The optical signal can be measured with cost-efficient CCD cameras, while NIR signals require more sophisticated detection hardware. The contrast agents used in XLCT are partly translated from tracers used in laser stimulated NIR optical imaging. These probes which emit light with a higher wavelength than optical photons can penetrate deeper into soft tissue. XLCT imaging promises to surpass the depth-dependent restrictions of optical imaging even further as the X-rays can even excite contrast agents in very thick samples. Furthermore, X-rays produce no autofluorescent signal in normal tissue which is a problem in laser-excited optical imaging. These advantages will extend the applicability of tracers built from rare-earth nanophosphors in medical imaging.

Both XFCT and XLCT do not require X-ray detectors in the transmission direction. Hence, traditional CT imaging systems can be extended by XF or XL detection systems, providing X-ray CT with the ability to see molecular contrasts [4, 6, 8–10]. The information undetectable by X-ray attenuation (such as cellular and molecular activities and physiologic function) is critical to detect a disease at its early malignant stage, to differentiate between aggressive and non-aggressive phenotypes, and to understand how to treat a disease effectively [11–13].

The extension of XF imaging to XFCT is, to a large extent, analogous to the development of magnetic resonance imaging (MRI) from nuclear magnetic resonance (NMR) in the 1970s, which has fundamentally changed medical practice. Indeed, if the detection limit of XF analysis (1–10 ppm) can be fully realized in

XFCT, it will be sufficient to catch a cancerous lump of micrometric dimensions [14]. The method allows quantifying element concentrations in the active biological environment without the cumbersome and time-consuming analysis of sacrificed animals.

Potential challenges of XFCT imaging are currently molecular sensitivity, acquisition time, scatter contamination, and cost-effectiveness. The drawback of XFCT and XLCT is that ionizing radiation is used for the imaging which is harmful if used in high doses. This limits the sensitivity of the imaging modalities as only clinically and ethically acceptable doses can be used.

2 Combination of XFCT or XLCT with Transmission CT Imaging

Transmission X-ray and CT imaging are indispensable in preclinical and clinical studies, and CT imaging became a cornerstone for the evolution of tomographic imaging. The modality, however, falls short in providing sufficient contrast for probing the molecular bases of diseases. Combined with transmission CT, XFCT or XLCT offers an unprecedented method for visualizing subtle molecular processes in living subjects within a CT-based anatomical frame of reference. The establishment of fully integrated XF- or XLCT and CT imaging systems will allow the simultaneous acquisition of anatomical and molecular information in the same scan. By empowering X-ray imaging with the ability to extract molecular signatures through the simultaneous measurement of XF or XL signals, the molecular information can be extracted without additional dose for the patient. Due to the low mass attenuation coefficient of dilutions with low concentrations of XF or XL contrast agents, these probes are not detectable in transmission X-ray or CT images. The emergence of fully integrated XFCT/CT systems in laboratories and clinics using conventional polychromatic X-ray sources will satisfy the ever-growing interest in imaging of high atomic number ($Z > \sim 30$) elements.

On top of the benefits of multimodal imaging by combining anatomical and molecular information into one imaging system, CT images can also be used to improve the performance of XFCT imaging. The probability of Compton scatter at a given point is a function of the underlying material. As the material and density distributions are known from the CT images, the dual-modality implementation presents a unique opportunity for advanced attenuation and scatter correction (see also chapter “Scatter and Attenuation Correction”). While the CT image can directly be used for attenuation correction, the scatter corrections require more elaborate processing steps. The CT image can be used to run analytical or semi-analytical simulations to generate a scatter estimate as the CT pixel data provides the probability for the angle and energy of deflection for scattered X-rays given by the Klein-Nishina differential cross-section. The scatter estimate can then be used in one of the abovementioned scatter correction methods.

If pencil-beam excitation is used in a multimodal XFCT/CT system, the acquisition time of the CT image is longer than for a standalone CT. Nevertheless, the single line acquisition would lead to reduced scatter contamination in the CT data and further increase the CT image quality.

Similar to the attenuation and scatter correction in XFCT, the information from the anatomical CT image can be used to improve the modeling of the scatter and attenuation properties, required to solve the diffusion equation in XLCT image reconstruction. However, the absorption coefficient by the CT measurement is not directly related to the scatter probability and the absorption coefficients of optical or NIR photons. Therefore, segmentation and material identification/decomposition need to be performed on the reconstructed CT images to derive the correct prior knowledge for the XLCT image reconstruction. The additional information obtained from the CT images will improve the image quality and precision for retrieving the nanophosphor concentration from the measured luminescent signal.

3 Imaging and Instrumental Specifications

The performance of X-ray excited imaging depends on various parameters (e.g., source-subject distance, subject-detector distance, source and detector specifications, detector location, collimator design, etc.) which need to be optimized for enhanced sensitivity, spatial resolution, and scanning time. For polychromatic X-ray sources, beam filtering with various thicknesses of attenuating materials must be adapted for each distinct contrast element to provide X-ray energy spectra suitable to enhance emission photon efficiency from the contrast agent. Moreover, the optimal trade-off between imaging dose, filtration, output, sensitivity, and spatial resolution needs to be determined. While the majority of these parameters can be optimized from simulations for different applications, some of them require experimental validation or deduction. Proof of principle experiments with a single CdTe detector delivered sensitivities in the range of 2.5–5 mg/ml for K-shell XFCT imaging with gold nanoparticles [18]. A schematic of the image acquisition chain and photograph of this setup are shown in Fig. 2.

For higher energetic K-shell fluorescence from, e.g., gold or platinum, the stopping power of silicon is low, and silicon detectors do not provide sufficient photon detection efficiency. In this energy range, it is recommended to exploit the latest advances in room-temperature semiconductor detectors based on the new generation of pixelated cadmium-zinc-telluride (CZT) crystals to surmount the key technical hurdles of XFCT imaging. In recent years, technological advances have enabled manufacturers to grow large CZT crystals with high energy resolutions ($<1\%$ at 100 keV) and to produce pixelated arrays with small pixel sizes for high spatial resolution. Other essential detector parameters for XFCT imaging are shaping time, count rate performance, and energy resolution. It has to be emphasized that spatial resolution is generally not required for pencil-beam XFCT as the detector only needs to determine the amount of XF and scatter photons in a particular energy window. Hence, the detector is a veto detector reporting whether or not a contrast

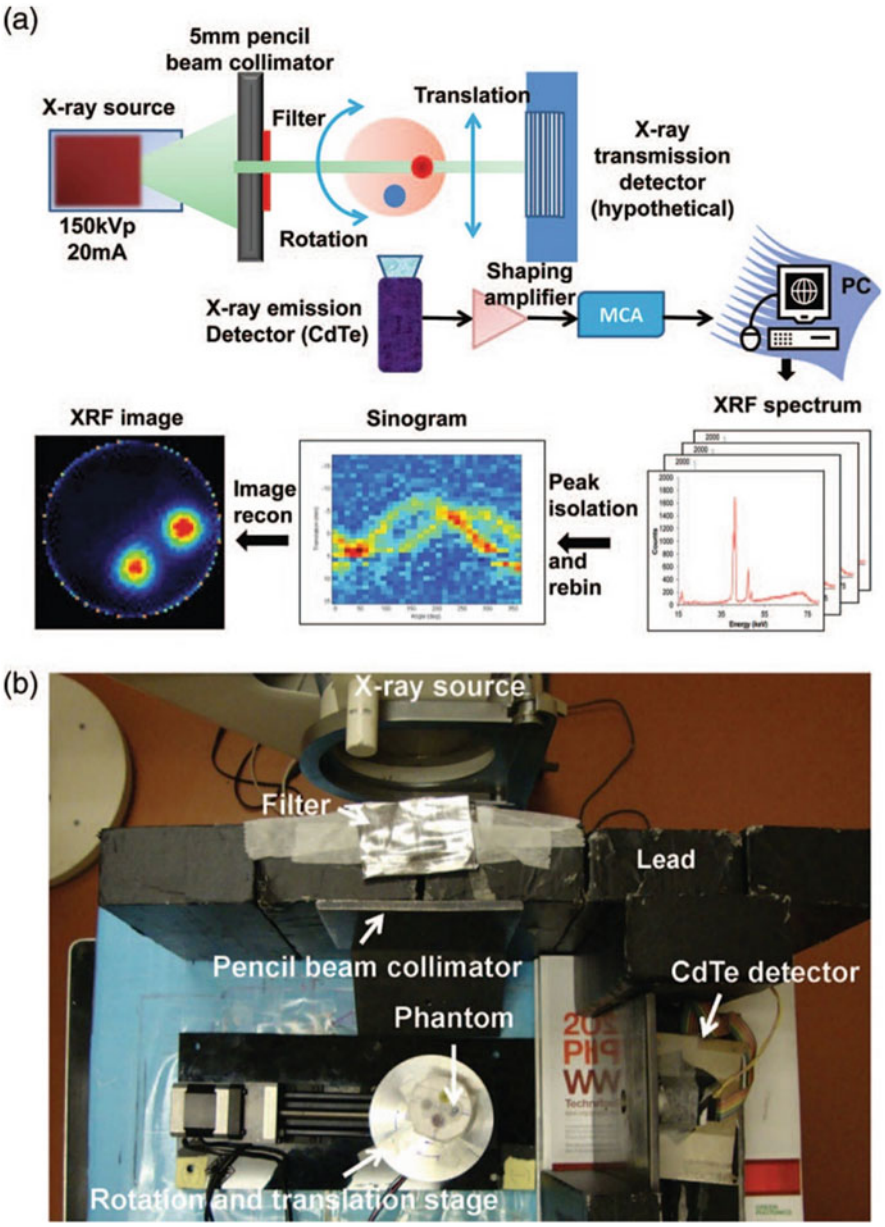

Fig. 2 (**a**) Schematic of the experimental setup including the filtered X-ray source, water phantom, and CdTe detector. (**b**) Photograph of the imaging system setup. A water phantom containing different concentrations of cisplatin insertion was moved on a rotation/transition stage while being irradiated by a narrow, filtered X-ray pencil beam (Reprint with permission from [18])

agent is present along the pencil-beam path. Nevertheless, spatial information is required for attenuation correction [15] and can become important for advanced scatter removal strategies (see chapter "Scatter and Attenuation Correction") or other XFCT imaging modes (see chapter "High-Resolution 2D Imaging").

The turnkey solution for high sensitivity is a high solid angle coverage as the fluorescent X-rays are emitted isotropically over the full 4π solid angle. For CZT detectors, large 4×4 cm^2 crystals are typically grown for efficient gamma- or X-ray detection, and they reach energy resolutions down to 3% FWHM at 122 keV. In collaboration with the group from Dr. He [16], we tested the Polaris large CZT crystal prototype detector with an energy resolution of 2.5% which is about three times worse than the energy resolution of the spectroscopic CdTe detector used in our previous experiments [6, 17–19]. The experiment was conducted with both detectors placed on the same distance to an iodine phantom that was excited with a 50 kVp X-ray source equipped with an Ag anode. The reconstructed images provide better contrast and higher sensitivity for the CZT detector. The improved performance results from the higher detection efficiency and the better angular coverage which even overcomes lower energy resolution and the X-ray absorbing shielding of the CZT detector.

In the scenario of lower energy X-rays from L-shell fluorescence of high atomic number contrast agents like gold or platinum and lower atomic number K-shell fluorescence from elements, for example, silver and iodine, the XF photons can be measured with advanced detector technology, e.g., a silicon drift detector (SDD). As SDDs are made of silicon, their stopping power for high energetic X-rays is meager. However, in the lower energy regime, their high energy resolution outperforms other detector materials. For example, our group showed that for L-shell imaging of gold as the contrast agent, SDD detectors exceed CdTe detectors [17]. In contrast to K-shell fluorescence of high atomic number contrast agents which is suitable in principle for whole-body clinical imaging, the lower energy regime of L-shell fluorescence is restricted to small animal preclinical applications and organ-specific surface close clinical applications due to the high X-ray attenuation of tissue for low energetic X-rays. There are two advantages of lower excitation energies. Firstly, at these energies, synthetic materials exist that can reflect and refract these X-rays [20]. Specifically, compound poly-capillary X-ray lenses are available either to focus the X-ray power to a small spot on the surface of the subject or to bend the X-rays for higher flux X-ray parallel beam [20]. In this design, the X-ray power is used efficiently compared to conservative pencil-beam collimation and focused on a narrower area. Moreover, synthetic materials can be used to produce X-rays mirrors with energy-dependent reflection indexes. Thus, these mirrors can be used to shape the exciting energy spectrum more precisely than with absorbing filter materials.

The second advantage of choosing lower X-ray excitation energies is that they can be stimulated from small form factor sources (X-ray energies up to 50 keV). The target anode in these sources is very close to the exit window or nozzle. Therefore, the imaged subject can be placed very close to the X-ray source focal spot for high X-ray exposure. These sources don't require advanced cooling methods and can be operated with compressed air or water cooling.

4 Scatter and Attenuation Correction

In XFCT imaging, Compton scatter states one of the major problems and must be dealt with adequately for high sensitivity. To reliably detect the fluorescence signal and to eliminate the adverse effects of the Compton scatter photons, fundamental strategies are required which estimate and correct scatter contamination or avoid scatter in the first place. The signal created by Compton scatter of the primary excitation X-rays interferes with the detection of fluorescent X-rays. For low concentrations of contrast agents, the scatter signal can be several times larger than the fluorescent signal itself. The primary technique to reduce scatter content is the employment of X-ray detectors with high energy resolution. As shown in Fig. 3, the ability to distinguish background scatter from the fluorescent X-rays is given by the energy resolution (manifested by the FWHM of the monoenergetic fluorescent X-rays).

Beyond energy resolution, a simple scatter removal method is realized by fitting the detected X-ray background at a few energy windows in the energy spectrum adjacent to the XF peak. With this method, an estimation of the scatter background below the XF peaks is generated which either can be subtracted from the measured spectrum before image reconstruction or can be applied as a scatter estimate during reconstruction [6, 21].

Another method to generate a scatter estimation is an additional XFCT scan before contrast agent injection. This method requires the X-ray source and detector

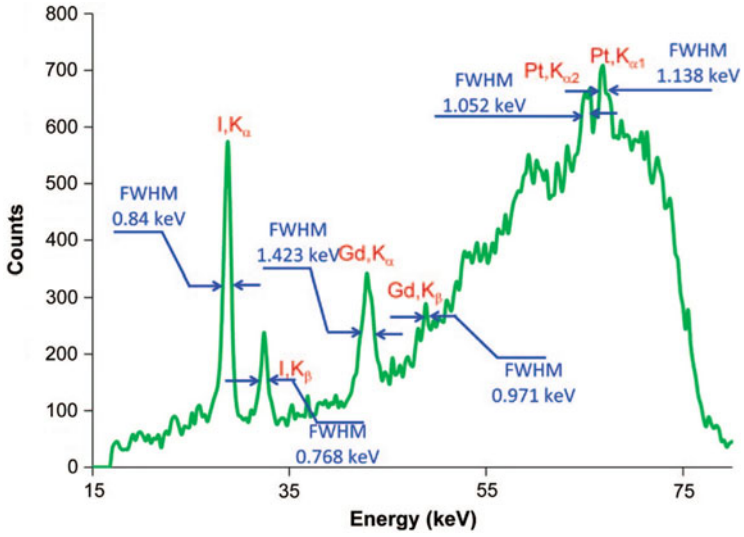

Fig. 3 A representative spectrum showing multiplexed detection in the water phantom of a mixture of 2% Pt, Gd, and I solutions. The energy resolution of a detector is proportional to energy width of the characteristic peaks. The continuous spectrum represents the scatter X-rays (Reprint with permission [18])

to operate without strong fluctuations and doubles the dose for the imaged object as the additional second scan is needed.

Generally, when incident photons collide with electrons of a medium, they give up some of their energy, and these Compton scattered photons, deflected out of their original direction of motion, have a distinct angular and energy distribution. In fact, this dependence can be exploited for scatter removal by determining the different spectro-spatial behaviors of the scattered and fluorescent X-rays [22]. The X-ray fluorescence signal has a fixed energy and is distributed uniformly in the 4π angular space. The Compton scatter instead is anisotropic: backscatter X-rays ($\Theta \approx 180°$) have lower energies than forward-scatter X-rays ($\Theta \approx 0°$). Thus, the two different types of events can be separated by placing the detector in an optimized position. Monte Carlo simulations with gold nanoparticles have shown that distinct angles can be found in which directions the overlap between the Compton and fluorescence photons are avoided or much reduced for different excitation spectrums [22]. In this study, the detection of the K_β lines of gold with $\Theta > 110°$ proved to be a better configuration than the full 4π coverage. This means that contrary to intuition, the optimized configuration simultaneously reduces the number of detectors and improves the imaging result.

By optimizing the fluorescence data acquisition geometry, the interfering Compton scatter X-rays can be reduced by orders of magnitude, which pushes the limit of detectable gold concentrations to 0.001% by weight (the corresponding molar concentrations of a mono-atomic gold solution is 50 μM, and the molar concentrations for nanoparticle solutions would be nM). By optimally placing the detectors with respect to these results, an order of magnitude increase in sensitivity is achievable.

In order to apply the principle of XFCT to a living organism, one must take the attenuation of X-rays by the surrounding tissues into account. Generally, elements such as gadolinium ($Z = 64$, $K_{\alpha 1} = 42$ keV), gold ($Z = 79$, $K_{\alpha 1} = 69$ keV), barium ($Z = 56$, $K_{\alpha 1} = 32$ keV), and iodine ($Z = 53$, $K_{\alpha 1} = 29$ keV) can be imaged at a depth of ~20 cm, making XFCT imaging of many elements a viable choice. As L-shell fluorescent photons are much stronger attenuated by tissue than K-shell fluorescent X-rays, the attenuation correction is more important in L-shell XFCT imaging. Nevertheless, suitable attenuation correction is required for quantitative imaging for all X-ray energies.

The iterative image reconstruction commonly used in XFCT imaging requires a system matrix. The attenuation of incoming and outgoing X-rays needs to be incorporated correctly into the system matrix with different linear attenuation coefficients for each XF energy [15]. Hence, the position of each fluorescent X-ray on the detector must be determined to calculate the probability of XF absorption along this specific line. The attenuation must be integrated into each system matrix element as each system matrix element represents the detection probability of one detector pixel with one image pixel/voxel. For each system matrix element, the attenuation is calculated by summing all line segments weighted with the attenuation coefficient obtained from the CT image. For both the line connecting to the detector pixel (with the attenuation coefficient for the XF energy) and the line created by the pencil beam

(with the attenuation coefficient for the excitation energy), the intersection length with all intersecting pixel/voxel needs to be calculated. The reconstructed images with included attenuation correction show even tracer distributions of uniformly distributed contrast agents, while uncorrected images would depict a decreased contrast agent concentration in the image center.

5 Contrast Agents

In XFCT imaging, three different classes of contrast agents provide a broad palette of opportunities for medical applications. While exogenous contrast agents are modified functional molecules with a bound signal carrier, metal-based therapeutic agents and endogenous contrast agents contain the XF signal carrier already in their native form. The latter two agents are ideal contrast agents as their unbiased bio-functionality can be imaged. For XLCT imaging, only exogenous contrast agents are available.

5.1 Exogenous Contrast Agents

Molecular probes for XFCT can be synthesized by labeling a chemical compound of interest with a high-Z element or nanoparticle (NP). The addition of a single atom to a molecule preserves the affinity of that molecule for biological processes; hence, its modified behavior is very similar to the original molecule of interest. This feature enables quantitative and unbiased measurements of biological processes. XFCT will also be able to image NPs made from high-Z elements, such as gold [23], silver [24], gadolinium oxide [25], zinc oxide [26], and so forth. Intensive research is ongoing in the biomedical community to use these NPs as molecular imaging probes, as vehicles for therapeutic drug delivery to target sites, or as sensitizers to enhance the delivery of photothermal ablation therapy or radiation therapy [27–34]. Hence, the ability to image the distribution of such NPs fulfills a critical need and can aid substantially in the design and evaluation of novel imaging and therapeutic strategies.

For the imaging with X-ray excitation energies (<30 keV), the use of silver and gold nanoparticle agents are recommendable because they are relatively inert biological elements. Furthermore, the surface chemistry of these nanoparticles can be modified to make them less reactive. The use of the K-shell X-rays from silver nanoparticles (22.2 keV) and L-shell X-rays from gold nanoparticles (9.7 and 11.4 keV) provides an energy range suitable for X-ray focusing optics (see chapter “Imaging and Instrumental Specifications”).

5.2 Metal-Based Therapeutic Agents

Metallodrugs are designed to induce pharmacological effects by interacting with proteins (in particular with catalytically active enzymes) or directly with DNA [35]. Because of their unique properties, metallodrugs are the subject of intense research efforts. Platinum-based complexes are examples of the most widely used anticancer agents. Currently researched compounds are mainly based on platinum but also other metals such as ruthenium, titanium, gallium, or silver are under investigation. Until now, no imaging technique was available to visualize the distribution of these drugs in living subjects. Because metals such as platinum emit energetic characteristic X-rays, they are highly amenable to imaging via XFCT [18]. XFCT will play a pivotal role in the biological characterization and optimization of metal-based drug complexes and their pharmacodynamics in vivo. By directly observing the trafficking of these therapeutic agents, the technique provides a novel opportunity to advance our understanding of their metabolism and the drug resistance of tumors. Furthermore, it will be possible to verify and monitor therapy response at an early stage allowing to tailor treatment, thereby avoiding unnecessary side effects and improving treatment outcomes.

5.3 Endogenous Trace Elements

Trace elements are dietary minerals required for the proper functioning of the organism. These elements, including Cr, Mn, Fe, Co, Ni, Cu, Zn, Se, Mo, and I, occur at very low concentrations (<100 ppm) under normal conditions and are indispensable to the biosynthesis of special metalloproteins and metalloenzymes. XF studies have shown that the concentration of these elements is perturbed in various disease states. For instance, elevated levels of copper were observed in breast cancer [36], while abnormally low levels of zinc were found in prostate cancer [37]. Iodine is also accumulated excessively in certain types of breast cancers that overexpress the sodium-iodine symporter [38]. The potential to image endogenous contrast mechanisms in vivo is unique and will provide new biological insights.

5.4 X-Ray Luminescent Contrast Agents

The majority of studied X-ray luminescent contrast agents are rare-earth nanoprobes which consist of a lanthanide-doped host material surrounded by a non-doped shell [39]. The luminescent behavior of the lanthanide-doped material has been well characterized over the years due to the broad use of scintillation materials in X-ray medical imaging applications [40]. Different experiments were conducted using $BaYF_5$, $NaYF_4$, or $NaLuF_4$ doped with ytterbium (Yr) and erbium (ER), or

Europium (EU) and delivered good optical and infrared photon emission when excited with X-rays [39, 41]. Following the literature, the majority of XLCT experiments were conducted with Eu- or Er-doped nanophosphors. Beyond these experiments also Tb, Cr, and La were used to study combined XLCT and optically stimulated luminescence imaging [42, 43]. Another efficient luminescent emitter is Gd_2O_2S:Eu (GOSE) which was used in proof-of-concept experiments [44], but it is not recommended as a biological tracer, due to its toxicity.

6 Comparison to Other Imaging Modalities

In the last decade, much effort has been dedicated to the development of instruments that can image both anatomical structure and molecular processes noninvasively. In the existing designs, a molecular imaging modality (e.g., PET, SPECT, optical fluorescence tomography (OFT)) is combined with X-ray CT or MRI, and both modalities are working independently (or even sequentially) to provide co-registered anatomical and molecular images [45–47]. However, these approaches have inherent limitations. Radionuclide tracer synthesis, for example, requires complex radiochemistry procedures, and commonly radiotracers must be produced on-site. The imaging needs to be performed within a short time window after radiotracer synthesis.

Systems combining CT and OFT [47] do not require radionuclides, but labeling a small molecule of interest (e.g., glucose) with a fluorescent dye without affecting its function and biodistribution is challenging, and very few fluorescent agents have found a use in the clinic. Tissue autofluorescence is also intractable and impedes the sensitive detection of fluorescent molecules. Gold nanoparticles can be excited optically via the plasmonic resonance effect and emit red-shifted light. Optical imaging methods are quite popular in mouse imaging studies because of their high sensitivity. However, the resolution suffers due to diffuse optical scattering. The typical resolution for optical fluorescence imaging at 1 cm depth is 3 mm [48], whereas XFCT imaging achieves sub-mm resolution.

The capability for simultaneous imaging of a large panel of elements in XFCT is an advantage in comparison to PET. In PET, only 511 keV photons can be measured; meaning only one target molecule at a time. Furthermore, the signal carriers in XFCT are stable over time, and each molecule can be excited multiple times which is not possible with radionuclides used in PET and SPECT. As a proof of concept for the imaging capability to simultaneously measure various elements, an XFCT acquisition was performed in a first-generation CT geometry, acquiring a single pencil-beam line integral at a time [6]. It was possible to measure Au, Gd, and Ba inclusions with a diameter of 5 mm with a single polychromatic and filtered X-ray beam. The 5 mm diameter pencil beam was produced by an X-ray tube operated at 150 kVp, and the phantom was imaged in the prototype system using 30 translational

steps (45 mm total displacement) and 31 rotational steps (360° total rotation). The XF photons of all three elements were detected with a single CdTe detector, and the success of the measurements exemplifies that no additional hardware is required for multitracer imaging.

To compare the molecular sensitivity of XFCT contrast agents and radionuclides, the following approximation is made. For AuNPs (50 kDa), 1 μg/ml is equivalent to a molar sensitivity of 20 pM, similar to PET and better than SPECT. We note that PET imaging probes have lower molecular weight than AuNPs, so mass sensitivity of PET and XFCT is not similar. The comparison of different signal carriers, such as nanoparticles and radiolabeled molecules, requires the consideration of distinct characteristics. The ability of signal carriers to accumulate in pathological tissues or target regions influences the molecular sensitivity as well as the efficiency of clearance from the background environment. An accurate comparison of sensitivity needs to account for the pharmacokinetics of the agents which needs to be compared for each specific application. For receptor imaging, for example, the number of available receptors might limit the amount of contrast agent, and large re-excitable nanoparticles might provide more signal per receptor than single-decay PET or SPECT probes [49].

To compare XFCT imaging with traditional X-ray transmission imaging, the following calculations are presented. Based on the gold bulk attenuation coefficient of 27.5 cm^2/g at 30 keV, the X-ray attenuation coefficient for a 10 μg/ml gold nanoparticle aqueous solution is 0.2272 cm^2/g, which is only 0.12% higher than the coefficient of water. For XFCT imaging instead, the intensity of the X-ray fluorescence photons in the emission spectrum is at least 10% greater than the intensity of the water background. Theoretically, this allows for two orders of magnitude higher sensitivity with XFCT compared to transmission X-ray-based imaging. It enables in vivo visualization of probes that cannot be imaged by any other means, such as metallodrugs as well as trace minerals.

As energy resolving detectors are also under investigation for CT imaging, preclinical and clinical spectral CT systems were established for research purposes in recent years. As the detection event rate in CT is approximately three orders of magnitude higher in transmission CT compared to XFCT, only detectors with rough energy resolution (with up to six energy bins) could be developed so far. Rough estimations predict that the molecular sensitivity of XFCT is improved by an order of magnitude compared to state-of-the-art transmission spectral CT.

7 Imaging Modes

Until now, the majority of proof of principle XFCT measurements were performed with pencil-beam excitation and uncollimated X-ray detectors. While this combination is the most intuitive form of image acquisition for XF imaging, other acquisition modes were suggested and realized. The selection of the best acquisition mode for an application is a delicate exercise due to the many parameters involved in XFCT

imaging. Commonly the choice is driven by trade-offs between sensitivity and acquisition time and often restricted by the XFCT hardware. Another way to localize XF emitters is the spatial selective X-ray excitation which can be combined with spatially resolving, energy-discriminating X-ray detectors. Akin to MRI, it is possible to partially encode the X-ray excitation to some of the spatial dimensions by collimation on the source side and to collimate the detectors to measure the remaining dimensions. Compared to the sinogram format provided by a rotating gantry, here the XFCT can directly be measured in image space, without the need for any image reconstruction (triple-collimation geometry).

7.1 Pencil-Beam XFCT

In the general concept of XFCT imaging, the excitation is limited to a line by creating a pencil beam. The X-ray pencil beam is commonly generated by collimating the X-ray photons emitted by a standard clinical X-ray source. For lower energies (<30 keV), it is also possible to focus X-rays as described in chapter "High-Resolution 2D Imaging". The collimation is usually realized with masks of high atomic number materials like lead or tungsten which block the excess X-rays emitted by the anode of the X-ray source. With this form of excitation, the emission of XF X-rays from the contrast agents is mainly limited to the line of excitation. Of course, it is possible that scatter or background X-rays excite target agents outside of the line of excitation, but this process is highly suppressed as scattered photons already lost too much energy to stimulate K-shell or L-shell fluorescence, respectively. However, it is recommended to utilize filtration for the polychromatic X-ray beam as the scatter background magnitude and dose to the imaged object is highly dependent on the shape of the energy spectra of the X-ray beam. The beam filtration cuts off the lower energy photons which generate dose to the object but are not energetic enough to produce fluorescent X-rays. It also attenuates higher energy X-rays, but in general this only increases the acquisition time slightly. The acceleration voltage of the X-ray source is also a parameter that influences the beam energy spectrum. Here, the higher energy part of the spectrum is shaped. It is recommended to produce fewer X-rays with excess energies above the K-shell excitation. These higher energetic X-rays increase the probability for scatter photons in the energy range of the XF signal. Furthermore, the scattered X-rays have enough energy to create XF signals outside of the line of excitation. For optimized performance, the source voltage and the filtration must be tuned for each contrast agent individually.

While there is an optimal configuration for each contrast agent, it was shown that multiplexed imaging of multiple contrast agents with a single filter and tube voltage configuration is possible [18]. In the study, the filter consisted of 1 mm Pb, 1.4 mm Cu, and 7.3 mm Al optimized for the imaging of platinum, gadolinium, and iodine simultaneously.

For K-shell fluorescence experiments with high emission energy elements, e.g., gold or platinum, the molecular sensitivity can be increased with a spectro-spatial

optimization of the detector placement [22]. The optimization is based on minimizing the Compton scatter X-rays, which are the primary source of interference in X-ray fluorescence imaging of low quantities of contrast agent. The study proposed an optimized anisotropic spatial orientation of detectors such that there is a low probability of acquiring scatter X-rays which have the same energy as fluorescence X-rays. In this optimization, X-ray detectors are placed at large scattering angles relative to the primary excitation beam. At large scattering angles, the Compton scatter X-rays loose enough energy in the scattering process to be separable from the fluorescent signal.

As a consequence, this optimized detector configuration allows higher molecular sensitivities which was validated in Monte Carlo simulations. A mouse-sized phantom, with a diameter of 2.25 cm, containing various low gold concentrations (10–100 μg/ml) of nanoparticles expected in molecular imaging applications was excited with different beam spectra (monoenergetic, Gaussian, and tungsten anode). It is shown that the optimized configuration, in which X-ray detectors cover only a specific portion of a sphere surrounding the imaging volume, performed better than the isotropic configuration (in which detectors cover the entire sphere). This was a counterintuitive result that forces a redesign of XF imaging instrumentation. The optimization results in a tenfold sensitivity improvement over isotropic detection for gold nanoparticles and established a theoretical sensitivity limit of 10 μg/ml. The sensitivity improvement significantly enhanced the potential of the X-ray fluorescence modality for future preclinical and clinical molecular imaging.

7.2 Compton Camera XFCT

The anisotropic detection principle, described above, can also be combined with Compton imaging [50]. The position and energy information of a fluorescent X-ray can be collected with a Compton camera. This information is used to restrict the possible emission of XF X-rays to a cone-surface in the image domain. Here we talk about electronic collimation on the detector side in comparison of physical collimation on the source side in pencil-beam XFCT. In contrast to physical collimation on the detector side, the electronic collimation reaches higher sensitivity as no valuable XF photons are absorbed by a collimator.

With the spatial information from the Compton camera, scatter events can be distinguished based on their emission direction which is specifically efficient for deep tissue imaging. This enables reasonable molecular sensitivity in clinical in vivo XF imaging and allows high-speed imaging as the target region can be excited with fan- or cone beams. Image reconstructions in our Monte Carlo studies were able to recover 5 mm diameter lesions in the center of a human lung. The results show that low concentrations down to 150 μg/ml can be detected for a CdTe energy resolution of 110 eV at 78 keV and a target dose of 30 mGy. Since the detector developments are not yet advanced enough to realize XFI with the Compton Imaging concept, further advances in detector instrumentation are required to realize clinically feasible Compton camera XF imaging.

7.3 Fan-Beam and Volumetric Imaging Modes

XFCT and XLCT allow more imaging modes than optical imaging and standard CT due to freedom in detector placement and due to the much lower absorption and scatter probability of X-rays compared to optical photons. As energetic X-rays mainly transverse the imaging medium on a linear path with exponential attenuation, the possible lines of response (LORs) can be either annotated by the source beam geometry or the detector collimation. Besides the pencil beam and Compton camera XFCT geometries described above, it is possible to use different detector collimation designs and combine them with different X-ray source collimation geometries. Basically, six different combinations of X-ray source and detector collimation are possible. Dual collimation of the source, the detector, or both yields LORs along which projective measurements can be performed. These LORs result from the intersection of two planes, wherein each plane is defined either by an excitation or detection collimator. Using this principle, a pencil-beam geometry is achieved by collimating the source in two orthogonal directions; a fan-beam geometry by collimating the beam and the detectors each once orthogonally; and the cone-beam geometry by collimating the detectors in two orthogonal dimensions. Each geometry offers a different trade-off in terms of spatial resolution, sensitivity, imaging time, and imaging dose. On top of these three basic collimation concepts, it is possible to directly measure elemental concentrations at "points of response" (PORs) with the use of three orthogonal collimation planes. This can either be achieved by a combination of a pencil-beam collimation and a strip collimator orthogonal to each other or by a fan-beam excitation perpendicular to a parallel hole collimator. In these designs, no ill-posed inverse problem must be solved for image reconstruction and quantitative images can be obtained with a direct attenuation correction on the measured data. This scheme offers the attractive possibility of directly probing the PORs of interest and also removes the noise amplification inherent to the image reconstruction process.

Last, pinhole collimators can be used in place of parallel hole collimators with cone-beam excitation. With the pinhole collimators, it is possible to achieve higher spatial resolutions than restricted by the dimensions of an exciting pencil beam. As pinhole collimation may reduce the sensitivity, the following approximation should motivate the approach: The goal is to achieve around 1 mm spatial resolution in molecular information extraction. We consider a 1 mm^3 volume element, filled with 10 μg/ml of AuNPs, irradiated with X-rays (10 cGy total dose, 81 keV) (similar to the dose used in microCT). This corresponds to an energy transfer of 100 μJ, or 7.7 billion photons. Out of those photons, about 0.05% interact with gold, while the remainder interacts with water (this is based on the higher density and attenuation cross-section of gold compared to water). Out of the 3.85 millions of photons that interact with gold, 99% do so via the photoelectric absorption, and 80% of these with the K-shell. Based on the fluorescence yield of gold (95%), roughly 3.66 million fluorescent X-rays are emitted. Assuming a 10% photon sensitivity (pencil beam, no detector collimator), 366,000 photons can be detected that emanate from a single

1 mm^3 volume element. With a SPECT-like pinhole collimator (0.01% sensitivity), 366 fluorescent photons per 1 mm^3 image voxel would be collected. Those statistics are sufficient for accurate image reconstruction.

7.4 High-Resolution 2D Imaging

Besides clinical and preclinical in vivo imaging, molecular imaging analysis of surgically removed tumors with high-resolution planar imaging is a potential application for XF or XL imaging. Currently, resected tumors are analyzed by pathologists which requires staining of the tissue with elaborate techniques. This procedure is cumbersome and time-consuming. In a 2D XF imaging approach, small tumor samples can be analyzed quickly with resolution ranging from 5 to 100 μm by translating the sample with a bilinear motion stage across a narrow pencil beam. Such imaging can be performed close to the operating room and return feedback about the analysis of the sample to the surgeon before closing the surgical site.

The analysis of small samples allows the use of low energetic X-rays which can be manipulated with X-ray optics made of hollow glass tubes. With classic collimation, the imaging process can take up to hours, but with polycapillary optics, the X-ray flux can be increased by orders of magnitude and stimulate a proportionally sizable fluorescent response [51]. This makes imaging within minutes possible.

7.5 Coded-Aperture Compressed XLCT

The pencil-beam XLCT approach provides a simple image reconstruction problem, but commonly the scanning time is prohibitive for in vivo imaging. In coded-aperture compressive XLCT (CAC-XLCT), a binary pseudorandom aperture mask encodes the X-ray excitation field for each angular projection. In this case, instead of exciting the sample one pencil beam at a time, the sample is simultaneously excited by a subset of multiple pencil beams. The specific excitation pattern created by the coded aperture mask is incorporated into the sensing matrix, and image reconstruction is performed using sparse regularization. This compressed-sensing image reconstruction approach that combines a pseudorandom coded aperture mask and sparse regularization allows for reconstructing high-quality images with far fewer measurements than what traditional sampling dictates. It was demonstrated that CAC-XLCT performance using five coded aperture masks per angular projection with a mask transmission of 20% can locate all target lesions in a mouse-sized phantom with good image quality. For comparison purposes, an image reconstructed with cone beam XLCT is not able to recover the true nanophosphor distribution. CAC-XLCT allows for accurately retrieving the nanophosphor distribution with 400 times fewer measurements than pencil-beam XLCT would require, indicating a 400-times faster acquisition time.

7.6 XFCT with Polarized X-Ray

It is possible to perform XFCT imaging with polarized X-rays. In synchrotrons, for example, X-rays are naturally emitted with a preferred polarization direction. For excitation it is possible to have an optimized setup with a detector positioning for suppressed scatter contamination. The reconstructed images in Fig. 4 show how this is beneficial for XFCT imaging performance.

8 Figures of Merit for Performance Analysis

The direct performance comparison of different systems and imaging modes is a delicate exercise as different studies utilize different system parameters for their experiments and different figures of merit for the performance analysis. The imaging sensitivity and resolution are commonly assessed in phantom experiments. Here, we propose some imaging configurations and figure of merits which have been proven useful for the performance analysis.

The molecular sensitivity is usually determined by measuring various medium-sized cylinders with different concentrations of contrast agent. The lowest detectable contrast agent concentration is then retrieved by a linear least square fit to the contrast-to-noise ratio (CNR) to concentration ratio where a contrast-to-noise ratio of 5 (*Rose Criterion*) is considered the minimal detection limit. In this context, the CNR is defined by:

$$\mathrm{CNR} = \frac{\mu_{\mathrm{ROI}} - \mu_{\mathrm{bkg}}}{\sigma_{\mathrm{bkg}}},$$

where μ_{ROI}, μ_{bkg}, and σ_{bkg} are the average voxel intensity of the region of interest (ROI) and background (bkg) and the standard deviation of the voxel intensity within the background region, respectively. Usually, the background region is a ROI sized region defined in the center of the field of view (FOV).

A figure of merit for spatial accuracy is the Dice coefficient (DC). For phantoms without background concentration, the coefficient extracts the precision of the image acquisition and reconstruction to correctly position the contrast agent into the image and the ability of the image reconstruction to reduce scatter background and noise. The DC is calculated as follows:

$$\mathrm{DC} = \frac{2\sum I_{\mathrm{ROIs}}}{\sum I_{\overline{\mathrm{ROIs}}} + 2\sum I_{\mathrm{ROIs}}},$$

where I_{ROIs} is the voxel intensity inside the ROIs and $I_{\overline{\mathrm{ROIs}}}$ the voxel intensity outside of the ROIs. If no contrast agent is located outside of the ROIs, then a perfect acquisition and reconstruction results in a DC of one.

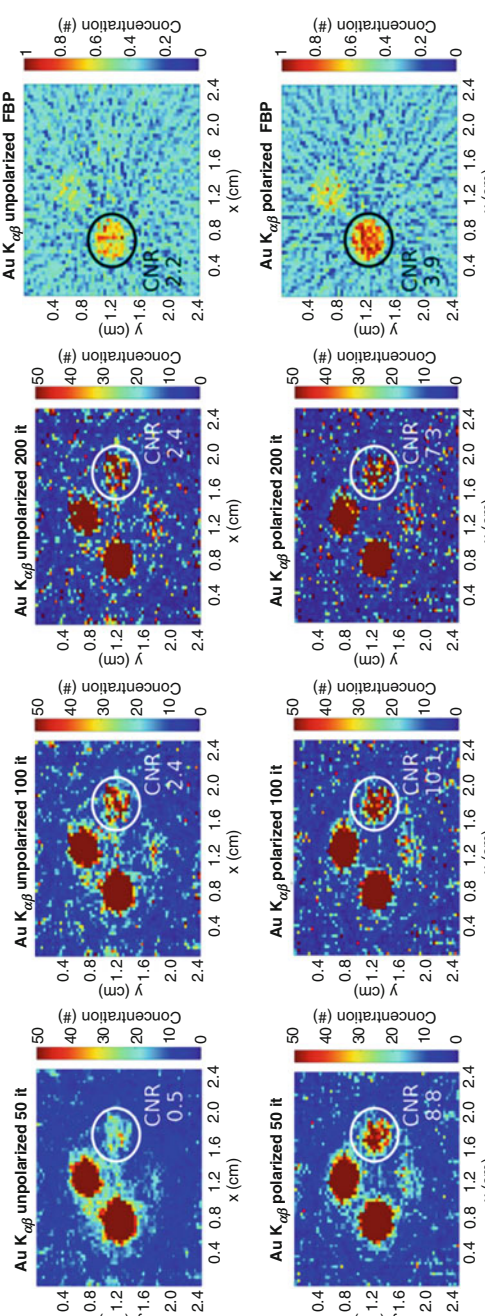

Fig. 4 Images reconstructed for the CZT large crystal geometry for unpolarized X-rays (upper row) and linear polarized X-rays (lower row). The images are reconstructed with 50,100, and 200 iterations for both excitation modes. The images are scaled to a maximal concentration intensity of 50 (arb. units) to compare the visibility of the 20 s µg/ml target. The last column depicts the images reconstructed with filtered-backprojection and CNR for the highest gold concentration for comparison (Reprint with permission [7])

A quantitative figure of merit for the determination of correct signal amplitudes is the contrast recovery coefficient (CRC). For the analysis, phantoms with known background concentrations are typically used where the high contrast agent concentration is embedded in a low contrast agent background. The contrast is normalized to the expected value for the contrast. The explicit form is given by:

$$\mathrm{CRC} = 100 \frac{\frac{\mu_{\mathrm{high}}}{\mu_{\mathrm{low}}} - 1}{\frac{a_{\mathrm{high}}}{a_{\mathrm{low}}} - 1},$$

where a_{high}, a_{low}, μ_{high}, and μ_{low} are the mean values of the known and reconstructed low and high contrast agent concentrations, respectively.

Another metric for image analysis is the normalized mean square error (NMSE). It is a valuable figure of merit when the actual contrast agent distribution is known, e.g., in simulations. The NMSE is calculated as follows:

$$\mathrm{NMSE} = \frac{\|x - x_{\mathrm{T}}\|_2^2}{\|x_{\mathrm{T}}\|_2^2},$$

where x is the reconstructed image and x_{T} is the true contrast agent distribution. The NMSE is especially useful as it considers the whole FOV for the performance analysis.

9 Potential of Clinical X-Ray Excited Imaging

The concepts and strategies of XFCT and XLCT can be extended in the future to clinical human in vivo imaging. Although moving from small-animal imaging to human imaging will result in higher attenuation of the characteristic X-rays, XFCT remains a feasible approach for elements such as gold and platinum. The characteristic X-rays emitted by these elements are energetic enough to propagate through ~20 cm tissue with only minor attenuation. For XFCT with elements emitting lower characteristic energies and XLCT, imaging is still possible in examinations with clinical merits like breast, head and neck, hand, and shallowly seated lymph nodes where and depth is not a major issue. Here, L-shell fluorescence signals (15–20 kV) can also be utilized to enhance the SNRs dramatically, as was demonstrated in our recent studies in simulation [15] and experiment [17]. In clinical L-shell applications, a full gantry rotation is likely redundant as only excitations from the skin side will contribute recoverable information. Hence, optimized compressed sensing approaches are required to provide quantitative images of high quality for gantry excitation arcs from $\pi/2-\pi$.

The concept of XFCT has been proposed mainly in the realm of monochromatic synchrotron sources, but a turnkey solution fully utilizing the potential of the XF

signals for in vivo molecular imaging has yet to be developed. It was shown that polychromatic X-rays from clinical sources are still able to detect low concentrations of XF signals when all of the described XFCT data acquisition strategies are exploited to their full potential. In fact, most of these strategies are also compatible with monochromatic excitation which usually leads to sensitivity improvements by one order of magnitude better with monochromatic excitation. In this context, developments in the field of inverse Compton scattering are intriguing as they allow the establishment of laboratory scaled monochromatic X-ray sources feasible for clinical environments.

This chapter discussed studies which lay the foundation for the future development of human XFCT. While the concepts and initial results of XFCT are intriguing, its widespread acceptance for molecular imaging depends critically on the achievable sensitivity, and further technology is required to increase the sensitivity. For example, advanced imaging techniques like Compton imaging [50, 52] or time-of-flight information will help to reach clinical sensitivities comparable to sensitivities shown here.

Contrast agents like Gd- or Pt-based drugs have already been approved by the FDA, and no regulatory hurdles need to be addressed for immediate clinical use.

When fully implemented in the clinic, XFCT will provide crucial information about molecular processes taking place within the patient. Considering the large number of CT exams done annually in the USA (~69 million/year, with an observed annual growth rate of about 8% [53]), the potential impact of XFCT will be enormous.

Acknowledgments The authors would like to thank the NIH for the support of several XFCT and XLCT research projects and to the many researches who were involved in the related work at our institute.

Compliance with Ethical Standards

Conflict of Interest Author Don Vernekohl declares that he has no conflict of interest. Author Lei Xing declares that he has no conflict of interest.

Ethical Approval This article does not contain any studies with human participants or animals performed by any of the authors.

References

1. Xiang L, Han B, Carpenter C, Pratx G, Kuang Y, Xing L (2013) X-ray acoustic computed tomography with pulsed x-ray beam from a medical linear accelerator. Med Phys 40:010701
2. Rizk SL, Rizk SL, Sky-Peck HH (1984) Comparison between concentrations of trace elements in normal and neoplastia human breast tissue. Cancer Res 44:5390–5394
3. Somervaille LJ, Chettle DR, Scott MC (1985) In vivo measurement of lead in bone using X-ray fluorescence. Phys Med Biol 30:929

4. Cheong S-K, Jones BL, Siddiqi AK, Liu F, Manohar N, Cho SH (2010) X-ray fluorescence computed tomography (XFCT) imaging of gold nanoparticle-loaded objects using 110 kVp x-rays. Phys Med Biol 55:647
5. Cong W, Shen H, Cao G, Liu H, Wang G (2013) X-ray fluorescence tomographic system design and image reconstruction. J Xray Sci Technol 21:1–8
6. Kuang Y, Pratx G, Bazalova M, Meng B, Qian J, Xing L (2013) First demonstration of multiplexed X-ray fluorescence computed tomography (XFCT) imaging. IEEE Trans Med Imaging 32:262–267
7. Vernekohl D, Tzoumas S, Zhao W, Xing L (2018) Polarized x-ray excitation for scatter reduction in x-ray fluorescence computed tomography. Med Phys 45:3741–3748
8. Cesareo R, Mascarenhas S (1989) A new tomographic device based on the detection of fluorescent x-rays. Nucl Instrum Methods Phys Res Sect A 277:669–672
9. La Riviere PJ, Vargas P, Fu G, Meng LJ (2009) Accelerating X-ray fluorescence computed tomography. Conf Proc IEEE Eng Med Biol Soc 2009:1000–1003
10. Bazalova M, Kuang Y, Pratx G, Xing L (2012) Investigation of X-ray fluorescence computed tomography and K-edge CT imaging. IEEE Trans Med Imaging 31:1620–1627
11. Weissleder R (2006) Molecular imaging in cancer. Science 2006:1168–1171
12. Massoud TF, Gambhir SS (2003) Molecular imaging in living subjects: seeing fundamental biological processes in a new light. Genes Dev 17:545–580
13. Weissleder R, Ross BD, Rehemtulla A, Gambhir SS (2010) Molecular imaging: principles and practice. People's Medical Publishing House, Shelton
14. Hayashi Y, Okuyama F (2010) New approach to breast tumor detection based on fluorescence x-ray analysis. Ger Med Sci 8
15. Bazalova MA, Ahmad M, Pratx G, Xing L (2013) XFCT imaging of cisplatin with L-shell x-rays. Phys Med Biol 59:219–232
16. Vernekohl D, Streicher M, Ahmad M, Xing L (2016) Comparison of a large area czt detector to a spectroscopic cdte detector for x-ray fluorescence computed tomography. In: IEEE nuclear science symposium, medical imaging conference and room-temperature semiconductor detector workshop (NSS/MIC/RTSD), Strassbourg
17. Bazalova-Carter M, Ahmad M, Xing L, Fahrig R (2015) Experimental validation of L-shell x-ray fluorescence computed tomography imaging: phantom study. J Med Imaging 2:043501
18. Kuang Y, Pratx G, Bazalova M, Qian J, Meng B, Xing L (2013) Development of XFCT imaging strategy for monitoring the spatial distribution of platinum-based chemodrugs: instrumentation and phantom validation. Med Phys 40:030701
19. Ahmad M, Bazalova-Carter M, Fahrig R, Xing L (2015) Optimized detector angular configuration increases the sensitivity of X-ray fluorescence computed tomography (XFCT). IEEE Trans Med Imaging 34:1140–1147
20. Dhez P, Chevallier P, Lucatorto TB, Tarrio C (1999) Instrumental aspects of x-ray microbeams in the range above 1 keV. Rev Sci Instrum 70:1907–1920
21. Gottschlag H, Kosters T, Vernekohl D, Reygers K, Schafers KP, Wubbeling F, Wessels JP (2013) Towards quantitative image reconstruction using Monte-Carlo simulations in multi-wire proportional chamber-based small animal PET. IEEE Trans Nucl Sci 60:3343–3354
22. Ahmad M, Bazalova M, Xiang L, Xing L (2014) Order of magnitude sensitivity increase in X-ray fluorescence computed tomography (XFCT) imaging with an optimized spectro-spatial detector configuration: theory and simulation. IEEE Trans Med Imaging 33:1119–1128
23. Kim JH, Kim JS, Choi H, Lee SM, Jun BH, Yu KN, Kuk E, Kim YK, Jeong DH, Cho MH, Lee YS (2006) Nanoparticle probes with surface enhanced Raman spectroscopic tags for cellular cancer targeting. Anal Chem 78:6967–6973
24. Lee K-S, El-Sayed MA (2006) Gold and silver nanoparticles in sensing and imaging: sensitivity of Plasmon response to size, shape, and metal composition. J Phys Chem B 110:19220–19225
25. McDonald MA, Watkin KL (2006) Investigations into the physicochemical properties of dextran small particulate gadolinium oxide nanoparticles. Acad Radiol 13:421–427

26. Gupta AK, Gupta M (2005) Synthesis and surface engineering of iron oxide nanoparticles for biomedical applications. Biomaterials 26:3995–4021
27. Ngwa W, Makrigiorgos GM, Berbeco RI (2012) Gold nanoparticle enhancement of stereotactic radiosurgery for neovascular age-related macular degeneration. Phys Med Biol 57:6371–6380
28. Chattopadhyay N, Cai Z, Kwon YL, Lechtman E, Pignol JP, Reilly RM (2013) Molecularly targeted gold nanoparticles enhance the radiation response of breast cancer cells and tumor xenografts to X-radiation. Breast Cancer Res Treat 137:81–91
29. Hossain M, Su M (2012) Nanoparticle location and material dependent dose enhancement in X-ray radiation therapy. J Phys Chem C Nanomater Interfaces 116:23047–23052
30. Cho SH (2005) Estimation of tumour dose enhancement due to gold nanoparticles during typical radiation treatments: a preliminary Monte Carlo study. Phys Med Biol 50:N163–N173
31. Geng F, Song K, Xing JZ, Yuan C, Yan S, Yang Q, Chen J, Kong B (2011) Thio-glucose bound gold nanoparticles enhance radio-cytotoxic targeting of ovarian cancer. Nanotechnology 22:285101
32. Allemann E, Brasseur N, Benrezzak O, Rousseau J, Kudrevich SV, Boyle RW, Leroux JC, Gurny R, van Lier JE (1995) PEG-coated poly(lactic acid) nanoparticles for the delivery of hexadecafluoro zinc phthalocyanine to EMT-6 mouse mammary tumours. J Pharm Pharmacol 47:382–387
33. Khlebtsov B, Panfilova E, Khanadeev V, Bibikova O, Terentyuk G, Ivanov A, Rumyantseva V, Shilov I, Ryabova A, Loshchenov V, Khlebtsov NG (2011) Nanocomposites containing silica-coated gold-silver nanocages and Yb-2,4-dimethoxyhematoporphyrin: multifunctional capability of IR-luminescence detection, photosensitization, and photothermolysis. ACS Nano 5:7077–7089
34. Wason MS, Colon J, Das S, Seal S, Turkson J, Zhao J, Baker CH (2013) Sensitization of pancreatic cancer cells to radiation by cerium oxide nanoparticle-induced ROS production. Nanomedicine 9:558–569
35. Timerbaev A, Sturup S (2012) Analytical approaches for assaying metallodrugs in biological samples: recent methodological developments and future trends. Curr Drug Metab 13:272–283
36. Geraki K, Farquharson MJ, Bradley DA (2002) Concentrations of Fe, Cu and Zn in breast tissue: a synchrotron XRF study. Phys Med Biol 47:2327
37. Costello LC, Franklin RB (1998) Novel role of zinc in the regulation of prostate citrate metabolism and its implications in prostate cancer. Prostate 35:285–296
38. Tazebay UH, Wapnir IL, Levy O, Dohan O, Zuckier LS, Zhao QH, Deng HF, Amenta PS, Fineberg S, Pestell RG, Carrasco N (2000) The mammary gland iodide transporter is expressed during lactation and in breast cancer. Nat Med 6:871–878
39. Naczynski DJ, Sun C, Turkcan S, Jenkins C, Koh AL, Ikeda D, Pratx G, Xing L (2015) X-ray-induced shortwave infrared biomedical imaging using rare-earth nanoprobes. Nano Lett 15:96–102
40. Chen D, Zhu S, Yi H, Zhang X, Chen D, Liang J, Tian J (2013) Cone beam x-ray luminescence computed tomography: a feasibility study. Med Phys 40:031111
41. Yi Z, Lu W, Xu Y, Yang J, Deng L, Qian C, Zeng T, Wang H, Rao L, Liu H, Zeng S (2014) PEGylated NaLuF4: Yb/Er upconversion nanophosphors for in vivo synergistic fluorescence/X-ray bioimaging and long-lasting, real-time tracking. Biomaterials 35:9689–9697
42. Cong W, Wang C, Wang G (2014) Stored luminescence computed tomography. Appl Optics 53:5672–5676
43. Carpenter CM, Sun C, Pratx G, Rao R, Xing L (2010) Hybrid x-ray/optical luminescence imaging: characterization of experimental conditions. Med Phys 37:4011–4018
44. Pratx G, Carpenter CM, Sun C, Rao RP, Xing L (2010) Tomographic molecular imaging of x-ray-excitable nanoparticles. Opt Lett 35:3345–3347
45. Beyer T, Townsend DW, Brun T, Kinahan PE, Charron M, Roddy R, Jerin J, Young J, Byars L, Nutt R (2000) A combined PET/CT scanner for clinical oncology. J Nucl Med 41:1369–1379
46. Schillaci O (2005) Hybrid SPECT/CT: a new era for SPECT imaging? Eur J Nucl Med Mol Imaging 32:521–524

47. Schulz RB, Ale A, Sarantopoulos A, Freyer M, Soehngen E, Zientkowska M, Ntziachristos V (2010) Hybrid system for simultaneous fluorescence and X-ray computed tomography. IEEE Trans Med Imaging 29:465–473
48. Wang B, Zhao Q, Barkey NM, Morse DL, Jiang H (2012) Photoacoustic tomography and fluorescence molecular tomography: a comparative study based on indocyanine green. Med Phys 39:2512–2517
49. Pratx G, Carpenter CM, Sun C, Xing L (2010) X-ray luminescence computed tomography via selective excitation: a feasibility study. IEEE Trans Med Imaging 29:1992–1999
50. Vernekohl D, Ahmad M, Chinn G, Xing L (2016) Feasibility study of Compton cameras for x-ray fluorescence computed tomography with humans. Phys Med Biol 61:8521–8540
51. Vernekohl D, Ahmad M, Dai X, Zhao W, Cheng K, Xing L (2019) Reduced acquisition time for L-shell x-ray fluorescence computed tomography using polycapillary x-ray optics. Med Phys. https://doi.org/10.1002/mp.13822
52. Tzoumas S, Vernekohl D, Xing L (2018) Coded-aperture compressed sensing X-ray luminescence tomography. IEEE Trans Biomed Eng 65:1892–1895
53. Division IMI (2008) CT census database and market summary report. IMV, L'Aigle

Top Med Chem (2020) 34: 149–184
DOI: 10.1007/7355_2019_90

Published online: 11 March 2020

Applications of Fluorescent Protein-Based Sensors in Bioimaging

Uday Kumar Sukumar, Arutselvan Natarajan, Tarik F. Massoud, and Ramasamy Paulmurugan

Contents

Abstract In the last two decades, there have been enormous developments in the area of reporter gene imaging for various bioimaging applications, especially to track cellular events that are occurring in intact cells and cells within living animals. As part of this process, there has been a significant interest in identifying new reporters or developing new substrates that can allow us to image multiple cellular events simultaneously without any signal overlap between the targets. Even though chemical dyes are useful for some of these applications, reporter proteins which mimic biological properties of proteins when tagged directly with the target proteins are very useful. Although molecular imaging has significantly advanced through use of different imaging probes (radiolabeled ligands, MR contrast agents, CT contrast agents, fluorescent dyes, fluorescent and bioluminescent proteins) and techniques (PET, SPECT, MRI, CT, optical, ultrasound, and photoacoustic imaging), optical imaging, such as fluorescence and bioluminescence imaging, has shown promising applications in various preclinical settings, especially in imaging cellular pathways and studies involving drug development. This is mainly owing to its simple and easy

U. K. Sukumar, A. Natarajan, T. F. Massoud, and R. Paulmurugan (✉)
Molecular Imaging Program at Stanford, Department of Radiology, Stanford University School of Medicine, Stanford, CA, USA
e-mail: paulmur8@stanford.edu

nature in performing the assay and also its high-throughput and cost-effective applications. In this chapter, we review the evolution of optical imaging with specific emphasis on fluorescent proteins, as well as an introduction regarding the general approach of optical imaging in in vitro and in vivo applications. We explain this by briefly introducing different optical imaging methods and fluorescent assays developed based on fluorescent dyes and fluorescent proteins followed by a detailed review of different fluorescent proteins currently used for various assay developments and applications.

Keywords BRET, Fluorescence dyes, Fluorescent proteins, FRET, In vivo imaging

1 Introduction

Fluorescent proteins and fluorescent dyes are routinely used to monitor biological processes of cells in culture or cells in living animals; hence they are called fluorescent reporters (FR). This includes fluorescent proteins, organic dyes, and inorganic photonic materials. Fluorescent reporters are commonly used for developing assays involving fluorescence spectroscopy, fluorescence microscopy, and whole-body preclinical imaging and to some extent in human applications for image-guided surgery in the operating room [1, 2]. Fluorescent reporters in combination with an optical imaging system can provide key information in clinical oncologic research while providing the opportunity to develop transgenic animal models for studying various diseases, including cancer. Fluorescent dyes are widely used in various bioassay applications. Here, we mainly discuss the role of fluorescent protein as reporters (FPR) in various sensor designs and applications in bioimaging, drug delivery, and drug discovery systems. We also briefly discuss the role of fluorescent dyes in imaging applications (Fig. 1).

2 Fluorescent Biosensors and Evolution of Fluorescent Protein Palette

Fluorescent proteins are frequently used for studying molecular mechanisms of cells and physiological processes involved in cellular biological pathways. A plethora of fluorescent proteins with characteristic excitation and emission spectra offer enormous scope for researchers to "paint" living cells as they desire [3]. At present we have gone a step further and created sophisticated biosensors engineered with single or multiple fluorescent proteins, including Förster Resonance Energy Transfer (FRET)-based biosensors for studying macromolecular interactions in cells [4]. These fluorescent proteins exhibit environment-dependent changes in fluorescent

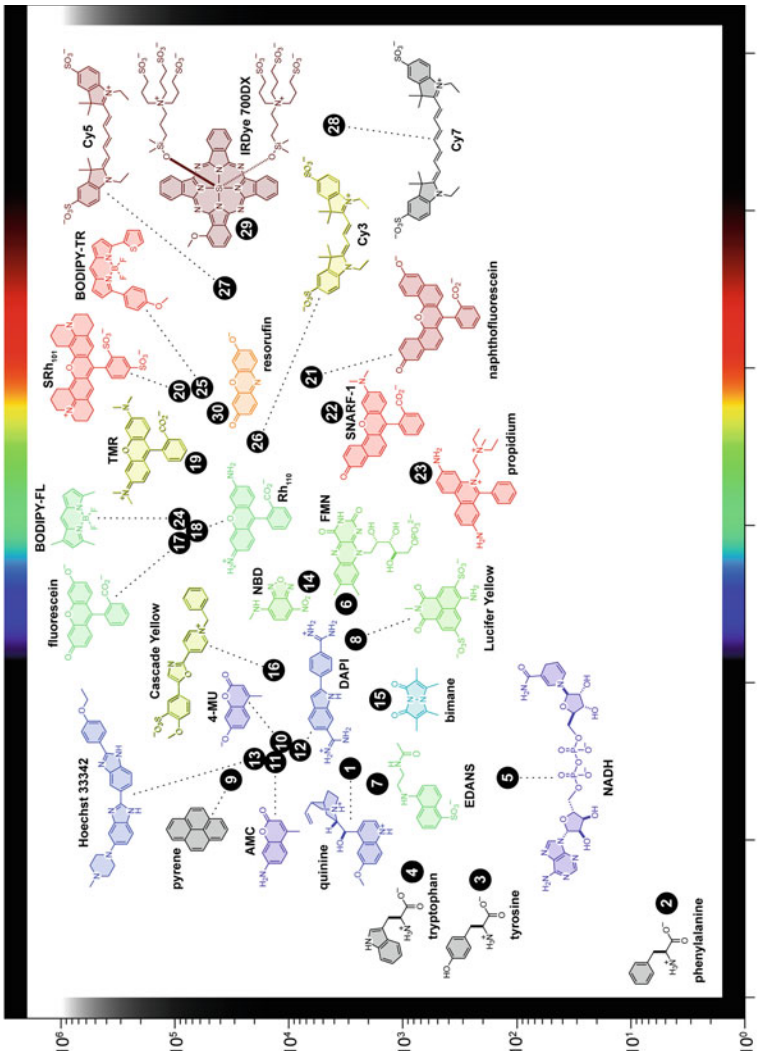

Fig. 1 Fluorescent dyes of various spectral properties developed in the last several decades and used for bioimaging applications in preclinical and clinical studies Adapted with permission from ACS Chem. Biol., 2008, 3(3), pp. 142–155 [2]

spectral characteristics and act as biosensors (1) to measure target enzyme functions (e.g., protein kinases and proteases); (2) to measure the concentration of intracellular ions, metabolites, and messengers (H^+, Ca^{2+}, Cl^-, H_2O_2, cAMP, etc.); (3) to monitor cellular physicochemical parameters (i.e. specific analyte, covalent modification, mechanical influence, redox potential, membrane potential); and (4) for high-throughput screening of drug candidates and their evaluations in preclinical studies. One of the earliest fluorescent proteins to be discovered was green fluorescent protein (GFP), when, in 1962, a Japanese organic chemist and marine biologist Osamu Shimomura stumbled upon this remarkable protein in the jellyfish *Aequorea victoria* [5]. At present this discovery has reached beyond the realm of science and our homes with the development of transgenic fluorescent fishes and green fluorescent pigs and cats [6, 7]. The first use of GFP as a fluorescent tag for in vivo labeling was demonstrated in 1995 by Dhandayuthapani et al., where they reported the application of GFP-engineered mycobacteria (*M. smegmatis* and *M. bovis* BCG) for analysis of fundamental biological and pathogenesis related to mycobacteria [8]. It was rather serendipitous that GFP turned out to be a natural monomer which enabled its wide use for labeling of various proteins of interest by simple in-frame fusion to the –COOH or $–NH_2$ terminus or even as an insert within a flexible loop of a protein [9].

Biosensing encompasses a diverse array of techniques for the generation of an experimentally accessible "readout" of a molecular interaction between a biomolecule-derived molecular recognition element (MRE) (e.g., a protein domain) and an analyte of interest (e.g., a small molecule, another protein, or an enzymatic activity) [10, 11]. Molecular entities or devices that enable biosensing are generally referred to as biosensors. The primary challenge of creating biosensors is transducing the nanometer-scale event of a biorecognition process into an observable change in a macroscopic property such as color or fluorescence hue [12]. One of the nanometer-scale changes that typically accompany biorecognition events is the change in molecular "geometry" of the MRE. This change could be a distance between the MRE and its analyte, as in the case of a protein-protein interaction, or a conformational change of the MRE, as in the case of allosteric proteins [13–15]. As we will discuss in this chapter, researchers have now devised a variety of strategies to develop fluorescent protein-based biosensors for many applications [16].

The protein-based fluorescent biosensors can be broadly categorized into two classes based on the construction method: the first class are genetically encoded fluorescent proteins such as GFP and its variants, whereas the second class comprises of chemically constructed biosensors made of natural protein scaffolds and artificial fluorescent molecules [17]. We will primarily discuss protein-based fluorescent biosensors in this chapter. In the case of genetically encoded biosensors (GFP-based), the GFP protein acts as a signal transducer that manifests change in fluorescence intensity or wavelength shift in response to triggered stimuli. Different versions of such biosensors have been established in the past, including single FP-based biosensors, split GFP-based biosensors, and dual FP-fused FRET-based biosensors [18]. Such biosensors are a powerful tool for in-cell imaging and/or elucidating biological events of cells in normal and pathological processes.

With the rapid progresses being made in exploring diverse applications of fluorescent proteins in biosensors, one of the major considerations is improving the "brightness" of the fluorophore to achieve higher sensitivity. The brightness of fluorescent protein depends on how well a molecule absorbs light and how fast it emits light. Light absorption by a fluorophore is quantified in terms of molecular extinction coefficient, whereas emission of light intensity is quantified by quantum yield. A promising fluorescent protein for designing a biosensor is identified based on the high quantum yield of the protein. The quantum yield relates the efficiency at which a fluorescent molecule converts absorbed photons into emitted photons, i.e., number of photons emitted divided by the number of photons absorbed, with an efficiency of 1.0 being the maximum possible value. Since it is difficult to know the precise number of photons absorbed without specialized instrumentation, the typical practice of measuring quantum yield depends on comparing the unknown to a known standard [19, 20]. In most of the fluorescent proteins, the quantum yield of the fluorophore is not solely determined by absorbed photons but also by other environmental factors such as pH, temperature, polarity, etc.

The construction of fluorescent biosensors generally relies on the rational design of the strategy, which begins with an effort to find a macromolecular receptor with appropriate affinity and specificity to the target. The second step integrates the receptor molecular recognition event into suitable fluorescent signal transduction, which involves foreign reporter moieties such as an engineered autofluorescent protein (AFP). The resultant possibilities for the engineered biosensor are then screened based on biosensor quantum yield, sensitivity, and measurement dynamics [21]. In spite of a seemingly simple procedure, researchers are attempting to fabricate a novel fluorescent biosensor for a given target that would inevitably struggle with unexpected labor intensity in screening such large possibilities of random mutagenesis. The field of computational biology and machine learning offers an exceptional brute force approach in screening the such large sea of variants, by placing a "virtual" molecule of interest in the binding site of a virtual receptor [22]. The program sequentially mutates the receptor amino acids involved in binding the ligand, searching for sequences that form a surface complementary to the ligand. Typically, even with 12–18 amino acids mutations, around 10^{23} variants arise which excludes the possibility of in vitro screening. Finding productive biosensors with high quantum yield and sensitivity in such a large number of possibilities requires powerful computational algorithms. The success of such algorithms depends on how precisely the model recapitulates the energy (or "fitness") of the interacting groups. However, when approaching this problem computationally, not only the amino acid sequence of the receptor must be specified but also the orientation of the ligand, as well as the various conformations that might be adopted by the side chains of the mutated amino acids. Different models have evolved over the course of time for protein biosensor engineering, for instance, Rangefinder, a computational algorithm developed by Mitchell et al., which performs in-silico screening of dye attachment sites in a ligand-binding protein for the conjugation of a dye molecule to act as a Förster acceptor for a fused fluorescent protein [23]. Such computational protein designs have been successfully used to precisely arrive at efficient protein models; a

few to highlight here include a hyperthermophilic protein [24], two small molecule biosensor proteins [25], two novel enzymes [26, 27], and a novel protein fold [28]. Thus, computational in-silico approach holds great promise in future for designing and optimization of biosensors. While developing mutants for designing biosensors, it is also important to consider the use of infrared and near-infrared (NIR) fluorescent proteins as a choice for enhancing the in vivo imaging capability of the developed biosensors.

Green fluorescent protein (native state) is a 21 kDa protein consisting of 238 amino acid residues forming a secondary structure of 5 α-helices and 1 11-stranded β-pleated sheet, where each strand contains 9–13 amino acid residues each [29]. Substitution of specific amino acids has generated a wide range of GFP variants with distinct spectral characteristics. For instance, substituting Tyr66 for His, Trp, or Phe results in blue-shifted spectral variants. Extensive mutagenesis of *Aequorea victoria* GFP has produced a series of monomeric FPs of a variety of colors: blue [30, 31], violet [32], cyan [30, 31, 33, 34], green [35–37], and yellow [38]. This palette enables multicolor labeling of proteins of interests and FRET-based techniques. Breakthrough in the red fluorescent protein field occurred only after the discovery of DsRed and other red fluorescent and chromoproteins from Anthozoa species [39–41]. These discoveries opened the way for the development of orange, red, and far-red FPs with emission peaks located as far as 655 nm [42]. However, the vast majority of natural FPs and chromoproteins cloned from various species during the past 10 years are tetramers, such as FPs from anthozoa [39–41] and copepods [43, 44], or dimers, such as anm2CP and phiYFP from hydrozoa [44].

3 Genetically Encoded Sensors (GES)

The genetically encoded fluorescent proteins have opened new avenues for developing biosensors to visualize and quantify activity or conformational state of proteins of interest, especially changes in the concentration of molecular and physiological events in cells, tissues, or whole organism [45]. The intercellular/intracellular signaling pathways, cell communications, differentiation, and development have been investigated extensively with these fluorescent proteins [46]. One of the promising applications include in vivo imaging of individual neurons in transgenic animals with calcium-responsive genetically encoded biosensors [47]. At the intracellular levels, genetically encoded biosensors can be used to spatiotemporally decipher the complex network of interactions that occur between proteins, nucleic acids, and other macromolecules (Fig. 2) [48]. The chemically synthesized sensitive fluorescent dyes differ greatly from fluorescent proteins in terms of their relevance, sensitivity, specificity, development, and applications. The genetically encoded fluorescent protein sensors are introduced into the host cells as genetic materials by either transient transfection or knock-in techniques which allows cellular endogenous biogenesis pathways to express these as proteins [49]. Such an intricate integration with endogenous biogenesis eliminates the possibility of unintended

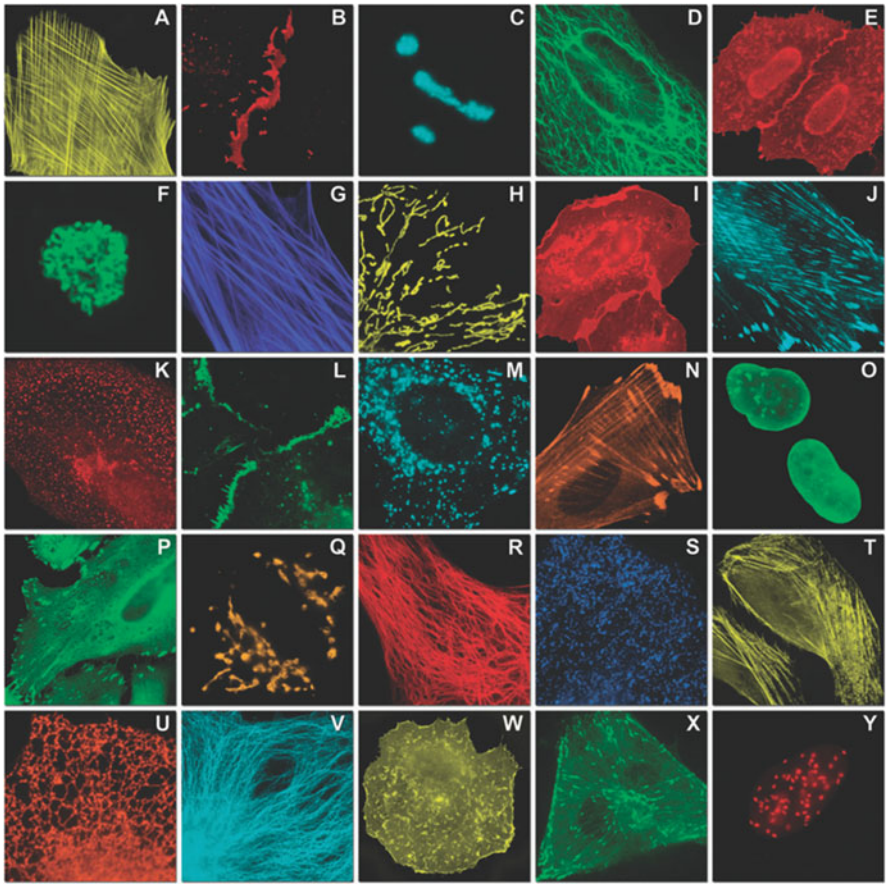

Fig. 2 Different fluorescent protein constructs with specific subcellular localization; FP-fusion partner: (**a**) mOrange2-b-actin, (**b**) mApple-Cx43, (**c**) mTFP1-fibrillarin, (**d**) mWasabi-cytokeratin, (**e**) mRuby-annexin (A4), (**f**) mEGFP-H2B, (**g**) EBFP2-b-actin, (**h**) mTagRFP-T-mitochondria, (**i**) mCherry-C-Src, (**j**) mCerulean-paxillin, (**k**) mKate-clathrin (light chain), (**l**) mCitrine-VE-cadherin, (**m**) TagCFP-lysosomes, (**n**) TagRFP, (**o**) superfolderGFP-lamin, (**p**) EGFP-a-v-integrin, (**q**) tdTomato-Golgi, (**r**) mStrawberry-vimentin, (**s**) TagBFP-Rab, (**t**) mKO2-LC-myosin, (**u**) DsRed2-endoplasmic reticulum, (**v**) ECFP-a-tubulin, (**w**) tdTurboRFP-farnesyl, (**x**) mEmerald, (**y**) mPlum-CENP-B. Adapted with permission from Richard et al., with copyrights [48]

perturbation in endogenous pathways by the biosensor itself while probing target; thus, they allow fluorescence imaging with a closer representation to the in vivo system over a longer period of time [50]. On the other hand, fluorescent dyes are limited by their stability, photobleaching, and cytotoxicity, which are often driven by their non-native interaction with biomolecules that interferes with endogenous fate of the analytes, and thus might limit relevance of such a study to single time point analysis alone [51]. Furthermore, unlike dyes, GES are not prone to leakage during long-term experiments and offer high-throughput screening in drug development.

GES, by virtue of being derived from naturally evolved proteins or protein components of cells, open the possibility for targeting them virtually to any compartment or microcompartment of cells through fusion with an appropriate domain or by introducing short terminal peptides to form appropriate signal motifs [58–60]. The design of fluorescent biosensors is based on a rationale of introducing a nimble manipulation of target domains or fluorescent proteins, which involves conformational changes in the spectral properties of fused domains or distance change, dipole orientation shift between two proteins capable of FRET. FRET is a physical phenomenon in which a donor fluorophore upon excitation transfers the energy non-radiatively to a neighboring acceptor fluorophore, thereby causing the acceptor to emit its characteristic fluorescence of longer wavelength range [18]. Since FRET is highly sensitive to the distance between donor and acceptor dipoles within the 1–10 nm range, they have become a valuable tool to deduce biochemical events involving changes in molecular proximity, such as protein-protein interactions, conformational changes in proteins, intracellular ion concentrations, and enzyme activities [61].

The genetically encoded fluorescent sensors can be broadly categorized into four groups according to the basic principles of the designs (Fig. 3):

1. Intrinsic environment sensitive fluorescent protein biosensor (single FP-based sensors)
2. Engineered single FP-based sensors
   (a) Incorporating a conformationally sensitive detector domain
   (b) Circularly permuted FP sensors
3. FRET-based sensors containing two FPs
4. Translocation sensors/assays

Each of these sensor categories has distinct applications owing to their characteristics. Single native fluorescent proteins are the preferred option for ion sensors, whereas engineered fluorescent proteins and two protein systems are better options for deducing structural changes or a protein-protein FRET interaction, respectively.

3.1 Intrinsic Environment-Sensitive Fluorescent Protein Biosensor (Single FP-Based Sensors)

As an intrinsic property of GFP and its derivatives, the spectral properties of the chromophores are determined by the environment (i.e., pH or conformational change). This property has been exploited to develop biosensors that measure pH [53, 62, 63], halide anions [64], and redox potentials [65, 66]. The environment-induced change within the chromophore pocket of fluorescent protein offers flexibility for generating variation in the fluorescence spectrum to probe analyte-specific signal.

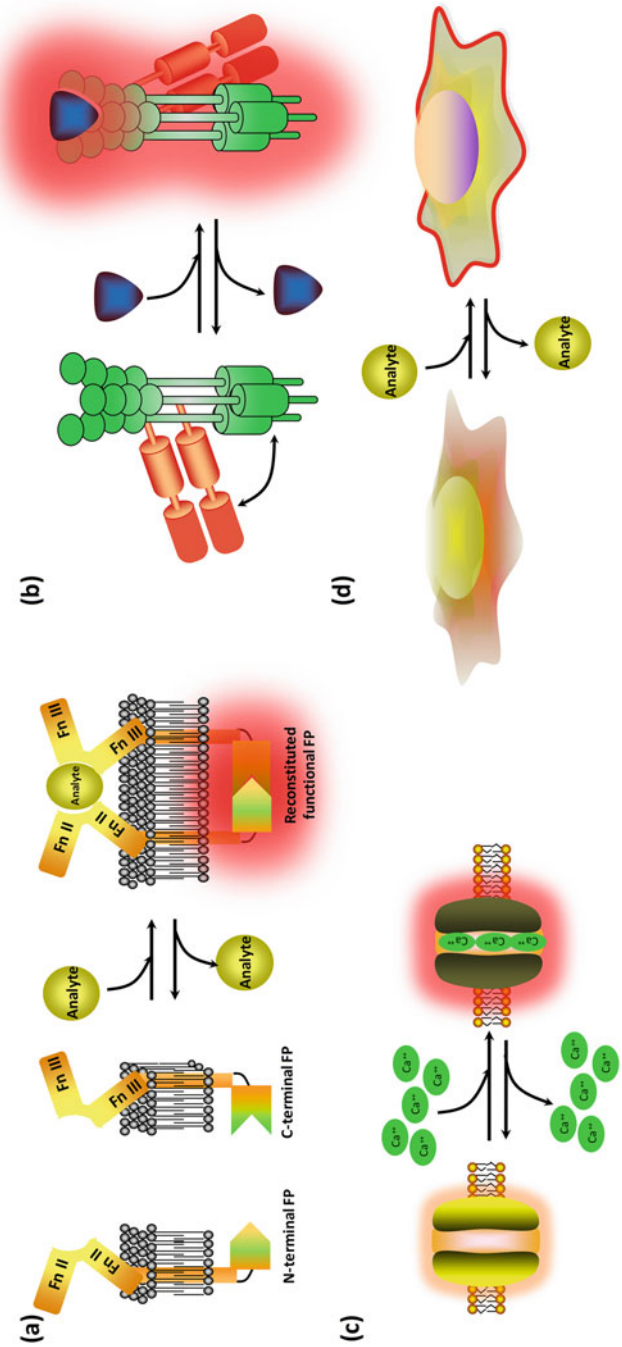

Fig. 3 Different types of FP-based fluorescent sensors: (**a**) circularly permuted FP fused to specific sensitive domain(s). (**b**) Two FPs of different colors are fused to sensitive domain(s); those conformational changes influence the efficiency of FRET between these FPs. (**c**) Intrinsically sensitive FP undergoes ion-dependent changes in spectral properties (brightness or excitation-emission wavelengths), e.g., pH. (**d**) Translocation sensors: FP fused to specific protein domains demonstrates environmentally dependent changes in intracellular localization

3.1.1 Fluorescent Biosensors as Tool for Detection of Intracellular Ion Concentrations

The pH-responsive fluorescent proteins have been used to monitor exocytosis and recycling of proteins based on the rationale of prevalent acidic pH of the secretory vesicles [52, 67] (Table 1). The chromophores of most of the fluorescent proteins naturally possess sensitivity to pH, specifically those carrying GFP-like or DsRed-like chromophores, which indicates that any FP can be used as a sensor to monitor pH changes in living cells [53, 68]. Especially in proteins with GFP-like chromophores, the proportion of charged ground-state chromophores (with excitation peak at ~480 nm) grows with increase in pH, up to pH 9.0, whereas the proportion of protonated chromophores (with excitation at ~400 nm) declines. This property explains the observed increase in fluorescence of green or yellow fluorescent protein with increase in pH upon excitation at 480–500 nm. The shift in fluorescence intensity in pH is rapid and reversible (<1 ms) [63]. Overall, the pH sensitivity of fluorescent sensors is determined by the p*K*a of the charged chromophore, which in turn determines the pH value at which the intensity of green fluorescence begins to decline by 50% of I_{max}, and the Hill coefficient determined by slope of fluorescence versus pH at a given p*K*a point. Fluorescent proteins with p*K*a of ~6.0 are suitable to measure pH changes in acidic compartments, while some of the less acid-tolerant yellow FPs can be used to measure pH changes in the cytosol [67]. Fluorescent proteins with different p*K*a values are generated by rational modification of core amino acids in the chromophore pocket or by random mutagenesis. A pH-sensitive mutant variant called super-ecliptic pHluorin manifests ~50-fold increase in fluorescence in response to change in pH from 5.5 to 7.5 and has been used for monitoring synaptic vesicle cycling at nerve terminals [69]. Another such variant of monomeric red FP, mKeima, exhibits a large Stokes shift with respect to change in pH. Depending upon the neutral (protonated) and anionic (deprotonated) state of chromophore, it exhibits bimodal excitation spectra with peaks at 438 and 550 nm, with a single emission peak at 620 nm [70, 71]. The chromophore has p*K*a of 6.5, and the pH acts as a ratiometric pH sensor based on the ratio of ionized state at a given pH. Another crucial factor in determining the implication of such fluorescent sensors for pH sensing is also based on their stability in different pH range. In this

Table 1 Genetically encoded fluorescent sensors – single fluorescent protein (FP) sensors

Analyte	Sensor name	Components	Sensor type	Reference
pH	SynaptopHluorin	pHluorin	pH-sensitive green FP	[52]
pH	mNect.hCNT3	mNectarine	pH-sensitive red FP	[53]
Ca^{2+}	GCaMP3	M13-cpGFP-calmodulin	Single cpFP	[54]
Ca^{2+}	Case12	M13-cpGFP-calmodulin	Single cpFP	[55]
Ca^{2+}	Camgaroo-2	Calmodulin domain into YFP	Peptide insertion	[56]
H_2O_2	HyPer	OxyR	Single cpFP	[57]

aspect, mKeima exhibits high resistance to lysosomal enzyme-mediated degradation; this inspired and resulted in the modification of mKeima as an autophagy sensor, specifically to detect the event of conversion of autophagosomes to autolysosomes. In the fluorescent pH sensor, mKeima was fused with light chain 3 (LC3) of microtubule-associated protein [72]. Under starvation-induced autophagy, LC3 is cleaved and allows recruitment of phosphatidylethanolamine to the outer and inner membranes of autophagosome, which then fuses with the lysosomes leading to the degradation of packaged cargo under a highly acidic environment [73]. The mKeima-LC3 probe enabled visualization of these autolysosomal maturation events by detection of the acidification-induced color change of mKeima and provided a cumulative fluorescent readout of autophagic activity, with the deduction of the hallmark event of autophagy, i.e., LC3 localization. Another variant of mKeima, pH-Red, was developed with a specific purpose of achieving pH-dependent readout in near-infrared region. This property can provide the advantage of light emission with higher penetration and less light scattering in biological tissues and thus offer advantage for deep tissue pH monitoring across a broad pH range. pHRed with an apparent pKa of 6.6 demonstrated nearly tenfold change in ratio of fluorescence emission upon excitation with a wavelength of 585 nm [74].

To date, various GES for monitoring pH have been generated in such as way they can respond with either changes in fluorescent brightness of a single fluorescence peak or ratiometric changes with two excitation peaks [75]. The latter type of pH sensors imply ratiometric measurement of fluorescence brightness excited at two different wavelengths and hence are free from artifacts that arise owing to variable protein concentrations, cell thickness associated signal attenuation, cell movement, or excitation intensity since measurement in one peak can normalize the other peak that was used for pH measurement [75]. Ratiometric pH sensors commonly respond with a change in the ratio of excitation efficiency at 400 nm versus 480 nm owing to a shift in the protonated/deprotonated chromophore ratio [52]. An internal control of overall signal stability can be the intensity of fluorescence excitation at the isosbestic point between the two excitation peaks, at ~430 nm. Another type of ratiometric GES that utilizes the pH-sensitive efficiency of excited state proton transfer (ESPT) from the protonated GFP chromophore excited at 400 nm. These sensors are excited at 400 nm and respond with a change of fluorescence ratio between 450 nm and 510 nm [62]. Ratiometric pH sensors can also be developed by fusing pH-stable and pH-sensitive fluorescent protein variants of different colors. In this case, changes in the fluorescence brightness ratio of the two fused FPs can be measured along with FRET efficiency between the two FPs, as discussed in detail below.

Fluorescent protein-based sensors for measuring metal ions in living cells can be categorized into intensiometric sensors which change in fluorescence intensity when the chromophore bound to a metal ion and ratiometric biosensors that exhibit shift in the absorption or emission spectra when the chromophore bound to a metal ion. The intensiometric fluorescent sensors are the preferred option for developing quantitative assays, since their fluorescence intensity has been determined by the sensor concentration in each cell and the path length in addition to the ion concentration.

Ratiometric biosensors are severely limited for quantitative estimations owing to their lower sensitivity (i.e., smaller dynamic range), larger spectral bandwidth, and the need to acquire images with two combinations of excitation and emission filters for fluorescence measurement.

The sensitivity of biosensor for measuring ionic concentration has been determined by its binding affinity for an ion and its dynamic range. Binding affinity of an ion can be defined in terms of dissociation constant (Kd), which is the ion concentration at which 50% of the sensor binding sites are occupied. This can be experimentally determined by sensor titration experiments. Dynamic range is essentially an indicator of a sensor's measurement sensitivity and its signal-to-noise ratio (SNR). In order to monitor ion concentration changes, it is preferable to choose a sensor that is 20% saturated at baseline, whereas a sensor that is ~50% saturated at baseline is more suitable for comparing differences in resting ion concentrations in different cells or different environmental conditions. For instance, Cameleon-Nano sensors have lower Kd and are better for quantitative measurement of cytosolic Ca^{2+} in some cell types, whereas D1ER is preferred for ER measurement because Ca^{2+} levels are high in the ER and the Kd of D1ER is much higher than other Cameleons. Tables 2 and 3 summarize Kd and DRs of some ratiometric ion sensors which are designed for measuring ion concentrations in subcellular organelles.

3.2 Fluorescent Protein Complementation (Split Fluorescent Proteins) Sensors

3.2.1 Sensors Fused with Intermediate Recognition Domains from Target Proteins for Designing the Biosensors

To expand the scope of sensors specific to some analytes, an analyte-specific extrinsic recognition domain has been inserted into FPs. In the conventional design of bimolecular fluorescent complementation (BiFC) sensors, a FP is split into two fragments and then fused to recognition domains that are associated with the analytes of interest [86, 87]. The two halves of the FP do not emit fluorescence in the state of dissociation since no intact chromophore will be reconstituted. Upon the analyte-induced change in the recognition domains, the complementary fragments of the FP are brought into close proximity and reconstitute the β-barrel chromophore structure of the FP, resulting in the recovery of the fluorescence signal. In general, split FP strategies have a much lower background so that it may produce a greater dynamic range than those of FRET and single FP-based biosensors. On the other hand, a major drawback of split FP-based biosensors is that they are not reversible. While irreversibility provides a significant advantage for detecting transient and/or weak interactions, it is not suitable for analyzing dynamics of an analyte in real time [88]. Study of protein-protein interaction involves split FP fragments that do not associate with each other spontaneously. In this strategy, the fluorescent protein halves are fused to two different target proteins of interest. In the event of interaction

Table 2 Ratiometric biosensors for imaging Ca^{2+} and Zn^{2+} ions

Ratiometric Ca^{2+} biosensors						
Fluorescent proteins used	Sensors name	Ca^{2+}-responsive elements	Kd′ for Ca^{2+}	Hill coeff.	Comments	Reference
Yellow Cameleon series	YC2.60	CaM, M13p	93.5 nM	2.7	Not available	[76]
Yellow Cameleon series	YC3.60	CaM E104Q, M13p	215 nM, 779 nM	3.6, 1.2	High dynamic range	[77]
Yellow Cameleon Nano series	YC-Nano50	CaM, M13p	52.5 nM	2.5	Optimized for detecting subtle cytosolic Ca^{2+} in living organisms	[76]
D-family Cameleons	D1	mCaM, mM13p	0.8 μM, 60 μM	1.18, 1.67	Does not bind endogenous CaM; optimized for ER	[78]
D-family Cameleons	D3	cpV mCaM, mM13p	0.6 μM	0.74	Does not bind to endogenous CaM; optimized for cytosol and mitochondria	[79]
Troponin C family	TN-XXL	mTpC	800 nM	1.5	Optimized for imaging of neurons; fast response	[80]
Ratiometric Zn^{2+} biosensors						
Fluorescent proteins used	Sensors name	Zn^{2+}-responsive elements	Kd′ for Zn^{2+}	Hill coeff.	Comments	Reference
Zap family	ZapCY1	Zap	2.53 pM	1	Optimized for ER, Golgi, and mitochondria; high dynamic range	[81]
ZinCh family	eZinCh	CFP and YFP	8.2 μM	1	Targeted to vesicles by fusion to VAMP2	[82]
eCALWY family	eCALWY4	Atox1 and the WD4 domain of ATP7B	630 pM	1	Optimized for cytosol	[81]
Zap family	ZapCY2	mZap	811 pM	0.44	Optimized for cytosol	[83]

between target proteins, the split FP halves are brought together, resulting in assembly of functional fluorescent protein with intact chromophore which results in the appearance of fluorescence. This approach provides straightforward interpretation for extent and location of target protein interaction in the cell. A drawback of BiFC as compared to FRET sensors is that upon reassociation of split FP fragments,

Table 3 Sensors targeted to subcellular locations

Subcellular location	Ca^{2+} sensors	Zn^{2+} sensors	Reference
Golgi	None	Golgi-ZapCY1	[83]
ER	D1ER	ER-ZapCY1	[78, 83]
Vesicles	Ycam2	eZinCh	[81, 84]
Mitochondria	4mt-D3cpV	Mito-ZapCY1	[79]
Nucleus	D3cpV	ZapCY2	[83, 85]
Cytosol	D3cpV	eCALWY-4, ZapCY2	[81, 83, 85]

it takes from minutes to hours for the chromophore to mature and produce fluorescent signal, which limits their applications in real-time detection of protein-protein interactions [86]. Apart from this, the split FP assembly is irreversible in most cases, although there have been reports of partial recovery of split FP [89]. On the other hand, the BiFC system achieves higher sensitivity and detects even weak interactions as it accumulates signal over time, thus prevailing over FRET sensors in this aspect [90]. Numerous variants of split fluorescent protein-based sensors with different spectral properties have emerged over the years, e.g., blue (EBFP), cyan (ECFP, Cerulean, SCFP3A), green (EGFP), and yellow (EYFP, Venus, Citrine) mutants of *Aequorea victoria* GFP [91–94]. In addition split variants of red and far-red FPs such as mRFP1 [94], mCherry [95], DsRed-monomer [96], and mKate [97] have their origin from other fluorescent proteins. As a result of common origin from same FP, fragments from different color mutants with complementary fragments also yield cross-associated species with distinct spectral properties, which extends the application of these systems in competitive protein binding interactions [92, 98]. The other possibility of using two split FPs of different origins capable of hybrid formation may be applied to visualization of two independent pairs of protein-protein interactions [95, 96]. The combination of cross-associated BiFC and non-cross-associated BiFC system enables simultaneous detection of three pairs of protein-protein interactions taking place within the same cells at any given time point [97].

In the cases of certain BiFC, chimeric proteins consisting of fragments from different proteins sometimes reconstitute chromophore and emit fluorescence, which offers diverse fluorescent shades capable of tracking multiple events simultaneously in cells [96]. As an example of such a multicolor BiFC chimera, the event of ligand-dependent oligomerization (homodimer and heterodimer) between adenosine A 2A and dopamine D2 receptors was evaluated effectively in a differentiated neuronal cell model [99].

Another emerging strategy is based on incorporation of unnatural amino acids (UAAs) into a natural chromophore of fluorescent protein for developing single FP sensors. The incorporation UAA to proteins has recently emerged as a strategy to generate novel rationally engineered single FP sensors [100]. One of the earliest reports on this approach was made by Yun and coworkers wherein GFP-dopa mutant was generated by replacing all tyrosine residues in the GFP with metal-chelating L-DOPA [101]. The mutant variant functioned as a selective Cu^{2+} sensor. Similarly

another group introduced a metal-binding amino acid, HqAla (2-amino-3-(8-hydroxyquinolin-5-yl)propanoic acid), into the Tyr66 of a cpsfGFP variant that enabled this construct to achieve a 7.2-fold increase in fluorescence intensity in the presence of Zn^{2+} ions in living *E. coli* cells [102]. Apart from affinity-based unnatural amino acids, chemically reactive UAAs also serve as an option for reaction-based fluorescent protein biosensors. Schultz and coworkers exploited this approach in designing an FP sensor (UFP-Tyr66pBoPhe) for detection of H_2O_2 by substituting Tyr66 of GFP with *p*-borono-L-phenylalanine (pBoPhe) carrying an H_2O_2-reactive arylboronate side chain [102]. In the absence of H_2O_2, the chromophore remains electron deficient owing to the presence of electron withdrawing vacant 2p orbital of boron, and as a result of which, the sensor does not produce fluorescence. However, in the presence of H_2O_2, pBoPhe is oxidized to the original tyrosine residue, leading to quick recovery of fluorescence [103]. Although initially UAA-based sensors were speculated to behave unsuccessfully in in vivo systems owing to the synthetic origin of UAA, a few recent reports have achieved the same in mammalian cells. An UAA-based H_2S sensor was developed by substitution of Tyr66 with *p*-azido-L-phenylalanine (pAzF) and was successfully expressed in mammalian cells and illustrated as response time of mere ~7 min upon addition of 50 μM of NaHS [104]. The azide-modified chromophore in the presence of H_2S is selectively reduced which results in the observed fluorescence enhancement. The same group also developed genetically encoded mammalian cells compatible for peroxynitrite probe on the basis of the similar strategy [105].

The oligomeric aspect of fluorescent proteins offers flexibility for designing dimerization-dependent fluorescent sensors that also enables reversible fluorescence change upon complementation [106]. For instance, the oligomeric Discosoma red FP (DsRed) and the RFP heterodimer (ddRFP-A1B1) exhibit weak fluorescence in the monomeric state but upon heterodimerization manifest tenfold higher fluorescence with a Kd of 33 μM. A series of red intensiometric biosensors based on a diverse color palette ddRFP, ddGFP, and ddYFP have been created for detection of PPIs, Ca^{2+} dynamics, and protease activity with improved brightness and contrast [107]. The efficient SNR of the system enabled imaging of endomembrane proximity between endoplasmic reticulum and mitochondria clearly distinguishable.

3.2.2 Biosensors Designed Using Circularly Permuted FPs

The close proximity of N- and C-termini observed in many three-dimensional protein structures has been used in the past to perform circular permutation experiments on many different proteins [108]. The circularly permuted FP (cpFP)-based GES are quite promising owing to the potentially high dynamic range of fluorescence spectral shifts. A circular permutation is a relationship between proteins whereby they have a changed order of amino acids in their peptide sequence resulting in a reconstituted protein with overall similar 3D shape but with different N- and C-termini [109]. In the case of cpFP-based sensors, conformational changes of sensory domains yield structural changes in the chromophore environment and

thus strongly influence change in the spectral properties of the cpFPs. The influence is usually brought by factors such as protonation/deprotonation of a GFP-like chromophore, as well as changes in its fluorescence quantum yield and molar extinction coefficient. A rationally engineered cpGFP offers robust variants which sustains fluorescence emission even after insertion of peptides or proteins to the new terminus. The predominant permuted variants as per GFP sequence arise from a permutation point in the vicinity of amino acid positions [62, 66]. The proximity of sensitive fusion domains to the chromophore pocket in the fluorescent protein determines extent of influence on the native spectral properties. In the case of cpECFP, cpEGFP, and cpEYFP, insertion of calmodulin (Ca^{2+}-binding protein) in a specific position localized it in close proximity to the chromophore in the folded 3D conformation, which resulted in deprotonation of the chromophore and subsequent shift in fluorescence emission [60, 110]. As a follow-up to this pioneering study, several groups developed single cpFP-based biosensors with different binding domains for the detection of calcium [54, 111, 112], cGMP [113], H_2O_2 [57], and Zn(II) [114].

In cpFPs, the recognition domain in the presence of an analyte can undergo a conformational change by itself as well as influence conformational change in the fused fluorescent protein that is reflected by change in the fluorescence spectra. One example of this approach is a G-CaMP sensor for Ca^{2+}, which has a calmodulin (Ca^{2+}-binding protein) fused to the C-termini of a cpEGFP and a M13 peptide (a synthetic peptide with calmodulin-binding domain) fused to the N termini [115]. The success of the G-CaMP biosensor design inspired further modification for improving the sensitivity while developing a diverse range of color palettes for multicolor imaging of Ca^{2+} level in different organelles of cells, such as cytosol, nucleus, and mitochondria, at single-cell level [116].

The routine approach of permutation in FPs involves fusion of sensitive domains close to the chromophore in order to manifest a change in its spectral properties [77, 117]. With this strategy, numerous calcium sensors [55, 112, 118, 119] and hydrogen peroxide sensors [57], phosphorylation sensors [120], and membrane potential sensors [121, 122] have emerged successfully in the recent past. Incorporation of binding protein with competitive analyte affinity can serve as a new type of ratiometric sensor. Incorporation of adenylate binding protein GlnK1 with differential affinity for ATP and ADP into cpYFP could generate sensors with different spectral properties depending upon the analyte ADP or ATP [123].

Hydrogen peroxide is an important signaling molecule, and a sensor specific for detection of hydrogen peroxidase, i.e., HyPer, was designed based on yellow cpFP incorporated into the H_2O_2-sensitive OxyR regulatory domain [124]. The sensor detects submicromolar concentration of H_2O_2 by selective oxidation of OxyR residues and leads to change in yellow cpFP chromophore environment with corresponding ratiometric change in fluorescence excitation spectrum, i.e., fluorescence ratio upon excitation at 420 nm with respect to excitation at 500 nm. The sensor was later successfully modified for the detection of wounds using zebra fish as a model organism [125].

3.3 FRET Sensors

The phenomenon of Förster or Fluorescence Resonance Energy Transfer (FRET) was first described by Theodor Förster in 1946 [126]. In principle FRET is a physical phenomenon in which a donor fluorophore in its excited state non-radiatively transfers its excitation energy to a neighboring acceptor fluorophore which is located in close proximity, thereby causing the acceptor to emit its characteristic fluorescence. As FRET involves non-radiative transfer of energy, it is highly sensitive to the distance between donor and acceptor dipoles within the 1–10 nm range [127]. Thus, FRET has found extensive application as a spectroscopic ruler in monitoring molecular interactions, because the distances that can be measured are much shorter than the diffraction limit of conventional microscopy and even super resolution microscopy. In case of fluorescent protein-based FRET sensors, the donor and the acceptor are fluorescent proteins with distinct spectral properties. The two proteins upon interaction undergo conformational change and alter the proximity of chromophores and its orientation, which promotes the occurrence of FRET [128]. The efficiency of FRET is inversely proportional to the sixth power of distance within the short range of 10 nm [129]. The inverse sixth power law relation leads to detectable change in energy transfer even for change in orientation/proximity at the molecular scale between the interacting chromophores. Such small-scale molecular interactions include protein-protein interactions, conformational changes, intracellular ion concentrations, and enzyme activities (Fig. 4).

The efficiency of FRET (i.e., the quantum yield of the energy transfer) between any two FPs is determined by the overlap of the emission spectrum of the donor and the excitation spectrum of acceptor, quantum yield of donor fluorescence, and extinction coefficient of the acceptor. A 30% or higher overlap in the emission spectra of donor and excitation spectra of acceptor is a prerequisite for achieving sufficient FRET signal with a reliable detection limit. Apart from this, the proximity of the donor and acceptor governs the FRET efficiency by inverse power law. The quantum yield and extinction coefficient of fluorophores determine the sensitivity and yield of FRET signal. For any given pair of chromophores involved in FRET, an integral factor representing the abovesaid parameters is denoted by the Förster distance (R_0), which is the distance at which the FRET efficiency is 50% of its maximal value.

With the advent of a wide range of GFP variants with distinct excitation and emission spectra, the possibility of donor/acceptor combination has increased dramatically. Initial FRET-based biosensors were predominantly based on BFP as energy donor, which was hampered by its instability and lower brightness. Recently, cyan fluorescent protein (CFP) and donor yellow fluorescent protein (YFP) have become the most useful FRET pairs for many in vitro studies. Following this trend, two novel FRET pairs (mAmetrine/tdTomato and mCitrine/mTFP1) were developed for simultaneous imaging of two different enzymes in a single-cell level.

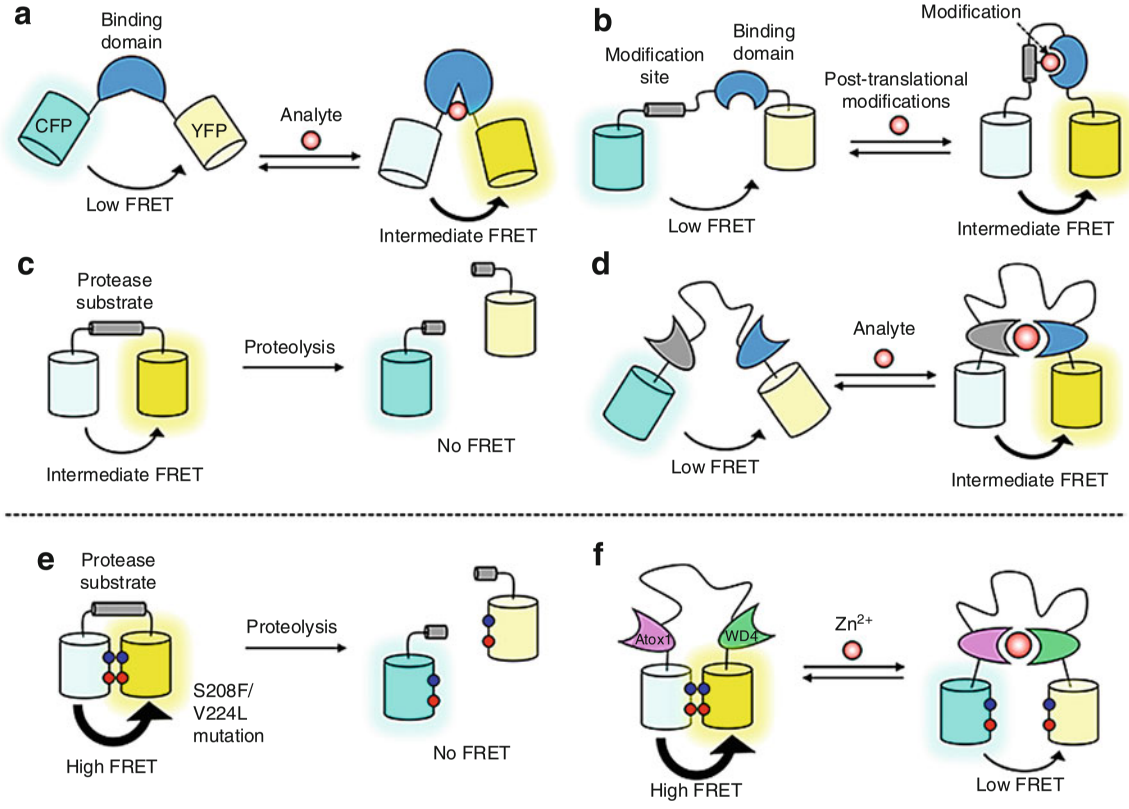

Fig. 4 Representative design formats for FRET-based biosensor: (**a**) a single binding domain undergoes a conformational change upon binding analyte. (**b**) Biosensors to monitor posttranslational modifications. (**c**) Biosensors to detect protease activity. (**d**) Biosensors based on an analyte-dependent protein-protein interaction. (**e**, **f**) FRET-based sensors based on self-associating FPs. (**e**) Protease sensor. (**f**) eCALWY sensor for Zn^{2+}. Adapted from Tamura et al., with copyrights [128]

Table 4 FRET-based fluorescent protein sensors

Sensor type	Sensor name	Components	Principle of work	Reference
cGMP	cGES-DE5	YFP-GKI-B-CFP	Structural rearrangement of domain	[130]
Ca^{2+}	TN-XXL	CFP-2x (COOH-terminal lobe of troponin C)-cpYFP	Structural rearrangement of domain	[80]
Ca^{2+}	Yellow Cameleon3.6	ECFP-calmodulin-M13-cpVenus	Interaction of domains	[77]
Ca^{2+}	Cameleon D3	ECFP-calmodulin-M13-cpVenus (redesigned calmodulin and M13)	Interaction of domains	[79, 131]
Caspase-3 activity	CaspeR3	TagGFP-DEVD-TagRFP	Cleavage of the linker	[132]
PKA activity	AKAR1	ECFP-14-3-3-substrate-YFP	Interaction of domains	[133]
Membrane potential	Mermaid	Ci-VSP-mUKG-mKOk	Structural rearrangements near membrane	[134]
Membrane potential	VSFP2.4	Ci-VSP-YFP-mKate2	Structural rearrangements near membrane	[135]

3.3.1 Types of FRET Biosensors

The intramolecular FRET probes/sensors involve two fluorescently tagged proteins that bring them into close proximity in the event of an interaction between the two analytes to generate FRET signal. In the following section, we also classify FRET biosensors by their way of transforming a biological change into a change in FRET efficiency. A brief list of such FRET-based biosensors is summarized in Table 4.

3.3.2 Cleavage-Based FRET Biosensors

The cleavage-based FRET biosensors are the most prevalent sensors because of their versatility in design and application. The constituent FRET pair is linked by a short cleavable peptide sequence that in its uncleaved state shows FRET signal owing to the proximity of the donor and acceptor, whereas in the presence of a linker peptide as a specific enzyme, cleavable substrate leads to dissociation of two fluorophores and loss of FRET signal upon cleavage. This signal is evident as a shift in acceptor emission to donor emission. One of the major drawbacks of such FRET systems as compared to other counterparts is the irreversibility of the sensors because they are driven by irreversible cleavage of linker peptides; this limits their ability to sense target analytes to only one event. Therefore, they find application mostly to

Table 5 Cleavage-based FRET biosensors

Target	Type	FRET pair	Reference
Caspase-3	Apoptosis	CFP, YFP	[136]
Caspase-3 and caspase-6	Apoptosis	CFP, YFP, mRFP	[137]
Caspase-3 and caspase-8	Apoptosis	CFP, YFP	[138]
Caspase-3 and caspase-8	Apoptosis	seCFP, Venus, mRFP1	[139]
RIPK1 and RIPK3	Necroptosis	–	[140]
Atg4A and Atg4B	Autophagy	CFP, YFP	[141]
MT-MMP1	ECM – remodeling	Ypet, ECFP	[142]
MT-MMP1	ECM – remodeling	Orange2, Cherry	[143]

determine the activation of specific proteases, often following the stimulation of a pathway. For example, in the case of the caspase-3 biosensor, in the presence of active enzyme, the single-peptide sensor DEVD (caspase cleavage sequence) is cleaved, increasing the distance between CFP and eYFP, resulting in increased CFP fluorescence and decreased FRET [136]. Another major limitation is that measuring loss of signal is a readout for measuring FRET rather than measuring an increase in signal, which is preferred for most biological studies (Table 5).

3.3.3 Conformational Change-Based FRET Biosensors

FRET biosensors for measuring conformational changes in proteins and other macromolecules are the most prevalent subclass, followed by cleavage-based FRET biosensors. The ability of a protein to form a structural conformation that can execute its biological function is the driving factor for these FRET biosensors. Such conformational changes are also contributed to a large extent by posttranslational modifications such as phosphorylation, glycosylation, ubiquitination, S-nitrosylation, methylation, acetylation, lipidation, sumoylation, and proteolysis. An advantage of a conformational change specific sensor is that upon design optimization and validation for a specific analyte, it lends flexibility to cover a wide range of biological processes. The conformational change-based biosensors are also reversible, which offers new avenues for dynamic analyte sensing. For example, regarding the glucose biosensor, the glucose-/galactose-binding protein MglB (D-galactose-binding periplasmic protein, from *E. coli*), consisting of two lobes and a hinge region, is coupled terminally with a CFP and a YFP. The binding of glucose to the sensor leads to increase in FRET signal [144] (Table 6).

3.3.4 Mechanical Force-Based FRET Biosensors

The three-dimensional structure of a protein can be changed not only by modifying the protein itself but also by applying an external mechanical force. A good example for this would be the proteins contained in spider silk. These often feature helical

Table 6 Conformational change-based FRET biosensors

Target	Type	FRET pair	Reference
CyclinB1-Cdk1	Cell division	mCerulean, Ypet	[145]
AKT	Signal transduction	ECFP, Ypet	[146]
AKT-PDK1	Mechano-transduction	CFP, YFP	[147]
FAK	Mechano-transduction	ECFP, Ypet	[148]
Src	Mechano-transduction	ECFP, EYFP	[149]
ATP	Metabolite quantification	GFP, OFP	[150]
Glucose	Metabolite quantification	EYFP, ECFP	[151]
Lactate	Metabolite quantification	mTFP, Venus	[152]
Ca^{2+}	Metabolite quantification	BFP, GFP	[153]
BCR-ABL	Drug efficacy	M1Venus, ECFP	[154]
Src	Drug efficacy	ECFP, EYFP	[155]
ZAP-70	T-cell interaction	CFP, YFP	[156]
Lck	T-cell interaction	ECFP, EYFP	[157]

Table 7 Mechanical force-based FRET biosensors

Target	Type	FRET pair	Reference
Vinculin	Focal adhesion	mTFP1, Venus	[158]
VE-cadherin, PECAM-1	Fluid shear stress	mTFP1, Venus	[159]
E-cadherin	Fluid shear stress	mTFP1, Venus	[160]

segments which can stretch out to a great extent, giving the thread its elasticity. Mechanical forces (such as tension) not only are a stress to cells but play a central role in many developmental, physiological, and pathological processes, especially regarding the transduction of signals. One of the exciting results in this field was produced by Grashoff et al., who have designed a tension sensor module (TSMod) to examine the mechanical forces across vinculin during cell migration [158]. In this sensor, a 40-amino-acid-long elastic domain was inserted between two fluorophores (mTFP1 and Venus (A206K)) as a potential fluorescence resonance energy transfer (FRET) pair. The elastic domain derived from the spider silk protein flagelliform consists of repetitive amino acid motifs that form entropic nanosprings suitable for measuring piconewton forces. Since FRET is highly sensitive to the distance between the fluorophores, FRET efficiency changes under tension (Table 7).

3.3.5 FRET Sensors for Assessing Microenvironmental Changes

The three classes of biosensors discussed in the preceding section manifest decrease or increase in FRET upon change in distance between donor and acceptor, whereas microenvironment-responsive FRET sensors exploit the sensitivity of a fluorophore to certain microenvironmental conditions. One such microenvironment-sensitive fluorescent protein is YFP, which makes it a promising choice as one of the FRET pairs. For example, the oxygen biosensor FluBO for detecting intracellular oxygen

Table 8 Microenvironment-based FRET biosensors

Type	Target	FRET pair	Reference
Oxygen and reactive oxygen species (ROS)	Oxygen	YFP, FbFP	[161]
Oxygen and ROS	ROS	ECFP, EYFP	[163]
pH	pH	GFP, YFP	[164]
pH	pH	ECFP, EYFP	[165]

uses an oxygen-insensitive donor fluorescent protein FbFP (hypoxia-tolerant flavin-binding fluorescent protein) that is intramolecularly linked to an oxygen-sensitive acceptor fluorescent protein, and thus FRET only occurs in the presence of oxygen [161]. Blood flow, oxygen delivery and consumption, and hypoxia are important aspects of in vivo cancer biology. The dual imaging of these factors that may influence tumor behavior with altered drug target signaling could potentially be co-monitored using these distinct but interdependent types of FRET biosensor readouts [162] (Table 8).

3.4 Translocation Sensors/Assays

A unique field of application for FP sensors is in tracking the redistribution of proteins between different cellular compartments such as the nucleus, endosome, membrane, cytosol, and mitochondria [166, 167]. The translocation of proteins between cellular compartments in response to different external stimuli has been considered common phenomenon that involves protein redistribution into different compartments of the living cells. Tracking proteins and their distribution patterns opens up the possibility of monitoring the activity of various signaling pathways and associated intracellular events. Fusion of proteins such as phosphatases, transcription factors, receptors, and kinases with fluorescent proteins can act as ready-to-use translocation sensors for deduction of cellular metabolic and biogenesis pathways. Such a fusion construct can localize outside or inside the nucleus, or on the cell membrane, cytosol, endosome, etc., and such protein trafficking can be monitored in real time with the help of translocation sensors. These sensors are reversible, enabling time-dependent tracking of specific proteins in various cellular compartments. In this context, the spatial and functional division into the two dynamic intracellular compartments, i.e., nucleus and the cytoplasm, can easily be distinguished using microscopy. Modern microscopy platforms enable high-content screening using translocating FPs.

In such high-throughput screening assays, screened compounds can be assessed for their potential effects on protein translocation or used to study the inhibition of

protein translocation in response to an agonist or external stimuli. A combination of high-resolution microscopy and advanced image recognition software enables quantitative analysis of translocation events with reliable information on the efficiency of the influencing stimulus. Recently Fetz et al. have developed three classes of modular protein translocation biosensors tailored to investigate (1) signal-mediated nucleocytoplasmic transport, (2) protease activity, and (3) protein-protein interactions [168]. Besides the mapping of protein function, the biosensors can also be applied to identify chemicals and/or (nano)materials modulating the respective protein activities and be used for RNAi-mediated genetic screens. In general, the rapidly developing field of translocation sensors appears very promising both for basic science studies and in drug development applications.

4 Advances in Biosensors for Animal Imaging

Whole-body animal imaging with fluorescent proteins has been shown to be a powerful technology to develop various disease models. The red-shifted proteins with brighter emission wavelengths are preferred candidates for in vivo models as they are more sensitive owing to the reduced light absorption by tissue with much lower scattering. For example, a protein called Katushka driven by the hybrid CAG promoter activated upon Cre-mediated recombination has been developed by Hurtado et al., for deep tissue imaging in mice models. This group successfully demonstrated the expression of Katushka exclusively in a specific cell population within the deep animal body such as pancreatic beta cells which can be monitored by noninvasive whole-body imaging [169]. The implication of imaging biosensors in animal studies is severely affected by the level of biosensors expression and the wavelength of fluorescent proteins used for imaging [170]. For example, Audet et al. [171] have developed a double transgenic mouse line co-expressing the beta-2 adrenergic receptor fused to *Renilla luciferase* (beta(2)AR-Rluc) and beta-arrestin-2 fused to a green fluorescent protein (GFP2-beta arr2). Although the two halves of a bimolecular reporter are driven by the same ostensibly ubiquitous reporter, the first reporter was expressed reasonably brighter in a number of tissue types, whereas the second reporter appeared only in testes. In addition, the low-level expression of sensors with tissue-specific promoters further hampers the in vivo imaging ability of sensors constructed using fluorescent proteins. The effective FRET studies also cannot be carried out in vivo because of extremely low SNRs. The implication of a fluorescent protein for whole-body imaging is largely determined by the emission region and the brightness. Transgenic animal models with fluorescent proteins have been utilized for tracking tumor growth and metastasis, gene expression, angiogenesis, and bacterial infection even at subcellular resolution depending on the position of the cells in the animal [172]. Deep tissue imaging in animal models has been severely limited by the interference by skin autofluorescence. Apart from this, in few instances, overexpression of biosensors also leads to unintended changes like embryonic lethality or even perturbation of the physiological relevance of the sensor

[173]. However, with recent progress in CRISPR/Cas9 genome engineering techniques, it has become possible to edit more precisely the genomes of diverse cell types and organisms and routinely insert fluorescent protein tags into endogenous genomic loci in some organisms. Hara et al. [173] reported expression of an endoplasmic reticulum (ER) Ca^{2+} biosensor in transgenic mouse pancreas. The expression of a yellow cameleon3.3er (YC3.3er) transgene with mouse insulin 1 promoter was limited to pancreatic beta cells within islets of Langerhans and absent in the exocrine pancreas and other tissues [173]. The study established that by controlling transgene transcription with a cell-specific promoter, transgenic expression of FRET-based Ca^{2+} sensors can be incorporated in mammals to facilitate real-time optical imaging of signal transduction events in living tissues. Yang et al. developed a red fluorescent protein-based cAMP indicator named "Pink Flamindo" which could effectively trace the spatiotemporal dynamics of intracellular cAMP generated by photoactivated adenylate cyclase in response to light and in dual-color imaging studies using a green Ca^{2+} indicator.

The elevation of cAMP levels in vivo in cerebral cortical astrocytes was successfully monitored by two-photon imaging. The cAMP-PKA signaling pathway plays a key role in the excitability of neurons. In order to study its role, protein kinase A (PKA) expression in neurons has been mapped in whole-brain context in live animals. In a study by Gervasi et al., in vivo multiphoton imaging was used to measure the dynamics of PKA responses to dopamine and octopamine in the MB neurons of living flies. The PKA activity was monitored on real-time basis by using the genetically encoded FRET probe AKAR2 [133]. The AKAR2 probe is based on yeast-derived phosphothreonine-binding domain (FHA1) and an optimized PKA substrate domain. The substrate domain upon phosphorylation by PKA interacts with the binding pocket of the FHA1 domain, increasing the FRET between two GFP variants CFP and citrine [174]. A recent study by Sun et al. developed a genetically encoded GPCR-activation-based-DA (GRAB DA) sensors to measure DA changes reliably and specifically with high spatiotemporal precision in *Drosophila* (Fig. 5ii) [175]. The GRAB DA sensor could resolve a single-electrical-stimulus-evoked DA release in mouse brain slices and detect endogenous DA release in living flies with subcellular resolution, sub-second kinetics, and excellent molecular specificity. Similarly, Portugues et al. studied the dynamics and spatial distribution of neuronal activities during optokinetic response in zebra fish larvae. The whole-brain activity dynamics was assigned by specific hue based on the timing of its response relative to the stimulus, which enabled categorization of brain regions into distinct response-based functional modules (Fig. 5iii) [176]. Another recent technique is called "Brainbow" that used the combinatorial expression of a series of four different color fluorescent proteins resulting in at least 90 different colors of cells in the brain such that the lineage of each neuron can be traced [177]. For translational purposes, mammalian systems such as mouse are appealing targets for similar in vivo studies. However, there are a number of challenges for in vivo kinase studies, particularly in living mice. A RhoA-FRET biosensor-based transgenic mouse was recently developed by Nobis et al., for real-time longitudinal, intravital imaging of RhoA deregulation in invasive mammary and pancreatic cancers [178].

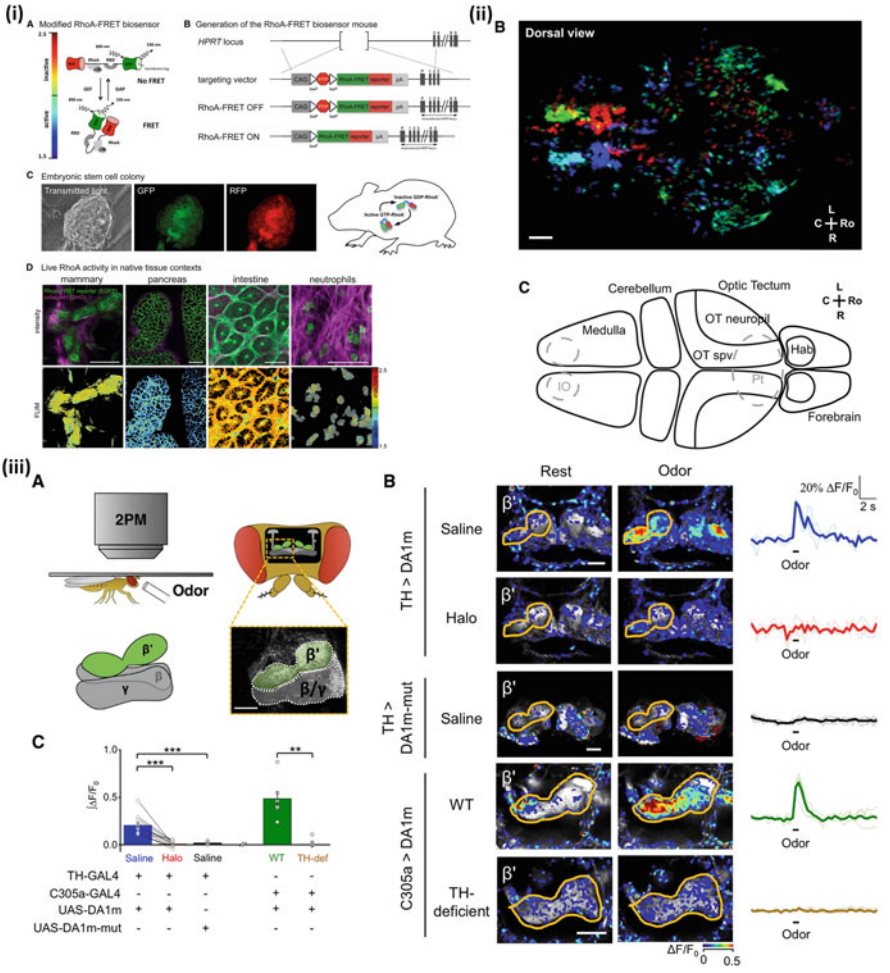

Fig. 5 (*i*) Generation of the RhoA-FRET biosensor mouse: (**a**) schematic of the Raichu-RhoA biosensor; (**b**) targeted to the Hprt locus to generate the RhoA-FRET biosensor mouse. (**c**) Embryonic stem cell colony expressing the RhoA-FRET biosensor (GFP, green; RFP, red). (**d**) RhoA activity in the mammary fat pad, pancreas, intestine, and neutrophils of RhoA-ON mice. (*ii*) In vivo imaging of DA dynamics in the *Drosophila* brain: (**a**) schematic for odor stimulation during two-photon microscopy in *Drosophila*. (**b**) Fluorescence changes of DA1m- or DA1m-mut-expressing flies to 1 s of odor stimulation. (**c**) Group analysis of the odor-evoked fluorescence responses. (*iii*) Clustering of fluorescence traces reveals four temporal clusters in zebra fish; anatomical distribution of activity clusters in one fish. Sum projection showing the distribution of the four clusters of activity in the same fish (top), with colors corresponding to the color traces (bottom). Scale bar 50 μm. (Figures in different panels are reproduced with permission from (*i*) Cell Rep. 2017 Oct 3;21(1):274–288 [178]; (*ii*) Cell. 2018 Jul 12;174(2):481–496 [175]; (*iii*) Neuron. 2014 Mar 19;81(6):1328–1343 [176])

Apart from mice, *Caenorhabditis elegans* is a widely used animal model for studying neurodegenerative disorders. Transgenic *C. elegans* strains expressing green, yellow, or red fluorescent proteins in embryos were developed by Heppert et al., to image embryos expressing fluorescent proteins under the same conditions with probe mNeonGreen. Monomeric green (GFP, mNeonGreen [mNG]), yellow (mNG, monomeric yellow fluorescent protein for energy transfer [mYPet]), and red (TagRFP-T, mRuby2, mCherry, mKate2) fluorescent proteins were evaluated for comparative in vivo experiments in *C. elegans* [179]. Since *C. elegans* is a transparent small animal, fluorescent protein-based sensors provide sensitive imaging ability to track its biological events in a much better way compared to large animals. Hirayama et al. designed a first-generation near-IR turn-on fluorescent sensor, CS790AM, to report dynamic copper fluctuations in vivo and detected the basal, endogenous levels of exchangeable copper in living mice platform to monitor labile copper pools role in murine Wilson's disease model [180].

5 Drawbacks Associated with the Use of Fluorescent Proteins in Biosensors

Although fluorescent protein-based biosensors offer a realistic, cost-effective, and high-throughput imaging approach for studying various biological processes of cells, their application is also limited by the inherent problem of photobleaching, phototoxicity, low quantum yield, high background signal, and especially tissue attenuation in in vivo imaging applications. Upon repeated cycles of excitation, the fluorophore of the sensor protein gets damaged and leads to loss of fluorescence signal which can result in non-specific sensor signal. In addition, it severely limits the application of fluorescent protein biosensors for real-time imaging where time-dependent pattern of biosensor signal is important for achieving reliable result for the studies [181, 182]. On the other hand, exposure to higher-energy photons tends to generate reactive oxygen species (ROS) which are highly reactive species capable of inflicting damage to cellular biomolecules like DNA, RNA, and proteins by oxidation, which in turn limits the possibilities of multiplexing the assays in in vitro and in vivo imaging applications [183]. In the event of avoiding photobleaching and phototoxicity, the narrow operation bandwidth and shorter imaging time leave us with lower quantum yield of these fluorescent proteins with limited sensitivity. The cells by itself possess biomolecules that prominently contribute to autofluorescence and render high background while imaging such fluorescent proteins with low quantum yield, which limits the spectral resolution and sensitivity of the biosensor [184, 185]. To overcome the limitation of tissue attenuation, the development of fluorescent proteins with high quantum yields and far-red or near-infrared (NIR) shifted absorption and emission wavelengths are preferred. Currently there are several fluorescent protein variants which emit light in the NIR range and have been developed from bacterial phytochrome photoreceptors and are used in various biosensor applications [186, 187].

6 Conclusion and Future Perspectives

The course of evolution of fluorescent proteins from the first known member GFP to a completely new family of fluorescent proteins spanning across the visible spectra has emerged in relatively short time span. The rapid growth and applications of the FP repertoire for in vivo imaging continuously shed light on studying crucial cellular events which play a vital role in development and progression of diseases. With the present capabilities of FPs, multicolor labeling of proteins and nucleic acids; tracking of protein movements, interactions, activities, degradation, organelle motility, and fusion-fission events; and monitoring of promoter activation, as well as multiparameter imaging of various cellular processes, including changes in concentration of signal molecules, changes of membrane potential and cell state, etc., can be deduced efficiently. Although extensive variants of biosensors for specific applications have been developed, it is expected that further improvements in brightness, photostability, maturation rate, pH stability, and performance in fusions will gain priority in the future. Even though a significant progress has been made in the demonstration of novel fluorescent protein-based biosensors for in vivo models, further research is required to establish consistent, reproducible, and reliable imaging instruments with far-red shifted fluorescent proteins, and animal models for disease investigations. Although rapid strides have been made in this field, further improvements on deep tissue imaging with higher sensitivity and long-term noninvasive imaging would open wide range of applications for biosensors. Addressing the drawback of loss of fluorescent proteins during tissue fixation or subsequent processing can also improve ex vivo histopathological analysis of tissues from transgenic animals.

Acknowledgments We would like to thank the Canary Center at Stanford, Department of Radiology, for providing facility and resources. We also thank SCi3 Small Animal Imaging Service Center, Stanford University School of Medicine, for providing imaging facilities and data analysis support. We acknowledge Dr. Sanjiv Sam Gambhir, Chair of the Department of Radiology, Stanford University, for his constant support and help.

Compliance with Ethical Standards

Conflicts of Interest There are no actual or potential conflicts of interest in regard to this chapter.

Funding This research was supported by NIH R01CA209888 and NIH R21EB022298. This work was also in part supported by the Center for Cancer Nanotechnology Excellence for Translational Diagnostics (CCNE-TD) at Stanford University through an award (grant no. U54 CA199075) from the National Cancer Institute (NCI) of the National Institutes of Health (NIH).

Ethical Approval All applicable international, national, and/or institutional guidelines for the care and use of animals were followed.

References

1. Bu L, Shen B, Cheng Z (2014) Fluorescent imaging of cancerous tissues for targeted surgery. Adv Drug Deliv Rev 76:21–38
2. Lavis LD, Raines RT (2008) Bright ideas for chemical biology. ACS Chem Biol 3(3):142–155
3. Tsien RY (2010) Nobel lecture: constructing and exploiting the fluorescent protein paintbox. Integr Biol 2(2–3):77–93
4. Vigneshvar S et al (2016) Recent advances in biosensor technology for potential applications – an overview. Front Bioeng Biotechnol 4:11
5. Shimomura O, Johnson FH, Saiga Y (1962) Extraction, purification and properties of aequorin, a bioluminescent protein from the luminous hydromedusan, Aequorea. J Cell Comp Physiol 59:223–239
6. Gong Z, Ju B, Wan H (2001) Green fluorescent protein (GFP) transgenic fish and their applications. Genetica 111(1–3):213–225
7. Lai L et al (2002) Transgenic pig expressing the enhanced green fluorescent protein produced by nuclear transfer using colchicine-treated fibroblasts as donor cells. Mol Reprod Dev 62 (3):300–306
8. Dhandayuthapani S et al (1995) Green fluorescent protein as a marker for gene expression and cell biology of mycobacterial interactions with macrophages. Mol Microbiol 17(5):901–912
9. Zacharias DA et al (2002) Partitioning of lipid-modified monomeric GFPs into membrane microdomains of live cells. Science 296(5569):913–916
10. McCombs JE, Palmer AE (2008) Measuring calcium dynamics in living cells with genetically encodable calcium indicators. Methods 46(3):152–159
11. Mank M, Griesbeck O (2008) Genetically encoded calcium indicators. Chem Rev 108 (5):1550–1564
12. Xiao T et al (2017) In vivo analysis with electrochemical sensors and biosensors. Anal Chem 89(1):300–313
13. Takanaga H, Chaudhuri B, Frommer WB (2008) GLUT1 and GLUT9 as major contributors to glucose influx in HepG2 cells identified by a high sensitivity intramolecular FRET glucose sensor. Biochim Biophys Acta 1778(4):1091–1099
14. Ha JS et al (2007) Design and application of highly responsive fluorescence resonance energy transfer biosensors for detection of sugar in living Saccharomyces cerevisiae cells. Appl Environ Microbiol 73(22):7408–7414
15. Hires SA, Zhu Y, Tsien RY (2008) Optical measurement of synaptic glutamate spillover and reuptake by linker optimized glutamate-sensitive fluorescent reporters. Proc Natl Acad Sci U S A 105(11):4411–4416
16. Tainaka K et al (2010) Design strategies of fluorescent biosensors based on biological macromolecular receptors. Sensors 10(2):1355–1376
17. Mehrotra P (2016) Biosensors and their applications – a review. J Oral Biol Craniofac Res 6(2):153–159
18. Bajar BT et al (2016) A guide to fluorescent protein FRET pairs. Sensors 16(9):1488
19. Laverdant J et al (2011) Experimental determination of the fluorescence quantum yield of semiconductor nanocrystals. Materials 4(7):1182–1193
20. Rurack K, Spieles M (2011) Fluorescence quantum yields of a series of red and near-infrared dyes emitting at 600-1000 nm. Anal Chem 83(4):1232–1242
21. Verma D, Grigoryan G, Bailey-Kellogg C (2015) Structure-based design of combinatorial mutagenesis libraries. Protein Sci 24(5):895–908
22. Saito Y et al (2018) Machine-learning-guided mutagenesis for directed evolution of fluorescent proteins. ACS Synth Biol 7(9):2014–2022
23. Mitchell JA et al (2016) Rangefinder: a semisynthetic FRET sensor design algorithm. ACS Sensors 1(11):1286–1290
24. Malakauskas SM, Mayo SL (1998) Design, structure and stability of a hyperthermophilic protein variant. Nat Struct Biol 5(6):470–475

25. Looger LL et al (2003) Computational design of receptor and sensor proteins with novel functions. Nature 423(6936):185–190
26. Jiang L et al (2008) De novo computational design of retro-aldol enzymes. Science 319(5868):1387–1391
27. Rothlisberger D et al (2008) Kemp elimination catalysts by computational enzyme design. Nature 453(7192):190–195
28. Kuhlman B et al (2003) Design of a novel globular protein fold with atomic-level accuracy. Science 302(5649):1364–1368
29. Yang F, Moss LG, Phillips Jr GN (1996) The molecular structure of green fluorescent protein. Nat Biotechnol 14(10):1246–1251
30. Heim R, Prasher DC, Tsien RY (1994) Wavelength mutations and posttranslational autoxidation of green fluorescent protein. Proc Natl Acad Sci U S A 91(26):12501–12504
31. Heim R, Tsien RY (1996) Engineering green fluorescent protein for improved brightness, longer wavelengths and fluorescence resonance energy transfer. Curr Biol 6(2):178–182
32. Tomosugi W et al (2009) An ultramarine fluorescent protein with increased photostability and pH insensitivity. Nat Methods 6(5):351–353
33. Kremers GJ et al (2006) Cyan and yellow super fluorescent proteins with improved brightness, protein folding, and FRET Forster radius. Biochemistry 45(21):6570–6580
34. Rizzo MA et al (2004) An improved cyan fluorescent protein variant useful for FRET. Nat Biotechnol 22(4):445–449
35. Cormack BP, Valdivia RH, Falkow S (1996) FACS-optimized mutants of the green fluorescent protein (GFP). Gene 173(1):33–38
36. Heim R, Cubitt AB, Tsien RY (1995) Improved green fluorescence. Nature 373 (6516):663–664
37. Yang TT, Cheng L, Kain SR (1996) Optimized codon usage and chromophore mutations provide enhanced sensitivity with the green fluorescent protein. Nucleic Acids Res 24 (22):4592–4593
38. Ormo M et al (1996) Crystal structure of the Aequorea victoria green fluorescent protein. Science 273(5280):1392–1395
39. Gittins JR et al (2015) Fluorescent protein-mediated colour polymorphism in reef corals: multicopy genes extend the adaptation/acclimatization potential to variable light environments. Mol Ecol 24(2):453–465
40. Lukyanov KA et al (2000) Natural animal coloration can be determined by a nonfluorescent green fluorescent protein homolog. J Biol Chem 275(34):25879–25882
41. Matz MV et al (1999) Fluorescent proteins from nonbioluminescent Anthozoa species. Nat Biotechnol 17(10):969–973
42. Shkrob MA et al (2005) Far-red fluorescent proteins evolved from a blue chromoprotein from Actinia equina. Biochem J 392(Pt 3):649–654
43. Evdokimov AG et al (2006) Structural basis for the fast maturation of Arthropoda green fluorescent protein. EMBO Rep 7(10):1006–1012
44. Shagin DA et al (2004) GFP-like proteins as ubiquitous metazoan superfamily: evolution of functional features and structural complexity. Mol Biol Evol 21(5):841–850
45. Germond A et al (2016) Design and development of genetically encoded fluorescent sensors to monitor intracellular chemical and physical parameters. Biophys Rev 8(2):121–138
46. Tavare JM, Fletcher LM, Welsh GI (2001) Using green fluorescent protein to study intracellular signalling. J Endocrinol 170(2):297–306
47. Palmer AE et al (2011) Design and application of genetically encoded biosensors. Trends Biotechnol 29(3):144–152
48. Day RN, Davidson MW (2009) The fluorescent protein palette: tools for cellular imaging. Chem Soc Rev 38(10):2887–2921
49. Song W, Strack RL, Jaffrey SR (2013) Imaging bacterial protein expression using genetically encoded RNA sensors. Nat Methods 10(9):873–875
50. Thorn K (2017) Genetically encoded fluorescent tags. Mol Biol Cell 28(7):848–857

51. Rowland CE et al (2015) Intracellular FRET-based probes: a review. Methods Appl Fluoresc 3 (4):042006
52. Miesenbock G, De Angelis DA, Rothman JE (1998) Visualizing secretion and synaptic transmission with pH-sensitive green fluorescent proteins. Nature 394(6689):192–195
53. Johnson DE et al (2009) Red fluorescent protein pH biosensor to detect concentrative nucleoside transport. J Biol Chem 284(31):20499–20511
54. Tallini YN et al (2006) Imaging cellular signals in the heart in vivo: cardiac expression of the high-signal Ca2+ indicator GCaMP2. Proc Natl Acad Sci U S A 103(12):4753–4758
55. Souslova EA et al (2007) Single fluorescent protein-based Ca2+ sensors with increased dynamic range. BMC Biotechnol 7:37
56. Griesbeck O et al (2001) Reducing the environmental sensitivity of yellow fluorescent protein. Mechanism and applications. J Biol Chem 276(31):29188–29194
57. Belousov VV et al (2006) Genetically encoded fluorescent indicator for intracellular hydrogen peroxide. Nat Methods 3(4):281–286
58. Gallegos LL, Kunkel MT, Newton AC (2006) Targeting protein kinase C activity reporter to discrete intracellular regions reveals spatiotemporal differences in agonist-dependent signaling. J Biol Chem 281(41):30947–30956
59. Goedhart J et al (2007) Sensitive detection of p65 homodimers using red-shifted and fluorescent protein-based FRET couples. PLoS One 2(10):e1011
60. Miyawaki A et al (1997) Fluorescent indicators for Ca2+ based on green fluorescent proteins and calmodulin. Nature 388(6645):882–887
61. Berney C, Danuser G (2003) FRET or no FRET: a quantitative comparison. Biophys J 84 (6):3992–4010
62. Hanson GT et al (2002) Green fluorescent protein variants as ratiometric dual emission pH sensors. 1. Structural characterization and preliminary application. Biochemistry 41 (52):15477–15488
63. Kneen M et al (1998) Green fluorescent protein as a noninvasive intracellular pH indicator. Biophys J 74(3):1591–1599
64. Jayaraman S et al (2000) Mechanism and cellular applications of a green fluorescent protein-based halide sensor. J Biol Chem 275(9):6047–6050
65. DiPilato LM, Cheng X, Zhang J (2004) Fluorescent indicators of cAMP and Epac activation reveal differential dynamics of cAMP signaling within discrete subcellular compartments. Proc Natl Acad Sci U S A 101(47):16513–16518
66. Hanson GT et al (2004) Investigating mitochondrial redox potential with redox-sensitive green fluorescent protein indicators. J Biol Chem 279(13):13044–13053
67. Ashby MC, Ibaraki K, Henley JM (2004) It's green outside: tracking cell surface proteins with pH-sensitive GFP. Trends Neurosci 27(5):257–261
68. Llopis J et al (1998) Measurement of cytosolic, mitochondrial, and Golgi pH in single living cells with green fluorescent proteins. Proc Natl Acad Sci U S A 95(12):6803–6808
69. Sankaranarayanan S et al (2000) The use of pHluorins for optical measurements of presynaptic activity. Biophys J 79(4):2199–2208
70. Henderson JN et al (2009) Excited state proton transfer in the red fluorescent protein mKeima. J Am Chem Soc 131(37):13212–13213
71. Violot S et al (2009) Reverse pH-dependence of chromophore protonation explains the large Stokes shift of the red fluorescent protein mKeima. J Am Chem Soc 131(30):10356–10357
72. Fang EF et al (2017) In vitro and in vivo detection of mitophagy in human cells, C. Elegans, and mice. J Vis Exp 129:e56301
73. Shinoda H, Shannon M, Nagai T (2018) Fluorescent proteins for investigating biological events in acidic environments. Int J Mol Sci 19(6):1543
74. Tantama M, Hung YP, Yellen G (2011) Imaging intracellular pH in live cells with a genetically encoded red fluorescent protein sensor. J Am Chem Soc 133(26):10034–10037
75. Shcherbakova DM, Subach OM, Verkhusha VV (2012) Red fluorescent proteins: advanced imaging applications and future design. Angew Chem Int Ed Engl 51(43):10724–10738

76. Horikawa K et al (2010) Spontaneous network activity visualized by ultrasensitive Ca(2+) indicators, yellow Cameleon-Nano. Nat Methods 7(9):729–732
77. Nagai T et al (2004) Expanded dynamic range of fluorescent indicators for Ca(2+) by circularly permuted yellow fluorescent proteins. Proc Natl Acad Sci U S A 101 (29):10554–10559
78. Palmer AE et al (2004) Bcl-2-mediated alterations in endoplasmic reticulum Ca2+ analyzed with an improved genetically encoded fluorescent sensor. Proc Natl Acad Sci U S A 101 (50):17404–17409
79. Palmer AE et al (2006) Ca2+ indicators based on computationally redesigned calmodulin-peptide pairs. Chem Biol 13(5):521–530
80. Mank M et al (2008) A genetically encoded calcium indicator for chronic in vivo two-photon imaging. Nat Methods 5(9):805–811
81. Vinkenborg JL et al (2009) Genetically encoded FRET sensors to monitor intracellular Zn2+ homeostasis. Nat Methods 6(10):737–740
82. Evers TH et al (2007) Ratiometric detection of Zn(II) using chelating fluorescent protein chimeras. J Mol Biol 374(2):411–425
83. Qin Y et al (2011) Measuring steady-state and dynamic endoplasmic reticulum and Golgi Zn2+ with genetically encoded sensors. Proc Natl Acad Sci U S A 108(18):7351–7356
84. Emmanouilidou E et al (1999) Imaging Ca2+ concentration changes at the secretory vesicle surface with a recombinant targeted cameleon. Curr Biol 9(16):915–918
85. Palmer AE, Tsien RY (2006) Measuring calcium signaling using genetically targetable fluorescent indicators. Nat Protoc 1(3):1057–1065
86. Kerppola TK (2008) Bimolecular fluorescence complementation (BiFC) analysis as a probe of protein interactions in living cells. Annu Rev Biophys 37:465–487
87. Kerppola TK (2008) Bimolecular fluorescence complementation: visualization of molecular interactions in living cells. Methods Cell Biol 85:431–470
88. Kodama Y, Hu CD (2012) Bimolecular fluorescence complementation (BiFC): a 5-year update and future perspectives. Biotechniques 53(5):285–298
89. Kerppola TK (2006) Visualization of molecular interactions by fluorescence complementation. Nat Rev Mol Cell Biol 7(6):449–456
90. Magliery TJ et al (2005) Detecting protein-protein interactions with a green fluorescent protein fragment reassembly trap: scope and mechanism. J Am Chem Soc 127(1):146–157
91. Hu CD, Chinenov Y, Kerppola TK (2002) Visualization of interactions among bZIP and Rel family proteins in living cells using bimolecular fluorescence complementation. Mol Cell 9 (4):789–798
92. Hu CD, Kerppola TK (2003) Simultaneous visualization of multiple protein interactions in living cells using multicolor fluorescence complementation analysis. Nat Biotechnol 21 (5):539–545
93. Shyu YJ et al (2006) Identification of new fluorescent protein fragments for bimolecular fluorescence complementation analysis under physiological conditions. Biotechniques 40 (1):61–66
94. Waadt R et al (2008) Multicolor bimolecular fluorescence complementation reveals simultaneous formation of alternative CBL/CIPK complexes in planta. Plant J 56(3):505–516
95. Fan JY et al (2008) Split mCherry as a new red bimolecular fluorescence complementation system for visualizing protein-protein interactions in living cells. Biochem Biophys Res Commun 367(1):47–53
96. Kodama Y, Wada M (2009) Simultaneous visualization of two protein complexes in a single plant cell using multicolor fluorescence complementation analysis. Plant Mol Biol 70 (1–2):211–217
97. Chu J et al (2009) A novel far-red bimolecular fluorescence complementation system that allows for efficient visualization of protein interactions under physiological conditions. Biosens Bioelectron 25(1):234–239

98. Grinberg AV, Hu CD, Kerppola TK (2004) Visualization of Myc/Max/Mad family dimers and the competition for dimerization in living cells. Mol Cell Biol 24(10):4294–4308
99. Vidi PA et al (2008) Ligand-dependent oligomerization of dopamine D(2) and adenosine A (2A) receptors in living neuronal cells. Mol Pharmacol 74(3):544–551
100. Niu W, Guo J (2013) Expanding the chemistry of fluorescent protein biosensors through genetic incorporation of unnatural amino acids. Mol Biosyst 9(12):2961–2970
101. Ayyadurai N et al (2011) Development of a selective, sensitive, and reversible biosensor by the genetic incorporation of a metal-binding site into green fluorescent protein. Angew Chem Int Ed Engl 50(29):6534–6537
102. Niu W, Guo J (2017) Novel fluorescence-based biosensors incorporating unnatural amino acids. Methods Enzymol 589:191–219
103. Wang F et al (2012) Unnatural amino acid mutagenesis of fluorescent proteins. Angew Chem Int Ed Engl 51(40):10132–10135
104. Chen S et al (2012) Reaction-based genetically encoded fluorescent hydrogen sulfide sensors. J Am Chem Soc 134(23):9589–9592
105. Chen ZJ et al (2013) Genetically encoded fluorescent probe for the selective detection of peroxynitrite. J Am Chem Soc 135(40):14940–14943
106. Alford SC et al (2012) A fluorogenic red fluorescent protein heterodimer. Chem Biol 19 (3):353–360
107. Alford SC et al (2012) Dimerization-dependent green and yellow fluorescent proteins. ACS Synth Biol 1(12):569–575
108. Thornton JM, Sibanda BL (1983) Amino and carboxy-terminal regions in globular proteins. J Mol Biol 167(2):443–460
109. Bliven S, Prlic A (2012) Circular permutation in proteins. PLoS Comput Biol 8(3):e1002445
110. Miyawaki A et al (1999) Dynamic and quantitative Ca2+ measurements using improved cameleons. Proc Natl Acad Sci U S A 96(5):2135–2140
111. Tian L, Hires SA, Looger LL (2012) Imaging neuronal activity with genetically encoded calcium indicators. Cold Spring Harb Protoc 2012(6):647–656
112. Nakai J, Ohkura M, Imoto K (2001) A high signal-to-noise Ca(2+) probe composed of a single green fluorescent protein. Nat Biotechnol 19(2):137–141
113. Nausch LW et al (2008) Differential patterning of cGMP in vascular smooth muscle cells revealed by single GFP-linked biosensors. Proc Natl Acad Sci U S A 105(1):365–370
114. Mizuno T et al (2007) Metal-ion-dependent GFP emission in vivo by combining a circularly permutated green fluorescent protein with an engineered metal-ion-binding coiled-coil. J Am Chem Soc 129(37):11378–11383
115. Mao T et al (2008) Characterization and subcellular targeting of GCaMP-type genetically-encoded calcium indicators. PLoS One 3(3):e1796
116. Suzuki J, Kanemaru K, Iino M (2016) Genetically encoded fluorescent indicators for organellar calcium imaging. Biophys J 111(6):1119–1131
117. Baird GS, Zacharias DA, Tsien RY (1999) Circular permutation and receptor insertion within green fluorescent proteins. Proc Natl Acad Sci U S A 96(20):11241–11246
118. Nagai T et al (2001) Circularly permuted green fluorescent proteins engineered to sense Ca2+. Proc Natl Acad Sci U S A 98(6):3197–3202
119. Ohkura M et al (2005) Genetically encoded bright Ca2+ probe applicable for dynamic Ca2+ imaging of dendritic spines. Anal Chem 77(18):5861–5869
120. Kawai Y, Sato M, Umezawa Y (2004) Single color fluorescent indicators of protein phosphorylation for multicolor imaging of intracellular signal flow dynamics. Anal Chem 76 (20):6144–6149
121. Gautam SG et al (2009) Exploration of fluorescent protein voltage probes based on circularly permuted fluorescent proteins. Front Neuroeng 2:14
122. Knopfel T et al (2003) Optical recordings of membrane potential using genetically targeted voltage-sensitive fluorescent proteins. Methods 30(1):42–48

123. Berg J, Hung YP, Yellen G (2009) A genetically encoded fluorescent reporter of ATP:ADP ratio. Nat Methods 6(2):161–166
124. Hernandez-Barrera A et al (2015) Hyper, a hydrogen peroxide sensor, indicates the sensitivity of the Arabidopsis root elongation zone to aluminum treatment. Sensors 15(1):855–867
125. Niethammer P et al (2009) A tissue-scale gradient of hydrogen peroxide mediates rapid wound detection in zebrafish. Nature 459(7249):996–999
126. Forster T (1946) Energiewanderung und Fluoreszenz. Naturwissenschaften 33(6):166–175
127. Ma L, Yang F, Zheng J (2014) Application of fluorescence resonance energy transfer in protein studies. J Mol Struct 1077:87–100
128. Tamura T, Hamachi I (2014) Recent progress in design of protein-based fluorescent biosensors and their cellular applications. ACS Chem Biol 9(12):2708–2717
129. Day RN, Davidson MW (2012) Fluorescent proteins for FRET microscopy: monitoring protein interactions in living cells. Bioessays 34(5):341–350
130. Nikolaev VO, Gambaryan S, Lohse MJ (2006) Fluorescent sensors for rapid monitoring of intracellular cGMP. Nat Methods 3(1):23–25
131. Wallace DJ et al (2008) Single-spike detection in vitro and in vivo with a genetic Ca2+ sensor. Nat Methods 5(9):797–804
132. Shcherbo D et al (2009) Practical and reliable FRET/FLIM pair of fluorescent proteins. BMC Biotechnol 9:24
133. Zhang J et al (2001) Genetically encoded reporters of protein kinase A activity reveal impact of substrate tethering. Proc Natl Acad Sci U S A 98(26):14997–15002
134. Tsutsui H et al (2008) Improving membrane voltage measurements using FRET with new fluorescent proteins. Nat Methods 5(8):683–685
135. Mutoh H et al (2009) Spectrally-resolved response properties of the three most advanced FRET based fluorescent protein voltage probes. PLoS One 4(2):e4555
136. Tyas L et al (2000) Rapid caspase-3 activation during apoptosis revealed using fluorescence-resonance energy transfer. EMBO Rep 1(3):266–270
137. Wu X et al (2006) Measurement of two caspase activities simultaneously in living cells by a novel dual FRET fluorescent indicator probe. Cytometry A 69(6):477–486
138. Bozza WP et al (2014) The use of a stably expressed FRET biosensor for determining the potency of cancer drugs. PLoS One 9(9):e107010
139. Kominami K et al (2012) In vivo imaging of hierarchical spatiotemporal activation of caspase-8 during apoptosis. PLoS One 7(11):e50218
140. Sipieter F et al (2014) Shining light on cell death processes – a novel biosensor for necroptosis, a newly described cell death program. Biotechnol J 9(2):224–240
141. Li M et al (2012) A high-throughput FRET-based assay for determination of Atg4 activity. Autophagy 8(3):401–412
142. Lu P et al (2011) Extracellular matrix degradation and remodeling in development and disease. Cold Spring Harb Perspect Biol 3(12):a005058
143. Eichorst JP, Clegg RM, Wang Y (2012) Red-shifted fluorescent proteins monitor enzymatic activity in live HT-1080 cells with fluorescence lifetime imaging microscopy (FLIM). J Microsc 248(1):77–89
144. Hou BH et al (2011) Optical sensors for monitoring dynamic changes of intracellular metabolite levels in mammalian cells. Nat Protoc 6(11):1818–1833
145. Gavet O, Pines J (2010) Progressive activation of CyclinB1-Cdk1 coordinates entry to mitosis. Dev Cell 18(4):533–543
146. Miura H, Matsuda M, Aoki K (2014) Development of a FRET biosensor with high specificity for Akt. Cell Struct Funct 39(1):9–20
147. Yoshizaki H et al (2007) Akt-PDK1 complex mediates epidermal growth factor-induced membrane protrusion through Ral activation. Mol Biol Cell 18(1):119–128
148. Seong J et al (2013) Distinct biophysical mechanisms of focal adhesion kinase mechanoactivation by different extracellular matrix proteins. Proc Natl Acad Sci U S A 110 (48):19372–19377

149. Wang Y et al (2005) Visualizing the mechanical activation of Src. Nature 434 (7036):1040–1045
150. Vevea JD et al (2013) Ratiometric biosensors that measure mitochondrial redox state and ATP in living yeast cells. J Vis Exp 77:50633
151. Fehr M et al (2003) In vivo imaging of the dynamics of glucose uptake in the cytosol of COS-7 cells by fluorescent nanosensors. J Biol Chem 278(21):19127–19133
152. San Martin A et al (2013) A genetically encoded FRET lactate sensor and its use to detect the Warburg effect in single cancer cells. PLoS One 8(2):e57712
153. Nagai T, Miyawaki A (2004) A high-throughput method for development of FRET-based indicators for proteolysis. Biochem Biophys Res Commun 319(1):72–77
154. Mizutani T et al (2010) A novel FRET-based biosensor for the measurement of BCR-ABL activity and its response to drugs in living cells. Clin Cancer Res 16(15):3964–3975
155. Nobis M et al (2013) Intravital FLIM-FRET imaging reveals dasatinib-induced spatial control of src in pancreatic cancer. Cancer Res 73(15):4674–4686
156. Randriamampita C et al (2008) A novel ZAP-70 dependent FRET based biosensor reveals kinase activity at both the immunological synapse and the antisynapse. PLoS One 3(1):e1521
157. Paster W et al (2009) Genetically encoded Forster resonance energy transfer sensors for the conformation of the Src family kinase Lck. J Immunol 182(4):2160–2167
158. Grashoff C et al (2010) Measuring mechanical tension across vinculin reveals regulation of focal adhesion dynamics. Nature 466(7303):263–266
159. Conway DE et al (2013) Fluid shear stress on endothelial cells modulates mechanical tension across VE-cadherin and PECAM-1. Curr Biol 23(11):1024–1030
160. Borghi N et al (2012) E-cadherin is under constitutive actomyosin-generated tension that is increased at cell-cell contacts upon externally applied stretch. Proc Natl Acad Sci U S A 109 (31):12568–12573
161. Potzkei J et al (2012) Real-time determination of intracellular oxygen in bacteria using a genetically encoded FRET-based biosensor. BMC Biol 10:28
162. Conway JR, Carragher NO, Timpson P (2014) Developments in preclinical cancer imaging: innovating the discovery of therapeutics. Nat Rev Cancer 14(5):314–328
163. Bernardini A et al (2015) Type I cell ROS kinetics under hypoxia in the intact mouse carotid body ex vivo: a FRET-based study. Am J Physiol Cell Physiol 308(1):C61–C67
164. Awaji T et al (2001) Novel green fluorescent protein-based ratiometric indicators for monitoring pH in defined intracellular microdomains. Biochem Biophys Res Commun 289 (2):457–462
165. Urra J et al (2008) A genetically encoded ratiometric sensor to measure extracellular pH in microdomains bounded by basolateral membranes of epithelial cells. Pflugers Arch 457 (1):233–242
166. Heydorn A et al (2006) Protein translocation assays: key tools for accessing new biological information with high-throughput microscopy. Methods Enzymol 414:513–530
167. Knauer SK et al (2005) Translocation biosensors to study signal-specific nucleo-cytoplasmic transport, protease activity and protein-protein interactions. Traffic 6(7):594–606
168. Fetz V, Stauber RH, Knauer SK (2018) Translocation biosensors-versatile tools to probe protein functions in living cells. Methods Mol Biol 1683:195–210
169. Dieguez-Hurtado R et al (2011) A Cre-reporter transgenic mouse expressing the far-red fluorescent protein Katushka. Genesis 49(1):36–45
170. Yamaguchi Y et al (2011) Live imaging of apoptosis in a novel transgenic mouse highlights its role in neural tube closure. J Cell Biol 195(6):1047–1060
171. Audet M et al (2010) Protein-protein interactions monitored in cells from transgenic mice using bioluminescence resonance energy transfer. FASEB J 24(8):2829–2838
172. Hoffman RM (2005) The multiple uses of fluorescent proteins to visualize cancer in vivo. Nat Rev Cancer 5(10):796–806
173. Hara M et al (2004) Imaging endoplasmic reticulum calcium with a fluorescent biosensor in transgenic mice. Am J Physiol Cell Physiol 287(4):C932–C938

174. Zhang J et al (2005) Insulin disrupts beta-adrenergic signalling to protein kinase A in adipocytes. Nature 437(7058):569–573
175. Sun F et al (2018) A genetically encoded fluorescent sensor enables rapid and specific detection of dopamine in flies, fish, and mice. Cell 174(2):481–496.e19
176. Portugues R et al (2014) Whole-brain activity maps reveal stereotyped, distributed networks for visuomotor behavior. Neuron 81(6):1328–1343
177. Livet J et al (2007) Transgenic strategies for combinatorial expression of fluorescent proteins in the nervous system. Nature 450(7166):56–62
178. Nobis M et al (2017) A RhoA-FRET biosensor mouse for intravital imaging in normal tissue homeostasis and disease contexts. Cell Rep 21(1):274–288
179. Heppert JK et al (2016) Comparative assessment of fluorescent proteins for in vivo imaging in an animal model system. Mol Biol Cell 27(22):3385–3394
180. Hirayama T et al (2012) Near-infrared fluorescent sensor for in vivo copper imaging in a murine Wilson disease model. Proc Natl Acad Sci U S A 109(7):2228–2233
181. Giloh H, Sedat JW (1982) Fluorescence microscopy: reduced photobleaching of rhodamine and fluorescein protein conjugates by n-propyl gallate. Science 217(4566):1252–1255
182. White J, Stelzer E (1999) Photobleaching GFP reveals protein dynamics inside live cells. Trends Cell Biol 9(2):61–65
183. Dixit R, Cyr R (2003) Cell damage and reactive oxygen species production induced by fluorescence microscopy: effect on mitosis and guidelines for non-invasive fluorescence microscopy. Plant J 36(2):280–290
184. Niswender KD et al (1995) Quantitative imaging of green fluorescent protein in cultured cells: comparison of microscopic techniques, use in fusion proteins and detection limits. J Microsc 180(Pt 2):109–116
185. Shaner NC, Steinbach PA, Tsien RY (2005) A guide to choosing fluorescent proteins. Nat Methods 2(12):905–909
186. Shcherbakova DM, Verkhusha VV (2013) Near-infrared fluorescent proteins for multicolor in vivo imaging. Nat Methods 10(8):751–754
187. Nishihara R et al (2019) Highly bright and stable NIR-BRET with blue-shifted coelenterazine derivatives for deep-tissue imaging of molecular events in vivo. Theranostics 9(9):2646–2661

Top Med Chem (2020) 34: 185–202
DOI: 10.1007/7355_2019_87

Published online: 14 January 2020

Fluorescent Probes for Diagnostics of β-Galactosidase: From Micro to Macro

Anyao Bi, Xinchen Jiang, Tang Gao, Shuqi Yang, Yi Liu, Xiaohui Liu, and Wenbin Zeng

Contents

Abstract β-Galactosidase (β-gal) is an enzyme commonly served as a reporter for the examination of transcription and transfection efficiencies. Due to its overexpression in primary and metastatic ovarian cancers, β-gal was also usually regarded as a molecular target for visualizing peritoneal metastases from ovarian cancers. Moreover, β-gal has been studied as a potential therapeutic target for lactose intolerance via gene replacement therapy in recent years. Interestingly, there were some reports that β-gal has been abnormally accumulated in senescent cells, which allowing this senescence-associated β-gal to be a significant biomarker for senescence. The great significance of β-gal has attracted many researchers' attentions in developing highly selective and sensitive approaches to monitor the activity of this enzyme in vitro and in vivo. In this review, we reported the recent development of the various materials for β-gal detection and their application in disease progression monitoring, with a focus on fluorescent probe, nanomaterials, and biomolecules. Finally, the trends for the further development of the probe for fluorescence-guided diagnosis in clinical cases and its preclinical potential value were proposed.

A. Bi, X. Jiang, T. Gao, S. Yang, Y. Liu, X. Liu, and W. Zeng (✉)
Xiangya School of Pharmaceutical Sciences, Central South University, Changsha, China

Molecular Imaging Research Center, Central South University, Changsha, China

Keywords β-Galactosidase, AIE, Fluorescence, Nanomaterials, Tumor

1 Introduction

β-Galactosidase (β-gal), an enzyme that catalyzes the hydrolysis of a glycosidic bond of β-galactopyranoside within a carbohydrate such as lactose, ganglioside GM1, and lactoceramides, is regarded as a very significant biomarker for cell senescence and primary ovarian cancers [1, 2]. And its deficiency is reported to be associated with β-galactosialidosis and Morquio B syndrome. On the other hand, β-gal serves as an important reporter for verifying the efficiency of transcription and transfection as well. Commonly, it acts as a biomarker to monitor the gene expression of lacZ1. Moreover, β-gal has been studied as a potential therapeutic target for lactose intolerance via gene replacement therapy in recent years [3]. According to the great significance of β-gal, it has attracted many researchers' attention in developing highly selective and sensitive approaches to monitor the activity of the enzyme in vitro and in vivo. There are various detection techniques, including MR [4], single-photon emission computed tomography (SPECT) [5], positron emission tomography (PET) [6], colorimetric [7], fluorogenic [8], chemiluminescence [9], and bioluminescence [10] approaches. By contrast, fluorescent probes are of great interest owing to their conveniences like high sensitivity, simple handling procedures, inexpensive instruments, and bioimaging ability. Herein, we reported the progress of fluorescent nanomaterials in various fields, especially in chemical sensing and biomedical imaging such as the detection of β-gal, and recent advances related to the nanomaterial for β-gal detection have also been mentioned.

2 Fluorescent Probe for β-Galactosidase Activity Detection

2.1 Fluorescent Probe Based on Coumarins, Fluoresceins, and Rhodamines

Recent research has illustrated that β-gal can be used as a molecular target for visualizing peritoneal metastases originating from primary ovarian cancers. As a result, great efforts have been devoted to developing a real-time tracking method for β-gal. A number of fluorescent probes based on coumarins, fluoresceins, and rhodamines have been synthesized for monitoring β-gal activity.

In 2014, Lee et al. [11] reported a two-photon β-gal fluorescent probe **1** and applied it to the detection of β-gal activity quantitatively in living cells and in aged tissues during cellular senescence. In their strategy, 6-(benzo[d]thiazol-2-yl)-2-(methylamino)-naphthalene was used as the probe fluorophore and β-D-galactopyranoside-derived benzyl carbamate as the β-gal hydrolytic site. After

exposing to β-gal, the carbamate compound was cleaved to afford the amino group as the electron donor. An internal charge transfer (ICT) effect was observed to shift the emission to the stronger fluorescent emission. After treating with β-gal in PBS buffer (10 mM, pH 7.4, 37°C), the fluorescent intensity of a 1 μM probe solution increased gradually at 540 nm while decreased at 460 nm. The ratio of the emission intensities at 410–460 nm and 520–570 nm increased by 120-fold upon reaction. Meanwhile, D-galactose, a well-known competitive inhibitor of β-gal, could not trigger this fluorescent emission, indicating that the fluorescent enhancement is specific to β-gal activity. A linear relationship was observed against the β-gal concentration ranging from 0 to 2.0 nM, indicating that probe **1** could quantify β-gal in the low concentration range. Next, the application practicability of **1** has been examined in a representative cell senescence model via monitoring the endogenous SA-β-gal activity. Doubling times and population were recorded in this process, during the middle stages of senescence, suggesting that the probe could sensitively detect the slight increases in SA-β-gal. Further, the probe was successfully applied for tissue imaging. Using 7- and 26-month-old Sprague−Dawley rat skin tissues, the TPM images of probe **1** clearly showed the distribution of β-gal activity at a depth of about 140 μm (Fig. 1).

Later in 2015, Hirabayashi et al. [12] made great efforts in fluorescent detection of β-gal. They reported a silicon-substituted fluorescein, which had a carboxylic group at the 2-position of the benzene moiety, to construct a red-fluorescent probe **2** for β-gal. Firstly, TokyoMagenta (TM), a moiety of fluorescein which has been employed, was modified with enzyme substrates at the 3′ and 6′ positions to form the colorless and nonfluorescent status. Then they applied **2** to test β-gal for the enzymatic reaction. The solution of probe **2** was almost colorless and nonfluorescent initially, but a sharp shift of red color was observed and strongly fluorescence enhancement (>1,000-fold) appeared after the incubation with β-gal. In the same year, Asanuma et al. [13] reported a strategy to synthesize a hydroxymethyl rhodol (HMR) derivative bearing β-gal, HMRef-β-gal (**3**), which enabled highly sensitive

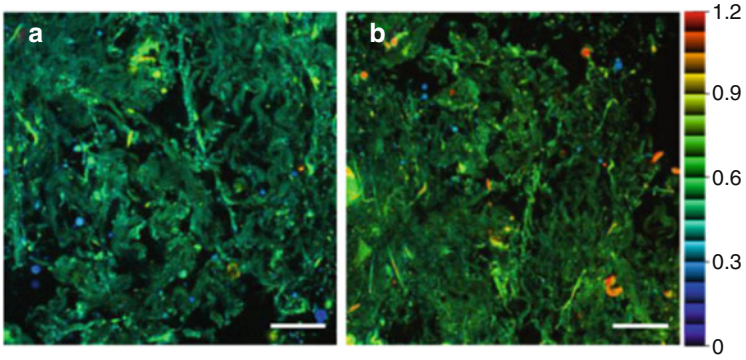

Fig. 1 Pseudocolored ratiometric TPM images (F_{yellow}/F_{blue}) of (**a**) 7-month-old and (**b**) 26-month-old Sprague−Dawley rat skin tissues stained with 10 μM SG1 (Reproduced from ref. [11] with permission from ACS)

detection of β-gal activity in living cells. The probe exhibited a weak fluorescence at pH 7.4 without β-gal, while an obvious high fluorescence increase (1,400-fold) was observed upon the reaction with β-gal. They further applied probe **3** for imaging several cultured ovarian cancer cells. The results showed that the enhanced fluorescence could be decreased by a competitive β-gal inhibitor, indicating the high specificity of **3** to detect intracellular β-gal activity. Further, SHIN3 cells were used to test the practicability of cancer imaging in a mouse model. The metastases as small as 1 mm were visualized clearly and specifically after injection of **3** in 5 min. This results clearly indicated potential value of the probe for fluorescence-guided diagnosis of peritoneal metastases from ovarian cancers.

In recent years, Zhang et al. [14] reported a small molecule fluorescent probe named 4-hydroxyl-*N*-butyl-1,8-naphthalimide–β-gal (NI–β-gal, **4**) for the detection of β-gal. Upon incubation with β-gal, probe **4** would turn into 4-hydroxyl-*N*-butyl-1,8-naphthalimide with a large Stokes shift and sharp fluorescent enhancement according to the restoring of ICT character. The synthetic strategy was well prepared so as all the reactions conditions were mild. After a three-step procedure, 4-bromo-1,8-naphthalic anhydride was adopted to afford 4-hydroxyl-*N*-butyl-1,8-naphthalimide. Upon addition of β-gal into probe **4** in PBS buffer (pH 7.4), a large fluorescence increase was observed at 545 nm and a decrease at 440 nm. Correspondingly, the F_{545}/F_{440} ratio acted as an enhancement behavior of 680-fold. Subsequently, probe **4** turned out to be qualified to image stable β-gal expression within tumors in living mice, and bright fluorescence could be observed in the transfected tumor at 75 min after administration of **4**, whereas the control group exhibits a negative signal. In comparison with non-transfected tumors, transfected tumors showed an approximately tenfold higher fluorescence intensity at 2 h after administration of **4**. Therefore, probe **4** maybe a useful tool in biomedical research such as gene therapy for cancer in the future.

2.2 NIR Fluorescent Probe

Conventional fluorophores with wavelengths less than 600 nm exhibited several shortcomings in vivo, such as poor tissue penetration and strong background fluorescence from bio-specimens. In order to overcome preceding drawbacks as well as elevate the signal-to-noise ratio, near-infrared fluorescent probes targeting β-gal have been prepared by incorporating β-galactose residues into near-infrared fluorophores like cyanine and squarylium dye scaffolds.

Redykeisar et al. [15] reported QCy7-based probe **5** targeting β-gal, which possessed long-wavelength fluorescence and a turn-on option. The fluorophore named quinone-cyanine-7 (QCy7), which was prepared by a simple two-step procedure, had strong emission in the NIR region but no emission after linking with β-galactose residues. To assay the turn-on imaging option in vivo, probe **5** were then injected subcutaneously into mice and the signal was monitored over time. The results showed that probe **5** possessed excellent in vivo compatibility and exhibited

an enhanced NIR fluorescent emission with the high signal-to-background ratio in mice. In the same year, Han et al. [16] reported a fluorescent turn-on probe termed AcGQCy7 (**6**) to detect β-gal activity in living cells. Because of its disrupted *p*-conjugated system, the prepared probe **6** was nonfluorescent in the NIR region, but after the enzymatic cleavage of β-galactose by β-gal under physiological conditions, the probe emitted strong fluorescence. The probe (300 μM) was dissolved in HBSS was tested for the presence or absence of β-gal (15 U mL^{-1}) at 37°C for 30 min. The color of the solution rapidly turned into dark blue when it was in contact with β-gal, and a broad absorbance band covering of 400–580 nm was detected. The fluorescence intensity of the β-gal-treated solution was 110-fold higher than that of the solution without it. The cellular imaging capability of the probe was studied in two cell lines, rat glial tumor C6 (control, no β-galactosidase expression) and its derivative, C6/LacZ, which constitutively expresses β-gal. C6/LacZ or C6 cells were incubated in HBSS buffer containing probe **6** (1 mM) at 37°C for 40 min. As expected, a bright fluorescence signal was detected only in the β-gal-positive C6/LacZ cells but not in the β-gal-negative C6 cells. Co-localization studies indicated that the cleaved product that specifically targeted mitochondria as the red fluorescence from **6** was overlapped with the MTG signal. This finding agrees with the author's another research of QCy7 as an excellent mitochondria mark.

In 2016, Gu et al. [17] reported a ratiometric near-infrared probe (DCM-β-gal) which was able to be activated by β-gal for the real-time fluorescent quantification in vivo and in situ. They designed **7** by grafting a β-gal activatable unit onto an NIR fluorophore DCM-OH. Upon excitation of the new absorption peak at 535 nm, a strong NIR fluorescence enhancement was observed with a peak at 685 nm. The color changed from faint yellow to rose red, which allows the colorimetric detection of β-gal using the naked eye. Furthermore, owing to the alteration in concentration-dependent ratio, the detection limit of DCM-β-gal was 1.7×10^{-4} U mL^{-1}. In order to get living cells generating endogenous β-gal, lacZ gene was introduced into 293T cells through a gene transfection method to overexpress β-gal. After incubation with **7** (10 μM) at 37°C for 30 min, the lacZ-(+) 293T cells successfully overexpressed β-gal and were observed to exhibit a decreased fluorescence in the green channel as well as a concomitant increase in the red channel. These results suggested that **7** could be specifically activated in β-gal-expressing cells, hence offering a ratiometric and light-up NIR readout for the in situ quantitative tracking and visualization of endogenous β-gal in living cells (Figs. 2 and 3).

2.3 ESIPT and AIE Fluorescent Probes

Besides ICT mentioned above, the β-gal could also be detected through varieties of other mechanisms, such as excited-state intramolecular proton transfer (ESIPT), the aggregation-induced emission (AIE), and so on. ESIPT is a fast photochemical process in which a proton transfers from a hydroxyl (or amino) unit to a carbonyl oxygen (or imine nitrogen) atom in the excited state of a fluorophore [18, 19]. ESIPT

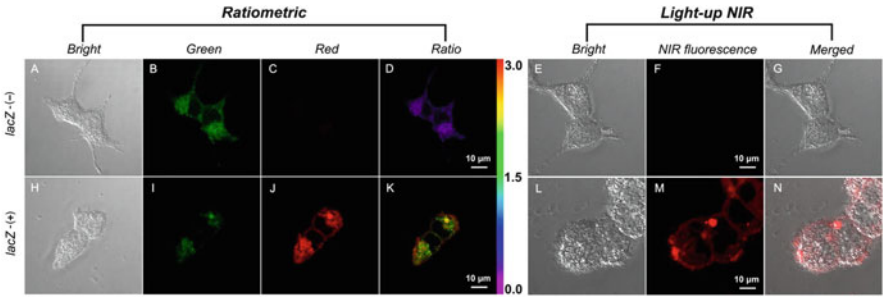

Fig. 2 Confocal and ratiometric images of 293T and OVCAR-3 cells incubated with DCM-β-gal (10 μM) for 30 min: (**a**–**g**) lacZ-(−) 293T cells without overexpressed β-gal and (**h**–**n**) lacZ-(+) 293T cells with overexpressed β-gal pretreated with inhibitor for 30 min (Reproduced from ref. [17] with permission from ACS)

compounds generally have high fluorescence quantum yield, large Stokes shift, and dual-wavelength emission (emission of enol and ketone form). Hence ESIPT-based fluorophores are ideal candidates for acting as a signal component to detect biomolecules [20]. In recent years, several ESIPT fluorophores, including 2-(benzothiazol-2′-yl)-phenols, and salicylaldehyde azine (SA) derivatives have been developed to constitute fluorescent probes for the β-gal detection [21–23]. For example, Otsubo et al. [21] selected 2-(benzothiazol-2-yl)-phenol derivatives as the substrates to synthesize a series of fluorescence dyes for β-gal detection. At first, they found the fluorescent wavelength could be controlled by adjusting the electronic character of phenol or benzothiazole ring. Compared with the compound with no substituent, an electron-donating effect at the meta-position of phenolic hydroxyl moiety could cause an obvious blue shift of the fluorescent wavelength. On the contrary, the electron-donating effect at para-position made the fluorescent wavelength shift toward the longer side. Moreover, the further shift to the longer-wavelength end could be caused by the reduction of electron density of the benzothiazole ring. Then, these substrates were coupled with 2,3,4,6-tetra-*O*-acetyl-D-galactopyranosyl bromide and converted to 2-(benzothiazol-2-yl)-phenyl-2,3,4,6-tetra-*O*-acetyl-β-D-galactopyranoside derivatives; afterward, all the acetyl groups were removed and the fluorescent probes for β-gal detection have been successfully synthesized. These probes exhibited no or weak fluorescence in solution because their ESIPT effect was blocked; however, after reacting with β-gal from *Aspergillus oryzae*, the fluorescent probes were hydrolyzed and the ESIPT effect could be restored, resulting in greatly enhanced fluorescence intensities. Their ratios of fluorescence intensity before and after enzyme reaction were high enough to detect β-gal accurately. In addition, it was worth mentioning that these probes could trace β-gal at low pH, and because of their immobility or poor solubility to water, the probes might stain live cells on the outer surface or interior of a cell membrane without fixing or permeabilizing in the future.

In 2014, Cellier et al. [22] designed and synthesized a series of 2-arylbenzothiazole derivatives-enzyme substrates as fluorogenic probes in order

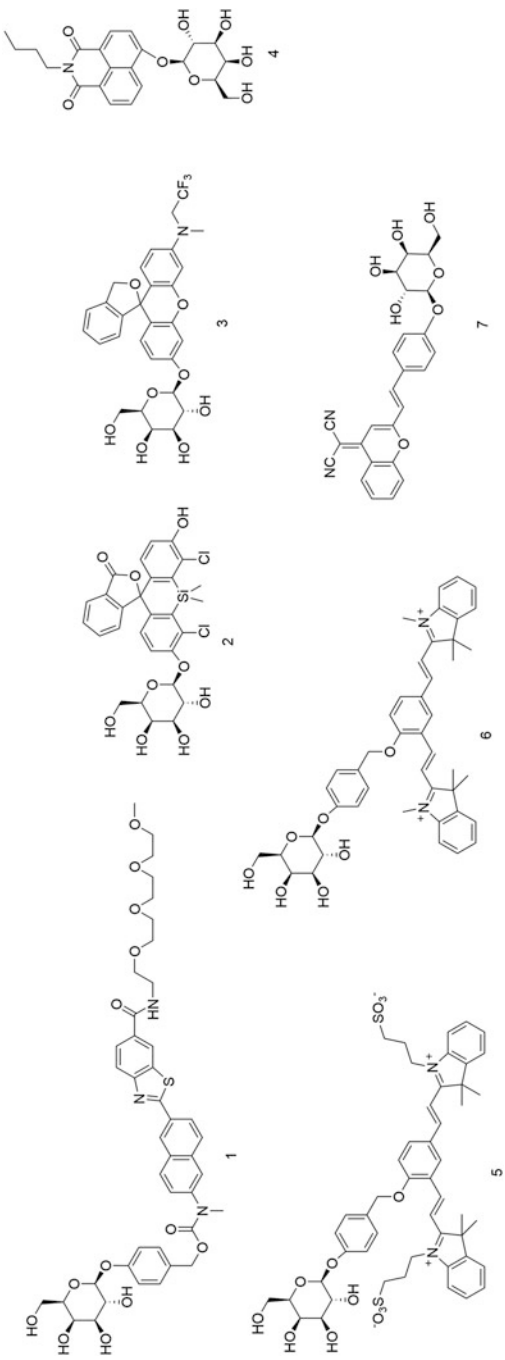

Fig. 3 Fluorescent probe based on coumarins, fluoresceins, and rhodamines 1–7 for β-gal detection

to detect β-gal and other enzymatic activities. The core 2-arylbenzothiazole derivatives were highly fluorescent, and this had been rationalized by ESIPT process. When combined with the enzymic substrates, the ESIPT effect of 2-arylbenzothiazole derivatives was blocked because there were no more hydroxyl protons at the ortho-position. However, enzyme-induced hydrolysis of weakly fluorescent enzyme substrate derivatives respectively liberated either fluorescent compounds. In addition, the coliform bacteria had also been detected because they could grow in the presence of a β-gal substrate which was transformed by β-gal into a fluorescent product that could readily be detected. Moreover, Wei et al. [23] successfully reported a series of ESIPT-based 2-(benzothiazol-2′-yl)-phenol fluorogenic substrates for β-gal detection in 2017. They developed a novel efficient method for the synthesis of important indoxyl glycoside substrates by using 1-acetylindol-3-ones as intermediates and synthesized new precipitating fluorogenic substrates for β-gal detection based on 2-(benzothiazol-2′-yl)-phenols and the ESIPT effect. And they have also assessed the application of the fluorogenic substrates in the detection of foodborne pathogenic bacteria.

Recently, although some fluorescent probes for β-gal have been developed, most of the reported sensors were fabricated with traditional fluorophores, which suffered from ACQ effect [17]. It causes the fluorescence in the aggregate state to be weaker than with that in solution. Therefore, it is still highly demanded to explore β-gal fluorescent probes, which could accumulate in living cells or tumor tissue imaging without ACQ effect. In 2001, Tang's group firstly found and reported the phenomenon of "aggregation-induced emission (AIE)" [24]. The compounds with AIE effect are almost nonluminescent when they are dissolved in a good solvent but emit intensely in a poor solvent. Meanwhile, the compounds with AIE effect have significant advantages, such as bright luminescent in the aggregate state and large Stokes shift [25–27]; thus, they have been greatly developed for detection of β-gal [28, 29]. In 2015, Peng et al. [28] reported a salicylaldehyde azine derivative SA-β-gal (**11**) for light-up detection of β-gal activity in living cells based on both AIE and ESIPT effects. When the hydroxyl groups at the ortho-position on the benzene ring of salicylaldehyde azine were substituted by β-galactopyranoside, ESIPT process was blocked. Upon the addition of β-gal, the β-galactopyranoside group on SA-β-gal was cleaved, and the restored hydroxyl group occurred in ESIPT to regain the AIE characteristics, resulting in bright fluorescence. Contrary to traditional β-gal fluorescent sensors, SA-β-gal could emit strongly in the aggregation state, which can well avoid the ACQ phenomenon. The probe showed a large Stokes shift, a high light-up ratio, and a high sensitivity (0.014 UmL^{-1}) toward β-gal. Moreover, it was worth mentioning that the probe could also be well retrained in living cells emitting strong fluorescence (Fig. 4).

In 2017, Jiang et al. [29] designed and synthesized a tetraphenylethylene-based turn-on probe TPE-Gal (**12**) for β-gal detection with AIE effect in aqueous samples and in living cells. TPE-Gal was designed to bear a positively charged pyridinium pendant. And a substrate of β-galactosidase-D-galactose residue was conjugated to the terminal of the pyridinium pendant. In the presence of β-gal, the D-galactose residue was cleaved and resulted in a phenolate intermediate. Then the intermediate

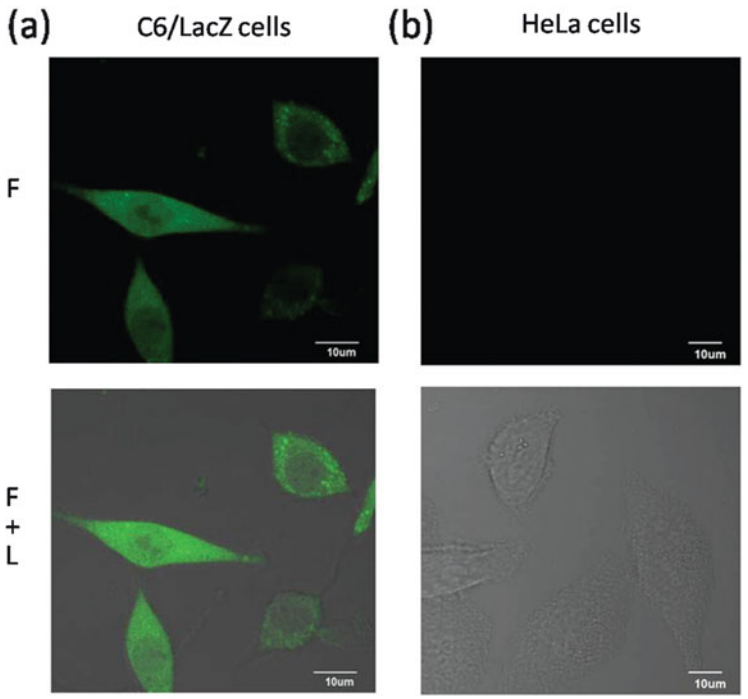

Fig. 4 Imaging b-galactosidase activity in cells. Images of probe SA-β-gal (50 mM) in (**a**) C6/LacZ cells and (**b**) HeLa cells for 2 h at 37°C; the excitation was set at 405 nm (Reproduced from ref. [28] with permission from RSC)

could undergo 1,6-elimination of *p*-quinone methide to generate a tetraphenylethylene-pyridinium compound with poor solubility, resulting in the appearance of aggregation effect and a light-up fluorescence of the TPE moiety based on the AIE effect. The TPE-Gal displayed distinguishable advantages such as high specificity toward β-gal, no self-quenching at high concentration, large Stokes shift and so on. Moreover, the researchers also tested the applicability of TPE-Gal for sensing β-gal not only in aqueous solution but also in living cells. The results showed that TPE-Gal could exhibit excellent fluorescence properties in these environments (Fig. 5).

3 Nanomaterial for β-Galactosidase Activity Detection

The nanomaterial has attracted considerable attentions from the early 1980s due to its special physical and chemical properties and promising application. Entering the twenty-first century, the researches of nanomaterials have been extended in various fields, especially in chemical sensing and biomedical imaging such as the detection

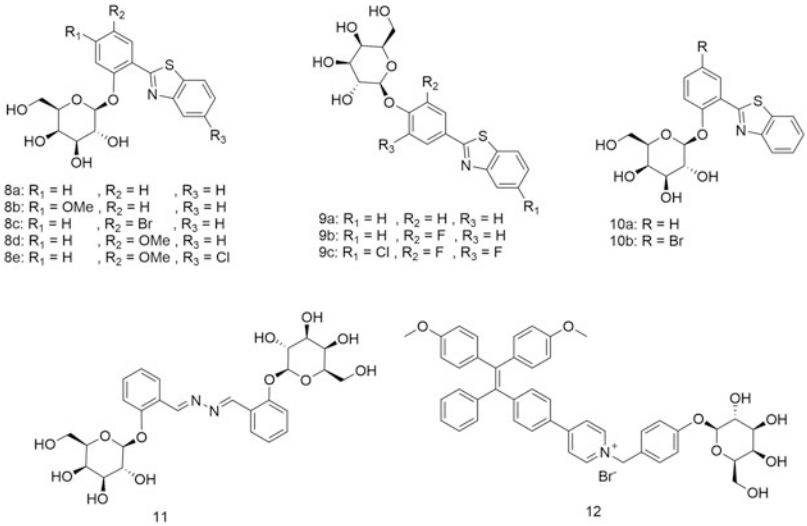

Fig. 5 ESIPT and AIE fluorescent probes **8**–**12** for β-gal detection

of β-gal, and some studies related to the nanomaterials for β-gal detection have also been reported.

3.1 Thiolated Copper Nanoclusters (CuNCs) and Silica Nanoclusters

Huang et al. [30] used glutathione (GSH) as the protecting ligand and reducing agent to successfully synthesize thiolate-protected copper nanoclusters (CuNCs) with aggregation-induced luminescence, which can self-assemble into dots by aluminum cations via a coordination reaction and then emit bright red luminescence. CuNCs are one of the most emerging luminescent materials because of their AIE properties [31–33] and long decay times in microseconds. And unlike organic AIE dots, thiolated CuNCs are better at avoiding the interference of autofluorescence in biosystems for their long emission times and red/NIR emission. However, the extremely low emission efficiency in neutral solution and poor stability to temperature, pH, and solvent greatly limit its application. Therefore, Chen et al. [34] utilized glutathione as a protector for CuNCs allowing their good stability in not only neutral but also weak alkaline solutions, which enabled their practicability under physiological conditions. And aluminum cations were found to be able to induce the dispersed CuNCs' (only emit very faint light) assembly into red bright luminescent dots quite effectively in water, which was probably due to the strong coordination of aluminum ions to GSH on the surface of the CuNCs. And the

formation of a huge amount of coordinate bonds between GSH and aluminum ions limited the vibration and rotation of the GSH ligands and then reduced the non-radiative decay rate, allowing the enhancement of emission. According to transmission electron microscopy (TEM) images, the mean diameter of CuNCs that existed dispersedly in water was about 2–5 nm, and the dots were monodispersive both in luminescence and in size, which benefit for analytical applications a lot. Furthermore, GSH-protected CuNCs were reported that their luminescence intensity was responsive to changes in pH. Huang believed this phenomenon was mostly because of the alternation of pH value, leading to the change of the aggregation state of the CuNCs. At lower pH, the CuNCs aggregated with intensive luminesce, while at higher pH the CuNCs were dispersed, showing weak emission. Interestingly, the reversibility of this pH-driven luminescence switch was observed clearly, as it didn't fatigue after five continuous cycles. Hence, Huang claimed that CuNCs would make an excellent luminescent pH indicator and a potential β-galactosidase probe. Huang and his team found that the luminescence of the CuNC dots assembled by Al^{3+} was gradually quenched by increasing amount of *p*-nitrophenol, indicating that there was significant interaction between these two taking place. The coordination between Al^{3+} and *p*-nitrophenol was owing to the highly efficient electron transfer between the CuNC dots and *p*-nitrophenol. And based on that, Huang reckoned that it could be utilized to assay β-gal using 4-nitrophenyl-b-D-galactopyranoside (NPGal) as the substrate. NPGal would rapidly hydrolyzed into galactose and *p*-nitrophenol in the presence of β-gal, and the latter was going to attach on the surface of CuNC dots via a coordinate bond, causing luminescence quenching. And the quenching behavior corresponds to the amount of β-gal, illustrating that CuNC dots could serve as a potential monitor of β-gal in a continuous and real-time way.

Agostini et al. [35] also used nanoclusters targeting SA-β-gal presenting specifically in senescent cells to deliver drugs for the purpose of avoiding senescence-related disease. The activity of SA-β-gal is encoded by the GLB1 gene [36, 37], which is a biomarker for increased lysosome number or activity and has been associated with replicative senescence [38, 39] and organismal aging [40, 41] for a long time. And the nano-device involved was mesoporous silica nanoparticles (MSNs) capped with a galacto-oligosaccharide (GOS). The structure of MSNs contained unique mesoporous materials with large specific volume and easer functionalization [42]. It could be absorbed by living cells through endocytosis. Moreover, using molecular/supramolecular ensemble on the external surface of MSNs could make them functional to develop gated MSNs, which released their cargo in response to external stimulant while not releasing the payload if there was only the hybrid material alone, and the latter phenomenon was called "zero delivery." In their study, Auvray et al. [43] selected MCM-41-based MSNs as the scaffold and loaded with Rhodamine B as a model drug after calcining. Then the oligosaccharide derivative GOS was capped onto MSNs to obtain the final product (S1). The MSN S1 nanoparticles were roughly spherical with a diameter of about 100 nm and an average pore diameter of 2.5 nm, and the maximum loading of Rhodamine B was approximately 0.14 g per gram SiO_2. Moreover, S1 was capable of releasing their

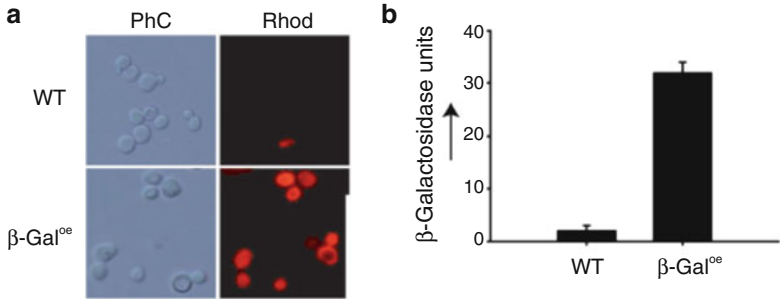

Fig. 6 Internalization and release of cargo in β-gal overexpressing yeast cells and human senescent cells. (**a**) Controlled release of Rhodamine-loaded S1 nanoparticles in wild-type (WT) and β-gal overexpressing yeast cells. (**b**) Quantitation of β-gal activity in WT and β-Galoe yeast cells (Reproduced from ref. [35] with permission from Wiley)

cargo selectively in SA-β-gal-positive cells like β-gal yeast cells and human fibroblasts DC1787. While interesting, no drug release in cells without SA-β-gal such as wild-type yeast cells was observed. Therefore, the MSN S1 nanoparticles were highly specific but no detectable toxicity for imaging SA-β-gal in senescent cells (Fig. 6).

3.2 Carbon Quantum Dots

Other than being an important biomarker for senescence, β-gal has been a biomarker for visualizing peritoneal metastases from ovarian cancers where it's overexpressed [2, 13]. Tang et al. [44] developed functional carbon quantum dots (CQDs) to assay glycosidase enzymes based on a combined host-guest recognition and specific static quenching-induced signal transduction mechanism. Compared with conventional fluorescent probes, CQDs possess much superiority including excellent biocompatibility, stable light emitting, and good photostability [45–47], for which it's believed to be alternatives to molecular fluorophores. β-Gal, which could catalyze the hydrolysis of 4-nitrophenyl-β-D-galactopyranoside (NPGal) into the corresponding glycose and *p*-nitrophenol, was picked up as a glycosidase example. Then NPGal selectively associated with β-cyclodextrin linking to CQD (β-CD-CQDs) for the hydrophobicity and agreeable size match of the cavity. And the formed nonfluorescent inclusion complex rendered the fluorescence quenching with high efficiency. On the contrary, the presence of β-gal could trigger the preceding processes and finally resulted in a sharp change in the fluorescence signal. Through the intracellular sensing and cytotoxicity tests, β-CD-CQDs nanoprobe exhibited excellent biocompatibility, membrane permeability, and capability of imaging β-gal in the OVCAR3 cells. The detection limit of β-CD-CQDs for β-gal could be lower up to 0.6 UL^{-1}, and the real-time monitoring of the β-gal level in ovarian cancer cells was also achieved. It's promising that the preceding established detection strategy could be expanded as a universal approach.

4 Targeted Fluorescent Probes for β-Galactosidase Detection

Targeted imaging by NIR fluorescent probes has been developed as an efficient alternative to the conventional methods for improving the diagnosis of a particular disease and therapeutic response of applicable drugs. A variety of targeting moieties, including antibodies, peptides, and low molecular weight non-peptide ligands, have been used in various formulations to selectively target the tumor site for the delivery of diagnostic agents and/or drugs.

Kim et al. [48] developed a ratiometric fluorescent probe (DCDHF-β-gal, **13**) for β-gal visualization in vivo. Probe **13** possessed β-D-galactopyranoside unit which not only behaved as a substrate of β-gal but acted as a ligand of asialoglycoprotein receptor (ASGPR). The β-D-galactopyranoside bond was cleaved by intracellular β-gal, thereby releasing NIR fluorophore and exhibiting ratiometric optical response. Initial fluorescence emission at 615 nm of probe **13** would red-shifted to 665 nm upon the incubation with the enzyme. Cellular studies further indicated that DCDHF-β-gal had great capability to target hepatocytes via ASGPRs without significant cytotoxicity. Furthermore, as a ratiometric fluorescent probe, the fluorescent spectra changes of **13** could be measured at two different emission bands, which renders relatively higher sensitivity and accuracy with concentration independence of probes or environmental conditions. Taken together, the novel ratiometric fluorogenic DCDHF-β-gal with NIR emission wavelength could be selectively delivered into ASGPR-positive cells, where it allowed effective noninvasive visualization of the β-gal activity (Fig. 7).

Prost and Hasserodt [49] reported a new kind of activatable imaging pre-pro-fluorescent probe applying the concept of "AND-type logic gate," which meant it emitted fluorescent signal only after being consecutively converted by two different enzymes. A β-gal unit was linked via an eliminating para-hydroxybenzyloxycarbonyl spacer to the leucine unit, which in return was linked to the silenced fluorophore through aminomethylpiperidine cyclizing spacer [50]. The fluorescent signal was observed only at the presence of both enzymes. The probe's simplicity indicated that there was a possible extension to triple-gating probes but still much remains to be explored.

5 Conclusion and Prospective

In general, it has been demonstrated that β-gal is a significant biomarker for cell senescence and primary ovarian cancers. Many efforts have been devoted to treating β-gal as an enzymatic target and visualizing its activity in preclinical diagnosis with fluorescent probes. Molecular bioimaging of enzyme activity in vivo is rapidly emerging as a powerful strategy for accurate disease diagnostics. The development of "smart" noninvasive imaging reagents for the determination of specific enzyme

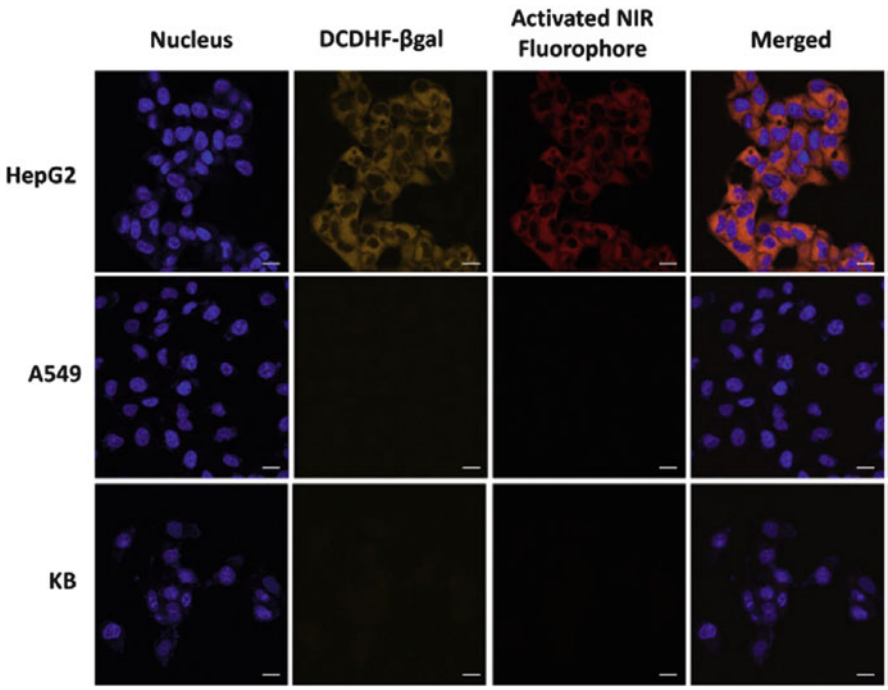

Fig. 7 Cell-specific targeting of DCDHF-β-gal. Cellular fluorescence images of DCDHF-β-gal in HepG2, A549, and KB cells. Cells were treated with 10 mM of DCDHF-β-gal for 24 h (Reproduced from ref. [48] with permission from Elsevier)

activity in vitro and in vivo is vitally required for cancer diagnosis. Moreover, at the side of the single-wavelength fluorescence-intensity-based systems, ratiometric fluorescence probes are of crucial practical advantages like enhanced signal-to-background ratio, in which the detectable ratio signal can be obtained via two isolated read-out channels of activated versus unreacted probes and bringing about improved and reliable signal quantification.

Nanomaterials has been regarded as one of most emerging biomedical imaging probes because of their special properties are being more and more studied for the detection of β-gal. Compared to conventional fluorescent probes, nanomaterials possess unique superiority such as smaller size, higher selectivity, and better biocompatibility. For example, pH-driven-luminescence GSH-protected CuNCs with AIE property and long decay time are promising to monitor β-gal continuously, and GOS-capped MSNs loaded with certain drugs are potential probes targeting SA-β-gal as well as device for drug delivery. Another used nanoprobe is β-CD-CQDs, which is based on a combined host-guest recognition and specific static quenching-induced signal transduction mechanism, because of their stable fluorescence emitting, excellent photostability, and low detection limit.

There are a number of fluorogenic probes being developed for detecting β-gal, but their applications are limited by a few drawbacks such as poor cellular permeability,

narrow emission wavelength, and low penetration depth. Meanwhile, NIR fluorescent probes have reduced tissue absorbance, high photostability, large Stokes shift, and long emission wavelengths, which make them highly suitable for noninvasive in vivo imaging of specific target. Interestingly, a novel activatable imaging pre-pro-fluorescent probe is being researched using a concept of "AND-type logic gate." That is the probe emits fluorescent signal only after being consecutively converted by two different enzymes and allegedly it's of great possibility of increased precision in the assay of β-gal. In this paper, we summarized diverse selective fluorescent probes targeting β-gal, all of which have their own superiority, yet there is inferiority holding back their application or some of them still remain to be further studied. Nevertheless, it's promising and thriving that fluorescent probes targeting β-gal would be put into application not only in molecular imaging but also in drug delivery systems, location of disease, and so on.

Acknowledgments We are grateful for the financial supports from the National Natural Science Foundation of China (81971678, 81671756), Key Research Project of Science and Technology Foundation of Hunan Province (2017SK2093 and 2019SK2211), Key Research Project of Science and Technology Foundation of Changsha (kq1801063), and Fundamental Research Funds for the Central Universities of Central South University (2018zzts041, 2018dcyj067).

Compliance with Ethical Standards

Conflict of Interest: There are no conflicts to declare.

Ethical Approval: There is no ethical approval to declare.

Informed Consent: There is no informed consent to declare.

References

1. Alam J, Cook JL (1990) Reporter genes: application to the study of mammalian gene transcription. Anal Biochem 188(2):245
2. Chatterjee SK, Bhattacharya M, Barlow JJ (1979) Glycosyltransferase and glycosidase activities in ovarian cancer patients. Cancer Res 39(6):1943
3. Salehi S, Eckley L, Sawyer GJ et al (2009) Intestinal lactase as an autologous beta-galactosidase reporter gene for in vivo gene expression studies. Hum Gene Ther 20(1):21
4. Kodibagkar VD, Yu J, Liu L et al (2006) Imaging β-galactosidase activity using ^{19}F chemical shift imaging of LacZ gene-reporter molecule 2-fluoro-4-nitrophenol-β-d-galactopyranoside. Magn Reson Imaging 24(7):959
5. Van Dort ME, Lee KC, Hamilton CA et al (2008) Radiosynthesis and evaluation of 5-[125i] iodoindol-3-yl-β-d-galactopyranoside ([125i]IBDG) as a β-galactosidase imaging radioligand. Mol Imaging 7(4):187
6. Celen S, Deroose C, De Groot T et al (2008) Synthesis and evaluation of F-18- and C-11-labeled phenyl-galactopyranosides as potential probes for *in vivo* visualization of LacZ gene expression using positron emission tomography. Bioconjug Chem 19(2):441
7. Yamamoto A, Adachi S, Kawamura S et al (1974) Localized β-galactosidase deficiency. Arch Intern Med 134(4):627
8. Zhang YZ, Naleway JJ, Larison KD et al (1991) Detecting lacZ gene expression in living cells with new lipophilic, fluorogenic beta-galactosidase substrates. FASEB J 5(15):3108

9. Liu Y, Feng B, Cao X et al (2019) A novel "AIE + ESIPT" near-infrared nanoprobe for the imaging of γ-glutamyl transpeptidase in living cells and the application in precision medicine. Analyst 144:5136–5142. https://doi.org/10.1039/c9an00773c
10. Wehrman TS, Von DG, Krutzik PO et al (2006) Luminescent imaging of beta-galactosidase activity in living subjects using sequential reporter-enzyme luminescence. Nat Methods 3 (4):295
11. Lee HW, Heo CH, Sen D et al (2014) Ratiometric two-photon fluorescent probe for quantitative detection of β-galactosidase activity in senescent cells. Anal Chem 86(20):10001
12. Hirabayashi K, Hanaoka K, Takayanagi T et al (2015) Analysis of chemical equilibrium of silicon-substituted fluorescein and its application to develop a scaffold for red fluorescent probes. Anal Chem 87(17):9061
13. Asanuma D, Sakabe M, Kamiya M et al (2015) Sensitive β-galactosidase-targeting fluorescence probe for visualizing small peritoneal metastatic tumours *in vivo*. Nat Commun 6:6463
14. Zhang XX, Wu H, Li P et al (2016) A versatile two-photon fluorescent probe for ratiometric imaging E. coli β-galactosidase in live cells and *in vivo*. Chem Commun 52(53):8283
15. Redykeisar O, Kisinfinfer E, Ferber S et al (2014) Synthesis and use of QCy7-derived modular probes for the detection and imaging of biologically relevant analytes. Nat Protoc 9(1):27
16. Han J, Han MS, Tung CH (2013) A fluorogenic probe for β-galactosidase activity imaging in living cells. Mol BioSyst 9(12):3001
17. Gu K, Xu Y, Li H et al (2016) Real-time tracking and in vivo visualization of β-galactosidase activity in colorectal tumor with a ratiometric near-infrared fluorescent probe. J Am Chem Soc 138(16):5334
18. Berezin MY, Achilefu S (2010) Fluorescence lifetime measurements and biological imaging. Chem Rev 110(5):2641
19. Hsieh CC, Cheng YM, Hsu CJ et al (2008) Spectroscopy and femtosecond dynamics of excited-state proton transfer induced charge transfer reaction. J Phys Chem A 112(36):8323
20. Murale DP, Kim H, Choi WS et al (2013) Highly selective excited state intramolecular proton transfer (ESIPT)-based superoxide probing. Org Lett 15(15):3946
21. Otsubo T, Minami A, Fujii H et al (2013) 2-(Benzothiazol-2-yl)-phenyl-β-d-galactopyranoside derivatives as fluorescent pigment dyeing substrates and their application for the assay of β-d-galactosidase activities. Bioorg Med Chem Lett 23(7):2245
22. Cellier M, Fazackerley E, James AL, Orenga S, Perry JD, Turnbull G, Stanforth SP (2014) Synthesis of 2-arylbenzothiazole derivatives and their application in bacterial detection. Bioorg Med Chem 22(4):1250
23. Wei X, Wu Q, Zhang J et al (2016) Synthesis of precipitating chromogenic/fluorogenic β-glucosidase/β-galactosidase substrates by a new method and their application in the visual detection of foodborne pathogenic bacteria. Chem Commun 53(1):103
24. Mei J, Leung NLC, Kwok RTK et al (2015) Aggregation-induced emission: together we shine, united we soar! Chem Rev 115(21):11718
25. He XP, Zang Y, James TD et al (2016) Fluorescent glycoprobes: a sweet addition for improved sensing. Chem Commun 53(1):82
26. Dong Y, Wang W, Zhong C et al (2014) Investigating the effects of side chain length on the AIE properties of water-soluble TPE derivatives. Tetrahedron Lett 55(8):1496
27. Cao D, Yang L, Wang L (2014) Application of aggregation-induced emission (AIE) systems in sensing and bioimaging. Curr Org Chem 18(8):1028
28. Peng L, Gao M, Cai X et al (2015) A fluorescent light-up probe based on AIE and ESIPT processes for β-galactosidase activity detection and visualization in living cells. J Mater Chem B 3(47):9168
29. Jiang G, Zeng G, Zhu W et al (2017) A selective and light-up fluorescent probe for β-galactosidase activity detection and imaging in living cells based on an AIE tetraphenylethylene derivative. Chem Commun 53(32):4505

30. Huang Y, Feng H, Liu W et al (2017) Cation-driven luminescent self-assembled dots of copper nanoclusters with aggregation-induced emission for β-galactosidase activity monitoring. J Mater Chem B 5:5120
31. Jia X, Li J, Wang E (2013) Cu nanoclusters with aggregation induced emission enhancement. Small 9(22):3873
32. Jia X, Yang X, Li J et al (2014) Stable Cu nanoclusters: from an aggregation-induced emission mechanism to biosensing and catalytic applications. Chem Commun 50(2):237
33. Wu Z, Liu J, Gao Y et al (2015) Assembly-induced enhancement of Cu nanoclusters luminescence with mechanochromic property. J Am Chem Soc 137(40):12906
34. Chen PC, Li YC, Ma JY et al (2016) Size-tunable copper nanocluster aggregates and their application in hydrogen sulfide sensing on paper-based devices. Sci Rep 6:24882
35. Agostini A, Mondragón L, Bernardos A et al (2012) Targeted cargo delivery in senescent cells using capped mesoporous silica nanoparticles. Angew Chem Int Ed 51(42):10556
36. Antropova YG, Bryantsev AL, Kalinina NI et al (2002) Proliferative activity and expression of cyclin-dependent kinase inhibitor p21WAF1 and p53 protein in endothelial cells of human aorta during replicative aging in vitro. Bull Exp Biol Med 134(1):81
37. Lee BY, Han JA, Im JS et al (2006) Senescence-associated β-galactosidase is lysosomal β-galactosidase. Aging Cell 5(2):187
38. Leckaczernik B, Moerman EJ, Shmookler Reis RJ et al (1997) Cellular and molecular biomarkers indicate precocious in vitro senescence in fibroblasts from SAMP6 mice. Evidence supporting a murine model of premature senescence and osteopenia. J Gerontol 52(6):B331
39. Gu Y, Wu Q, Zhu M et al (2011) Efficient pipeline configuration in distributed heterogeneous computing environments. Aging Cell 10(2):338
40. Chigira S, Sugita K, Kita K et al (2003) Increased expression of the Huntingtin interacting protein-1 gene in cells from Hutchinson Gilford Syndrome (Progeria) patients and aged donors. J Gerontol 58(10):B873
41. Cabrera S, Haskouri JE, Guillem C et al (2000) Generalised syntheses of ordered mesoporous oxides: the atrane route. Solid State Sci 2(4):405
42. Vallet-Regí M, Balas F, Arcos D (2007) Mesoporous materials for drug delivery. Angew Chem Int Ed 46(40):7548
43. Auvray X, Petipas C, Anthore R et al (1995) X-ray diffraction study of the ordered lyotropic phases formed by sugar-based surfactants. Langmuir 11(2):433
44. Tang C, Zhou J, Qian Z et al (2017) A universal fluorometric assay strategy for glycosidases based on functional carbon quantum dots: β-galactosidase activity detection in vitro and in living cells. J Mater Chem B 5(10):1971
45. Chen Y, Zhu C, Yang Z et al (2012) A new "turn-on" chemodosimeter for Hg^{2+}: ICT fluorophore formation via Hg^{2+}-induced carbaldehyde recovery from 1,3-dithiane. Chem Commun 48(42):5094
46. Zheng XT, Ananthanarayanan A, Luo KQ et al (2015) Glowing graphene quantum dots and carbon dots: properties, syntheses, and biological applications. Small 11(14):1620
47. Lim SY, Shen W, Gao Z (2015) Carbon quantum dots and their applications. Chem Soc Rev 44 (1):362
48. Kim EJ, Kumar R, Sharma A et al (2017) In vivo imaging of β-galactosidase stimulated activity in hepatocellular carcinoma using ligand-targeted fluorescent probe. Biomaterials 122:83
49. Prost M, Hasserodt J (2014) "Double gating" – a concept for enzyme-responsive imaging probes aiming at high tissue specificity. Chem Commun 50(94):14896
50. Thorn-Seshold O, Vargas-Sanchez M, McKeon S et al (2012) A robust, high-sensitivity stealth probe for peptidases. Chem Commun 48(50):6253

Top Med Chem (2020) 34: 203–224
DOI: 10.1007/7355_2019_84

Published online: 8 February 2020

The Present and Future of Optical Imaging Technologies in the Clinic: Diagnosis and Therapy

Evan P. Stater, Magdalena Skubal, Ryo Tamura, and Jan Grimm

Contents

Abstract Medical techniques based upon optical imaging technologies are important tools in clinical practice. The use of optical imaging in medical diagnosis is well established, and a large array of techniques are in current use, such as white light endoscopy, autofluorescence imaging, and optical coherence tomography. The applications of these techniques are expanding, and newer imaging technologies are becoming available to address problems and limitations associated with existing methods. Beyond diagnostics, optical imaging is increasingly a useful component of interventional medical procedures, such as image-guided surgery. In procedures such as surgical tumor resection, fluorescence imaging can aid surgeons in improving both accuracy and completeness of removal. Relevant to both diagnostic and therapeutic applications, Cerenkov luminescence imaging is a potential clinical technique which relies upon generation of visible-spectrum light by beta particles in a dielectric medium; this method could allow for coupling of a multimodal optical component to existing molecular imaging techniques, such as positron emission tomography, and also provide a means of monitoring distribution of administered clinically relevant radionuclides such as lutetium-177.

E. P. Stater
Weill Cornell Medicine, New York, NY, USA

M. Skubal and R. Tamura
Memorial Sloan Kettering Cancer Center, New York, NY, USA

J. Grimm (✉)
Weill Cornell Medicine, New York, NY, USA

Memorial Sloan Kettering Cancer Center, New York, NY, USA
e-mail: grimmj@mskcc.org

Keywords Cerenkov luminescence imaging, Clinical imaging, Diagnostic imaging, Endoscopy, Intraoperative imaging

1 Introduction

Optical imaging modalities are a crucial component of medical diagnosis and treatment. They are widely utilized for both diagnostic and interventional procedures. Thanks to the rapid pace of innovation in optical imaging technologies, clinicians have a wider array of imaging tools available than ever before. Furthermore, a number of promising new modalities are approaching clinical viability, for a broad variety of applications. This review will describe the current state of optical-based imaging modalities in diagnosis via endoscopic imaging and in treatment via image-guided surgery. Additionally, Cerenkov luminescence imaging, a promising new technology with many potential medical applications, will be described in detail.

2 Diagnostic Endoscopic Imaging

Endoscopy, a classification of medical procedures which utilize an endoscope to examine the endoluminal surfaces of internal body cavities, is a vitally important clinical tool, both for diagnosis and for guidance of interventional procedures such as surgery. Information gleaned from diagnostic endoscopic examinations help clinicians diagnose diseases and guide treatment decisions. Naturally, optical imaging technologies are integral to endoscopic procedures. This review section will discuss the current state and technological horizon of optical imaging modalities in diagnostic medical endoscopy.

Optical Imaging and Clinical Endoscopy The current standard of care for most clinical endoscopic imaging is non-fluorescent white light endoscopy (WLE). This optical imaging modality relies upon full-spectrum visible light illumination for visualizing internal anatomy. It can be used both for wide-field imaging and, with magnification, for examination of internal microanatomy. Although WLE is widely used clinically and does not require the administration of contrast agents, it has many shortcomings. Endoscopic diagnosis with WLE relies mainly upon the clinician's subjective ability to recognize macroscopic or microscopic morphological abnormalities in surface mucosa and other superficial structures. Generally, WLE is useful for the detection of conspicuous and superficial abnormalities; indistinct and non-facile abnormalities may escape detection with WLE. Furthermore, WLE detection of lesions is often not sufficient to merit diagnosis; invasive tissue biopsy

samples and subsequent histopathological analysis are frequently required for confirmation. Due to these limitations, newer optical imaging technologies are coming to the forefront to improve both the utility and versatility of endoscopy as a diagnostic technique.

Visible-Spectrum Modalities Several visible-spectrum optical imaging technologies have emerged with the aim of improving the accuracy, sensitivity, and specificity of WLE. The most widely used, chromoendoscopy, utilizes the administration of colored dyes as contrast agents to provide differentiating contrast to specific tissues and anatomical structures. A wide variety of application-specific dyes can be used for chromoendoscopic procedures. Administered dyes can be absorptive to specific epithelia or tissue types (e.g., methylene blue with upper gastrointestinal endoscopy for detection of Barrett's esophagus), non-absorptive to highlight extracellular structure and tissue topography (e.g., indigo carmine with colonoscopy for detection of colon polyps), or reactive to detect specific biochemical processes (e.g., phenol red with gastroendoscopy to visualize gastric *Helicobacter pylori* infection). A key advantage of this method is that it does not require the purchase of expensive specialized endoscopes, but rather can be performed with existing WLE equipment. However, it does require patient administration of contrast dyes, which can be unpleasant and invasive, and/or carry the risk of potential side effects. Furthermore, many chromoendoscopic procedures require removal of mucus in the region of interest prior to application of the contrast dyes, increasing the clinical time, complexity, and cost of the procedure.

Narrowband imaging (NBI) is a newer technology based on visible-spectrum light, in which white endoscopic illumination light is filtered into specific wavelengths, typically at 415 nm (blue light) and/or 540 nm (green light). These light bands correspond to the optimal absorptive wavelengths of hemoglobin contained in shallow mucosal blood vessels or deeper basal layer blood vessels, respectively. NBI endoscopy therefore enhances the optical contrast of blood vasculature over conventional WLE without requiring the administration of contrast agents (Fig. 1a). It can be useful for improving visual identification of vascular abnormalities that are associated with disease conditions, such as neoplasia. However, performing NBI endoscopy requires the purchase of NBI-capable endoscope systems.

So-called "digital endoscopy" procedures utilize legacy WLE equipment with the addition of software-based image post-processing to improve the quality of endoscopic images and provide more relevant information to clinicians. Post-processing is flexible and can be applied to conventional WLE, NBI, or chromoendoscopic procedures (Fig. 1b). Software suites available for this purpose include Fuji Intelligent Chromo Endoscopy (FICE) by Fujinon Corporation (Saitama, Japan) and Pentax i-SCAN by HOYA Corporation (Tokyo, Japan.) Usage of these software suites has shown some benefits in certain clinical diagnostic applications, but comparative results have generally been mixed. The i-SCAN suite has been shown to improve diagnosis of esophagitis when coupled with WLE versus WLE alone [6]; however, it also failed to show significant improvement in diagnosis of gastric neoplasia or small adenomatous colon polyps [7, 8]. Similarly, FICE software has

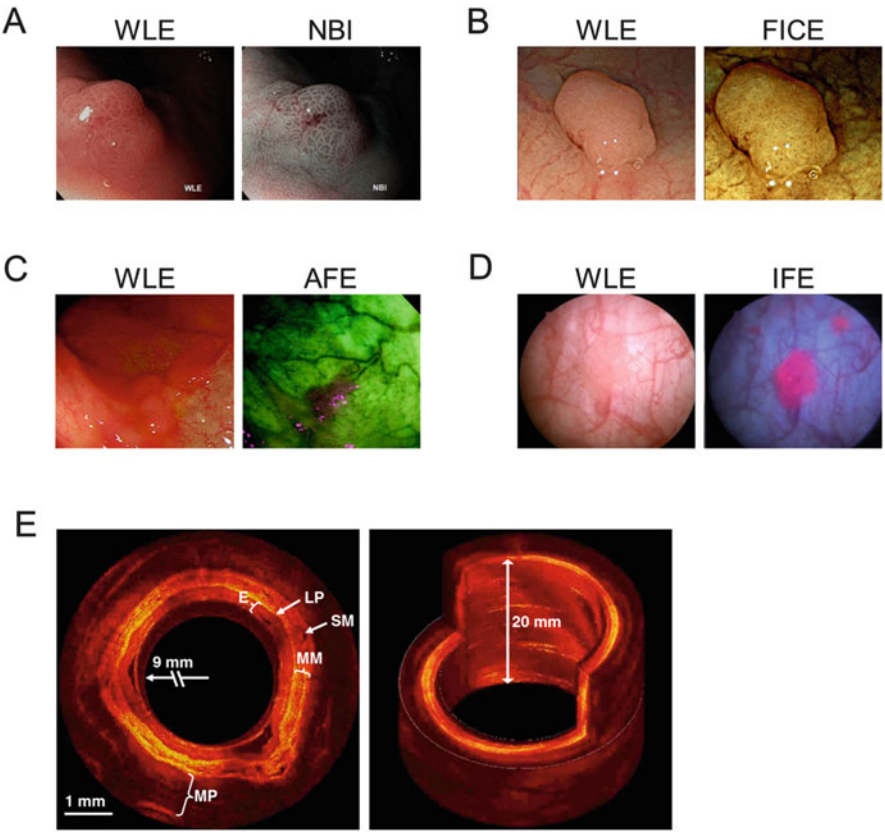

Fig. 1 (**a–d**) Comparison of endoscopic optical imaging modalities to conventional white light endoscopy (WLE). (**a**) An intestinal dysplasia imaged by WLE and narrowband imaging (NBI) [1]. (**b**) A neoplastic colon polyp imaged by WLE with and without Fuji Intelligent Chromo Endoscopy software (FICE) image post-processing [2]. (**c**) A colon adenoma imaged by WLE and autofluorescence imaging (AFE) [3]. (**d**) A papillary bladder lesion imaged in bladder cystoscopy with hexaminolevulinate by WLE and induced fluorescence endoscopy (IFE) [4]. (**e**) Example of 2D cross-sectional and 3D reconstructed images of a porcine esophagus imaged via optical coherence tomography (OCT), demonstrating micron-scale resolution of subsurface esophageal strata. Muscularis propria (MP), submucosae (SM), muscularis mucosae (MM), lamina propria (LP), and epithelium (E) can be identified [5]. Referenced figure panels have been adapted and reprinted with permission of their respective owners

shown improvement in detection of depressed-type gastric neoplastic lesions [9] but not in detection of adenomatous colon polyps [10].

Fluorescence Imaging Modalities Fluorescence imaging is an emerging and promising avenue for the present and future of clinical imaging, including in endoscopic applications. Analogous to WLE in visible-spectrum light imaging, the most widely used form of fluorescence imaging in endoscopic procedures is autofluorescence endoscopy (AFE). AFE endoscopes exploit differences in the

concentrations of naturally occurring fluorophore biomolecules, such as collagen, to generate wide-area images of internal tissues without exogenous contrast agents. Fluorescence excitation is provided by illumination with a high-intensity blue light on the endoscope; emission is visualized (via false color video) with an optical camera configured to capture light at various emission wavelengths. AFE imagery can provide information about abnormalities that may not be easily detectable with WLE, such as differences in tissue density, epithelial thickness, or blood flow rate (Fig. 1c). Though AFE systems can address some of the limitations of standard WLE, they are constrained by many of the same drawbacks. Furthermore, although AFE has been shown to improve detection rates of lesions, it also typically has a higher rate of false positives, such as in detection of early gastric neoplasia [11], necessitating more frequent follow-up biopsy analyses.

Analogous to white light chromoendoscopy, induced fluorescence endoscopy (IFE) relies upon administration of exogenous fluorescent contrast agents and illumination with excitatory wavelength light to visualize specific internal anatomy. IFE can provide enhancement of visual contrast beyond what is possible with WLE, chromoendoscopy, NBI, or AFI. Furthermore, the use of far-red or near-infrared fluorophores with IFE can increase the penetration depth of imaging and enable detection of non-superficial structures and lesions, overcoming a key limitation of other optical endoscopic technologies. However, this newer technology has not yet seen widespread clinical adoption, due mainly to the limited number of fluorescent contrast agents available to clinicians. Frequently used contrast agents in clinical IFE include 5-aminolevulinic acid (5-ALA) and hexaminolevulinate (for cancer detection in upper gastroendoscopy and bladder cystoscopy, respectively) and the near-infrared fluorophore indocyanine green (ICG, for enhanced fluorescent labeling of vasculature) (Fig. 1d). Another near-infrared fluorochrome, methylene blue, is FDA- and EMA-approved as a chromogenic dye; because it is also fluorescent, its use with IFE has been investigated to help surgeons locate and avoid injury to the ureters of colorectal surgery patients [12]. Additionally, IFE holds promise for endoscopic visualization of targeted molecular probes; however, this application has not yet been exploited clinically, due to the lack of targeted fluorescent contrast agents with regulatory approval.

Previously described visible-spectrum imaging modalities are applicable to either wide-area imaging (e.g., during open or laparoscopic surgery) or magnification endoscopy. However, with respect to fluorescence imaging, confocal laser endomicroscopy (CLEM) is the preeminent technology for fluorescent endoscopic examination under magnification. CLEM combines blue laser fluorescence imaging with intravital confocal microscopy, enabling live confocal plane imaging of endoluminar microanatomy at cellular or subcellular resolutions. This enables superior image quality, increased penetration depth, and improved anatomical differentiation when compared to conventional magnification endoscopy. The development of clinical CLEM technology confers two primary benefits to endoscopic diagnosis: first, in some instances, it may permit completely optical percutaneous biopsy of patients, negating the need for potentially traumatic tissue sample collection and outside histopathological analyses; second, in cases where traditional tissue biopsies

are still required, it can enable more accurate identification of relevant biopsy sites. A variety of contrast agents are used in CLEM, though all are currently used off-label for this application. Fluorescein is administered intravenously to provide fluorescent contrast to blood vasculature. Other contrast agents can be applied topically at the imaging site, which may or may not require prior removal of mucin from the surface. Topical imaging agents can include fluorescent stains to highlight intracellular regions and lamina propria (fluorescein sodium) or cell nuclei (cresyl violet or acriflavine). Additional fluorescent contrast agents with longer-wavelength excitation, such as methylene blue, have been demonstrated in preclinical research and could be used in future clinical work as well; however, currently, only scopes equipped with blue light lasers (488 nm) are approved for clinical use. The microscopic field of view of CLEM necessitates wide-area image-guided placement of the CLEM probe prior to image acquisition. Existing CLEM endoscopes usually rely on simultaneous wide-area WLE for correct placement of the microscopic probe at the lesion of interest. Therefore, the CLEM examination site selection is subject to the same limitations inherent to macroscopic WLE. However, other probe guidance methods have been used with CLEM, such as ultrasonography or X-ray fluoroscopy [13, 14].

Near-Infrared Imaging Modalities Beyond fluorescence imaging in the clinic, a new technique, optical coherence tomography (OCT), utilizes interferometry with near-infrared (NIR) light backscattering to construct a high-resolution image of three-dimensional tissues from a series of two-dimensional tomographic cross-sectional images. From an application point of view, OCT is similar in function to high-frequency ultrasonography; however, OCT relies on light rather than sound for generation of an image. Furthermore, the emitted near-infrared light is able to traverse air-filled spaces; unlike HF ultrasonography, it does not require direct probe contact (nor a water interface) with the tissue areas of interest. This makes it a useful imaging modality for mapping the surface and subsurface topology of large or expansive endoluminal cavities and therefore highly suited for endoscopic imaging. OCT scans can provide information on cutaneous and subcutaneous endoluminal surface density and morphology, enabling rapid wide-area identification of subsurface abnormalities. OCT endoscopes provide excellent spatial resolution, with sub-20 μm resolutions possible. OCT systems also provide temporal resolution by scanning multiple times per second, thus allowing acquisition and observation of images in real time. The primary benefit of OCT to clinical endoscopy comes in the ability to rapidly map the volumetric microstructure of large and complex endoluminal cavity surfaces (Fig. 1e). Though NIR provides improved light penetration into tissue compared to shorter wavelengths, the depth of OCT scanning is limited to a few millimeters due to excessive light scattering at greater depths. Endoscopic OCT has been clinically approved for upper GI endoscopic procedures and for intravascular endoscopy. It is also being evaluated for a variety of new indications, including diagnosis of urothelial carcinoma in the bladder [15], and imaging of bronchial airway remodeling in patients with chronic obstructive pulmonary disease [16]. A compact OCT endoscope housed within a small,

self-contained capsule-shaped module has been developed for esophageal OCT; the "capsule" is swallowed by a fully conscious patient and then recovered via a narrow tethering fiber. This development raises the possibility of esophageal endoscopy without the need for sedation, which is a significant barrier to early screening of Barrett's esophagus [17].

Multimodal Imaging Despite advances in imaging technology, all endoscopic imaging modalities are constrained by inherent physical or technical limitations which limit clinical usefulness. To overcome this, different imaging modalities could be combined together into a single endoscopic procedure, with the ultimate goal of mitigating the shortcomings in one imaging modality by supplementing it with others that are not subject to the same disadvantages. Aside from the use of wide-field WLE, which is routinely used in conjunction with other endoscopic modalities (e.g., to guide magnification endoscopy techniques such as CLEM), multimodal endoscopic imaging is mostly at the investigative stage. Several novel applications have been demonstrated in clinical pilot studies; for example, a trimodal endoscope was devised to combine WLE, NBI, and AFI to reduce the high false-positive rate associated with AFI colonoscopy in screening for colorectal adenomas and for gastric neoplasia [11, 18]; in another study, OCT was combined with WLE and IFE cystoscopy (with hexaminolevulinate) to reduce false positives in the diagnosis of urothelial carcinoma [15].

Preclinical Modality Pipeline A number of promising new optical imaging technologies are being evaluated for endoscopic applications.

Raman spectroscopy, an imaging technique which relies upon inelastic scattering of laser light to detect differences in vibrational or rotational molecular states, has been investigated for in vivo imaging systems, including endoscopy. Raman spectroscopy is particularly notable for its chemical specificity, which is useful for measuring biochemical states and changes in biological tissue. It can be combined with far-red or near-infrared light sources for deep tissue penetration. Though promising, Raman spectroscopic endoscopy and other Raman-based imaging methods thus far have faced technical obstacles, primarily due to the low intensity of inelastic light scattering signatures, which limit the accuracy and speed of image acquisition compared to existing clinical modalities. A variety of innovative Raman-based imaging technologies have been developed to overcome these limitations, such as selective-sampling Raman spectroscopy, coherent anti-Stokes Raman spectroscopy, surface-enhanced Raman spectroscopy, and spatially offset Raman spectroscopy. Endoscopic Raman spectroscopy has been evaluated in patient feasibility studies for a variety of applications, including colonoscopic identification of precancerous adenomatous polyps, endoscopic diagnosis of gastric dysplasia, and detection of nasopharyngeal cancers [19–21].

Cerenkov luminescence (CL), light emissions caused by the transit of charged particle radiation through a dielectric medium at greater than the speed of light, has been evaluated for medical imaging purposes. The resultant technology, called *Cerenkov luminescence imaging* (CLI), utilizes Cerenkov light generated by the decay of an injected β particle-emitting isotope, which are typically used to provide

radiocontrast in positron emission tomography (PET) scans or for targeted radiotherapy. CLI is adaptable to endoscopy for selected applications and could be useful for optical detection of radiotracers via an endoscope. A prototype CLI endoscope has been demonstrated in animal studies using conventional endoscopic equipment coupled with the PET radiotracer ^{18}F-fluorodeoxyglucose [22]. Further medical applications of CLI are discussed at length in the latter section of this review.

Incident light that is reflected by tissues is modified in numerous ways by the physical and biochemical properties of that tissue, which manifests in changes to absorbance via intensities of specific wavelengths, variation in angular trajectories, alteration of light polarity, etc. *Reflectance spectroscopy* takes advantage of these resultant differences, using advanced analysis to construct quantitative "scattering signatures" of reflected light to reveal morphological and biochemical information about probed tissues without labeling. For endoscopy, reflectance spectroscopy has several promising applications, most notably to detect the oxygenation level of blood. The ratio of oxyhemoglobin to deoxyhemoglobin can be extrapolated by the differential absorbance and reflectance profiles of each compound, providing an endoscopic tool for detection of poorly perfused regions in mucosal tissue. A white light reflectance spectroscopy method has been used to measure via colonoscopy to analyze the success of induced colon polyp ischemia procedures in real time, as well as identification of sites of mesenteric ischemia [23, 24].

Two-photon endomicroscopy (TPEM) is yet another emerging technology with potential to be translated into clinical endoscopy. Two-photon imaging utilizes two excitation photons using a femtosecond pulsed beam to produce fluorescent emission by excitation of individual atoms by two simultaneous photons. This method can utilize near-infrared excitation sources for deep tissue penetration. Furthermore, simultaneous absorbance of two photons is an extremely low-probability event outside of the focal point due to insufficient photon density; therefore, emission from outside the focal point is negligible. This permits exclusion of background light outside of the focal plane, but without the pinhole aperture required in confocal microscopy. TPEM is therefore a potentially advantageous alternative to CLEM, with acquisition of deeper images possible. Like CLEM, however, TPEM would require administration of fluorescent contrast agents. Prototype TPEM units have been demonstrated in animal models but thus far have not yet been evaluated in human patients [25, 26]. Clinical TPEM also requires further development and approval of fluorescent contrast agents which are optimized for two-photon excitation.

Summary Diagnostic endoscopic procedures are arguably the most commonly used and most diverse application of optical imaging in medicine today. Nearly every modality of optical imaging in current clinical use is represented in the array of endoscopic imaging technologies currently available to physicians. Furthermore, endoscopic procedures also have the largest frontier of technological advancement, with a number of novel advanced optical technologies at or near the clinical translation threshold.

3 Optical Imaging in Interventional Procedures

Beyond diagnostic procedures, optical imaging technologies are of increasing importance in current and future interventional medical techniques. For example, in oncology, surgery is the primary treatment modality for most solid tumors. Although optical imaging plays an essential role in cancer diagnosis and preoperative planning, during the surgery, the operating surgeon often depends on visual appearance and manual palpation to differentiate between tumor and normal tissue and to establish a sufficient tumor-free margin. Reliance on white light limits the visual contrast apparent to the surgeon to a narrow dynamic range in the colorimetric spectrum. Thus, limitations in specificity and sensitivity are a critical aspect of oncologic surgeries, and real-time image guidance is highly desirable in the operating room [27–29].

In this review, we explain the concept of optical image-guided surgery in surgical oncology. Image-guided surgery enables surgeons to perform surgery under the guidance of live intraoperative images, wherein surgeons are able to track the resection area on a monitor with reliable real-time feedback on any remaining tumor tissues or other diseased areas, such as ischemia. Because of the delicate nature and time sensitivity of surgery, the imaging time must be short, and image processing must be rapid – essentially in real time, at high temporal resolution and with minimal latency [30]. As a result, surgical procedures are easier to undertake with greater certainty that the critical landmarks are secured. Tumor cells left behind at the edge of the surgical resection area, defined as positive margins, result in increased recurrence and poor prognosis for patients with head and neck cancer, brain cancer, breast cancer, non-small cell lung cancer, colorectal cancer, and urogenital tract cancer [31–38]. Image guidance allows careful identification of primary and microscopic tumors and the complete removal of cancerous tissue [39].

Elevated cellular metabolism, increased expression of growth factor signaling receptors, hypoxia, and increased tumor angiogenesis are common traits that sustain the hyperproliferative potential of tumor cells. These biomarkers specific to cancer cells or the tumor microenvironment potentially allow cancer to be distinguished from normal tissue and could be exploited as potential targets to direct imaging agents [28]. An approach to incorporate biomarker-targeted molecular imaging agents in the imaging procedure improves the tumor-to-background signal ratio needed for fast assessment of lesions [30, 40]. Ease of image acquisition, relatively low-cost imaging devices, high resolution, and real-time applicability of imaging agents for use in optical imaging methods are highly desirable for use in real-time image-guided surgery [30]. However, there are substantial technical issues such as specific tumor labeling, imaging system portability, and patient-like animal models in which to develop the technology, which need to be addressed for image-guided surgery going forward toward clinical use [41].

Image-Guided Surgery Fluorescence-guided surgery emerged as a technique using fluorescence to visualize cancer cells to guide intraoperative procedures. Classical fluorescent techniques primarily use probes in the visible light spectrum

in the wavelength range of 400–600 nm. This spectrum region is related to a higher level of nonspecific background light and limited tissue penetration depth [28]. In the early years of this millennium, fluorescent imaging for cancer-specific navigation was successfully used in neurosurgery. Stummer et al. demonstrated that 5-ALA accumulates as fluorescent protoporphyrin IX in malignant gliomas and helps in their precise surgical resection. Complete resection of tumor tissue with maximal preservation of normal surrounding brain tissue significantly improved survival and life quality of glioblastoma patients (Fig. 2a) [45, 46].

To improve imaging depth with minimal interference of light scattering and tissue autofluorescence, optical modalities utilize fluorescent emission light in the NIR wavelengths of 700–900 nm, known as the first near-infrared window (NIR-I). Furthermore, fluorophores emitting in the range of 1,000–1,700 nm, in the second near-infrared window (NIR-II), were developed to enhance imaging quality at increased tissue depth [47, 48]. The NIR spectrum range allows a high ratio of signal to background in biological tissue and in oncologic imaging yields a high tumor-to-background ratio [30, 49]. Clinical applications of NIR fluorescence imaging have been demonstrated in sentinel lymph node (SLN) mapping, tumor imaging, and visualization of vasculature [50].

At present, clinically approved nontargeted contrast agents for image-guided surgery include ICG and methylene blue (Fig. 2b, c). Their fluorescence emission is localized within the NIR-I spectrum [28, 39]. Applications of ICG include induced NIR fluorescence in cancer-related surgery for SLN mapping, intraoperative identification of solid tumors, and angiography during reconstructive surgery [43] ICG-based imaging agents offer significant improvements during SLN mapping in prostate, breast, gastric, rectal, and vulvar cancers [51–55].

An integrated diagnostic approach based on premixing of ICG with ^{99m}Tc-nanocolloid resulted in an imaging agent that is both radioactive and fluorescent and enables preoperative and intraoperative SLN imaging in laparoscopic lymph node dissection. ICG-^{99m}Tc-nanocolloid injected into the prostate allowed the location of the pelvic sentinel lymph SLNs to be established preoperatively by SPECT/CT imaging. During surgery fluorescence was used to visualize previously identified nodes and improve surgical guidance. Correlation between the radioactive and fluorescent signal in the removed lymph nodes showed that ICG-^{99m}Tc-nanocolloid in combination with SPECT/CT and a fluorescence laparoscope can facilitate precise dissection of SLNs [51].

One of the greatest challenges for prostate cancer management is lymphatic spread of metastases, giving rise to tumor recurrences. Lymphatic mapping using radioguidance or fluorescence guidance in surgery via an agent targeting prostate-specific membrane antigen (PSMA) constitutes an alternative to traditional pelvic lymph node dissection. Preoperative PET imaging with ^{68}Ga-PSMA tracers was the most reliable method for identification of lymphatic macrometastases; by comparison, intraoperative lymphatic mapping with ICG-^{99m}Tc-nanocolloid via a fluorescence imaging camera combined with a handheld γ-ray probe was shown to be the most reliable for identifying micrometastases [56].

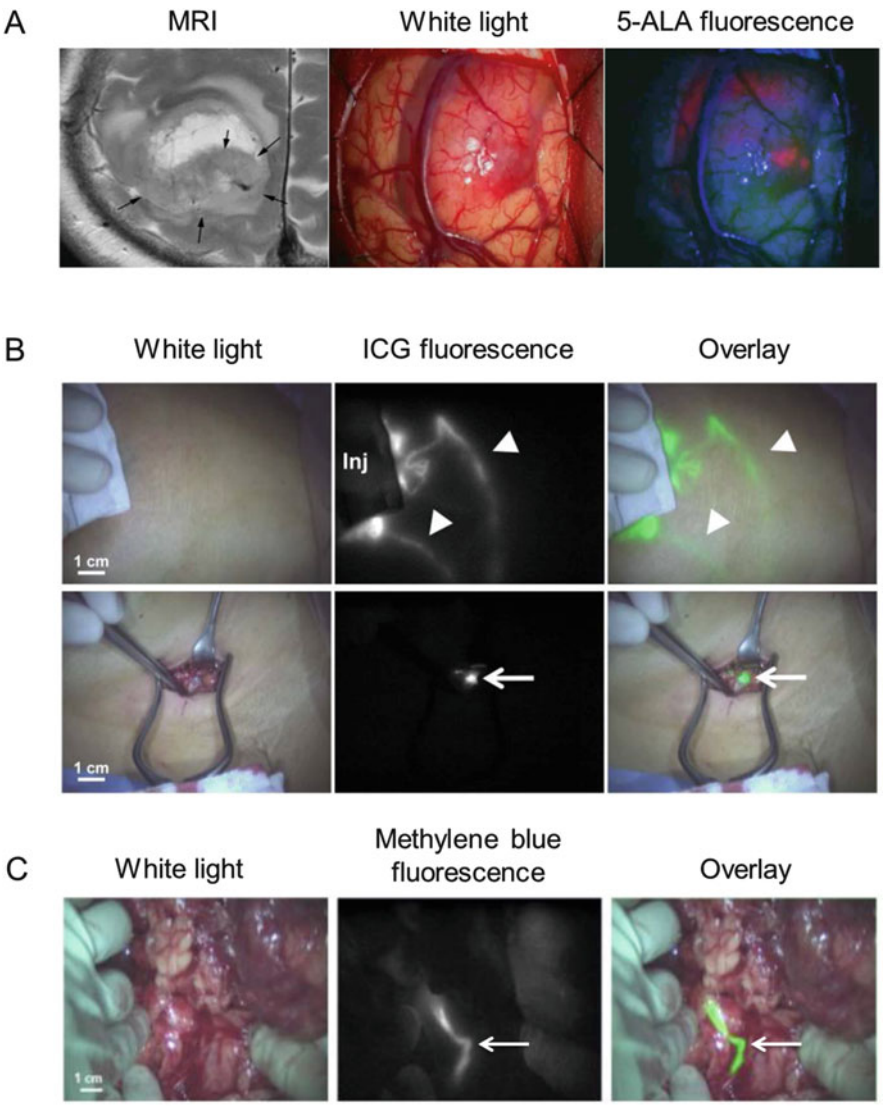

Fig. 2 Examples of intraoperative imaging for detection and guidance of surgical intervention. (**a**) Images from a glioblastoma patient. Left, an MRI scan of the tumor following 5-ALA administration. Arrows indicate a part of the tumor showing increase of signal following 5-ALA administration. Center and right, intraoperative images showing tumor contrast of the frontal lobe under white light and violet-blue excitation fluorescence, respectively [42]. (**b**) NIR fluorescence imaging of lymph node biopsy from a breast cancer patient following ICG injection during percutaneous assessment (upper row) and in exposed sentinel lymph node (lower row). NIR fluorescence light penetrates tissue, allowing noninvasive imaging method of lymph nodes and lymphatic flow [43]. (**c**) NIR fluorescence imaging of the ureter during abdominal surgery following intravenous administration of methylene blue [44]. Referenced figure panels have been adapted and reprinted with permission of their respective owners

Targeted contrast agents for intraoperative imaging include amino acids and peptides such as aminolevulinic acid, cyclic arginine-glycine-aspartate (cRGD), folate, chlorotoxin, and specific antibodies against antigens such as CA19-9, carcinoembryonic antigen (CEA), epithelial cell adhesion molecule (EPCAM), PSMA, and epidermal growth factor receptor (EGFR) [28, 39]. In organic probes, the NIR fluorophores are usually conjugated to a specific targeting ligand or monoclonal antibody. NIR agents target biomarkers expressed on certain types of cancers. Antibodies for imaging increased expression of growth factor receptors such as EGFR, Her2/neu receptor, or vascular endothelial growth factor (VEGF) receptor are labeled with Cyanine 5.5 and Alexa Fluor 750 fluorophores. Fluorophores bound to a specific ligand, e.g., VEGF or EGF, can be internalized, allowing uptake of the tracer to be monitored [28].

For imaging tumor angiogenesis, alpha-v-beta-3 ($\alpha_v\beta_3$) integrin, a well-characterized adhesion molecule found at the sprouting ends of newly formed blood vessels, can easily be targeted with molecular probes. For this reason, it has been used to model targeting of agents to tumors. High expression of adhesion receptors can be detected when targeting $\alpha_v\beta_3$ integrin with cRGD conjugated to Cyanine 5.5 or IRdye800CW [28]. Previous studies demonstrated that integrin $\alpha_v\beta_3$ or CD13 molecules, overexpressed specifically on the surfaces of endothelial or tumor cells, can serve as imaging targets for early tumor detection and NIR fluorescence-guided surgical navigation in glioblastomas [49, 57, 58].

Similar approaches using activatable fluorophores are followed when targeting the upregulation of tumor-associated proteolytic enzymes such as cathepsins and matrix metalloproteinases (MMP). This allows detection of proteases abundant in malignant tissue, which can be associated with specific invasive, aggressive, or metastatic characteristics of tumors. However, proteolytic enzymes are not specific for molecules in cancer cells, because cathepsins and matrix metalloproteinases are abundant in inflammatory tissue. NIR probes activated by proteases such as Cathepsin B and MMP-2 were injected in an inactivated state (quenched), and cleaved by enzymes that result in dequenching and increased fluorescence [28, 59].

Summary Integration of optical imaging in intraoperative guidance is necessary to improve the surgical accuracy and outcomes of clinical cancer surgery.

4 Cerenkov Luminescence Imaging and Therapy

Cerenkov Luminescence Cerenkov luminescence (CL) or Cerenkov radiation is a continuous spectrum of light peaking in the blue-to-ultraviolet spectrum. It is produced by subatomic charged particles traveling faster than the speed of light through a dielectric medium such as water or biological tissues. CL was discovered in 1934, but it was first recognized for biomedical research applications in 2009 due to advances in highly sensitive optical cameras [60, 61]. Since then, the applications of CL from clinically relevant radionuclides have been expanding to biomedical

imaging as well as cancer imaging and therapy. Cerenkov luminescence imaging (CLI) is a new medical imaging modality that captures CL emitted from clinically relevant radionuclides via optical imaging instruments and allows multimodal imaging in combination with positron emission tomography (PET) imaging. Further, CL has been applied with nanomaterials, small molecules, and biomolecules for better imaging and therapy in cancer research. This section covers the basics of CL and the recent advances of CLI for diagnosis of disease as well as its applications to cancer therapies.

In 1934, the Russian scientist Pavel Alekseyevich Cerenkov observed faint blue light when he accidentally placed a sulfuric acid solution over radium salts [62]. He concluded the observed visible light was produced by charged subatomic particles traveling faster than the phase velocity of light in a dielectric medium [63]. Further theoretical studies were conducted by Ilya Frank and Igor Tamm, who described the significance of particle energy, cone angle of emitted light, and refractive index of media. In 1958, Cerenkov, Frank, and Tamm were awarded the Nobel Prize in Physics for their discovery and explanation of the Cerenkov effect.

Positrons and electrons, collectively referred to as charged beta (β) particles, are produced by radioactive decay. In dielectric media (mainly tissue/water in biomedical contexts), β particles are traveling faster than the phase velocity of light. Charged β particles with high energy interact with surrounding water and polarize the randomly oriented water molecules. The polarized water molecules then relax to the ground state by emitting photons in the direction of the charged particle travel, creating a coherent wavefront [61]. The photons propagate at a forward angle (θ) from the direction of the charged particle vector.

Cerenkov Luminescence Imaging The Cerenkov phenomenon has been applied in the fields of physics and engineering in a variety of applications, such as in detectors for particle physics and nuclear power plants [64]. In 2009, the first biomedical imaging application of the Cerenkov phenomenon was reported by Robertson et al. who described Cerenkov luminescence imaging (CLI), using ^{18}F-fluorodeoxyglucose (^{18}F-FDG) in vivo imaged with widely used optical instrumentation for bioluminescence imaging, which provides the necessary sensitivity [60]. This study set the foundation of CLI, and biomedical applications of CLI have been rapidly expanding ever since. CLI provides a quantitative multimodal imaging system in conjunction with positron emission tomography (PET) and could be advantageous over the conventional imaging modalities in the clinic in terms of cost, time, and applicability of radionuclides (Fig. 3a, b). Some preclinical studies for CLI have been reported using clinically relevant radionuclides including ^{18}F, ^{89}Zr, ^{90}Y, ^{68}Ga, and ^{225}Ac [65, 67].

CLI for experimental imaging in small animals utilizes a bioluminescence imaging system equipped with a charged coupled device (CCD) camera in a chamber to exclude ambient light [68]. ^{18}F-FDG, a radiotracer for glycolytic metabolism, is one of the most common radiotracers for PET imaging because it preferentially accumulates in cancer cells [69]. CL from ^{18}F-FDG has been shown to strongly correlate with signal intensity in PET imaging [70]. In addition to small-molecule

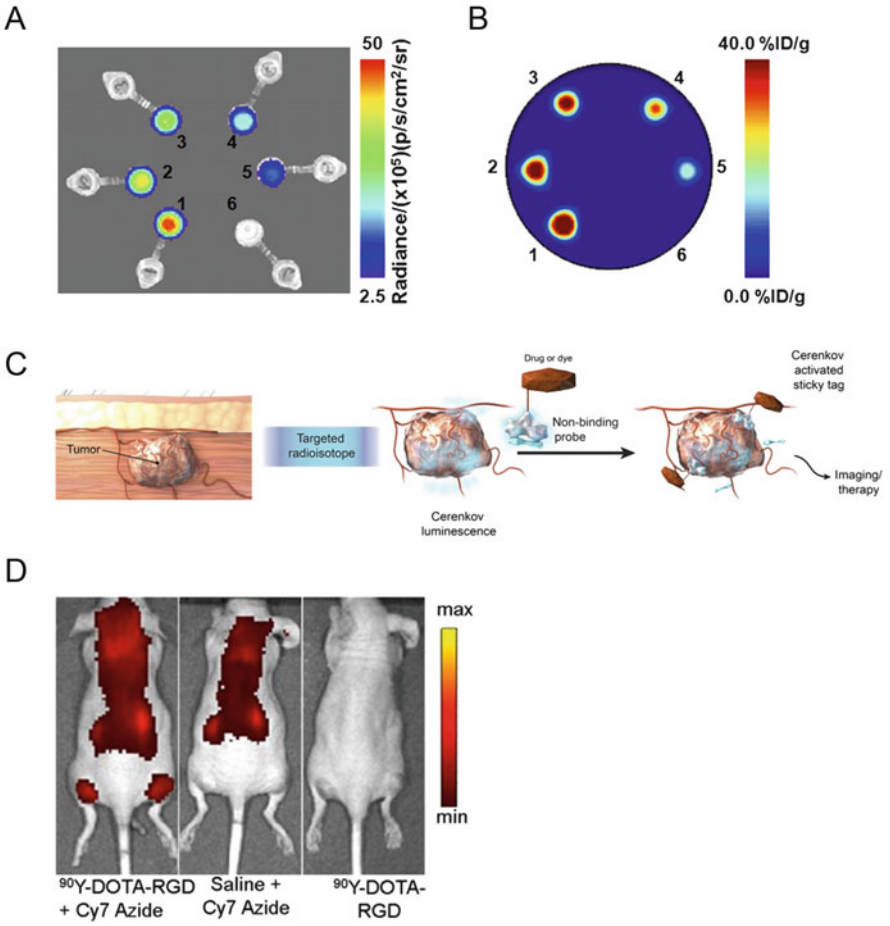

Fig. 3 (**a**) Cerenkov luminescence imaging and (**b**) PET imaging of ^{89}Zr in water. The activity concentrations of ^{89}Zr decrease sequentially in samples 1–6, ranging from 40.3 kBq/mL in sample 1 to 0.0 kBq/mL in sample 6 [65]. (**c**) Schematic of CL-activated "sticky tag" technology [66]. (**d**) Fluorescence image of mice injected with Cyanine 7-azide following previous administration of the $\alpha_v\beta_3$-integrin-binding radiotracer ^{90}Y-DOTA-RGD. Enrichment of Cyanine 7 signal can be observed in the $\alpha_v\beta_3$-integrin-expressing tumors on the left and right rear flanks due to activation of the azide group "sticky tag" by CL [66]. Referenced figure panels have been adapted and reprinted with permission of their respective owners

radiotracers, CLI with biomolecule radiotracers such as peptides and antibodies has also been reported. For example, a gastrin-releasing peptide receptor, or bombesin receptor, agonist was labeled with ^{90}Y and enabled imaging of prostate tumors in mice by CLI [71]. Further, the anti-prostate-specific membrane antigen (PSMA) antibody labeled with ^{64}Cu was shown to visualize PSMA-positive tumors in mice by both CLI and PET [72].

In addition to small molecules and biomolecules, CLI is also compatible with in vivo imaging of nanoparticles. Nanoparticles have gathered much attention in biomedical research because of their unique properties, including ease of preparations and modifications, and better pharmacological properties than some conventional chemotherapeutic agents. Some nanoparticles are excitable by Cerenkov light and emit in longer wavelengths. The imaging system utilizing this phenomenon is called synonymously secondary Cerenkov-induced fluorescence imaging (SCIFI) or Cerenkov radiation energy transfer (CRET). The higher optical cross section of certain nanoparticles sometimes permits SCIFI or CRET [61]. For example, quantum nanoparticles (Qtracker 705) and quantum dots (QD605) have been shown to be excited by CL to emit longer wavelengths of light, which is advantageous to overcome the poor tissue permeability of UV light [63, 73]. However, the system of SCIFI or CRET is not easily modulated because it can be activated regardless of the surrounding environment. Hence, smart activatable agents, which could be modulated by endogenous or exogenous stimuli when needed, may provide the basis of a more accurate imaging system. Photoactivation of caged luciferin by CL is one example of a smart activatable agent [74]. Luciferin is caged by an orthonitrobenzyl ether protecting group, which is known to be activated by UV light. CL from ^{18}F-FDG successfully uncaged luciferin, the substrate of luciferase, and induced bioluminescence from cancer cells expressing luciferase. Another example of smart activatable agent is protease-activatable SCIFI, which can be turned on by matrix metallopeptidase-2 enzyme activity [75]. Fluorescein is tethered with a peptide to a gold nanoparticle and quenched due to the proximity of fluorescein and a gold nanoparticle; once the enzyme cleaves the peptide, the gold nanoparticle quencher is released and fluorescein becomes excitable by CL.

The major limitation of CLI is its low intensity of signal compared to conventional optical fluorescence imaging. The prolonged scanning time degrades image quality due to confounding factors such as patient movement, and the duration of imaging is limited because of the radionuclide half-life. The CL-activated "sticky tag" strategy may potentially overcome these limitations by translating CL into fluorescence (Fig. 3c) [76]. The sticky tag consists of a fluorescent dye tethered by an aryl azide group. UV light irradiation from Cerenkov transforms the azide into a singlet nitrene, which can be chemically incorporated into biomolecules on cellular plasma membranes or proteins in the intracellular matrix. Therefore, radioactivity, from, e.g., ^{18}F-FDG or an ^{89}Zr-labeled antibody, is converted to fluorescence that is attached to the side of the radioactive decay. The photoactivation of Cyanine 7-azide is demonstrated in both in vitro and in vivo (Fig. 3d).

The first human CLI was performed in 2013. CL with 550 MBq of ^{131}I from the thyroid gland of a patient treated for hyperthyroidism was detected using an electron multiplied CCD camera [77]. In this study, photographic light and CL were successfully localized in the thyroid region. However, the first human study did not provide quantification of the thyroid. A more rigorous study was performed in the same year using ^{18}F-FDG in lymphoma patients, lung cancer, and breast cancer [78]. Patients undergoing diagnostic ^{18}F-FDG PET/CT scans were tested for the feasibility of CLI. A cooled CCD camera was used to monitor CL and quantification

was implemented. The study demonstrated the linear correlation between the activity of radionuclides and the intensity of CL and also showed that the diagnostic dose of ^{18}F-FDG is feasible for detecting nodal disease by CLI.

Cerenkov-Induced Therapy The applications of CL have also been rapidly expanding to cancer therapy. Photodynamic therapy (PDT) utilizes photosensitizers, which absorb light and produce reactive oxygen species (ROS) to kill cancerous cells. Conventional PDT uses red-to-infrared light from external light sources to excite the photosensitizers. Because the tissue permeability of light is poor, the light source needs to be delivered to the deep tumor site by insertion of fiber optics into the patient's body. This invasive approach could be avoided by CL-induced PDT. Photosensitizers in proximity to clinically relevant radionuclides may be excitable by CL, resulting in localized cytotoxic ROS generation. It was demonstrated that CL generated by ^{90}Y excites porphyrin, a photosensitizer, and inhibits cell growth [79]. Furthermore, nanoparticles have shown some promising results as a part of CL-based PDT strategies. For example, it was demonstrated that titanium dioxide could be excited by CL and generate ROS from water and oxygen molecules. Further, titanium dioxide in the presence of ^{18}F-FDG or ^{64}Cu could induce PDT in vivo [80]. In addition to titanium dioxide, some other nanoparticles have also been reported to induce PDT such as chlorin e6 nanoparticles and copper sulfide nanoparticles [81, 82].

Summary Cerenkov luminescence has garnered great attention in both science and medicine since the first biomedical application of CL was reported in 2009. CL provides an easy-to-prepare and cost-effective imaging modality. Because CL is generated by most PET imaging radiotracers, multimodal imaging with both CLI and PET may be possible. CL combined with small molecules, biomolecules, and nanoparticles has been studied to improve in vivo radiotracer tracking capabilities. Further, a new targeted therapeutic paradigm that selectively kills only cells in proximity to CL-generating radiotracers may be accomplished with CL. CL-induced PDT may provide a less invasive approach compared to the conventional PDT in the clinic. However, there are some limitations that must be overcome, such as the weak intensity of CL and prolonged exposure to high dose of radionuclides. Therefore, further development of this field is needed before clinical relevance can be achieved.

Compliance with Ethical Standards

Conflict of Interest: Evan P. Stater declares that he has no conflict of interest. Magdalena Skubal declares that she has no conflict of interest. Ryo Tamura declares that he has no conflict of interest. Jan Grimm declares that he has no conflict of interest.

Ethical Approval: This chapter does not contain any studies with human participants or animals performed by any of the authors.

Funding: Not applicable.

Informed Consent: Informed consent was obtained from all individual participants included in referenced studies.

References

1. Capelle LG, Haringsma J, de Vries AC, Steyerberg EW, Biermann K, van Dekken H, Kuipers EJ (2010) Narrow band imaging for the detection of gastric intestinal metaplasia and dysplasia during surveillance endoscopy. Dig Dis Sci 55(12):3442–3448
2. Yoshida N, Naito Y, Inada Y, Kugai M, Inoue K, Uchiyama K, Handa O, Takagi T, Konishi H, Yagi N et al (2012) The detection of surface patterns by flexible spectral imaging color enhancement without magnification for diagnosis of colorectal polyps. Int J Color Dis 27 (5):605–611
3. Sato R, Fujiya M, Watari J, Ueno N, Moriichi K, Kashima S, Maeda S, Ando K, Kawabata H, Sugiyama R et al (2011) The diagnostic accuracy of high-resolution endoscopy, autofluorescence imaging and narrow-band imaging for differentially diagnosing colon adenoma. Endoscopy 43(10):862–868
4. Chang TC, Marcq G, Kiss B, Trivedi DR, Mach KE, Liao JC (2017) Image-guided transurethral resection of bladder tumors – current practice and future outlooks. Bladder Cancer 3 (3):149–159
5. Fu HL, Leng Y, Cobb MJ, Hsu K, Hwang JH, Li X (2008) Flexible miniature compound lens design for high-resolution optical coherence tomography balloon imaging catheter. J Biomed Opt 13(6):060502
6. Kang HS, Hong SN, Kim YS, Park HS, Kim BK, Lee JH, Kim SI, Lee TY, Kim JH, Lee SY et al (2013) The efficacy of i-SCAN for detecting reflux esophagitis: a prospective randomized controlled trial. Dis Esophagus 26(2):204–211
7. Li CQ, Li Y, Zuo XL, Ji R, Li Z, Gu XM, Yu T, Qi QQ, Zhou CJ, Li YQ (2013) Magnified and enhanced computed virtual chromoendoscopy in gastric neoplasia: a feasibility study. World J Gastroenterol 19(26):4221–4227
8. Basford PJ, Longcroft-Wheaton G, Higgins B, Bhandari P (2014) High-definition endoscopy with i-SCAN for evaluation of small colon polyps: the HiSCOPE study. Gastrointest Endosc 79(1):111–118
9. Osawa H, Yamamoto H, Miura Y, Ajibe H, Shinhata H, Yoshizawa M, Sunada K, Toma S, Satoh K, Sugano K (2012) Diagnosis of depressed-type early gastric cancer using small-caliber endoscopy with flexible spectral imaging color enhancement. Dig Endosc 24(4):231–236
10. Aminalai A, Rosch T, Aschenbeck J, Mayr M, Drossel R, Schroder A, Scheel M, Treytnar D, Gauger U, Stange G et al (2010) Live image processing does not increase adenoma detection rate during colonoscopy: a randomized comparison between FICE and conventional imaging (Berlin Colonoscopy Project 5, BECOP-5). Am J Gastroenterol 105(11):2383–2388
11. Kato M, Kaise M, Yonezawa J, Goda K, Toyoizumi H, Yoshimura N, Yoshida Y, Kawamura M, Tajiri H (2009) Trimodal imaging endoscopy may improve diagnostic accuracy of early gastric neoplasia: a feasibility study. Gastrointest Endosc 70(5):899–906
12. Barnes TG, Hompes R, Birks J, Mortensen NJ, Jones O, Lindsey I, Guy R, George B, Cunningham C, Yeung TM (2018) Methylene blue fluorescence of the ureter during colorectal surgery. Surg Endosc 32(9):4036–4043
13. Karstensen JG, Cartana T, Constantinescu C, Dumitrascu S, Kovacevic B, Klausen P, Hassan H, Klausen TW, Bertani H, Bhutani MS et al (2018) Endoscopic ultrasound guided needle-based confocal laser endomicroscopy in solid pancreatic masses – a prospective validation study. Endosc Int Open 6(1):E78–E85
14. Meining A, Chen YK, Pleskow D, Stevens P, Shah RJ, Chuttani R, Michalek J, Slivka A (2011) Direct visualization of indeterminate pancreaticobiliary strictures with probe-based confocal laser endomicroscopy: a multicenter experience. Gastrointest Endosc 74(5):961–968
15. Schmidbauer J, Remzi M, Klatte T, Waldert M, Mauermann J, Susani M, Marberger M (2009) Fluorescence cystoscopy with high-resolution optical coherence tomography imaging as an adjunct reduces false-positive findings in the diagnosis of urothelial carcinoma of the bladder. Eur Urol 56(6):914–919

16. Ding M, Chen Y, Guan WJ, Zhong CH, Jiang M, Luo WZ, Chen XB, Tang CL, Tang Y, Jian QM et al (2016) Measuring airway remodeling in patients with different COPD staging using endobronchial optical coherence tomography. Chest 150(6):1281–1290
17. Gora MJ, Simmons LH, Queneherve L, Grant CN, Carruth RW, Lu W, Tiernan A, Dong J, Walker-Corkery B, Soomro A et al (2016) Tethered capsule endomicroscopy: from bench to bedside at a primary care practice. J Biomed Opt 21(10):104001
18. Rotondano G, Bianco MA, Sansone S, Prisco A, Meucci C, Garofano ML, Cipolletta L (2012) Trimodal endoscopic imaging for the detection and differentiation of colorectal adenomas: a prospective single-centre clinical evaluation. Int J Color Dis 27(3):331–336
19. Bergholt MS, Lin K, Wang J, Zheng W, Xu H, Huang Q, Ren JL, Ho KY, Teh M, Srivastava S et al (2016) Simultaneous fingerprint and high-wavenumber fiber-optic Raman spectroscopy enhances real-time in vivo diagnosis of adenomatous polyps during colonoscopy. J Biophotonics 9(4):333–342
20. Wang J, Lin K, Zheng W, Ho KY, Teh M, Yeoh KG, Huang Z (2015) Comparative study of the endoscope-based bevelled and volume fiber-optic Raman probes for optical diagnosis of gastric dysplasia in vivo at endoscopy. Anal Bioanal Chem 407(27):8303–8310
21. Ming LC, Gangodu NR, Loh T, Zheng W, Wang J, Lin K, Zhiwei H (2017) Real time near-infrared Raman spectroscopy for the diagnosis of nasopharyngeal cancer. Oncotarget 8 (30):49443–49450
22. Kothapalli SR, Liu H, Liao JC, Cheng Z, Gambhir SS (2012) Endoscopic imaging of Cerenkov luminescence. Biomed Opt Express 3(6):1215–1225
23. Friedland S, Benaron D, Parachikov I, Soetikno R (2003) Measurement of mucosal capillary hemoglobin oxygen saturation in the colon by reflectance spectrophotometry. Gastrointest Endosc 57(4):492–497
24. Friedland S, Benaron D, Coogan S, Sze DY, Soetikno R (2007) Diagnosis of chronic mesenteric ischemia by visible light spectroscopy during endoscopy. Gastrointest Endosc 65(2):294–300
25. Meng G, Liang Y, Sarsfield S, Jiang WC, Lu R, Dudman JT, Aponte Y, Ji N (2019) High-throughput synapse-resolving two-photon fluorescence microendoscopy for deep-brain volumetric imaging in vivo. elife 8
26. Bocarsly ME, Jiang WC, Wang C, Dudman JT, Ji N, Aponte Y (2015) Minimally invasive microendoscopy system for in vivo functional imaging of deep nuclei in the mouse brain. Biomed Opt Express 6(11):4546–4556
27. Weissleder R, Pittet MJ (2008) Imaging in the era of molecular oncology. Nature 452 (7187):580–589
28. Keereweer S, Kerrebijn JD, van Driel PB, Xie B, Kaijzel EL, Snoeks TJ, Que I, Hutteman M, van der Vorst JR, Mieog JS et al (2011) Optical image-guided surgery – where do we stand? Mol Imaging Biol 13(2):199–207
29. Rosenthal EL, Warram JM, de Boer E, Basilion JP, Biel MA, Bogyo M, Bouvet M, Brigman BE, Colson YL, DeMeester SR et al (2016) Successful translation of fluorescence navigation during oncologic surgery: a consensus report. J Nucl Med 57(1):144–150
30. Mondal SB, Gao S, Zhu N, Liang R, Gruev V, Achilefu S (2014) Real-time fluorescence image-guided oncologic surgery. Adv Cancer Res 124:171–211
31. Haque R, Contreras R, McNicoll MP, Eckberg EC, Petitti DB (2006) Surgical margins and survival after head and neck cancer surgery. BMC Ear Nose Throat Disord 6:2
32. Eldeeb H, Macmillan C, Elwell C, Hammod A (2012) The effect of the surgical margins on the outcome of patients with head and neck squamous cell carcinoma: single institution experience. Cancer Biol Med 9(1):29–33
33. Pirro V, Alfaro CM, Jarmusch AK, Hattab EM, Cohen-Gadol AA, Cooks RG (2017) Intraoperative assessment of tumor margins during glioma resection by desorption electrospray ionization-mass spectrometry. Proc Natl Acad Sci U S A 114(26):6700–6705
34. Sawabata N, Ohta M, Matsumura A, Nakagawa K, Hirano H, Maeda H, Matsuda H, Thoracic Surgery Study Group of Osaka U (2004) Optimal distance of malignant negative margin in excision of nonsmall cell lung cancer: a multicenter prospective study. Ann Thorac Surg 77 (2):415–420

35. Nagtegaal ID, Quirke P (2008) What is the role for the circumferential margin in the modern treatment of rectal cancer? J Clin Oncol 26(2):303–312
36. Dotan ZA, Kavanagh K, Yossepowitch O, Kaag M, Olgac S, Donat M, Herr HW (2007) Positive surgical margins in soft tissue following radical cystectomy for bladder cancer and cancer specific survival. J Urol 178(6):2308–2312. discussion 2313
37. Reyna C, DeSnyder SM (2018) Intraoperative margin assessment in breast cancer management. Surg Oncol Clin N Am 27(1):155–165
38. Hong X, Li T, Ling F, Yang D, Hou L, Li F, Tan W (2017) Impact of surgical margin status on the outcome of bladder cancer treated by radical cystectomy: a meta-analysis. Oncotarget 8 (10):17258–17269
39. Nguyen QT, Tsien RY (2013) Fluorescence-guided surgery with live molecular navigation – a new cutting edge. Nat Rev Cancer 13(9):653–662
40. Wang C, Wang Z, Zhao T, Li Y, Huang G, Sumer BD, Gao J (2018) Optical molecular imaging for tumor detection and image-guided surgery. Biomaterials 157:62–75
41. Hiroshima Y, Maawy A, Metildi CA, Zhang Y, Uehara F, Miwa S, Yano S, Sato S, Murakami T, Momiyama M et al (2014) Successful fluorescence-guided surgery on human colon cancer patient-derived orthotopic xenograft mouse models using a fluorophore-conjugated anti-CEA antibody and a portable imaging system. J Laparoendosc Adv Surg Tech A 24(4):241–247
42. Yamamoto J, Kakeda S, Yoneda T, Ogura SI, Shimajiri S, Tanaka T, Korogi Y, Nishizawa S (2017) Improving contrast enhancement in magnetic resonance imaging using 5-aminolevulinic acid-induced protoporphyrin IX for high-grade gliomas. Oncol Lett 13(3):1269–1275
43. Schaafsma BE, Mieog JS, Hutteman M, van der Vorst JR, Kuppen PJ, Lowik CW, Frangioni JV, van de Velde CJ, Vahrmeijer AL (2011) The clinical use of indocyanine green as a near-infrared fluorescent contrast agent for image-guided oncologic surgery. J Surg Oncol 104 (3):323–332
44. Verbeek FP, van der Vorst JR, Schaafsma BE, Swijnenburg RJ, Gaarenstroom KN, Elzevier HW, van de Velde CJ, Frangioni JV, Vahrmeijer AL (2013) Intraoperative near infrared fluorescence guided identification of the ureters using low dose methylene blue: a first in human experience. J Urol 190(2):574–579
45. Stummer W, Novotny A, Stepp H, Goetz C, Bise K, Reulen HJ (2000) Fluorescence-guided resection of glioblastoma multiforme by using 5-aminolevulinic acid-induced porphyrins: a prospective study in 52 consecutive patients. J Neurosurg 93(6):1003–1013
46. Stummer W, Pichlmeier U, Meinel T, Wiestler OD, Zanella F, Reulen HJ, Group AL-GS (2006) Fluorescence-guided surgery with 5-aminolevulinic acid for resection of malignant glioma: a randomised controlled multicentre phase III trial. Lancet Oncol 7(5):392–401
47. Shou K, Qu C, Sun Y, Chen H, Chen S, Zhang L, Xu H, Hong X, Yu A, Cheng Z (2017) Multifunctional biomedical imaging in physiological and pathological conditions using a NIR-II probe. Adv Funct Mater 27(23):1700995
48. Antaris AL, Chen H, Cheng K, Sun Y, Hong G, Qu C, Diao S, Deng Z, Hu X, Zhang B et al (2016) A small-molecule dye for NIR-II imaging. Nat Mater 15(2):235–242
49. Liu Y, Wang Z, Li X, Ma X, Wang S, Kang F, Yang W, Ma W, Wang J (2019) Near-infrared fluorescent peptides with high tumor selectivity: novel probes for image-guided surgical resection of orthotopic glioma. Mol Pharm 16:108–117
50. Vahrmeijer AL, Hutteman M, van der Vorst JR, van de Velde CJ, Frangioni JV (2013) Image-guided cancer surgery using near-infrared fluorescence. Nat Rev Clin Oncol 10(9):507–518
51. van der Poel HG, Buckle T, Brouwer OR, Valdes Olmos RA, van Leeuwen FW (2011) Intraoperative laparoscopic fluorescence guidance to the sentinel lymph node in prostate cancer patients: clinical proof of concept of an integrated functional imaging approach using a multimodal tracer. Eur Urol 60(4):826–833
52. Mieog JS, Troyan SL, Hutteman M, Donohoe KJ, van der Vorst JR, Stockdale A, Liefers GJ, Choi HS, Gibbs-Strauss SL, Putter H et al (2011) Toward optimization of imaging system and lymphatic tracer for near-infrared fluorescent sentinel lymph node mapping in breast cancer. Ann Surg Oncol 18(9):2483–2491

53. Vuijk FA, Hilling DE, Mieog JSD, Vahrmeijer AL (2018) Fluorescent-guided surgery for sentinel lymph node detection in gastric cancer and carcinoembryonic antigen targeted fluorescent-guided surgery in colorectal and pancreatic cancer. J Surg Oncol 118(2):315–323
54. Handgraaf HJ, Boogerd LS, Verbeek FP, Tummers QR, Hardwick JC, Baeten CI, Frangioni JV, van de Velde CJ, Vahrmeijer AL (2016) Intraoperative fluorescence imaging to localize tumors and sentinel lymph nodes in rectal cancer. Minim Invasive Ther Allied Technol 25(1):48–53
55. Verbeek FP, Tummers QR, Rietbergen DD, Peters AA, Schaafsma BE, van de Velde CJ, Frangioni JV, van Leeuwen FW, Gaarenstroom KN, Vahrmeijer AL (2015) Sentinel lymph node biopsy in vulvar cancer using combined radioactive and fluorescence guidance. Int J Gynecol Cancer 25(6):1086–1093
56. van Leeuwen FWB, Winter A, van Der Poel HG, Eiber M, Suardi N, Graefen M, Wawroschek F, Maurer T (2019) Technologies for image-guided surgery for managing lymphatic metastases in prostate cancer. Nat Rev Urol 16:159–171
57. Jain RK, Duda DG, Willett CG, Sahani DV, Zhu AX, Loeffler JS, Batchelor TT, Sorensen AG (2009) Biomarkers of response and resistance to antiangiogenic therapy. Nat Rev Clin Oncol 6 (6):327–338
58. Ribatti D, Ranieri G, Basile A, Azzariti A, Paradiso A, Vacca A (2012) Tumor endothelial markers as a target in cancer. Expert Opin Ther Targets 16(12):1215–1225
59. Mahmood U, Weissleder R (2003) Near-infrared optical imaging of proteases in cancer. Mol Cancer Ther 2(5):489–496
60. Robertson R (2009) Optical imaging of Cerenkov light generation from positron-emitting radiotracers. Phys Med Biol 54:N355–N365
61. Shaffer TM, Pratt EC, Grimm J (2017) Utilizing the power of Cerenkov light with nanotechnology. Nat Nanotechnol 12:106–117
62. Bolotovskii BM (2009) Vavilov – Cherenkov radiation: its discovery and application. Physics-Uspekhi 52:1099–1110
63. Das S, Thorek DLJ, Grimm J (2014) Cerenkov imaging. Adv Cancer Res 124:213–234
64. Thorek DLJ, Robertson R, Bacchus WA, Hahn J, Rothberg J, Beattie BJ, Grimm J (2012) Cerenkov imaging – a new modality for molecular imaging. Am J Nucl Med Mol Imaging 2:163–173
65. Ruggiero A, Holland JP, Lewis JS, Grimm J (2010) Cerenkov luminescence imaging of medical isotopes. J Nucl Med 51:1123–1130
66. Das S, Haedicke K, Grimm J (2018) Cerenkov-activated sticky tag for in vivo fluorescence imaging. J Nucl Med 59(1):58–65
67. Pratt EC, Shaffer TM, Grimm J (2016) Nanoparticles and radiotracers: advances toward radionanomedicine. WIREs Nanomed Nanobiotechnol 8:872–890
68. Tamura R, Pratt EC, Grimm J (2018) Innovations in nuclear imaging instrumentation: Cerenkov imaging. Semin Nucl Med 48:359–366
69. Calvaresi EC, Hergenrother PJ (2013) Glucose conjugation for the specific targeting and treatment of cancer. Chem Sci 4:2319–2333
70. Liu H, Ren G, Miao Z, Zhang X, Tang X, Han P, Sanjiv S (2010) Molecular optical imaging with radioactive probes. PLoS One 5:e9470
71. Lohrmann C, Zhang H, Thorek DLJ, Desai P, Zanzonico PB, O'Donoghue J, Irwin CP, Reiner T, Grimm J, Weber WA (2015) Cerenkov luminescence imaging for radiation dose calculation of a 90y-labeled gastrin-releasing peptide receptor antagonist. J Nucl Med 56 (5):805–811
72. D'Souza JW, Hensley H, Doss M, Beigarten C, Torgov M, Olafsen T, Yu JQ, Robinson MK (2017) Cerenkov luminescence imaging as a modality to evaluate antibody-based pet radiotracers. J Nucl Med 58(1):175–180
73. Dothager RS, Goiffon RJ, Jackson E, Harpstrite S, Piwnica-Worms D (2010) Cerenkov radiation energy transfer (CRET) imaging: a novel method for optical imaging of pet isotopes in biological systems. PLoS One 5(10):e13300

74. Ran C, Zhang Z, Hooker J, Moore A (2012) In vivo photoactivation without "light": use of Cherenkov radiation to overcome the penetration limit of light. Mol Imaging Biol 14:156–162
75. Thorek DLJ, Ogirala A, Beattie BJ, Grimm J (2013) Quantitative imaging of disease signatures through radioactive decay signal conversion. Nat Med 19:1345–1350
76. Das S, Haedicke K, Grimm J (2017) Cerenkov-activated sticky tag for in vivo fluorescence imaging. J Nucl Med 117:198549
77. Spinelli AE, Ferdeghini M, Cavedon C, Zivelonghi E, Calandrino R, Fenzi A, Sbarbati A, Boschi F (2013) First human Cerenkography. J Biomed Opt 18(2):20502
78. Thorek DL, Riedl CC, Grimm J (2014) Clinical Cerenkov luminescence imaging of (18)F-FDG. J Nucl Med 55:95–98
79. Hartl BA, Hirschberg H, Marcu L, Cherry SR, Clinic M (2016) Radiation generated from yttrium-90. J Environ Pathol Toxicol Oncol 35:185–192
80. Kotagiri N, Cooper ML, Rettig M, Egbulefu C, Prior J, Cui G, Karmakar P, Zhou M, Yang X, Sudlow G et al (2018) Radionuclides transform chemotherapeutics into phototherapeutics for precise treatment of disseminated cancer. Nat Commun 9:275
81. Kamkaew A, Cheng L, Goel S, Valdovinos HF, Barnhart TE, Liu Z, Cai W (2016) Cerenkov radiation induced photodynamic therapy using chlorin e6-loaded hollow mesoporous silica nanoparticles. ACS Appl Mater Interfaces 8(40):26630–26637
82. Goel S, Ferreira CA, Chen F, Ellison PA, Siamof CM, Barnhart TE, Cai W (2018) Activatable hybrid nanotheranostics for tetramodal imaging and synergistic photothermal/photodynamic therapy. Adv Mater 30:1–9

Index